New Control Algorithms for the Distributed Generation Interface in Grid-Connected and Micro-grid Systems

by

Yasser Abdel-Rady Ibrahim Mohamed

A thesis
presented to the University of Waterloo
in fulfillment of the
thesis requirement for the degree of
Doctor of Philosophy
in
Electrical and Computer Engineering

Waterloo, Ontario, Canada, 2008

AUTHOR'S DECLARATION

I hereby declare that I am the sole author of this thesis. This is a true copy of the thesis, including any required final revisions, as accepted by my examiners.

I understand that my thesis may be made electronically available to the public.

Abstract

Driven by economic, technical, and environmental reasons, the energy sector is moving into an era where large portions of increases in electrical energy demand will be met through widespread installation of distributed resources or what's known as distributed generation (DG). DG units can operate in parallel to the main grid or in a micro-grid mode. The later is formed by a cluster of DG units connected to a distribution network to maintain the reliability of critical loads, mainly when the grid supply is not available.

Distributed resources include variable frequency sources, high frequency sources, and direct energy conversion sources producing dc voltages or currents. The majority of distributed resources are interfaced to the utility grid or to the customer load via dc-ac pulse-width-modulated (PWM) voltage source inverter (VSI) systems. However, these interfaces introduce new issues, such as the absence of the physical inertia, wide-band of dynamics, limited overload capability, susceptibility to parameters variation, and switching harmonics generation. In addition, the uncertain and dynamic nature of the distribution network challenges the stability and control effectiveness of a grid-connected inverter-based DG interface. Generally, difficulties appear in the form of grid impedance and interfacing parameter variations, fast and slow grid-voltage disturbances, grid distortion and unbalance, and interactions between the inverter ac-side filter and the grid. On the other hand, a micro-grid system will be dominated by inverter-based DG units. Unlike conventional power system generators, inverter-based DG units have no physical inertia. This fact makes the micro-grid system potentially susceptible to oscillations resulting from system disturbances. Severe and random disturbances might be initiated in a micro-grid system, due to load changes, the power sharing mechanism of the inverters and other generators, and interactions between the DG interface and the network.

Motivated by the aforementioned difficulties, this thesis presents new control algorithms for the DG interface that guarantee stable and high power quality injection under the occurrence of network disturbances and uncertainties, in both the grid-connected and micro-grid systems. The control architecture of the proposed DG interface relies on the following subsystems. First, a newly designed deadbeat current regulation scheme is proposed. The proposed design guarantees high power quality current injection under the presence of different disturbing parameters such as grid voltage distortion, interfacing parameter variation, and inverter system delays. Further, it utilizes the maximum dynamic performance of the inverter in a way that provides a high bandwidth and decoupled control performance for the outer control loops. Different topologies of the ac-side filter are considered for the current control design. Second, a novel adaptive discrete-time grid-voltage sensorless interfacing scheme for DG inverters is proposed. The adaptive interface relies on a new interface-monitoring unit that is developed to facilitate accurate and fast estimation of the interfacing impedance parameters and the grid voltage vector (magnitude and position) at the point of common coupling. The estimated grid voltage is utilized to realize a grid-voltage sensorless interfacing scheme, whereas the interfacing parameters are utilized for the self-tuning control and interface-parameter monitoring. Further, a simple and robust synchronization algorithm and a voltage-sensorless average power control loop are proposed to realize an adaptive voltage-sensorless DG interface. The voltage-sensorless interface positively contributes to the elimination of the residual negative sequence and voltage feed-forward compensation errors, and to the robustness of the power sharing mechanism in paralleled inverter systems, where the power-sharing mechanism is generally based on open-loop controllers. Third, a new voltage control scheme for the DG interface featuring fast load voltage regulation and effective mitigation of fast voltage disturbances is proposed. The proposed voltage control scheme targets the problem of fast and large-signal-based voltage disturbances, which is common in typical distribution feeders. A hybrid voltage controller combining a linear with a variable-structure-control element is proposed for the DG interface. Positive and dual-sequence versions of the proposed voltage controller are developed to address the issue of unbalanced voltage disturbances. The proposed voltage controller successfully embeds a wide band of frequency modes through an equivalent internal model. Subsequently, wide range of balanced and unbalanced voltage perturbations, including capacitor-switching disturbances, can be effectively mitigated. Fourth, to constrain the drift of the low frequency modes in a conventional droop-controlled micro-grid, a new transient-based droop controller with adaptive transient-gains is proposed. The proposed power-sharing controller offers an active damping feature that is designed to preserve the dynamic performance and stability of each inverter unit at different loading conditions. Unlike conventional droop controllers, the proposed droop controller yields two-degree of freedom tunable controller. Subsequently, the dynamic performance of the power-sharing mechanism can be adjusted, without affecting the static droop gain, to damp the oscillatory modes of the power-sharing controller.

The overall robust DG interface facilitates a robust micro-grid operation and safe plug-and-play integration of DG units on existing distribution systems; hence increasing the system penetration of DG. The direct result of this development is huge financial saving for utilities by capturing the salient features of deploying DG into existing utility networks. Further, these developments are significant to the industry as they provide the blue print for reliable control algorithms in future DG units, which are expected to operate under challenging system conditions.

Acknowledgements

I would like to express my sincere gratitude to my advisor, Prof. Ehab El-Saadany, for his guidance and support throughout my research work.

I would like to thank Prof. Magdy Salama for his encouragement and support.

I would also like to thank the members of my committee, especially Prof. Gordon J. Savage and Prof. Géza Joós of McGill University.

Lastly, I would like to thank my parents, my wife, and my son for their understanding, continuous support, and encouragement.

Contents

List of Figures

Chapter 1

Introduction

1.1 Background

The environmental regulations due to green house gas emission, the electricity business restructuring, and the recent development in small scale power generation are the main factors driving the energy sector into a new era, where large portions of increases in electrical energy demand will be met through widespread installation of distributed resources or what's known as distributed generation (DG) [1]-[10]. DG facilitates electric power generation in proximity of load centers. As a result, DG can give commercial consumers various options in a wider range of high reliability-low price combinations. In addition, DG could appear as an autonomous power system, which meets both the customer and utility requirements, such as compensation of reactive power and higher harmonic components, compensation of power quality events, power factor correction, peak shaving, backup generation, and voltage reliability enhancement, in a way that is not possible with centralized generation [1]-[10]. DG can operate either in a grid-connected mode or in an islanded mode within a micro-grid [10]. In the micro-grid mode of operation, a cluster of DG units serviced by a distribution system is formed to maintain the reliability of critical loads, mainly when the utility supply is not available.

Environmental-friendly energy sources, such as fuel cells, micro turbines, wind turbines, hydro turbines, and photovoltaic arrays are commonly used to empower DG systems. These energy sources meet both the increasing demand of electric power and environmental regulations. Also, conventional synchronous generators empowered by gas-fired or diesel engines can be used in DG systems. However, the performance of the DG system is mainly dependent on whether the interfacing scheme is based on the direct coupling of rotary machines, such as synchronous or induction generators, or whether the DG system is interfaced via a power electronic converter. Unlike large generators, which are almost exclusively 50/60 Hz synchronous machines, DG units include variable frequency (variable speed) sources (such as wind energy sources), high frequency (high speed) sources (such as micro-turbines), and direct energy conversion sources producing dc voltages or currents (such as fuel cells and photovoltaic sources). The majority of distributed resources are interfaced to the utility grid or to the customer load via dc-ac pulse-width modulated (PWM) voltage source inverter (VSI) systems [2], [10]. Current power electronics technologies facilitate interfacing of different sizes of DG units, ranging from few kW up to 1.6 MW [11]. Modular construction of power electronic converters can increase the power capacity; for example a 50 MW high voltage dc (HVDC) light system, based on insulated gate bipolar transistors (IGBT), has been commissioned in 1999 [12]. Generally, inverter interfaces make the energy sources more flexible in their operation and control as compared to the conventional rotary generators. However, these interfaces introduce new issues, such as the absence of the physical inertia, wide-band of dynamics, limited overload capability, susceptibility to parameters variation, and switching harmonics generation. In addition, when installed in weak and micro-grids, an inverter-based DG system will be subjected to considerable network disturbances and parameter variations caused by the uncertain nature of the distribution system. These disturbances remarkably challenge the stability and control effectiveness of an inverter-based generator.

1.2 Technical Challenges Imposed on an Inverter-Based DG Interface

The dynamic and uncertain nature of a distribution network challenges the control and stability of the DG interface system. The fact that a typical distribution system is faced with unavoidable disturbances and uncertainties complicates the design of a practical inverter-based DG interface. Two scenarios can be considered, the grid-connected mode and the micro-grid mode.

In the grid-connected mode, most of system disturbances are related to the main grid due to the relatively small size of DG energy sources. Various grid disturbances can be imposed on the DG interface. Difficulties occur in the following ways:

1. Depending on the grid configuration, a large set of grid impedance values is yielded as DG is commonly installed in weak grids with long radial distribution feeders [13]-[14]. In addition, cable overload, saturation and temperature effects are all reasons for possible variations in the interfacing impedance seen by the inverter. The interfacing impedance variations directly affect the stability of the inner controls of the DG interface. In addition, the grid impedance interaction with the ac-side

filter of the DG interface might excite high-frequency resonance dynamics. In this case, the injected currents will be highly distorted and it can propagate through the system and drive other voltage and current harmonics.

2. There is a strong trend toward the use of current control for PWM inverters in DG systems [2], [9], [15], which offers the possibility of high power quality injection when it is properly designed. In this approach, it is commonly desired to design the inner current control loop with high bandwidth characteristics to ensure accurate current tracking, shorten the transient period as much as possible, and force the VSI to equivalently act as a current source amplifier within the current loop bandwidth. However, if the current control loop is designed with high bandwidth characteristics (e.g. deadbeat control performance), the sensitivity of the dominant poles of the closed loop current controller becomes very high to uncertainties in the total interfacing impedance (the impedance seen by the inverter at the point of common coupling, which is a function of the grid impedance). The instability of the current control loop accompanied by the saturation effect of the pulse width modulator leads to sustained oscillations in the injected current. This situation is addressed as the low-frequency instability.

3. The voltage at the PCC directly affects the control performance of the DG inverter. Due to the proliferation of nonlinear loads, the grid voltage at the PCC is more likely to be distorted [16]-[17]; particularly in weak grids with long radial distribution feeders. The grid voltage distortion and unbalance drive harmonic currents and increase the distortion in the exported power.

4. Severe and random voltage disturbances might be initiated by grid faults, time-varying loads, non-dispatchable generation, voltage transients associated with parallel connected loads, and voltage transients caused by capacitor switching. The DG interface should offer high immunity and the ability to override these disturbances; particularly in feeders with sensitive loads.

In the micro-grid mode of operation, a cluster of DG units serviced by a distribution system is formed to maintain the reliability of critical loads, mainly when the utility supply is not available. Despite the relatively small power-scale of a micro-grid system, it has many complexities; important among these are:

1. Normally, a micro-grid system will be dominated by inverter-based DG units. Unlike conventional power system generators, inverter-based DG units have no physical inertia. This fact makes the micro-grid system potentially susceptible to

oscillation resulting from system disturbances. Severe and random disturbances might be initiated in a micro-grid system due to load changes, the power sharing mechanism of the inverters and other generators, and interactions between the DG interface and the network.

2. Wide band of dynamic modes can be observed in a micro-grid-connected inverter system [18]. The frequency-scale separation between different modes is the natural result of the time-scale separation between the current, voltage, and power control loops. The dominant low-frequency modes are mainly dictated by the power sharing controllers and the power filters, which are designed with low bandwidth (in the range of 2-10 Hz). Normally, the power sharing mechanism is designed in the sense of a small signal model of the nonlinear power transfer mechanism. In the sense of the small-signal dynamics, it can be shown that as the demanded power of each inverter changes, the low-frequency modes of the power sharing dynamics drift to new locations yielding different dynamic performance. In particular, at higher power demands, the damping active and reactive powers required to stabilize the frequency and voltage, respectively are limited. In this case, the dominant modes of the power sharing dynamics move towards unstable region, making the system more oscillatory and eventually, instability can be yielded. The low damping of the oscillatory power modes yields low-frequency oscillations in the fundamental frequency. Consequently, low-frequency oscillations are imposed on the injected currents and terminal voltages. In addition, the low damping of the power controller modes generates dynamic coupling among the active and reactive power components; yielding poor sharing and might force large transient circulating currents that cause overload and might trip the overcurrent protection of the inverter unit. A micro-grid collapse scenario is very likely to take place due to the low damping of power sharing dynamics and the limited overload capacity (in terms of current and time) of an inverter unit. Unlike conventional rotary generators, inverter-based generators provide a very limited overload capability (normally: 1.2 to 1.5 p.u for less than half a cycle).

3. The load sharing mechanism in a micro-grid is challenging. Centralized control of a micro-grid, based on a communication infrastructure is possible. However, micro-grids in remote areas are characterized with large connection distance between inverters; so it is both impractical and costly to distribute the dynamic sharing signals, which are characterized by their high bandwidth. Autonomous control of micro-grid generators with a capability of close voltage/frequency control characteristics and effective damping of system disturbances should be found.

In the presence of the aforementioned system challenges in both modes of DG operation, other challenging design constraints might be imposed. In particular, the need to reduce the system cost and increase its reliability calls for an interfacing scheme with minimum sensing elements. Along with the reliability and cost enhancements, significant performance enhancements can be obtained by eliminating the grid voltage sensors in the inverter-based DG interface. Among these are: 1) the elimination of the residual negative sequence and voltage feed-forward compensation errors, and 2) the positive contribution to the robustness of the power sharing mechanism. Furthermore, cost and reliability constraints might call for a "function fusion" feature within the DG interface where a single unit can perform multiple tasks, such as grid monitoring, synchronization, and self-commissioning/self-tuning control.

1.3 Research Motivations

The uncertain and dynamic nature of the distribution network challenges the stability and control effectiveness of a grid-connected inverter-based DG interface. Generally, difficulties appear in the form of grid impedance and interfacing parameter variations, grid voltage disturbances, and interaction with existing grid harmonics and unbalance. On the other hand, robust control of a micro-grid system is an issue in the presence of network disturbances.

To facilitate a safe integration and larger penetration of DG, a robust DG interface should be developed to overcome these challenges. In particular, the DG interface should offer the following characteristics:

1. Accurate current control performance with a strong ability of rejecting the grid distortion and voltage disturbances caused by interfacing parameters mismatch; and compensating for inverter system delays.
2. Insensitivity to distribution system and ac-side filter parameters.
3. Grid-voltage sensorless operation with function-fusion to reduce system cost and increase the accuracy and reliability.
4. Fast voltage control performance with strong ability of mitigating fast and dynamic voltage disturbances.
5. Stable and high power quality micro-grid operation along the whole loading trajectories of micro-grid generators.

1.4 Research Objectives

This research aims at broadly developing new control algorithms for the DG interface that guarantee stable and high power quality injection under the occurrence of network disturbances and uncertainties.

To be fulfilled, the above objective needs to evolve and builds upon a number of tasks. Key tasks are:

1. Development of an effective current regulation system for the DG interface capable of high power quality current injection under the presence of grid voltage distortion, interfacing parameter variation, and inverter system delays.
2. Development of an interface-monitoring unit along with a grid-voltage sensorless interfacing scheme for inverter-based DG units.
3. Development of a voltage control system for the DG interface featuring fast load voltage regulation and effective mitigation of fast and dynamic voltage disturbances.
4. Development of an autonomous control strategy of a micro-grid system with effective damping of low frequency modes.
5. Integration of the developed control algorithms to realize a robust DG interface for gird-connected and micro-grid systems.

1.5 Thesis Layout

The remainder of this thesis is structured as follows:

Chapter 2 presents the state-of-the-art and a critical literature survey on DG technologies and controls of an inverter-based DG interface.

Chapter 3 presents newly designed current control schemes for the DG interface. Adaptive deadbeat current controllers are designed for different topologies of the ac-filter to achieve accurate current regulation performance in the presence of grid uncertainties, inverter system delays, and uncertainties; provide enough robustness against grid voltage disturbances, including harmonics and unbalance; and retrain the full compatibility with digital platforms to maintain design flexibility.

Chapter 4 presents an adaptive interface-monitoring unit. Estimation algorithms, based on adaptive observers and neural-network-based identification, are proposed to estimate the grid-voltage at the PCC along with the interfacing parameters seen by the inverter. The estimated quantities are utilized to realize an adaptive grid-voltage sensorless DG interface.

Chapter 5 presents a fast load voltage control scheme for the DG interface. Single and dual-sequence versions of the proposed voltage controller are reported. Further, an evolutionary tuning algorithm is developed to facilitate a structured and optimum tuning methodology for the proposed voltage control scheme. The proposed voltage control scheme provides means for mitigating fast and dynamic voltage disturbances and overriding system voltage unbalance.

Chapter 6 presents an adaptive decentralized power-sharing strategy for micro-grids. A newly designed droop controller, which utilizes a transient droop function along with adaptive gains, is introduced. The adaptive nature of the proposed controller ensures active damping of the power-sharing modes along the micro-grid loading trajectory; subsequently, the proposed scheme significantly contributes to preserving micro-grid stability and reliability.

Chapter 7 presents a novel DG interface, which combines the developed control algorithms to realize a robust and reliable operation under different system disturbances in grid-connected and micro-grid modes of operations while allowing seamless transfer between both modes.

Chapter 8 presents the thesis summary, contributions, and directions for future work.

Chapter 2

Background and Literature Survey

2.1 Introduction

This chapter presents a brief background on different types of DG, and a detailed literature survey on the inverter-based DG interface.

2.2 Distributed Generation

Figure 2.1 shows the common types of energy sources that can be utilized in DG systems. The salient features of these types are briefly introduced in the following subsections.

2.2.1 Micro-turbines

They are small capacity combustion turbines, which can operate using natural gas, propane and other types of fuels. In a simple form, they consist of a compressor, combustor, recuperator, small turbine, and generator [19]-[21]. Sometimes, they have only one moving shaft, and use air or oil for lubrication. Micro-turbines are small scale of 0.4-1.0 m^3 in volume and 20-500 kW in size. Unlike the traditional combustion turbines, micro-turbines run at less temperature and pressure and faster speed (up to 150,000 rpm), which sometimes require no gearbox. The small size is a big advantage of these systems due to the use of high-speed turbines with airfoil bearings. Due to the low price of natural gas, low installation cost, and low maintenance cost, micro-turbines are one of the most promising DG energy sources today [19]-[22].

A micro-turbine generator is interfaced to the gird or load via a power electronic converter; usually a voltage source inverter [2]. Being a dispatchable source, micro-turbines do not cause intermittent generation problems.

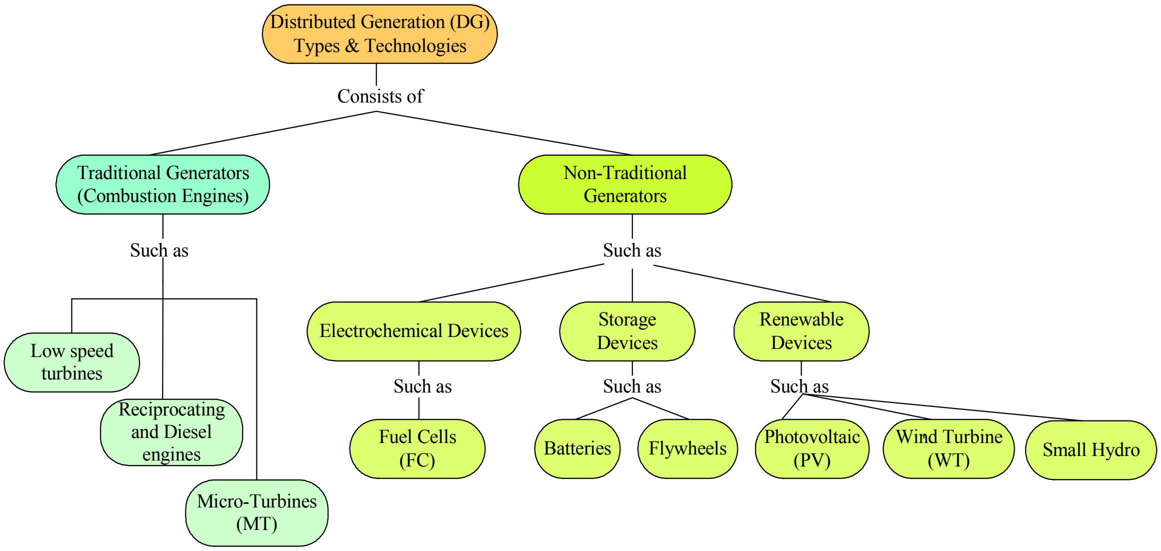

Figure 2.1: Distributed generation energy types and technologies.

2.2.2 Fuel Cells

The fuel cell is a device used to generate electric power and provide thermal energy from chemical energy through electrochemical processes. It can be considered as a battery supplying electric energy as long as its fuels are continued to supply. Unlike batteries, fuel cells do not need to be charged for the consumed materials during the electrochemical process since these materials are continuously supplied [23]-[25]. Fuel cell capacities vary from 1-kW to few MW for portable and stationary units, respectively. It provides clean power and heat for several applications by using gaseous and liquid fuels. Fuel cells can use a variety of hydrogen-rich fuels such as natural gas, gasoline, biogas or propane. They operate at different pressures and temperatures, which vary from atmospheric to hundreds of atmospheric pressure for a wide range of temperatures [23]-[25].

A fuel-cell generator is interfaced to the gird or load via a power electronic converter; usually a voltage source inverter [2]. Being a dispatchable source, fuel cells do not cause intermittent generation problems.

2.2.3 Wind Turbines

Wind energy is not a new form; it has been used for decades in electrical energy production. A wind turbine consists of a rotor, turbine blades, generator, drive or coupling device, shaft, and the nacelle (the turbine head) that contains the gearbox and the generator drive. Modern wind turbines can provide clean electricity as individuals or as wind farms. Wind turbine blades usually are two or three blades. Electricity capacity is limited by the amount of wind, so the wind plants should be installed in windy areas. It has expected electrical efficiency of 20-40%, and the expected power sizes are in the range of 0.3 kW to 5 MW [26]-[33].

There are four types of wind turbines; they are: Type A, B, C and D [33]. Types A, B, and C are connected to the grid or to the load via a rotary machine, normally, an induction generator. Type D, utilizes a full-scale power electronic converter, usually, a voltage source inverter, for grid interfacing [33].

Wind farms have been found in areas with heavy wind profile. Large ratings such as 640 MW have been reported [29]. Due to the large penetration of wind turbines and the chaotic nature of wind power generation, the impact of the wind generation on system performance is remarkable. Extensive research efforts are running in addressing and mitigating the impact of wind turbines on system operation [27], stability [28], planning and reliability [30], power quality [31], pricing and market [32], etc.

2.2.4 Photovoltaic (PV) Systems

The basic unit of a PV array is a cell that may be square or round in shape, made of doped silicon crystal. Cells are connected to form a module or panel and modules are connected to form an array to generate the required power from the sunlight.

Current ratings of PV arrays vary from 0.3 kW to few MW. However, larger sizes of PV generation units are limited. This is because the high cost of land, weak solar intensity in many areas around the world, and climate changes leading to unreliable sun exposure [10], [34]-[35]. Approximately, one acre of land would be needed to provide 150 kW of electricity [10]. Currently, the cost per kW of a PV system is around $6000, whereas it is $900 in micro-turbine generation. The cost per kW of other DG sources can be found in Figure 2.2.

Until the 1990s, the creation of photovoltaic farms (in analogy to wind farms) has been considered the preferred solution to increase the penetration of PV arrays. However, cost issues and the relatively low power generation of these farms made the concept of PV farms un-economical. Small scale distributed PV panels (1-100 kW) yield cost effective solutions with higher reliability. Recently, under the green energy policies adopted by many countries, some interest in large scale PV farms appears. In general, the impact of PV generation profile on the system level, mainly voltage fluctuations and possible harmonic injection, is weak and it can be mitigated by injecting a controlled-reactive power through the PV inverter itself [36]-[37] or via nearby controlled reactive power sources. Therefore, the majority of PV studies are directed either towards the internal controls of the PV generation system for better energy processing and precise power tracking [38] or towards the development of more exotic solar cell technology for greater efficiency and to lower the overall generation cost [39]. It is worth to mention that large wind and PV farms are normally connected at the sub-transmission or transmission levels, where the grid stiffness is higher and the impacts are less pronounced. Therefore, studies related to these farms in the context of distribution systems are not practical and will lead to flawed results.

A PV generator is interfaced to the gird or load via a power electronic converter; usually a voltage source inverter [2].

2.2.5 Other DG Sources

Other renewable energy sources, such as micro-hydro power, bio-energy, geothermal power, ocean thermal power, and ocean wave power can be utilized in DG systems. Currently, these sources are not commonly used due to economical reasons.

2.2.6 Energy Storage Devices

Current technologies enable efficient means of energy storage. Common among these are: batteries, super-capacitors, flywheels, and super-conducting magnetic energy storage [40]. Energy storage devices can have important roles in DG systems, such as enabling fast load pick-up, enhancing the reliability, and flatting the generation profile in non-dispatchable sources [41].

Energy storage generators are interfaced to the gird or load via a power electronic converter; usually a voltage source inverter [2].

2.2.7 Hybrid Systems

To improve the efficiency and generation characteristics, hybrid DG energy sources have been proposed. Recently, a solid oxide fuel cell has been combined with a gas micro-turbine to form a combined cycle power plant. The combined plant has an electrical efficiency of greater than 70% with ratings range from 250 kW to 2.5 MW [10], [43]. High efficiency, such as 75%, can be achieved with combined heat plants as well. Also, the wind energy sources have been utilized with other DG energy sources, such as fuel cells, PV, micro-turbines, energy storage devices or diesel-fired generators, particularly in weak and isolated networks [44].

Figure 2.2 illustrates the salient feature of common energy sources in DG system, from the point of view of rating, capital cost, grid-interfacing technology, efficiency, and

	Micro-turbines	Fuel Cells	Wind–Turbines	Photovoltaic Arrays	Fossil Fuels
Rating	20 - 500 kW	1 kW - 5 MW	0.3 kW - 5 MW	0.3 kW - 2 MW	Up to 100 MW
Capital Cost ($/kW)	900	2,800	3,000	5,500	500-900
Grid/load Interfacing Technology	Power Electronic Converter	Power Electronic Converter	Induction Generator and Power Electronic Converter	Power Electronic Converter	Synchronous Generator
Efficiency	20-30%	40-60%	20-40%	5-15%	33%
Fuel Type	natural gas, hydrogen, biogas, propane, diesel	hydrogen, natural gas, propane	wind	sunlight	Oil, diesel, natural gas, coal, etc.

Figure 2.2: Salient features of common energy sources in DG system.

fuel type. Most of this information has been published by the U.S. Department of Energy in [44].

In current standards, e.g. IEEE Standard 1547-2003 [45] and IEEE Standard 929-2000 [46], DG units are normally disconnected from the ac line when the grid is not present. However, in coming few years where higher penetration of DG will be there, it will be meaningless to discard these backup sources when the grid is not present. Therefore, DG units should be able to work in the islanded mode of operation serving sensitive loads; yielding to remarkable boosts in system reliability. Moreover, in rural and remote areas, where a public grid is not researchable, islanded operation mode is necessary. Figure 2.3 shows a network connection of DG in both modes of operation; Figure 2.3(a) shows a sample radial feeder with DG running parallel to the grid, whereas Figure 2.3(b) shows a sample micro-grid system.

2.3 Inverter-Based DG Interface

Unlike large generators, which are almost exclusively 50/60 Hz synchronous machines, DG includes variable frequency (variable speed) sources (such as wind energy), high

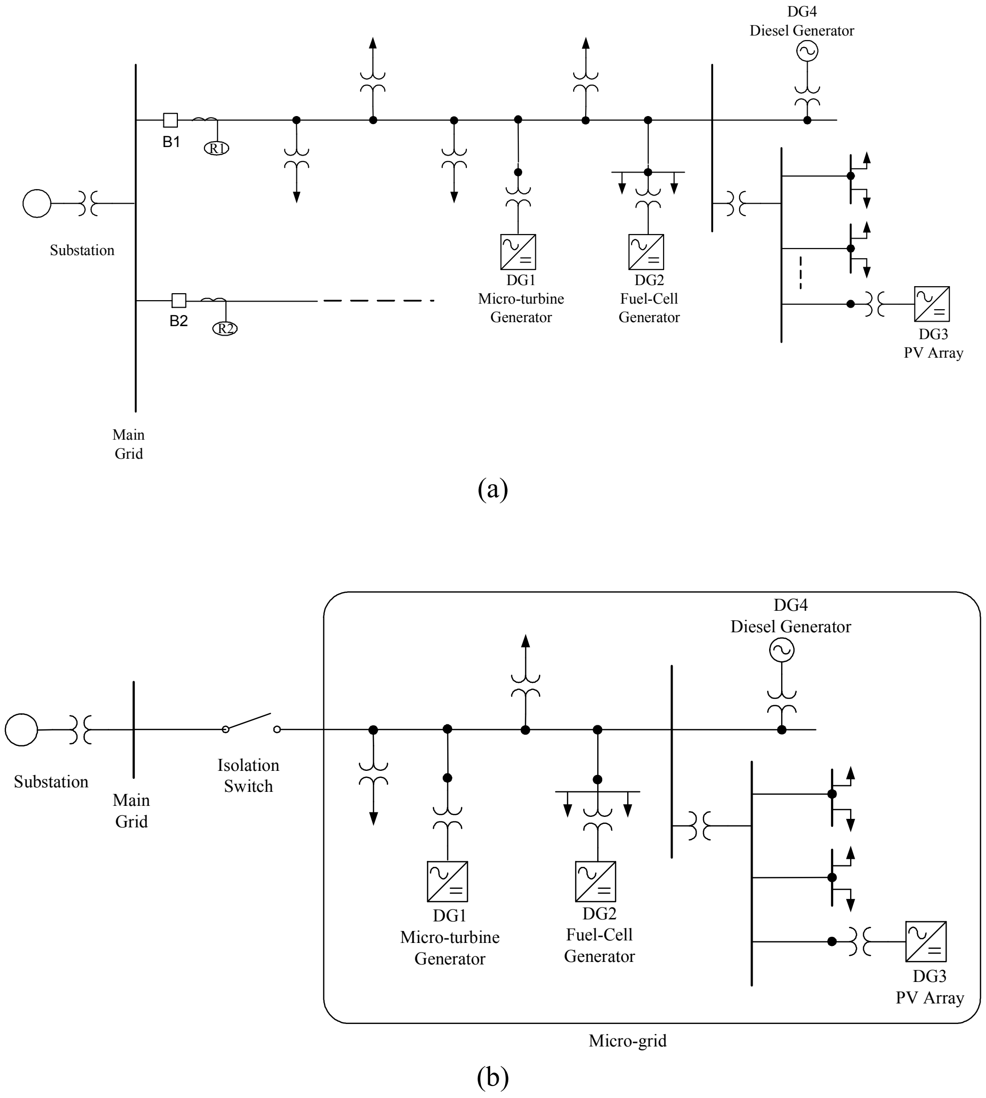

Figure 2.3: Network connection of DG. (a) Grid-connected mode. (b) Micro-grid mode.

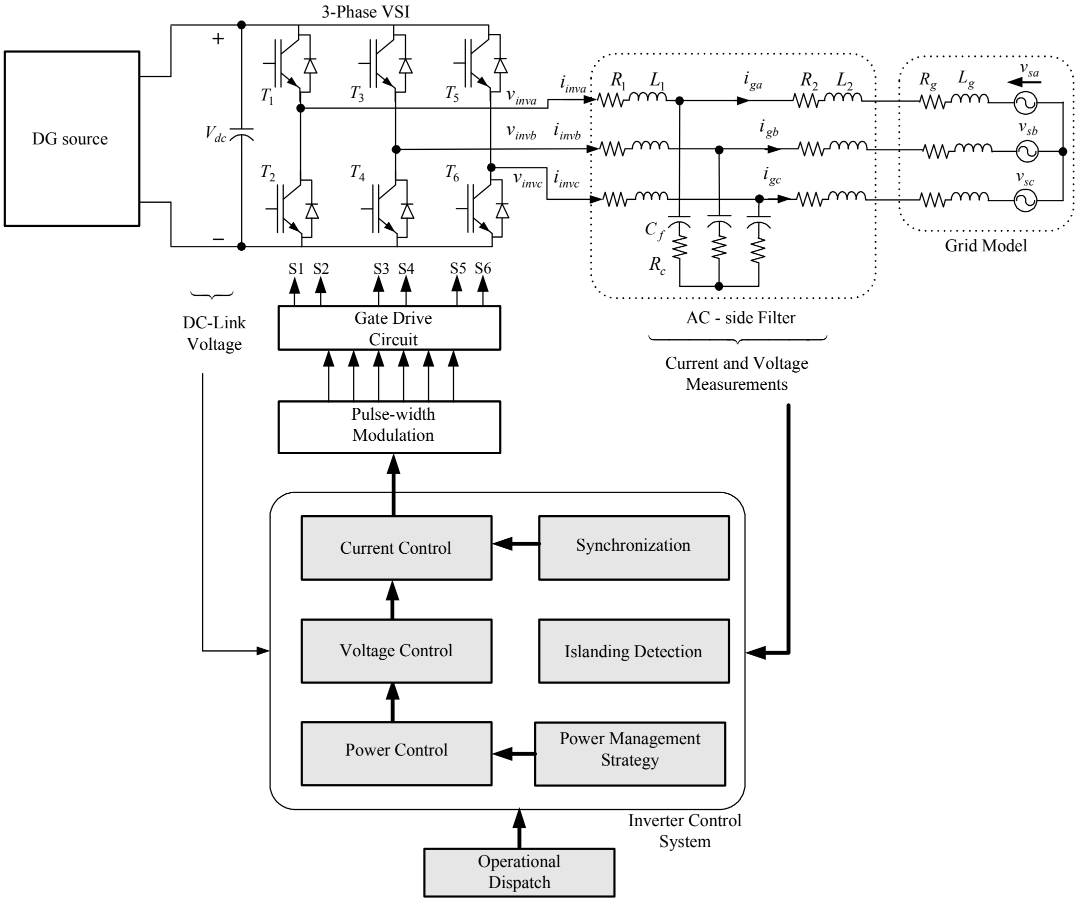

Figure 2.4: Power circuit and control functions of a DG inverter interface.

frequency (high speed) sources (such as micro-turbine generators), and direct energy conversion sources producing dc voltages/currents (such as fuel cells and photovoltaic). In these types of DG units, a voltage source inverter is necessary to facilitate DG interfacing to the utility, as shown in Figure 2.2. The inverter is considered as the most important functional block in the inverter-based DG.

Figure 2.4 shows the power circuit of a DG inverter interface and the associated control functions. A three-leg VSI with an ac-side filter form the power circuit, whereas different control loops form the inverter control structure. The inverter control system should be capable of providing flexible operation. For example, in the grid connected mode, grid voltage regulation might not be required if the grid voltage is stiff. Therefore, the DG unit will behave as a PQ generator and the voltage control will not be an option. On the contrary, if the stiffness of the grid is low, the DG unit might support the voltage profile by working as a PV generator. In the micro-grid mode of operation, voltage regulation might be critical for high power quality injection, whereas the power management and power control functions should take care of close load sharing of micro-grid loads according to the ratings of individual inverters. Regardless of the operation mode, the inner current control loop is necessary in order to have close control characteristics on the injected current and to force the VSI to work as a current-source amplifier within the current control bandwidth. A synchronization method is also required to achieve a controllable power flow.

A PWM scheme would ensure that the inverter current is free from low-order harmonic distortion. However, the high-frequency current distortion due to the switching frequency must be attenuated to cope with the power quality standards for connection of an inverter to the grid [45]; this is the main function of the ac-side filter.

In fact, the behavior of an inverter-based DG unit mainly relies on the effectiveness of the aforementioned control loops. In addition, it will be shown in this research that many of system-level impacts on the generation performance of DG and vice-versa (i.e., DG impacts on system operation) can be addressed by embedding the appropriate mitigation technique in the inverter control structure. This is also the case in the micro-grid system, where the frequency and voltage stability of the micro-grid system lies within the power and voltage controls of individual inverters.

The state-of-the-art of the controls of a DG inverter interface is presented in the following subsections.

2.3.1 Current Control

The current control system of a three-phase PWM-VSI is the key element in the control structure of an inverter-based DG system [2], [9]. The main objectives of the current controller in these applications are to provide a relatively high bandwidth to ensure accurate current tracking; shorten the transient period as much as possible; and force the VSI to equivalently act as a current source amplifier within the current loop bandwidth. In addition, the current loop is responsible for the injected-current power quality and over-current protection. Grid voltage harmonics, unbalance, transients and grid parameters directly affect the current control performance and might impair the power quality, and even the stability of the inverter system. However, it is only recently that the effects of supply harmonics on the control effectiveness of inverter-based DG have begun to be investigated [17], [14], [47]. Investigations in [17] show that small distortion in the grid voltage remarkably increases the total harmonic distortion in the injected current and eventually, inverter instability can be reached due possible interaction between grid distortion and inverter's power circuit filter. Therefore, grid disturbances suppression is one of the important properties that should be found in the current controller in a

VSI-based distributed generator.

The major techniques to regulate the output current of a current-controlled VSI include either a variable switching frequency such as the hysteresis control scheme or fixed-switching frequency schemes, such as the ramp comparison, stationary and synchronous frame proportional-integral (PI), and deadbeat predictive current control schemes [48]-[49]. Hysteresis based schemes give fast transient response; however they are documented to suffer from inter-phase distortion, and poor steady-state performance with errors up to twice the hysteresis band. Moreover, they result in unpredictable average converter switching frequency that varies with the load parameters and consequently the load current harmonics ripple is unpredictable. Even though some methods are reported to constrain the variations in switching frequency [50]-[52], the incompatibility with full-digital platforms and the additional complexity make this scheme far from being practical. Ramp comparison control using a PI regulator in the stationary-frame has a long history of use [53]; however it has the disadvantages of steady-state phase errors and sensitivity to system parameters. Recently, resonant stationary-frame controllers have been proposed to null the phase errors [54]-[56], however, resonant controllers provide internal model dynamics at preset frequency modes, and the tuning process of these controllers is not straightforward [56]. By using the synchronous rotating frame [57]-[58], the PI regulator can be used without the phase lag associated with stationary frame PI regulators. Yet, this scheme does not yield the optimal dynamic response from the converter due to its relatively slow transient response and the non-defined robustness properties.

From the point of view of robustness against grid disturbances, the compensation capability of the low-order harmonics in the case of PI controllers, either in the stationary or the synchronous reference frames, is very poor; yielding a major drawback when they are used in grid-connected and micro-grid systems. Resonant controllers, tuned for selective harmonics elimination, can relax this problem. However, these controllers are tuned at preset frequencies and the stability is not verifiably guaranteed for a large band of harmonic cancellations. These drawbacks are obvious in [17], where a stationary-frame resonant controller for grid-side current regulation is proposed. The same pitfalls can be traced in [47], where resonant synchronous-frame controllers are emerged in the current control structure to mitigate the effect of grid harmonics. An additional drawback of using the resonant controllers, either in the stationary or the synchronous reference-frame, is the interaction with variations in the grid impedance and ac-side filter parameters. Instability is yielded when a mismatch in the grid impedance or ac-side filter parameters shifts the bandwidth of the current controller to be lower than any of the resonant frequencies [14].

Instead of using a resonant controller, a robust high bandwidth current control of a PWM-VSI can extend the capabilities of the inverter controls. Important among these is the high disturbance rejection performance that can be obtained to reject low-order harmonics caused by grid disturbances. In addition, the tracking ability of a high bandwidth current controller makes it feasible to be applied to regulate the current in the natural and stationary reference frames. Hence, the effect of unbalanced grid voltages on the current injection performance can be effectively mitigated. Further, with a high bandwidth current control loop, current profiling can be made feasible. In addition, the internal current dynamics will appear almost ideal to the outer power sharing controls, hence, reducing the coupling among these loops; this is an important feature in micro-grid stability. However, the realization of a high bandwidth current regulation scheme, in the presence of inherent system delays and plant uncertainties, is a challenging task.

A fast transient response of the current control loop can be achieved if the current control loop is designed to yield a deadbeat response. Deadbeat current control techniques [59]-[71] offer the potential of achieving the fastest transient response, more precise current control, zero steady-state error, and full-compatibility with digital-control platforms. Moreover, this control scheme is found to provide the lowest distortion and the lowest current ripples [60]; hence, increasing the power quality of the injected currents[1]. However, inherent plant delays associated with the control voltage calculation, the nature of the PWM inverter as a zero-order-hold (ZOH), and synchronous frame rotation limit the bandwidth of a deadbeat current regulation algorithm and eventually, the deadbeat gain, and accordingly the closed-loop bandwidth, should be reduced to account for system delays. In addition, as a model-based controller, conventional deadbeat current controllers show large sensitivity to plant uncertainties. In the presence of grid harmonics and unbalance, there is no *a priori* knowledge of plant dynamics; i.e. a complete plant model is not known in advance.

Considering the delay issue, there are three approaches to implement a digital deadbeat current controller. First, it can be implemented with a relatively long control period, so that there will be enough space for control voltage calculation and dispatching the reference voltages to the modulator. This approach has been used in [72] to implement a complex multivariable state-feedback current controller. However, in discrete-time control, it is always required to have a short control period to enhance the control precision and to increase the control bandwidth. Therefore, a longer control period results in lower control accuracy and lower bandwidth characteristics, hence, loosing some of the

---

[1] It should be noted that the power quality of the injected currents, in terms of the harmonic content (particularly switching harmonics), unbalance, dc-offset, and uncontrolled transients can be a crucial factor that limits the DG hosting capacity in typical distribution systems.

favorable features of the deadbeat control. In the second approach, the calculation of the control voltage is implemented on programmable logic devices such as erasable programmable read-only memory (EPROM) [60] or field-programmable gate array (FPGA) [61]. In other cases, an FPGA co-processor structure is used in parallel with the main processor to give more computational resources [62]. By this way, the calculation time of the deadbeat algorithm is determined by the access time of the logic device, which is very small as compared to the control period. However, this approach requires additional hardware modules specific to the questioned application; and only simple control algorithm can be implemented due to the high engineering design costs associated with complex programmable logic devices. In the third approach, a small control period is selected and the deadbeat controller is implemented with a delay compensation method. In [63], a delay compensation method employing a feedback of the summation of current errors is proposed. However, this method shows a large overshoot and long transient period. In [64], digital deadbeat controllers for single and three-phase VSIs are proposed. The method compensates for the calculation and sampling delays by employing linear extrapolations for the line-voltage and a predictive observer for the current. However, the stability margin for parameter mismatch is poor. In [65], a discrete-time predictive current controller is proposed. The controller employs a delay compensation method by adopting a predictive observer for the current. However, the algorithm is sensitive to parameter variation. Furthermore, the algorithm does not provide the necessary phase advance for the reference current in order to minimize the phase lag in the measured current.

The nature of the deadbeat controller as a model-based controller makes it sensitive to plant uncertainties. In addition, the sensitivity of the deadbeat algorithm to plant uncertainties increases when the line voltage is estimated [67], [69]. In [69], only 20% error in the load inductance can be tolerated when the back EMF voltage is estimated. The parameter sensitivity issue is further addressed in [60], [68], where a PI regulator is connected in parallel to the deadbeat controller. However, the performance is unsatisfactory as the PI controller is working against unknown error dynamics. In [66], a fuzzy-logic-tuned deadbeat controller is proposed to overcome the parameter sensitivity problems. However, the control algorithm is based on assuming a fundamental back EMF voltage component, and it is complex for real-time implementation. Improved robustness can be achieved by estimating the voltage disturbance, which is caused by uncertainties, and using the estimate in a feed-forward control manner. This technique is employed in [70] and [71]; where the disturbance is estimated using the disturbance observer theory in [70], and the time delay control approach is used in [71]. However in both methods, the disturbance is estimated based on the inverse current dynamics, which yields a noise-prone estimate, and a low pass filter is adopted in the proposed estimators. The phase delay between the real voltage disturbance and the actual voltage disturbance degrades the compensation characteristics and limits the robustness range. Recently, an improved robustness against uncertainties in load inductance is reported in [67] by assuming, instead of zero, the targeted current error at the end of the period k is equal to the difference between the previous two current errors. However, the robustness and stability range is up to 53% mismatch in the load inductance. Even though the robustness range has been extended, the relative stability is still reduced with parameter variation; and there is a chance of instability for an unpredicted change in interfacing inductance and resistance, which remarkably vary with the grid impedance.

A deadbeat current control strategy that guarantees high power quality current-injection under the presence of grid voltage distortion, interfacing parameters variation, and inverter system delays demands special attention.

2.3.2 Voltage Control

Generally, there are two modes of voltage control in inverter-based DG units; they are: voltage control in grid-connected mode and voltage control in the islanded and micro-grid modes. In grid-connected inverters, voltage control can be an option to regulate the grid voltage at the PCC. While this is not allowed in stiff grids, it is a favorable solution in weak grids. Since DG units can be found in remote areas with long radial feeders, voltage support using existing DG units can be a favorable option. In other cases, DG units can be connected near sensitive loads where high voltage quality is required. In this case voltage control is a must. While it might be an option in grid-connected inverters, load-voltage regulation is necessary in the islanded and micro-grid modes, where the power quality is determined by the voltage quality. Being also responsible for the output frequency, the power delivered by the inverter must qualify as being *regulated power*. There are certain requirements in this mode of operation. First, a low total harmonic distortion (THD) of the output voltage must be obtained under different load conditions. This is an important objective as the harmonic currents produced by non-linear loads can remarkably distort the output voltage of the inverter [73]. Hence, affecting the power quality exported to other loads. Second, the inverter should provide effective voltage regulation performance in terms of low voltage dip and fast recovery in the case of load transients and network disturbances. These voltage performance requirements become more challenging when the unbalanced nature of grid/load voltages is considered.

In the both modes, grid-connected and micro-grid, it is the task of the voltage controller to maintain close voltage control characteristics. Therefore, fast load voltage regulation is a necessary requirement in a power distribution and micro-grid systems; particularly in feeders serving voltage-sensitive loads. Severe and random voltage disturbances might be initiated by time-varying loads, such as arc-furnaces [74]; non-dispatchable generation, such as fluctuating output power of wind generation [75] and photovoltaic [76]; voltage transients associated with parallel connected loads, such as line-start induction motors [77]; and voltage transients caused by capacitor switching [78]. These voltage disturbances are stochastic in nature, with durations that vary from a fraction of a cycle to few cycles.

Recently, grid-connected controlled reactive power sources, such as distribution static synchronous compensators (DSTATCOMs) [79]-[80], active power filters (APFs) [81], and inverter-based DG [82] are proposed for load voltage regulation at the PCC. In these applications, three-phase PWM current-controlled VSIs are commonly used, whereas the control algorithm is realized using the axis-theory for balanced three-phase systems. In the typical operation of these custom power devices, a reactive reference current is generated from a voltage controller to regulate the load bus voltage, and an internal current control loop is used to regulate the output current. However, existing voltage regulation techniques yield a relatively slow regulation performance. Typical voltage-recovery times in the range of 0.005-0.06 s with voltage dips of about 0.1-0.4 p.u. are reported [79]-[82]. With these figures, the voltage regulation performance might not be fast enough for voltage-sensitive loads. More importantly, existing voltage regulation schemes cannot mitigate fast voltage disturbances in the sub-cycle range, such as capacitor switching transients. A control structure for controlled-reactive power sources capable of fast voltage regulation and effective mitigation of fast voltage disturbances demands special attention. To date, fast and dynamic voltage disturbances, such as capacitor switching transients, form a major part of the power-quality problems that are left without appropriate mitigation strategy. In fact, a fast voltage regulation performance provides a universal solution to voltage quality problems, where voltage sag, swell and flicker can be inherently mitigated.

Generally, voltage regulation design in shunt-type custom power devices, such as DSTATCOM, APF and inverter-based DG, is twofold: 1) voltage control loop design, and 2) current control loop design. Considering the voltage control loop, several control methods have been reported. Conventionally, PI controllers have been used to generate the reactive current component [80]. However, these linear controllers are working against nonlinear error dynamics. In addition, there is difficulty in designing these controllers to regulate the fundamental frequency voltage and reject higher-frequency disturbances. PI regulators with their pole at zero-frequency cannot achieve fast voltage regulation and certainly cannot mitigate fast voltage disturbances. Similar observations can be found in [81], where a PI-based voltage controller has been added to the APF to regulate the voltage at the PCC. In [79], a nonlinear control based on feedback regulation of system states to the reference values, which are statically related to the reference phase voltage magnitude through system parameters, is proposed for a DSTATCOM. However, the method is complex and requires system parameters adaptation. In addition, the voltage dip due to load disturbance is large, i.e., about 0.3 p.u with a recovery time of about 5 ms. In [82], the DG interface is designed with a fuzzy-logic-based voltage controller to handle the nonlinearity of the voltage control loop. However, the voltage regulation response is sluggish, with a recovery time of about 0.05 s. To ensure perfect regulation of the voltage at the PCC and provide means for rejecting voltage disturbances, the frequency modes of the disturbances to be eliminated should be included in the stable closed loop system. At this condition, the tracking error will not contain these frequency modes. This criterion is satisfied if the voltage controller can supply an internal model [83]. Neither a linear controller nor a nonlinear controller can reject wide band of voltage disturbances unless an internal model for the voltage disturbances is provided. For periodic disturbances, the repetitive control approach can be applied for voltage regulation [84]. However, not all voltage disturbances are periodic by nature. Moreover, the repetitive control is not easy to stabilize for all unknown disturbances and cannot attain very fast response.

Further, a current control loop with high-bandwidth characteristics is necessary to allow accurate tracking of the highly dynamic reference trajectory generated by the voltage controller. This implies that the current controller should provide a good ability to track an arbitrary reference trajectory[2]. This calls for a high bandwidth current control loop. Again, the realization of a high bandwidth current control, in the presence of the system delays and uncertainties imposed by grid interaction, demands a special attention.

2.3.3 Micro-grid Control

While generation control in grid-connected inverters is straightforward, significant complexities appear in the micro-grid mode of operation. A reliable and robust operation of a micro-grid system strongly relies on an efficient control scheme of micro-grid generators. The basic control objective in a micro-grid is to achieve accurate power sharing while maintaining close regulation of the micro-grid voltage magnitude and frequency. Two control approaches can be followed to realize the abovementioned objective; they are: non-communication-based control and communication-based control [10], [18], [85]-[87].

---

[2] If the control loop is designed to offer a very fast step response, arbitrary trajectory tracking can be feasible.

Communication-based control of a micro-grid system relies on sharing control information among different generators. This technique requires a centralized micro-grid controller, which receives the terminal information of each inverter and loads to dispatch the inverter units at different load conditions [85]. There are many drawbacks in communication-based approach. First, high bandwidth communication infrastructure is needed to share the dynamic sharing information; this in an impractical and costly solution in micro-grids with long connection distances between inverters. Second, having one unit acting as a master provides a possibility for the occurrence of a single point failure. Third, the need to distribute control signals reduces the reliability of the micro-grid system, where the control information is critical for system operation. The reliability issues of the centralized control approach might counteract the positive reliability boosts gained by implementing DG micro-grids. Fourth, unlike conventional large power systems, the load profile of a micro-grid system is not predictable in advance. This fact imposes difficulties on the design of the dispatch algorithm.

Non-communication-based control relies on the ability of individual DG units to regulate the output voltage and frequency while sharing the active and reactive power demands. Signal injection is used as a decentralized power sharing mechanism in paralleled-inverters system [8]. However, the complexity of signal injection and the robustness of measuring output power variations caused by the injected signal make this scheme far from being practical. A simple non-communication-based power sharing strategy can be realized in the sense of frequency and voltage droop method. Following the same approach in conventional power system with multiple generators, the generators share the active power by drooping the frequency of each generator with the real output power delivered by the generator [87]-[88]. This allows each generator to take up changes in total load in a manner determined by its frequency droop characteristic, and essentially utilizes the system frequency as a virtual communication link between the generator control systems. Similarly, a droop in the voltage magnitude with the reactive power is used to ensure reactive power sharing.

The advantage of the droop method is that it does not require communication signals amongst units in parallel; thereby increasing the reliability of the system and reducing the cost significantly. Therefore, the droop method appears to be the standard control strategy in future micro-grid systems. However, because of the droop characteristics, the frequency and amplitude of the system voltage might drop to such a value that all unit will be operating in a new lower frequency and voltage that are different than the nominal values. Another drawback of this method is the lack of robustness against voltage measurement errors. Errors in the voltage/current measurement feedback signals can significantly affect the power sharing performance. This is due to the lack of the closed loop control on the power sharing performance [18].

In the context of micro-gird control, few results have been reported. In [18], [86]-[88], a static droop controller is utilized for power sharing. In [89], an enhanced droop control featuring a transient droop performance is proposed. To improve the active and reactive power decoupling performance, improved droop controllers with virtual output impedance are reported [89]-[90]. To account for nonlinear load sharing, harmonic droop controller is reported in [73], [91]. In fact, the power-sharing controller dictates the low-frequency dynamics of the inverter due to the time-scale separation between the power and current dynamics. However, existing droop controllers are synthesized in the sense of the small-signal model of the power transfer mechanisms; this can yield acceptable results for small load variation. While small variations in the power angle are expected in the normal operation of a conventional generator, large steps in the power angle command are expected in an inverter-based generator in a micro-grid. This is because of the absence of the concept of "base-load" in a micro-grid; in this case, inverters will be subjected to various loading conditions. In the sense of micro-grid dynamics, it can be shown that as the demanded power of each inverter changes, the low-frequency modes of the power sharing dynamics drift to new locations yielding different dynamic performance. In particular, at higher power demands, the damping active/reactive powers required to stabilize the frequency/voltage are limited. In this case, the dominant modes of the power sharing dynamics move towards unstable region, making the system more oscillatory and eventually, instability can be yielded. The low damping of the oscillatory power modes yields low-frequency oscillations in the fundamental-voltage frequency, and low-frequency oscillations will be imposed on the injected currents, which might excite unstable dynamics. In addition, the low damping of the power sharing modes generates large transient currents that might overload and trip the over-current protection of an inverter-based DG unit. The mismatch between load and generation can collapse the micro-grid system. Accordingly, a micro-grid collapse scenario is very likely to take place due to the low damping of power sharing dynamics and the limited overload capacity, in terms of current and time, of an inverter unit. Unlike conventional rotary generators, inverter-based generators provide a very limited overload capability (normally 1.2 to 1.5 p.u for less than half a cycle) [92].

The development of an autonomous power sharing strategy for micro-grid inverters with effective damping of low frequency modes demands special attention.

2.3.4 Effect of Grid Impedance and Harmonic Excitation

An inverter-based DG unit is a multi-input-multi-output nonlinear system with coupled dynamics. Wide range of dynamics can be observed in a VSI system, starting from the low frequency power generation/sharing dynamics (in the range of few Hz) to the high frequency dynamics of the ac-side filter (in the range of few kHz). With the uncertain nature of a distribution network, there is a possibility for dynamic interactions between the inverter and the network dynamics.

Of significant effect, the grid impedance can shift the resonance frequency of the ac-side filter of the DG inverter. The presence of grid harmonics gives chances to harmonic excitation. Additionally, uncertainty in the interfacing impedance (which is a function of the grid impedance) affects the stability of the current control.

To date, few studies have addressed the interaction issues of the DG interface with grid dynamics. The effect of grid impedance on the stability of the DG inverter is addressed to some extent in [14]. However, the study considered only the case of resonant current controllers. Furthermore, the provided solution depends on accurate knowledge of the grid impedance, which is an optimistic assumption.

2.3.5 Other Design Constraints

In the presence of the aforementioned system challenges in both modes of DG operation, other design constraints might be imposed. In particular, the need to reduce the system cost and increase its reliability calls for an interfacing scheme with a reduced number of sensors. Along with the reliability and cost enhancements, significant performance enhancements can be obtained by eliminating the grid voltage sensors in an inverter-based DG interface. The grid voltage is key information in a typical DG interface control system. Signal processing functions, such as sequence detection and phase locked loop (PLL) are performed on the voltage signals. However, when the grid voltage is measured, errors, such as a residual negative sequence and an accumulated grid vector position error are yielded. In addition, errors in the voltage measurement signals used for the feedback control can significantly affect the power sharing in micro-grid operation, due to the open loop nature of the power-sharing controllers. Voltage measurement errors may result from the voltage sensors or sensor-filters not quite being precisely identical. Since the injected currents are so sensitive to minute variations in the voltage command, which highly depends on the feed-forward components and the synchronization angle, it seems appropriate to design the control system without using grid-voltage sensors. This is addressed as a grid-voltage sensorless interfacing scheme, where the voltage information is estimated based on the current measurements. By this way, the extreme sensitivity to voltage measurements would be avoided.

Investigations on the sensorless operation of PWM rectifiers are reported [93]-[94]. The principle of direct power control is applied to realize voltage sensorless control of a PWM rectifier system [93]. In [94], a direct control of the converter instantaneous current, based on the direct power control and the estimation of the line voltage waveform, is proposed. The aforementioned voltage-sensorless control schemes, however, assume precise knowledge of the grid impedance parameters at the PCC. On the distribution level, distribution system parameters are time-varying and directly impact the performance of the control and estimation algorithms. Generally, any model-based grid-voltage estimator is by nature parameter-dependent. While the grid and interfacing parameters are time varying, the sensitivity of the interface control system to uncertainties in the interfacing impedance becomes higher as the voltage estimator dynamics is dependent on system parameters. The development of a robust grid voltage sensorless interfacing scheme for inverter-based DG demands special attention.

Additionally, cost and reliability constraints might call for a functions-fusion feature within the DG interface, where a single unit can perform multiple tasks, such as grid monitoring, synchronization, and self-commissioning/self-tuning control. A single unit that performs these functions in a computationally efficient manner has to be investigated.

2.4 Summary

In this chapter, a critical literature survey on the control techniques utilized in the inverter-based DG interface has been presented. The main outcome of this chapter is to pinpoint the lack of robustness in existing control strategies against grid/micro-grid disturbances. Accordingly, the development of new control strategies for the DG interface that overcome the aforementioned difficulties demands a special attention.

Chapter 3

New Current Control Algorithms for the DG Interface

3.1 Introduction

The current control system of a three-phase PWM-VSI is the key element in the control structure of an inverter-based DG system. In fact, the generation and power quality performance mainly depend on how well the injected current vector is regulated.

Depending on the topology of the power circuit of the inverter, two cases can be considered for current control design. First: inverter output current control, which is the case when the ac-side filter is either a single inductor (L) or an inductor-capacitor (LC) with inductor current control. Second: grid-side current control, which is the case when a decoupling inductor is used at the grid side along with the LC ac-side filter to form a T-type ac-side filter. The decoupling inductor is used to increase the decoupling between the active and reactive power components of the inverter, and/or to enhance the switching harmonics filtration with lower sizes of the LC filter. This is an important feature for small-scale inverters, such as photovoltaic inverters, to reduce the filter size and ease the packaging. However, due to the additional dynamics imposed by the T-filter, the control complexity increases.

This chapter presents newly designed current control algorithms for a VSI-based DG interface. The main design criteria are: to achieve accurate current regulation performance in the presence of grid and inverter system uncertainties, to provide enough robustness against grid voltage disturbances, including harmonics and unbalance, and to retrain the full compatibility with digital platforms to maintain design flexibility. First, the case of inverter output current control is considered. To achieve high bandwidth current control characteristics, a digital deadbeat current controller with delay compensation is adopted. The delay compensation method forces the delays elements, which are caused by voltage calculation, PWM, and synchronous frame rotation to be equivalently placed outside the close loop control system. Hence, their effect on the closed loop stability is eliminated and the current controller can be designed with a higher bandwidth. To ensure perfect tracking of the output current in the presence of grid disturbances and interfacing parameter variations, an adaptive uncertainty estimator is included within the current feedback structure. The estimated uncertainty dynamics provide the necessary energy shaping in the inverter control voltage to attenuate grid voltage disturbances and other voltage disturbances caused by interfacing parameter variation. Second, the case of grid-side current control in a DG interface with a T-type filter is considered. A modified power circuit model is presented. Then, a new grid-current control strategy, based on the intermediate voltage control with delay compensation, is presented. To ensure perfect tracking and high disturbance rejection of grid distortion, an adaptive uncertainty estimator for the intermediate voltage and grid-side current dynamics is included within the current feedback structure.

The remainder of this chapter is organized as follows. In Section 3.2, the proposed inverter output current control algorithm and the associated comparative evaluation results are presented. In Section 3.3, the proposed grid-side current control algorithm and the associated comparative evaluation results are presented. A summary is drawn in Section 3.4.

3.2 Inverter Output Current Control

3.2.1 System Configuration and Modeling

A system topology of a 3-phase grid-connected output-current-controlled VSI incorporated with the proposed inverter output current control scheme is depicted in Figure 3.1, where R and L represent the equivalent interfacing resistance and inductance seen by the inverter, respectively; $\boldsymbol{v}_s$ is the grid voltage; $\boldsymbol{v}_{inv}$ is the inverter output voltage; and $\boldsymbol{i}_{inv}$ is the inverter output current.

To impose an arbitrary current in the inductive R-L impedance, a current controller is usually adopted to shape the voltage applied on the inductor so that minimum current error is achieved. A PWM scheme would ensure that the inverter current is free from low-order harmonic distortion. However, the high-frequency current distortion due to the switching frequency must be attenuated to cope with the power quality standards for connection of an inverter to the grid [45]; this is the main function of the ac-side filter. Also, the current controller should not allow system uncertainties and disturbances, such as pre-existing grid voltage distortion and parameter variations, to drive harmonic

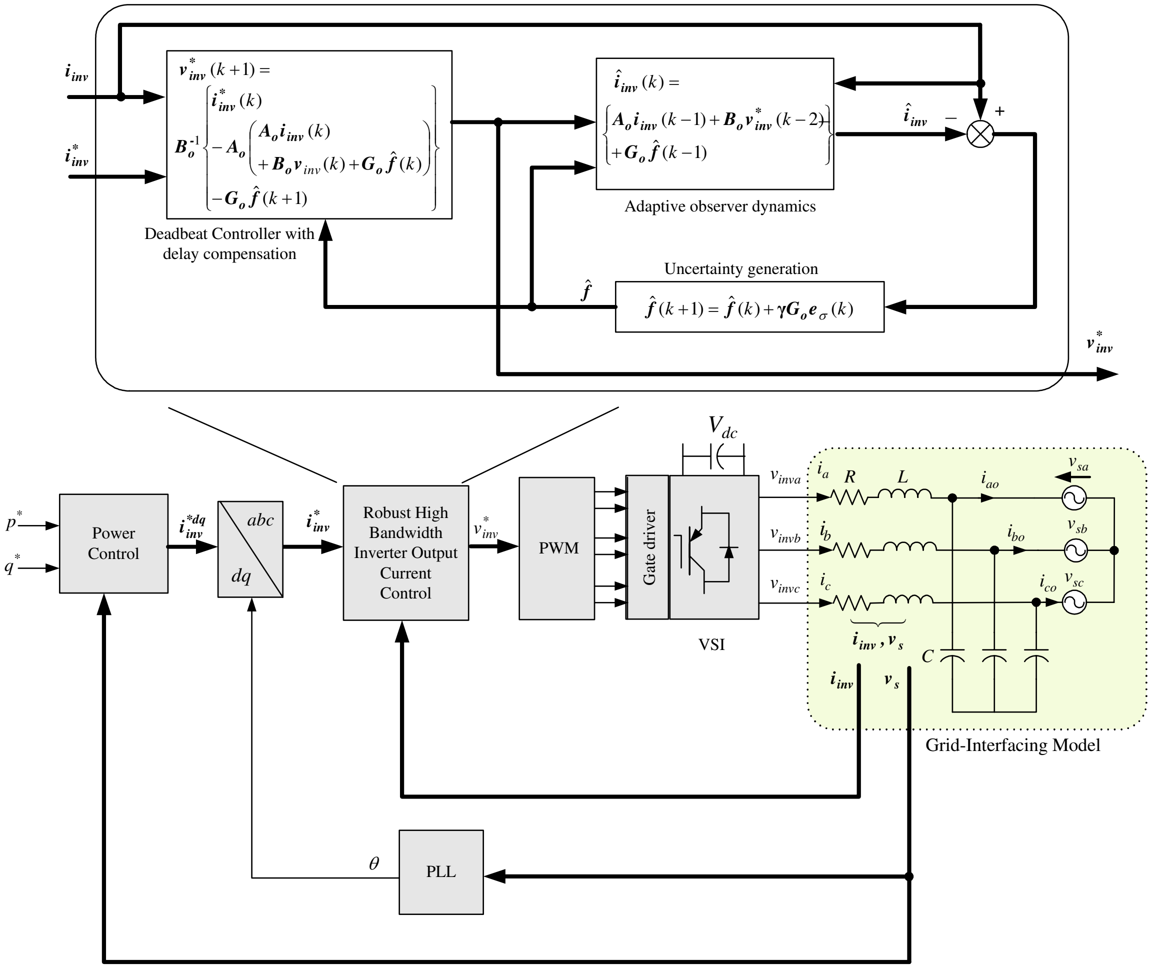

Figure 3.1: Proposed inverter output current control scheme.

currents through the inverter. The development of a robust high bandwidth current regulation scheme, which satisfies these requirements, is the main focus of this chapter.

If the current controller is designed with high bandwidth characteristics, it is possible to carry out the current regulation in any reference frame. In particular, the natural reference frame can be a viable candidate for current regulation to handle the grid voltage unbalance and harmonics with low complexity. In the natural reference-frame, the current dynamics can be represented by the following equation:

$$\frac{d\boldsymbol{i}_{inv}}{dt} = \boldsymbol{A}_c\boldsymbol{i}_{inv} + \boldsymbol{B}_c\boldsymbol{v}_{inv} + \boldsymbol{G}_c\boldsymbol{v}_s \tag{3.1}$$

where

$$\boldsymbol{i}_{inv} = \begin{bmatrix} i_{inva} & i_{invb} & i_{invc} \end{bmatrix}^T \qquad \boldsymbol{A}_c = \begin{bmatrix} -R/L & 0 & 0 \\ 0 & -R/L & 0 \\ 0 & 0 & -R/L \end{bmatrix}$$

$$\boldsymbol{v}_{inv} = \begin{bmatrix} v_{inva} & v_{invb} & v_{invc} \end{bmatrix}^T \qquad \boldsymbol{B}_c = \begin{bmatrix} 1/L & 0 & 0 \\ 0 & 1/L & 0 \\ 0 & 0 & 1/L \end{bmatrix}$$

$$\boldsymbol{v}_s = \begin{bmatrix} v_{sa} & v_{sb} & v_{sc} \end{bmatrix}^T \qquad \boldsymbol{G}_c = \begin{bmatrix} -1/L & 0 & 0 \\ 0 & -1/L & 0 \\ 0 & 0 & -1/L \end{bmatrix}.$$

Using the nominal system parameters and considering the grid voltages as dynamic disturbances, (3.1) can be rewritten as follows:

$$\frac{d\boldsymbol{i}_{inv}}{dt} = \boldsymbol{A}_{co}\boldsymbol{i}_{inv} + \boldsymbol{B}_{co}\boldsymbol{v}_{inv} + \boldsymbol{G}_{co}\boldsymbol{f} \tag{3.2}$$

where the subscript "o" denotes the nominal value; and $\boldsymbol{f}$ represents the lump of uncertainties caused by parameter variation, grid voltage disturbance, and other un-modeled dynamics; and it is given by

$$\boldsymbol{f} = \Delta R\boldsymbol{i}_{inv} + \Delta L\frac{d\boldsymbol{i}_{inv}}{dt} + \boldsymbol{v}_s + \boldsymbol{n} \tag{3.3}$$

where $R = R_o + \Delta R$, $L = L_o + \Delta L$, and $\boldsymbol{n}$ represents other uncertainties due to un-modeled dynamics.

Considering the physical constraints, the preceding model is subjected to the following limits. The load current is limited to the maximum continuous current of the inverter or to the maximum available current of the inverter in a limited short-time operation. The load voltage is limited to the maximum available output voltage of the inverter depending on the dc-link voltage.

For a symmetric inverter output voltage, the PWM-VSI can be assumed as a zero-order hold circuit with a transfer function $H(s)$:

$$H(s) = \frac{1 - e^{-sT}}{s} \tag{3.4}$$

where T is the discrete-time control sampling period and s is the Laplace operator.

For digital implementation of the control algorithm, the current dynamics in (3.2) can be represented in a discrete-time domain with the conversion $H(s)$ in (3.4), as follows:

$$\boldsymbol{i}_{inv}(k+1) = \boldsymbol{A}_o\boldsymbol{i}_{inv}(k) + \boldsymbol{B}_o\boldsymbol{v}_{inv}(k) + \boldsymbol{G}_o\boldsymbol{f}(k) \tag{3.5}$$

where $\boldsymbol{A}_o$, $\boldsymbol{B}_o$, and $\boldsymbol{G}_o$ are the nominal sampled equivalents of the continuous-time system matrices; and k is the iteration integer.

If the continuous system in (3.2) is sampled with interval T, which is much shorter than the load time constant, then the matrices of the discrete-time system $\boldsymbol{A}_o$, $\boldsymbol{B}_o$, and $\boldsymbol{G}_o$ can be obtained by Taylor's expansion as follows:

$$\begin{aligned}
\boldsymbol{A}_o &\simeq \begin{bmatrix} 1-TR_o/L_o & 0 & 0 \\ 0 & 1-TR_o/L_o & 0 \\ 0 & 0 & 1-TR_o/L_o \end{bmatrix} \\
\boldsymbol{B}_o &\simeq \begin{bmatrix} T/L_o & 0 & 0 \\ 0 & T/L_o & 0 \\ 0 & 0 & T/L_o \end{bmatrix} \\
\boldsymbol{G}_o &\simeq \begin{bmatrix} -T/L_o & 0 & 0 \\ 0 & -T/L_o & 0 \\ 0 & 0 & -T/L_o \end{bmatrix}.
\end{aligned} \tag{3.6}$$

3.2.2 Inverter Output Current Control Design

Assuming that the lump of uncertainties $\boldsymbol{f}(k)$ is known, and by using the discrete-time dynamics in (3.5), the conventional deadbeat current control performance [59] can be realized by the following control effort:

$$\boldsymbol{v}_{inv}^{*}(k) = \boldsymbol{B}_o^{-1}\left\{\boldsymbol{i}_{inv}^{*}(k+1) - \boldsymbol{A}_o\boldsymbol{i}_{inv}(k) - \boldsymbol{G}_o\boldsymbol{f}(k)\right\} \tag{3.7}$$

where the subscript "*" denotes reference values.

The control law in (3.7) doesn't account for system delays by assuming that the control period is much longer than the calculation time of (3.7). Practically, when the control period is chosen to be small in order to enhance the bandwidth, inherent and non-negligible delays associated with the implementation of the digital control scheme reduces the stability margins; particularly when high feedback gains are used. The control timing sequence of a practical digital current controller can be explained as follows. The k^{th} cycle generated by the PWM generator starts the control process. The synchronous sampling process starts at the k^{th} cycle. The calculation time of the control algorithm should end before the $(k+1)^{th}$ cycle, and the command voltage is uploaded into the PWM generator just before the $(k+1)^{th}$ cycle. During the $(k+1)^{th}$ period of the control process, the control voltages, which are calculated in the previous period, are applied to the load via the VSI. The resultant phase currents are sensed in the beginning of the $(k+2)^{th}$ cycle. Hence, from the starting time of the current control to the sensing time of the resultant phase currents, there are two-sampling-period delays. Physically, one sampling delay is caused by the calculation time of the digital control law, and the second is caused by the nature of the PWM-VSI as zero-order-hold. Usually, the controller bandwidth is reduced in order to account for practical system's delays. This results in lower control accuracy and failure to achieve a transient-following controller. On the other hand, if the delay effect is appropriately compensated, the bandwidth criterion is relaxed. In fact, the compensation of the time delay significantly increases the current controller bandwidth without increasing the inverter's switching frequency.

In order to enhance the bandwidth characteristics, in the presence of system delays, a new deadbeat current control is proposed. During the $(k+1)^{th}$ period of the control process, the current is forced by the control voltage $\boldsymbol{v}_{inv}(k+1)$ which is calculated in the k^{th} period. The resultant current, which is sensed at the beginning of the $(k+2)^{th}$ period, can be given by

$$\boldsymbol{i}_{inv}(k+2) = \boldsymbol{A}_o \boldsymbol{i}_{inv}(k+1) + \boldsymbol{B}_o \boldsymbol{v}_{inv}(k+1) + \boldsymbol{G}_o \boldsymbol{f}(k+1). \tag{3.8}$$

It is obvious that the current vector $\boldsymbol{i}_{inv}(k+2)$ is affected by the current vector $\boldsymbol{i}_{inv}(k+1)$ and the control voltage $\boldsymbol{v}_{inv}(k+1)$. By using the current vector $\boldsymbol{i}_{inv}(k+1)$, which is affected by the control voltage $\boldsymbol{v}_{inv}(k)$, the current vector $\boldsymbol{i}_{inv}(k+2)$ can be given by

$$\boldsymbol{i}_{inv}(k+2) = \boldsymbol{A}_o \left(\boldsymbol{A}_o i_{inv}(k) + \boldsymbol{B}_o \boldsymbol{v}_{inv}(k) + \boldsymbol{G}_o \boldsymbol{f}(k) \right) + \boldsymbol{B}_o \boldsymbol{v}_{inv}(k+1) + \boldsymbol{G}_o \boldsymbol{f}(k+1). \tag{3.9}$$

For current regulation, the current vector $\boldsymbol{i}_{inv}(k+2)$ can be regarded as the reference current vector. Accordingly, the appropriate control voltage can be predictably obtained as

$$\boldsymbol{v}^{*}_{inv}(k+1) = \boldsymbol{B}_o^{-1} \left\{ \boldsymbol{i}^{*}_{inv}(k+2) - \boldsymbol{A}_o \left(\boldsymbol{A}_o \mathbf{i}_{inv}(k) + \boldsymbol{B}_o \boldsymbol{v}_{inv}(k) + \boldsymbol{G}_o \boldsymbol{f}(k) \right) - \boldsymbol{G}_o \boldsymbol{f}(k+1) \right\}. \tag{3.10}$$

According to (3.10), the control voltage can be calculated with the measured quantities at the k^{th} sample; and the two-sample delay is equivalently removed outside the closed loop control to appear in the two-step ahead reference current vector. Under the assumption of known uncertainty dynamics $\boldsymbol{f}$, and by using (3.10), the output current vector can be given as

$$\boldsymbol{i}_{inv}(k) = \boldsymbol{i}^{*}_{inv}(k-2). \tag{3.11}$$

Therefore, a unity gain and a phase lag corresponding to the two-sampling-period delay, which is equivalently removed outside the closed loop to appear in the reference side, are yielded. To compensate for this delay at the power frequency, an equal and opposite phase shift is added to the reference trajectory using

$$H(e^{j\omega}) = e^{2j\omega_1 T} \tag{3.12}$$

where ω_1 is the supply fundamental angular frequency.

Unlike conventional model-based current controllers, where the grid voltage is usually measured or estimated by linear extrapolations [64] or by assuming it to be constant over 2 or 3 sampling periods [69], the proposed controller utilizes the one-step-ahead uncertainty dynamics $\boldsymbol{f}(k+1)$, which can be robustly predicted through a predictive uncertainty estimation algorithm as described below. The predictive nature of the proposed estimator has the necessary phase advance of the estimated disturbance, which compensates for system delays.

Generally, any implementation strategy of a model-based current controller is by nature parameter dependent. As seen in (3.11), robust control voltage generation can be achieved if the uncertainty dynamics $\boldsymbol{f}$ is known. However, in practical applications, the interfacing system parameters are subjected to considerable uncertainties. Furthermore, the grid voltage acts as a disturbance on the current dynamics and is not usually measurable. Therefore, a robust inverter output current control method is proposed. The robust controller is realized, with low computational demand, by including an adaptive internal model for the estimated uncertainty dynamics within the current feedback structure. The inclusion of the estimated uncertainty dynamics provides an efficient solution for attenuating the effects of the grid-voltage harmonics on the current control performance. This is because the frequency modes of the disturbances to be eliminated are included in the stable closed loop system. As a result, the controller can introduce very high attenuation at different frequency modes corresponding to the grid-voltage harmonics and other system uncertainties.

By considering the calculation delay, (3.5) can be re-written as

$$\boldsymbol{i}_{inv}(k) = \boldsymbol{A}_o \boldsymbol{i}_{inv}(k-1) + \boldsymbol{B}_o \boldsymbol{v}^*_{inv}(k-2) + \boldsymbol{G}_o \boldsymbol{f}(k-1). \tag{3.13}$$

Assuming that the nonlinearities associated with the inverter operation (particularly the blanking time and the voltage limitation effects) are properly compensated, the actual voltage components can be replaced with the reference ones, denoted by $\boldsymbol{v}^*_{inv}$ in (3.13). This assumption is justified by considering that the inverter's switching period is much smaller than the circuit time constant. As a result, the direct measurements which are affected by the modulation and acquisition noise are avoided.

To estimate unknown uncertainty dynamics $\boldsymbol{f}$, an adaptive natural observer with the following input/output relation can be constructed:

$$\hat{\boldsymbol{i}}_{inv}(k) = \boldsymbol{A}_o i_{inv}(k-1) + \boldsymbol{B}_o \boldsymbol{v}^*_{inv}(k-2) + \boldsymbol{G}_o \hat{\boldsymbol{f}}(k-1) \tag{3.14}$$

where the subscript "ˆ" denotes estimated values. Under the same input voltage and disturbance, the estimated state vector approaches the actual state vector even though the observer in (3.14) has an open loop structure. Therefore, convergence of the proposed observer can be achieved with an appropriate disturbance voltage adaptation using the estimation error. The estimation error vector can be defined as

$$\boldsymbol{e}_{\sigma}(k) \equiv \boldsymbol{i}_{inv}(k) - \hat{\boldsymbol{i}}_{inv}(k). \tag{3.15}$$

To derive the estimation algorithm, a discrete-type quadratic error function is defined as follows:

$$E(k) = \frac{1}{2}\boldsymbol{e}_{\sigma}^{T}(k)\boldsymbol{e}_{\sigma}(k). \tag{3.16}$$

The disturbance voltage can be adaptively estimated by minimizing the error function $E(k)$ by applying the generalized integral adaptation rule [95]. This algorithm yields a simple adaptation law in the present online estimation problem. In order to minimize the error function, one can evaluate the following Jacobian:

$$\boldsymbol{J} = \frac{\partial E}{\partial \hat{\boldsymbol{f}}} = \frac{\partial E}{\partial \hat{\boldsymbol{i}}_{inv}} \frac{\partial \hat{\boldsymbol{i}}_{inv}}{\partial \hat{\boldsymbol{f}}} = -\boldsymbol{G}_{o}\boldsymbol{e}_{\sigma}. \tag{3.17}$$

Therefore, the change in the estimate is calculated as

$$\begin{aligned} \hat{\boldsymbol{f}}(k+1) &= \hat{\boldsymbol{f}}(k) + \Delta\hat{\boldsymbol{f}}(k) = \hat{\boldsymbol{f}}(k) - \boldsymbol{\gamma}\boldsymbol{J} \\ &= \hat{\boldsymbol{f}}(k) + \boldsymbol{\gamma}\boldsymbol{G}_{o}\boldsymbol{e}_{\sigma}(k). \end{aligned} \tag{3.18}$$

where $\boldsymbol{\gamma}$ is a positive adaptation gain matrix.

The adaptive estimation law in (3.18) provides a simple iterative gradient algorithm designed to minimize (3.16). As a result, the estimate can be reliably used to embed an internal model for the uncertainty function within the current feedback structure, resulting in equivalent control to cancel the voltage disturbances.

The estimated uncertainty function can be used to robustly calculate the control voltage as follows:

$$\boldsymbol{v}_{inv}^{*}(k+1) = \boldsymbol{B}_{o}^{-1}\left\{\boldsymbol{i}_{inv}^{*}(k+2) - \boldsymbol{A}_{o}\left(\boldsymbol{A}_{o}\boldsymbol{i}_{inv}(k) + \boldsymbol{B}_{o}\boldsymbol{v}_{inv}(k) + \boldsymbol{G}_{o}\hat{\boldsymbol{f}}(k)\right) - \boldsymbol{G}_{o}\hat{\boldsymbol{f}}(k+1)\right\}. \tag{3.19}$$

The simplicity of the adaptation law in (3.18) makes the processing demand of the proposed adaptation scheme relatively low for real-time implementation, making it possible to achieve quite small control periods.

Since the reference current vector is generated in the synchronous reference-frame, the effect of the synchronous frame position should be considered to minimize the phase lag in the injected current. With the aforementioned control sequence, the synchronous frame rotates and there will be a position difference between the k^{th} and the $(k+1)^{th}$

interrupt times. Since the control voltage is applied during the $(k+1)^{th}$ period, the position difference can be adjusted by averaging the reference frame position over one switching period [96]. Therefore, the corrected voltage command can be given in the following space vector form:

$$\vec{\boldsymbol{v}}^{*}_{inv}(k+1) = \boldsymbol{v}^{*}_{inv}(k+1)e^{j(2.5\theta(k)-1.5\theta(k-1))} \tag{3.20}$$

where $\theta(k)$ is the synchronous frame position at the current sampling period. In addition, the additional cross-coupling terms appearing in the synchronous reference-frame can be easily augmented in the uncertainty function $\boldsymbol{f}$.

The robustness of the proposed control scheme can be analyzed by considering the discrete-time current dynamics (3.9) and the robust control law in (3.19). By substituting (3.19) in (3.9), $\boldsymbol{i}_{inv}(k+2)$ can be evaluated as

$$\begin{aligned}
\boldsymbol{i}_{inv}(k+2) &= \boldsymbol{A}_o\boldsymbol{i}_{inv}(k+1) + \boldsymbol{i}^{*}_{inv}(k+2) - \boldsymbol{A}_o\left(\boldsymbol{A}_o\boldsymbol{i}_{inv}(k) + \boldsymbol{B}_o\left[\boldsymbol{v}_{inv}(k) - \hat{\boldsymbol{f}}(k)\right]\right)\\
&\qquad + \boldsymbol{B}_o\tilde{\boldsymbol{f}}(k+1)\\
&= \boldsymbol{A}_o\boldsymbol{i}_{inv}(k+1) + \boldsymbol{i}^{*}_{inv}(k+2)\\
&\qquad - \boldsymbol{A}_o\left(\boldsymbol{A}_o\boldsymbol{i}_{inv}(k) + \boldsymbol{B}_o\left[\boldsymbol{v}_{inv}(k) - \boldsymbol{f}(k)\right] + \boldsymbol{B}_o\tilde{\boldsymbol{f}}(k)\right) + \boldsymbol{B}_o\tilde{\boldsymbol{f}}(k+1)\\
&= \boldsymbol{i}^{*}_{inv}(k+2) - \boldsymbol{A}_o\boldsymbol{B}_o\tilde{\boldsymbol{f}}(k) + \boldsymbol{B}_o\tilde{\boldsymbol{f}}(k+1).
\end{aligned} \tag{3.21}$$

Then, the tracking error can be obtained as follows:

$$\boldsymbol{i}^{*}_{inv}(k+2) - \boldsymbol{i}_{inv}(k+2) = \boldsymbol{A}_o\boldsymbol{B}_o\tilde{\boldsymbol{f}}(k) - \boldsymbol{B}_o\tilde{\boldsymbol{f}}(k+1) \tag{3.22}$$

or

$$\boldsymbol{i}^{*}_{inv}(k) - \boldsymbol{i}_{inv}(k) = -\boldsymbol{B}_o\tilde{\boldsymbol{f}}(k-1) + \boldsymbol{A}_o\boldsymbol{B}_o\tilde{\boldsymbol{f}}(k-2). \tag{3.23}$$

As seen in (3.23), the current tracking error is proportional to the uncertainty function estimation error. With the integral adaptation algorithm in (3.18) the convergence of the observation and uncertainty estimation errors is guaranteed. Therefore, $\boldsymbol{i}^{*}(k) - \boldsymbol{i}(k) \rightarrow \boldsymbol{0}$ as $k \rightarrow \infty$. In addition, (3.23) shows that high attenuation of the current tracking error due to the uncertainty estimation error is yielded. As a result, robust current control performance against grid-side disturbances and parameter variation can be obtained with proposed control algorithm.

3.2.3 Results

To evaluate the performance of the proposed control scheme, a grid connected PWM-VSI-based DG unit incorporated with the proposed control scheme, as reported in Figure

3.1, has been used. The system parameters are as follows: supply phase voltage=120 V at 60 Hz, dc-link voltage=400 V, nominal system parameters are: L_o=2.5 mH, R_o=1 Ω. The overall system is implemented in Matlab/Simulink environment. The real-time code of the control algorithm is generated using the Real-Time-Workshop toolbox in Matlab/Simulink environment. This tool facilitates accurate prediction of the real-time implementation requirements and enables the designer to execute a real-time code for a given embedded target [97]. The TMS320C31 digital signal processor (DSP) has been chosen as an embedded platform for real-time code generation. The execution time of the current control interrupt routine is about 120 μs. Subsequently a control period T=150 μs is selected. With this setting, a safe CPU load coefficient 80% and a switching frequency 6.7 kHz have been obtained. As these figures reveal, the processing demand of the proposed control scheme is relatively modest for a DSP system, making it possible to achieve quite high switching frequencies. Since the sharp IGBT commutation spikes impair the current acquisition process, the synchronous sampling technique with a symmetric space vector modulation scheme is adopted. With this method, the sampling is performed at the beginning of each modulation cycle.

Various comparative tests are conducted to verify the feasibility of the proposed controller under different operating conditions. Some results are reported as follows.

3.2.3.1 Effect of Grid Distortion

To illustrate the effect of grid distortion on the current control performance of an inverter-based DG system, the case of grid-voltage harmonics and unbalance is considered as follows:

Case #1: Grid voltage harmonics: 3% 5^{th} harmonic, 2% 7^{th} harmonic, and 1% 11^{th} harmonics.

Case #2: Grid voltage unbalance: 7% voltage unbalance factor.

Case #3: A combination of Case #1 and Case #2.

For the sake of performance comparison, the proposed current control system is compared to the conventional PI synchronous-frame current controller under different test cases. The stationary frame current controller is designed with nominal system parameters and a desired bandwidth of 1.0 kHz. The proposed controller is designed with nominal system parameters and an adaptation gain of 450. In both controllers, the d-axis current command is set at 20 A at $t \geq 0.0167$ s, whereas the q-axis current command is set to zero to achieve a unity power factor interface.

Figure 3.2 shows the control performance of the PI controller under the conditions of Case #1. Since the synchronous frame is rotating at the fundamental frequency, the

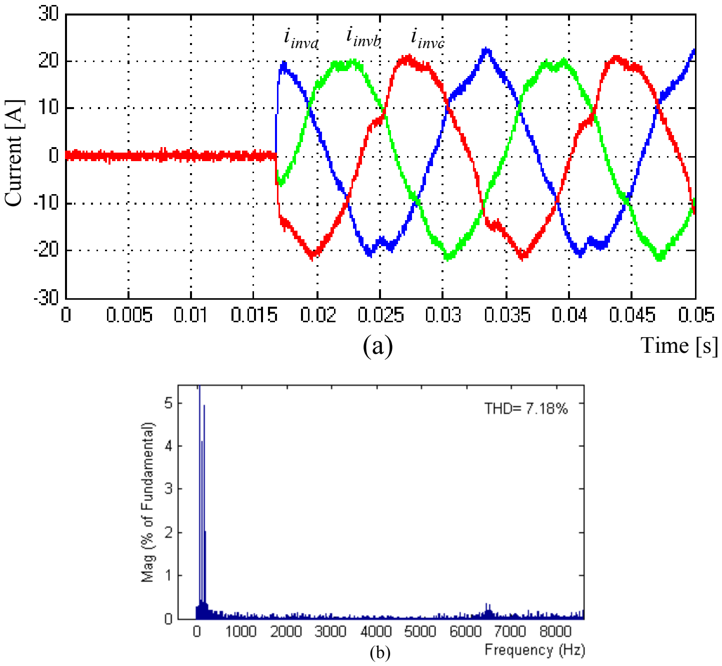

Figure 3.2: The control performance of the PI controller under the conditions of Case #1. (a) Injected currents. (b) Current spectra.

grid harmonics can't be effectively compensated and the inverter output current is highly distorted as shown in Figure 3.2(a). The effect of the feed-forward control of the grid voltage directly injects the grid harmonics to the control voltage vector applied to the inverter. Therefore, the output current in Figure 3.2(a) shows a THD of 7.18% (up to the 8.16 kHz) as shown in the current spectra Figure 3.2(b). This result doesn't meet the IEEE Standard 1547 requirement of THD [45], which is below 5%.

Figure 3.3 shows the control performance of the proposed controller under the conditions of Case #1. Figure 3.3(a) shows that high power-quality current injection is yielded with the proposed current control scheme. Figure 3.3(b) shows a THD of 0.93%, which is far below the recommended THD standards. The high-quality current injection is the natural result of the high disturbance rejection ability of the proposed current controller. Figure 3.3(c) shows the actual grid voltages and the estimated phase-a uncertainty function $\hat{f}_a$. The estimated uncertainty function closely tracks the actual grid voltage. Figure 3.3(d) shows the inverter voltage; the uncertainty modes can be effectively embedded in the control effort to cancel the effect of grid harmonics.

Figure 3.4 shows the control performance of the PI controller under the conditions of Case #2. Since the synchronous frame is rotating at the fundamental frequency, the grid voltage unbalance leads to a negative sequence component, which appears as a second harmonic. This second harmonic voltage disturbance can't be effectively compensated

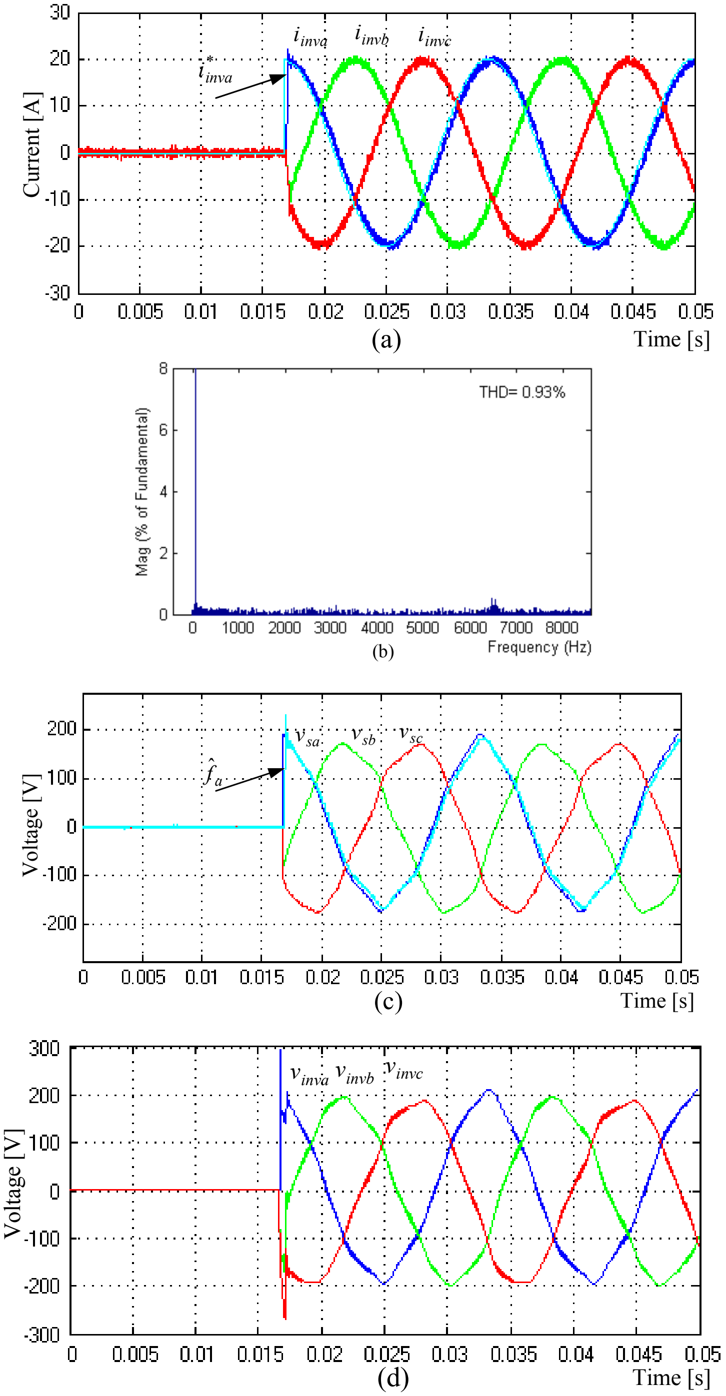

Figure 3.3: The control performance of the proposed inverter output current controller under the conditions of Case #1. (a) Injected current. (b) Current spectra. (c) Grid voltages and estimated phase-a uncertainty function. (d) Inverter control voltage.

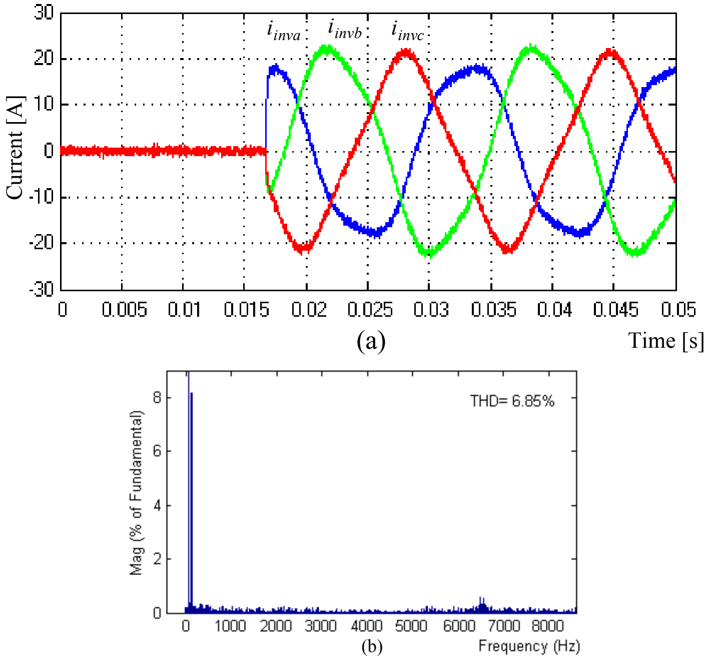

Figure 3.4: The control performance of the PI controller under the conditions of Case #2. (a) Injected currents. (b) Current spectra.

and the inverter output current is distorted as shown in Figure 3.4(a). The effect of the feed-forward control of the grid voltage directly injects the grid unbalance to the control voltage vector applied to the inverter. Therefore, the output current in Figure 3.4(a) shows a THD of 6.85% as shown in the current spectra Figure 3.4(b). This result doesn't meet the IEEE Standard 1547 [45].

Figure 3.5 shows the control performance of the proposed controller under the conditions of Case #2. Figure 3.5(a) shows that high power-quality current injection is yielded with the proposed current control scheme. Figure 3.5(b) shows a THD of 0.91%, which far below the standard THD. The high-quality current injection is the natural result of the high disturbance rejection ability of the proposed current controller. Figure 3.5(c) shows the actual unbalanced grid voltages and the estimated phase-a uncertainty function $\hat{f}_a$. The estimated uncertainty function closely tracks the actual grid voltage. Figure 3.5(d) shows the inverter control voltage; the uncertainty modes can be effectively embedded in the control effort to cancel the of grid voltage unbalance.

Figure 3.6 shows the control performance of the PI controller under the conditions of Case #3. This grid voltage harmonic and unbalance severely degrade the power quality of the injected current as shown in Figure 3.6(a). The effect of the feed-forward control of the grid voltage directly injects the grid unbalance and harmonics to the control voltage

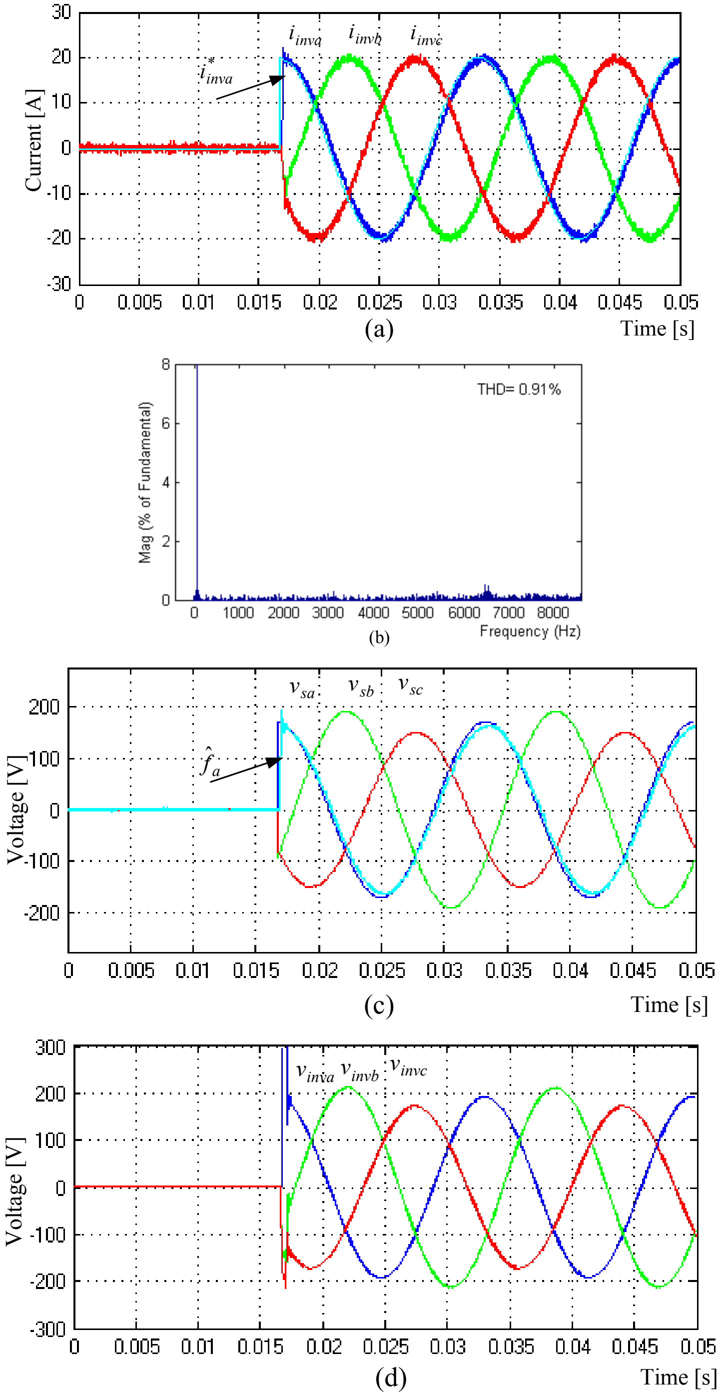

Figure 3.5: The control performance of the proposed inverter output current controller under the conditions of Case #2. (a) Injected current. (b) Current spectra. (c) Grid voltages and estimated phase-a uncertainty function. (d) Inverter control voltage.

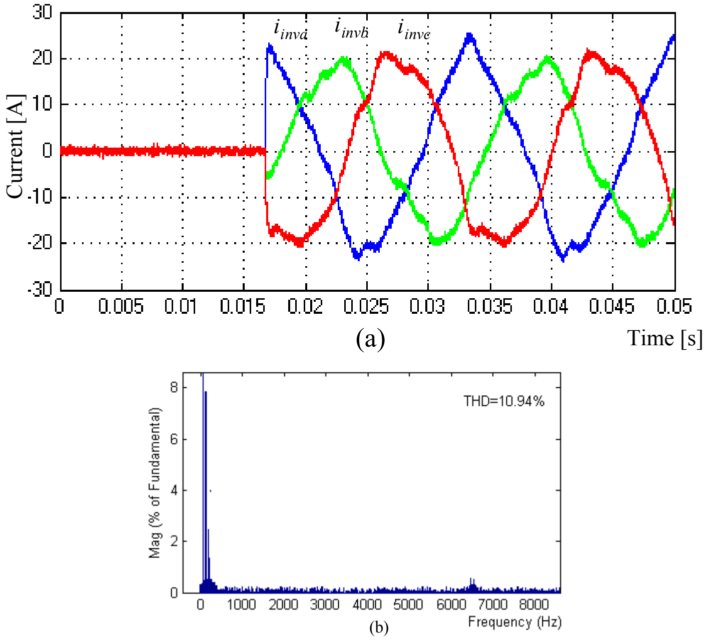

Figure 3.6: The control performance of the PI controller under the conditions of Case #3. (a) Injected currents. (b) Current spectra.

vector applied to the inverter. Therefore, the output current in Figure 3.6(a) shows a THD of 10.94% as shown in the current spectra in Figure 3.6(b). This result doesn't meet the IEEE Standard 1547 [45].

Figure 3.7 shows the control performance of the proposed controller under the conditions of Case #3. Figure 3.7(a) shows that high power-quality current injection is yielded with the proposed current control scheme. Figure 3.7(b) shows a THD of 1.05%, which is far below the standard THD. Figure 3.7(c) shows the actual distorted and unbalanced grid voltages and the estimated phase-a uncertainty function $\hat{f}_a$. The estimated uncertainty function closely tracks the actual grid voltage. Figure 3.7(d) shows the inverter control voltage; the uncertainty modes can be effectively embedded in the control effort to cancel the effect of grid voltage harmonics and unbalance.

3.2.3.2 Robustness and Stability Against Interfacing Parameter Variations

To illustrate the effect of interfacing parameters on the robustness and stability of the DG interface, the case of uncertainties in the interfacing parameters is considered. Possible variations in the interfacing impedance parameters can take place due to grid impedance variation, filter inductor saturation, and cable overload. Furthermore, the interfacing parameters are frequency dependent and can be considerably different at

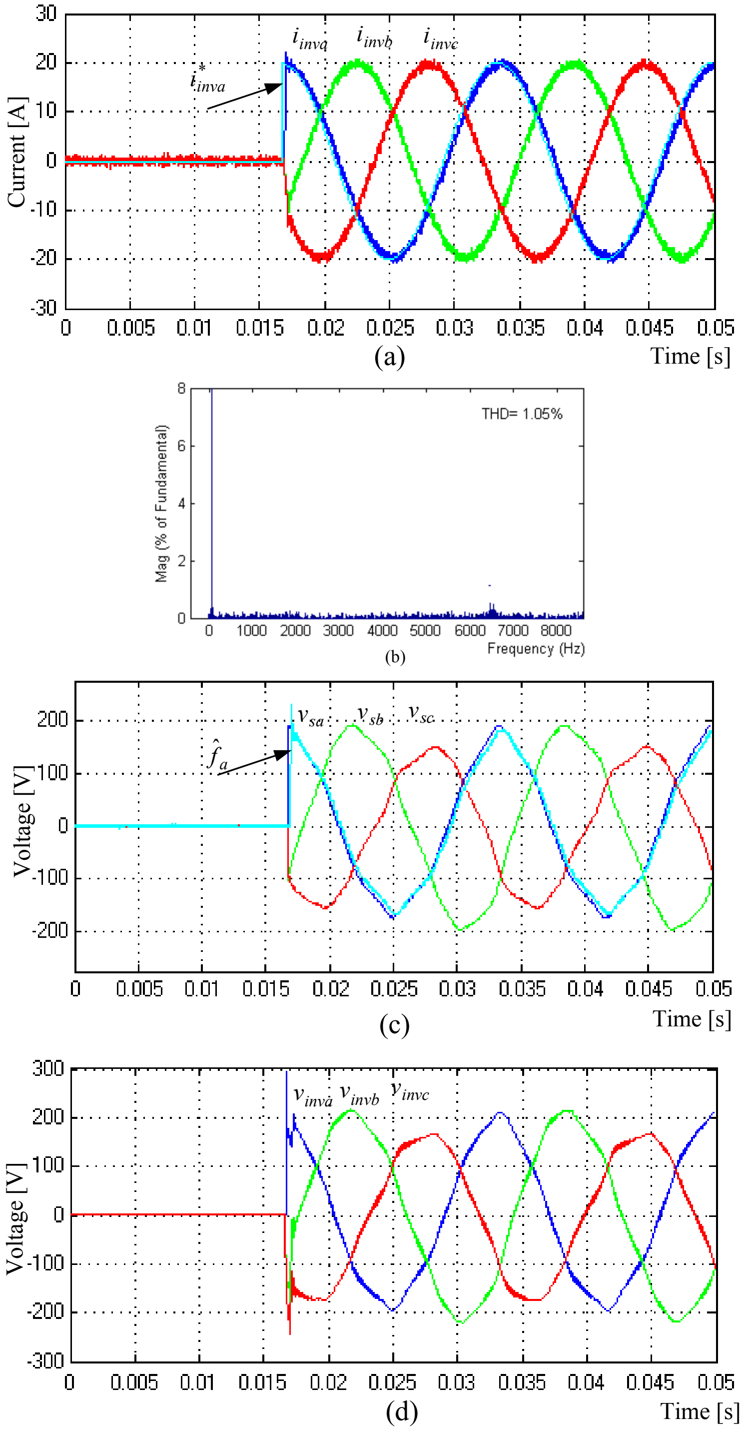

Figure 3.7: The control performance of the proposed inverter output current controller under the conditions of Case #3. (a) Injected current. (b) Current spectra. (c) Grid voltages and estimated phase-a uncertainty function. (d) Inverter control voltage.

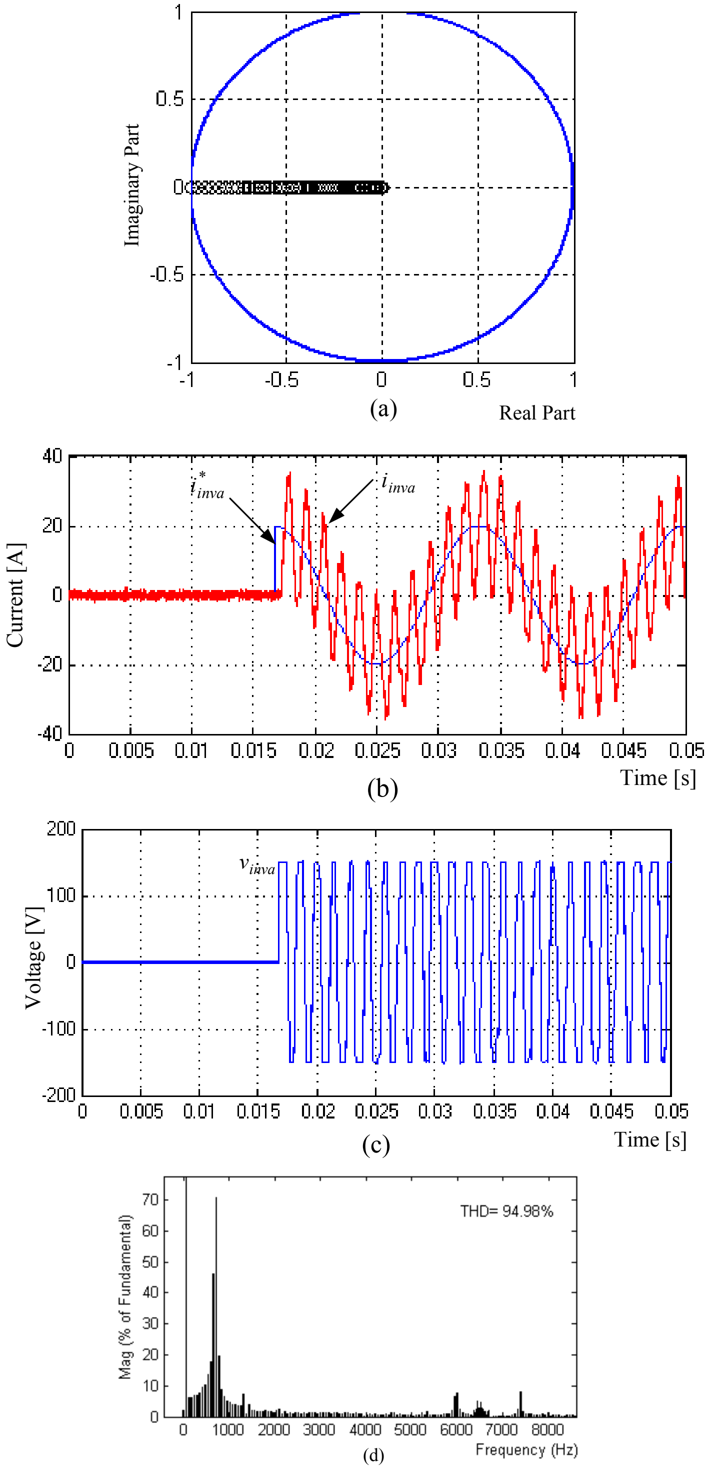

Figure 3.8: Robustness of the conventional deadbeat current control. (a) Locus of the dominant closed loop pole as a function of the interfacing inductance. (b) Current control performance with 25% mismatch in L. (c) The corresponding control effort. (d) The corresponding current spectra.

harmonic frequencies compared to their nominal values at the fundamental frequency.

Figure 3.8(a) shows the dominant pole of the closed loop current tracking transfer function with the conventional deadbeat current control law in (3.7) as a function of the interfacing inductance. Figure 3.8(a) shows that the current dynamics becomes unstable at 20% mismatch in the interfacing inductance. Figure 3.8(b) shows the time-domain current response of the conventional deadbeat controller with 25% mismatch in the interfacing inductance. The *d*-axis current command is set to 20 A at $t \geq 0.0167$ s, whereas the *q*-axis current command is set to zero. The instability of the current control loop with the saturation effect of the current controller and the pulse width modulator lead to sustained oscillations in the current response as shown in Figure 3.8(b). Figure 3.8(c) shows the corresponding control effort. Sustained oscillations in the inverter output voltage are yielded due to the instability of the current control loop saturation effect. Figure 3.8(d) shows the output current spectra, which shows a THD of 94.98% due to current control instability.

Figure 3.9 shows the control performance of the proposed current control scheme with 60% mismatch in L and 50% mismatch in R, whereas the *d*-axis current command is set to 20 A at $t \geq 0.0167$ s, whereas the *q*-axis current command is set to zero. Figure 3.9(a) shows the time-domain current response; Figure 3.9(b) shows the output current spectra; and Figure 3.9(c) shows the corresponding inverter control voltage obtained in this case. In contrast to conventional and existing deadbeat current regulation schemes [67], the proposed algorithm is still stable and generates the minimal low-order harmonics even with 60% mismatch in L and 50% mismatch in R. In this case, the THD up to 8.16 kHz is 0.96%.

The reported results indicate that the proposed control law in (3.19) can successfully provide the necessary energy shaping performance to attenuate the grid distortion and voltage disturbance associated with uncertainties in the DG-interface parameters. As a result, high power quality current injected is yielded at different operating conditions.

3.3 Current Control with Decoupling Inductor

3.3.1 System Configuration and Modeling

A system topology of a grid-connected current-controlled VSI with an LC filter and a decoupling inductor incorporated with the proposed control scheme is depicted in Figure 3.10, where R_1 and L_1 represent the resistance and inductance of the inverter-side filter inductor; R_2 and L_1 represent the resistance and inductance of the grid-side filter inductor and the grid resistance and inductance at the PCC; R_c and C_f represent

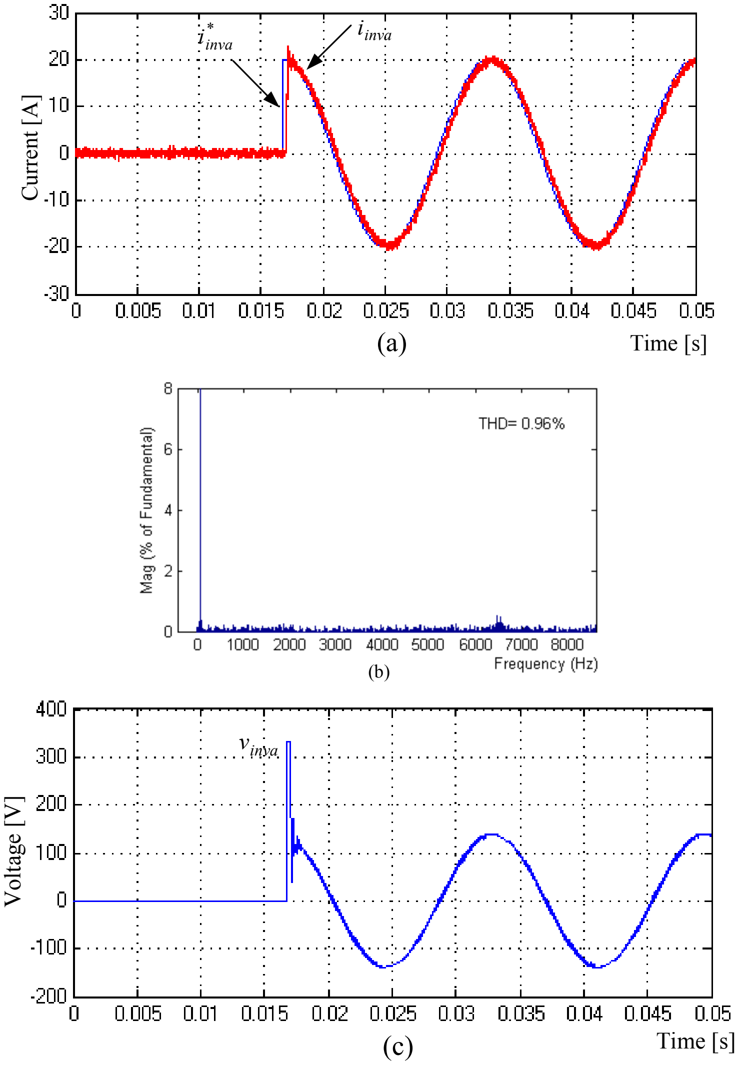

Figure 3.9: The control performance of the proposed current control scheme with 60% mismatch in L and 50% mismatch in R. (a) Reference and injected phase-a current. (b) Current spectra. (c) Inverter control voltage.

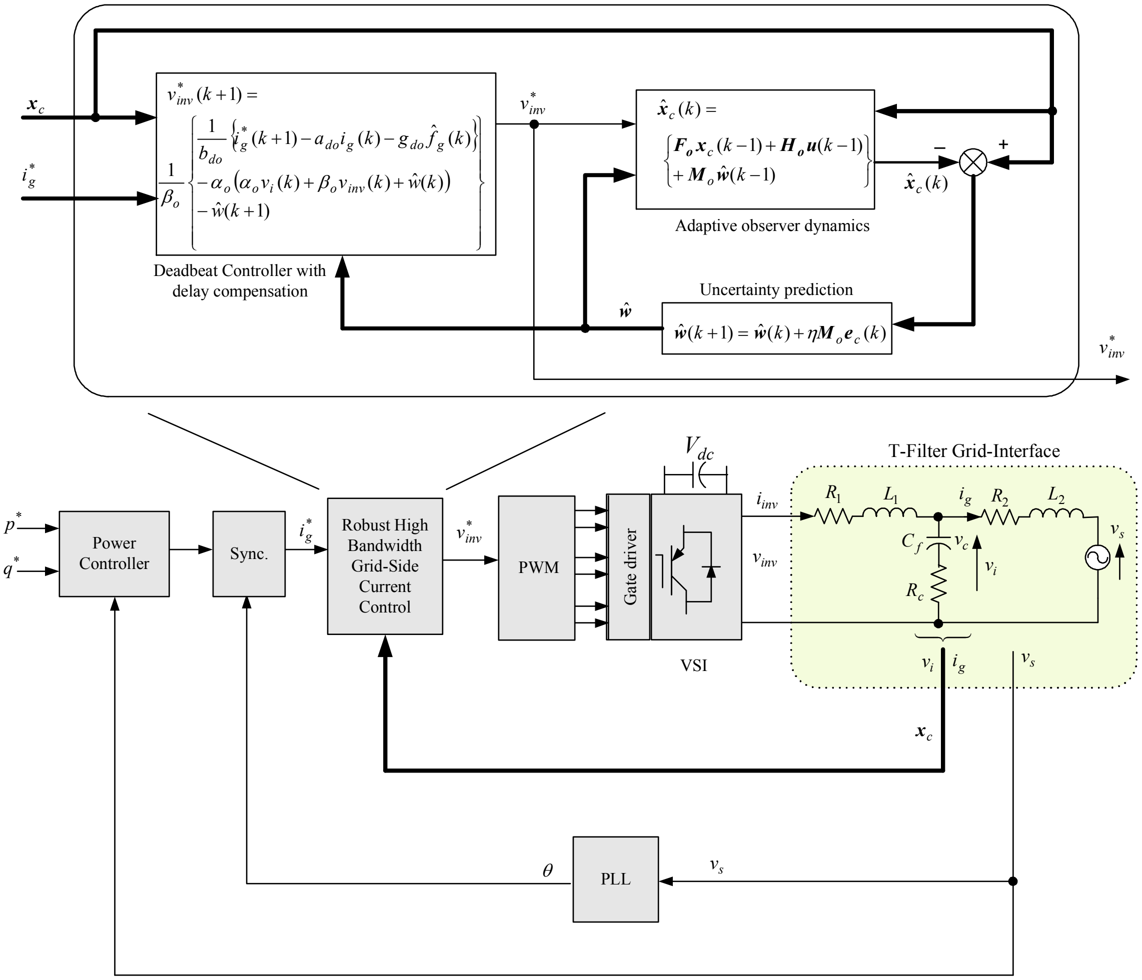

Figure 3.10: Proposed current control scheme with decoupling inductor.

the resistance and capacitance of the filter capacitor branch; v_s is the grid voltage; v_c is the filter capacitor voltage; v_i is the intermediate voltage; i_g is the injected grid current; i_{inv} is the inverter output current; and v_{inv} is the inverter output voltage.

In the natural reference frame, the per-phase system dynamics can be represented by the following model:

$$\frac{d\boldsymbol{x}_1}{dt} = \boldsymbol{A}_{tc}\boldsymbol{x}_1 + \boldsymbol{B}_{tc}v_{inv} \tag{3.24}$$

$$v_i = \boldsymbol{c}^T\boldsymbol{x}_1 \tag{3.25}$$

$$\frac{di_g}{dt} = a_c i_g + b_c v_i + g_c v_s \tag{3.26}$$

where

$$\boldsymbol{x}_1 = \begin{bmatrix} i_{inv} \\ v_c \\ i_g \\ d_g \end{bmatrix} \quad \boldsymbol{A}_{tc} = \begin{bmatrix} \frac{-(R_1+R_c)}{L_1} & \frac{-1}{L_1} & \frac{R_c}{L_1} & 0 \\ \frac{1}{C_f} & 0 & \frac{-1}{C_f} & 0 \\ 0 & 0 & 0 & 1 \\ 0 & 0 & 0 & 0 \end{bmatrix}$$

$$\boldsymbol{B}_{tc} = \begin{bmatrix} \frac{1}{L_1} \\ 0 \\ 0 \\ 0 \end{bmatrix} \quad \boldsymbol{C} = \begin{bmatrix} R_c \\ 1 \\ -R_c \\ 0 \end{bmatrix}$$

$$a_c = \frac{-R_2}{L_2} \qquad b_c = \frac{1}{L_2}$$

$$g_c = \frac{-1}{L_2}.$$

In the aforementioned dynamic model, the grid current i_g and its derivative $d_g = \dot{i}_g$ are augmented as a bias imposed on the inverter-side output current. The direct result of this modeling approach is the inherent decoupling between the LC filter circuit and the decoupling inductor. Therefore, a novel approach for controlling the grid-side current via the intermediate voltage can be achieved as follows.

For a symmetric output voltage of the inverter, the PWM-VSI can be assumed as a zero-order hold circuit with the transfer function given in (3.4). For digital implementation of the control algorithm, the power circuit dynamics in (3.24)-(3.26) can be represented in a discrete-time domain with the conversion $H(s)$ in (3.4), as follows:

$$\boldsymbol{x}_1(k+1) = \boldsymbol{A}_{td}\boldsymbol{x}_1(k) + \boldsymbol{B}_{td}v_{inv} \tag{3.27}$$

$$v_i(k) = \boldsymbol{c}^T\boldsymbol{x}_1(k) \tag{3.28}$$

$$i_g(k+1) = a_d i_g(k) + b_d v_i(k) + g_d v_s(k) \tag{3.29}$$

where A_{td}, B_{td}, a_d, b_d, and g_d are the sampled equivalents of the continuous-time system matrices and parameters in (3.24) and (3.26), and they are calculated by Taylor's expansion as follows:

$$\boldsymbol{A}_{td} \simeq \begin{bmatrix} 1-\frac{T(R_1+R_c)}{L_1} & \frac{-T}{L_1} & \frac{TR_c}{L_1} & 0 \\ \frac{T}{C_f} & 1 & \frac{-T}{C_f} & 0 \\ 0 & 0 & 1 & T \\ 0 & 0 & 0 & 1 \end{bmatrix} \quad \boldsymbol{B}_{td} \simeq \begin{bmatrix} \frac{T}{L_1} \\ 0 \\ 0 \\ 0 \end{bmatrix}$$

$$a_d \simeq 1 - \frac{TR_2}{L_2} \qquad b_d \simeq \frac{T}{L_2}$$

$$g_d \simeq \frac{-T}{L_2}$$

where T is the sampling interval.

3.3.2 Grid-Side Current Control Design

The output voltage in (3.28) can be given by

$$\begin{aligned} v_i(k+1) &= \boldsymbol{c}^T \boldsymbol{x}_1(k+1) \\ &= \alpha v_c(k) + \beta v_{inv}(k) + \gamma i_{inv}(k) + \delta i_g(k) + \phi d_g(k) \end{aligned} \tag{3.30}$$

where

$$\begin{aligned} \alpha &= 1 - \frac{TR_c}{L_1} & \beta &= \frac{TR_c}{L_1} \\ \gamma &= R_c\left(1 - \frac{T\left(R_c + R_1\right)}{L_1}\right) + \frac{T}{C_f} & \delta &= -\frac{T}{C_f} - R_c\left(\frac{TR_c}{L_1} + 1\right) \\ \phi &= TR_c. \end{aligned}$$

Then, the dynamics of $v_i(k)$ can be obtained as

$$v_i(k+1) = \alpha v_i(k) + \beta v_{inv}(k) + \bar{\gamma} i_{inv}(k) + \bar{\delta} i_g(k) + \phi d_g(k) \tag{3.31}$$

where

$$\begin{aligned} \bar{\gamma} &= \frac{T}{C_f} - \frac{TR_cR_1}{L_1} \\ \bar{\delta} &= -\frac{T}{C_f} - \frac{2TR_c^2}{L_1}. \end{aligned}$$

The voltage dynamics in (3.31) relates v_i to the inverter voltage and network currents, which act as disturbances. By considering possible variations in system parameters, the disturbed dynamics in (3.31) can be written as

$$v_i(k+1) = \alpha_o v_i(k) + \beta_o v_{inv}(k) + w(k) \tag{3.32}$$

where the subscript "o" denotes the nominal value and $w(k)$ is the lump of uncertainties imposed on v_i dynamics.

Equations (3.32) can be used to synthesize the inverter control voltage that yields a reference intermediate voltage in the sense of deadbeat control as follows:

$$v_{inv}(k) = \frac{1}{\beta_o}\left\{v_i(k+1) - \alpha_o v_i(k) - w(k)\right\}. \tag{3.33}$$

With the control timing sequence explained in Section 3.1.2, (3.33) doesn't account for system delays. Therefore, high bandwidth control is not feasible. A time delay compensator is necessary to alleviate this limitation. By assuming that $w(k)$ is known and following the same approach used to derive (3.10), the delay elements can be removed to the reference value as follows:

$$v_{inv}^*(k+1) = \frac{1}{\beta_o}\left\{v_i^*(k) - \alpha_o\left(\alpha_o v_i(k) + \beta_o v_{inv}(k) + w(k)\right) - w(k+1)\right\} \tag{3.34}$$

where the subscript “*” denotes the reference value.

The reference voltage $v_i^*(k)$ can be calculated to regulate the grid current using (3.29). The grid-current dynamics is subjected to grid uncertainties, including grid impedance variation and grid voltage disturbances; therefore, (3.29) can be written as

$$i_g(k+1) = a_{do} i_g(k) + b_{do} v_i(k) + g_{do} f_g(k) \tag{3.35}$$

where the subscript “o” denotes the nominal value and f_g is the lump of uncertainties imposed on i_g dynamics.

Assuming that $f_g(k)$ is known, and by using the discrete-time dynamics in (3.29), the reference voltage $v_i^*(k)$ can be calculated for a given grid current reference as follows:

$$v_i^*(k) = \frac{1}{b_{do}} \left\{ i_g^*(k+1) - a_{do} i_g(k) - g_{do} f_g(k) \right\} \tag{3.36}$$

where the subscript “*” denotes reference values.
Then, the inverter control voltage can be calculated as

$$\begin{aligned} v_{inv}^*(k+1) = \frac{1}{\beta_o} \Big\{ & \frac{1}{b_{do}} \left\{ i_g^*(k+1) - a_{do} i_g(k) - g_{do} f_g(k) \right\} \\ & - \alpha_o \left(\alpha_o v_i(k) + \beta_o v_{inv}(k) + w(k) \right) - w(k+1) \Big\}. \end{aligned} \tag{3.37}$$

It is clear that (3.32) and (3.35) represent the power circuit dynamics. However, unknown dynamics w and f_g should be estimated to robustly calculate the control voltage. Relying on the simplified system model given by (3.32) and (3.35), an adaptive system observer with the following input/output relation can be constructed:

$$\hat{\boldsymbol{x}}_c(k) = \boldsymbol{F}_o \boldsymbol{x}_c(k-1) + \boldsymbol{H}_o \boldsymbol{u}(k-1) + \boldsymbol{M}_o \hat{\boldsymbol{w}}(k-1) \tag{3.38}$$

where

$$\hat{\boldsymbol{x}}_c(k) = \begin{bmatrix} \hat{v}_i(k) \\ \hat{i}_g(k) \end{bmatrix} \qquad \boldsymbol{u}(k-1) = \begin{bmatrix} v_{inv}(k-1) \\ v_i(k-1) \end{bmatrix}$$
$$\hat{\boldsymbol{w}}(k-1) = \begin{bmatrix} \hat{w}(k-1) \\ \hat{f}_g(k-1) \end{bmatrix} \qquad \boldsymbol{F}_o = \begin{bmatrix} \alpha_o & 0 \\ 0 & a_{do} \end{bmatrix}$$
$$\boldsymbol{H}_o = \begin{bmatrix} \beta_o & 0 \\ 0 & b_{do} \end{bmatrix} \qquad \boldsymbol{M}_o = \begin{bmatrix} 1 & 0 \\ 0 & g_{do} \end{bmatrix}.$$

Under the same input voltage and disturbance, the estimated voltage approaches the actual one even though the observer in (3.38) has an open loop structure. Therefore, convergence of the voltage proposed observer can be achieved with an appropriate disturbance adaptation using the estimation error

$$\boldsymbol{e}_c(k) = \boldsymbol{x}_c(k) - \hat{\boldsymbol{x}}_c(k). \tag{3.39}$$

A simple adaptation algorithm, can be constructed to minimize the following error function:

$$E_c(k) = \frac{1}{2}\boldsymbol{e}_c^T(k)\boldsymbol{e}_c(k). \tag{3.40}$$

Then, the adaptation rule can be derived as follows:

$$\begin{aligned}\hat{\boldsymbol{w}}(k+1) &= \hat{\boldsymbol{w}}(k) + \Delta\hat{\boldsymbol{w}}(k)\\ &= \hat{\boldsymbol{w}}(k) - \eta\frac{\partial E_c}{\partial\hat{\boldsymbol{w}}} = \hat{\boldsymbol{w}}(k) + \boldsymbol{\eta}\boldsymbol{M}_o\boldsymbol{e}_c(k)\end{aligned} \tag{3.41}$$

where $\boldsymbol{\eta}= \begin{bmatrix} \eta_v & 0 \\ 0 & \eta_{ig} \end{bmatrix}$ is an adaptation gain matrix.

The adaptive estimation law in (3.41) provides a simple iterative gradient algorithm designed to minimize (3.40). As a result, the estimate can be reliably used to embed an internal model for the uncertainty function within the current feedback structure, resulting in equivalent control to cancel the power circuit disturbances. Therefore, the estimated uncertainty function can be used to robustly calculate the control voltage as follows:

$$\begin{aligned}v_{inv}^*(k+1) = \frac{1}{\beta_o}\Big\{&\frac{1}{b_{do}}\Big\{i_g^*(k+1) - a_{do}i_g(k) - g_{do}\hat{f}_g(k)\Big\}\\ &- \alpha_o\left(\alpha_o v_i(k) + \beta_o v_{inv}(k) + \hat{w}(k)\right) - \hat{w}(k+1)\Big\}.\end{aligned} \tag{3.42}$$

3.3.3 Results

To evaluate the performance of the proposed control scheme, a three-phase grid connected PWM-VSI-based DG unit, as reported in Figure 3.10, has been used. The system parameters are as follows: supply phase voltage=120 V at 60 Hz, dc-link voltage=400 V, nominal system parameters are as follows: L_1= 1.0 mH, R_1= 0.2 Ω, L_2= 1.2 mH, R_2= 0.5 Ω, C_f= 7.5 μF, and R_c= 0.1 Ω. The overall system is digitally simulated under Matlab/Simulink environment with real-time code generation support. A converter switching frequency of 6.67 kHz has been selected. As a result, a control sampling time T=150 μs is yielded.

For the sake of performance comparison, the performance of the proposed current regulation scheme is compared to that of the stationary frame proportional resonant controller (P-RES). The P-RES controller is a generalized version of the PI controller, which provides a potential in canceling the tracking errors by means of a resonant compensator; normally tuned at the fundamental frequency. The parameters of the P-RES controller are chosen according to the guidelines provided in [17] as a tradeoff between the grid harmonics attenuation and the dynamic performances. For both examined controllers, the magnitude of the current command is set at 20 A with unity power factor

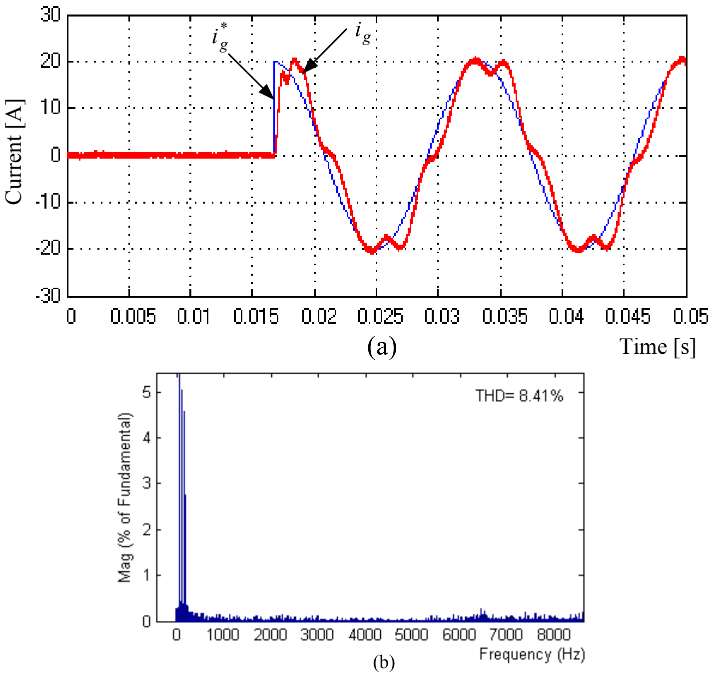

Figure 3.11: Dynamic performance and the grid distortion rejection ability of the P-RES controller tuned to yield a damped transient response. (a) Reference and injected gird currents. (b) Current spectra.

for $t \geq 0.0167$. The case of distorted grid voltage is examined where the grid voltage harmonics are: 3% 5^{th} harmonic, 2% 7^{th} harmonic, and 1% 11^{th} harmonic.

Figure 3.11 shows the dynamic performance and the grid distortion rejection ability of the P-RES controller. The controller is tuned to yield a damped transient response with a proportional gain of 0.6. It is evident in Figure 3.11(a) that the disturbance rejection performance is poor. The resultant THD in the injected current is 8.41% as given by the current spectra of Figure 3.11(b).

To increase the harmonic impedance of the P-RES current controller, the proportional gain has been increased to 1.1, which is just below the maximum proportional gain 1.26 that preserves system stability. Figure 3.12(a) shows the dynamic performance and the grid distortion rejection ability of the P-RES controller with higher harmonic impedance. Although the disturbance rejection has been improved, the transient response becomes more under-damped as depicted in Figure 3.12(a). Figure 3.12(b) shows the current spectra in this case; the THD in the injected current is 6.53%.

Since the proposed control structure relies on embedding the frequency modes of the grid harmonics and disturbances through the closed loop current controller, the current controller mainly handles the tracking task whereas the regulation performance is mainly

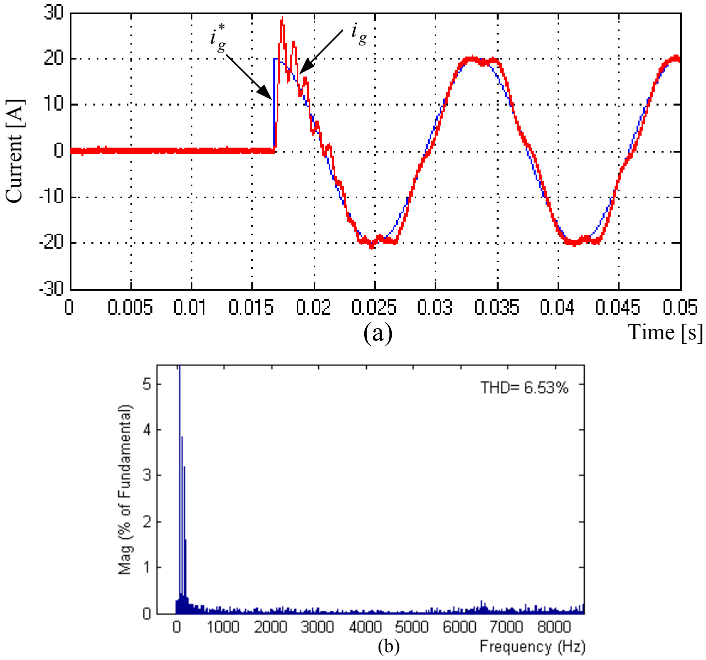

Figure 3.12: Dynamic performance and the grid distortion rejection ability of the P-RES controller tuned to yield high harmonic impedance. a) Reference and injected gird currents. (b) Current spectra.

realized through uncertainty estimation and compensation control. Figure 3.13 shows the dynamic performance and the grid distortion rejection ability of the proposed controller. The injected grid current is well controlled to the reference value with minimal harmonics as shown in Figure 3.13(a). The THD of the injected current is 0.95% as depicted in Figure 3.13(b). Figure 3.13(c) shows the actual and estimated grid-side uncertainty function. The estimate closely tracks the actual grid voltage disturbance. The estimate is used to embed the frequency modes of the grid distortion in the inverter control voltage, which is shown in Figure 3.13(d).

3.4 Summary

This chapter has presented newly designed current control algorithms for a VSI-based DG interface. First, to achieve high bandwidth current control characteristics, a digital deadbeat current controller with delay compensation has been designed. The delay compensation method forces the delays elements, caused by voltage calculation, PWM, and synchronous frame rotation to be equivalently placed outside the close loop control system. Hence, their effect on the closed loop stability is eliminated and the current controller can be designed with a higher bandwidth. Second, to ensure perfect tracking

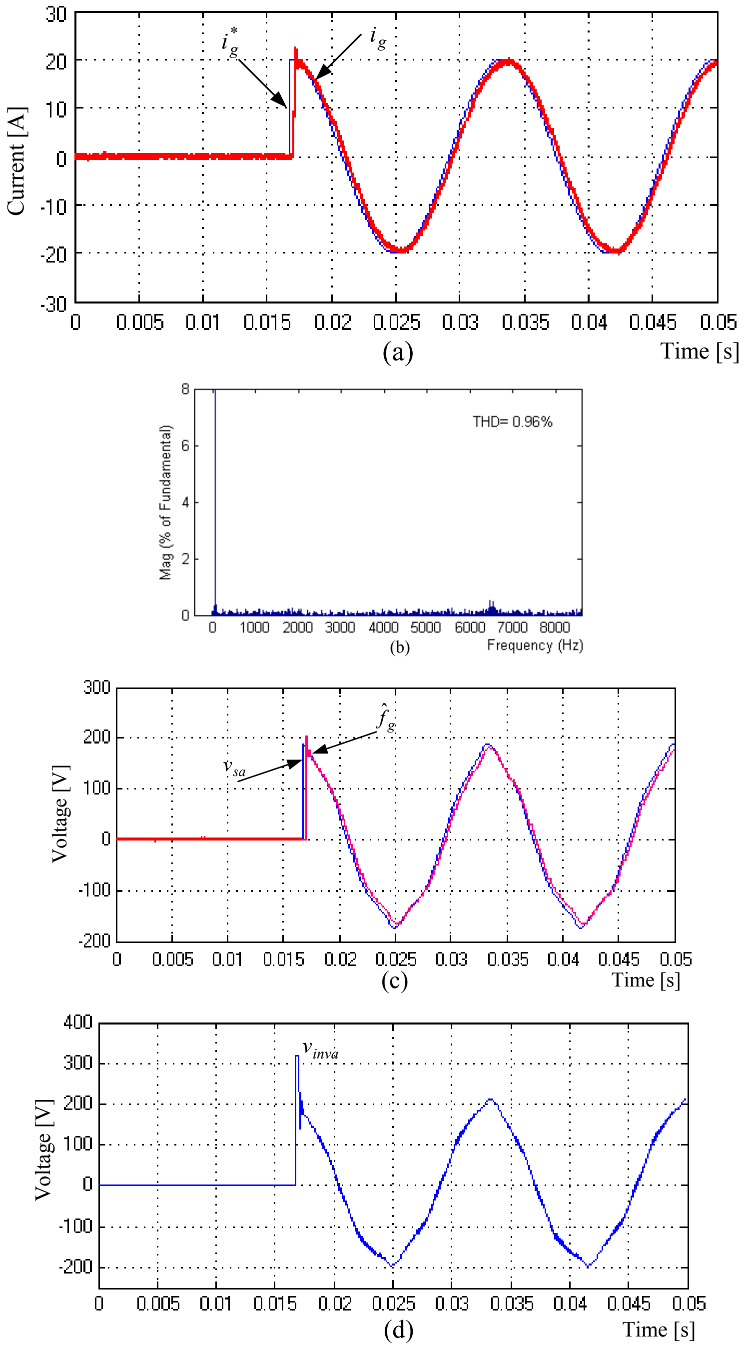

Figure 3.13: The dynamic performance and the grid distortion rejection ability of the proposed grid-side current controller. a) Reference and injected gird currents. (b) Current spectra. (c) Grid voltage and estimated gird-side uncertainty function. (a) Inverter control voltage.

of the output current in the presence of grid disturbances and interfacing parameter variation, an adaptive uncertainty estimator has been included within the current feedback structure. The estimated uncertainty dynamics provide the necessary energy shaping in the inverter control voltage to attenuate grid voltage disturbances and other voltage disturbances caused by interfacing parameter variations. The current control algorithm has been applied to the case of inverter output current control. It has been extended, through a modified power circuit model and a new intermediate voltage control approach, to the case of grid current control in a DG interface with a T-type filter

The salient features of the proposed current controllers are: 1) high power quality current injection even under distorted grid conditions; 2) high bandwidth characteristics with considerably low computational demand; 3) high robustness against uncertainties in the interfacing parameters; and 4) no additional hardware is needed for delay compensation.

Chapter 4

Interface Monitoring Unit Featuring Grid-Voltage Sensorless Operation

4.1 Introduction

To reduce system's cost and to increase its reliability, it is highly desirable to realize a grid-interfacing scheme with the minimum number of sensing elements. Along with the reliability and cost enhancements, significant performance enhancements can be obtained by eliminating the grid voltage sensors in an inverter-based DG interface. Among these are: 1) the elimination of the residual negative sequence and voltage feed-forward compensation errors (the injected currents are so sensitive to minute variations in the reference voltage vector, which highly depends on the feed-forward compensation control), and 2) the positive contribution to the robustness of the power sharing mechanism in paralleled inverter systems, where the power-sharing mechanism is generally based on open-loop controllers.

Since the current control and power sharing performances are so sensitive to minute variations in the voltage command, it seems appropriate to design the control system without using grid-voltage sensors. This is addressed as a grid-voltage sensorless interfacing scheme, where the voltage information is estimated based on the current measurements. By this way, the extreme sensitivity to voltage measurements would be avoided. However, any model-based grid-voltage estimator is by nature parameter-dependent. While the grid and interfacing parameters are time varying, the sensitivity of the interface control system to uncertainties in the interfacing impedance becomes higher as the voltage estimator dynamics will be dependent on system parameters. In addition, the resultant estimation problem becomes nonlinear when the grid voltage information is not available.

Further, cost and reliability constraints might call for a functions-fusion feature

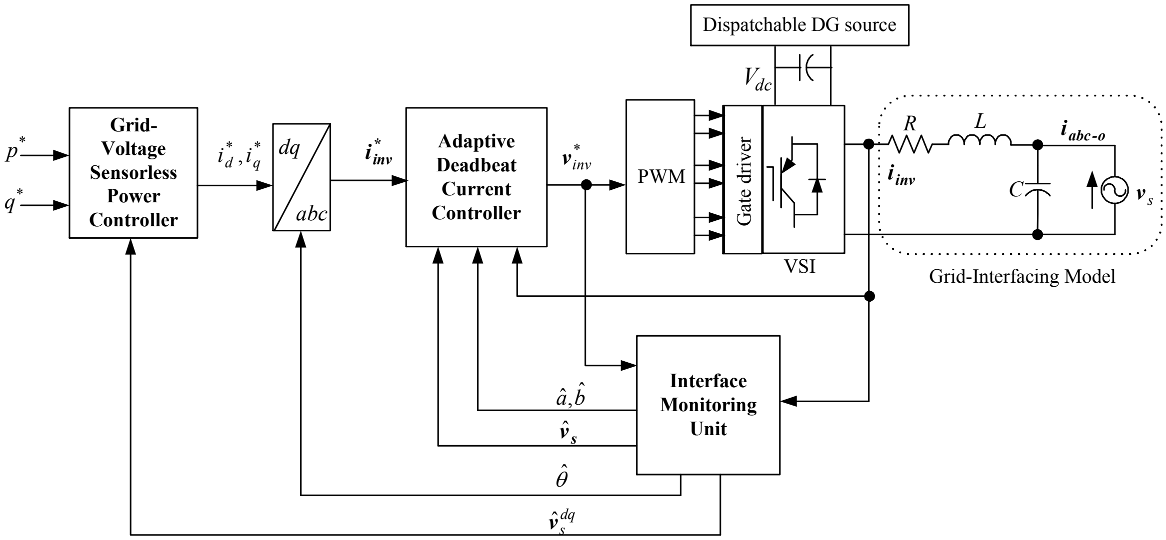

Figure 4.1: Proposed grid-voltage sensorless interfacing scheme.

within the DG interface, where a single unit can perform multiple tasks, such as grid monitoring, synchronization, and self-commissioning/self-tuning control. The development of a single unit that performs these functions in a computationally efficient manner demands special attention.

This chapter presents an interface-monitoring unit featuring grid voltage sensorless operation for inverter-based DG. Two designs are investigated. First, an interface-monitoring unit, based on parallel adaptive observers, is designed with low computational demand to estimate the grid voltage and the interfacing parameters simultaneously. Second, due to the nonlinear nature of the estimation problem and the periodic time-varying nature of the grid voltage, the second design of the adaptive estimation unit utilizes a neural network (NN)-based adaptation algorithm, which works as a real-time optimization agent. To robustly extract the grid voltage vector position, a resonant filter-based three-phase PLL is proposed. To guarantee high power quality injection, a grid-voltage sensorless average-power control loop is realized using the estimated grid voltage.

Figure 4.1 shows the proposed grid-voltage sensorless interfacing scheme with the interface monitoring unit. The scheme consists of an interface monitoring unit, which provides a real-time estimate of the interfacing parameters and the grid voltage vector at the PCC, a deadbeat current control loop to achieve optimal dynamic response from the inverter, and an average power controller to generate the reference current vector. Theoretical analysis and design procedure of different loops are provided in the subsequent sections as follows. Section 4.2 details the first design of the proposed monitoring unit. In Section 4.3, a second design, based on a NN-based optimization agent, is presented.

Section 4.4 presents a robust and simple method to estimate the position of the grid-voltage-vector. In Section 4.5, an adaptive self-tuning version of the proposed inverter output current deadbeat current controller, presented in Chapter 3, is introduced. The proposed average power controller is presented in Section 4.6. Simulation results are given in Section 4.7. A summary is drawn in Section 4.8.

4.2 Interface Monitoring Unit – Design #1

Accurate knowledge of the interfacing parameters seen by the inverter and the grid voltage is required in order to implement a robust voltage-sensorless interfacing scheme. This section presents a novel estimation unit, based on parallel observers, to estimate all of these parameters with low computational burden and high accuracy.

The monitoring unit is designed to estimate the interfacing parameters and the grid voltage simultaneously. A reliable solution to the present nonlinear estimation problem is realized by adopting two estimators working in parallel to linearize the estimation problem. A simple adaptation algorithm based on the steepest descent method is used to estimate the grid voltage at the PCC. The system's model becomes undisturbed when the estimated grid voltage is combined with the current dynamics. Relying on the simplified model, a natural adaptive observer is used to estimate unknown interfacing parameters by minimizing the parameter estimation error by an iterative gradient algorithm offered by the projection algorithm (PA) [98]. To properly tune the proposed estimation unit, a discrete-time Lyapunov stability analysis [95], based on the augmented estimation error dynamics, is presented. Figure 4.2 shows the adaptive-observers-based interface monitoring unit.

4.2.1 Estimation Algorithm

In the stationary reference frame, the current dynamics can be reasonably represented by the following equations:

$$\begin{bmatrix} \frac{di_\alpha}{dt} \\ \frac{di_\beta}{dt} \end{bmatrix} = \begin{bmatrix} -\frac{R}{L} & 0 \\ 0 & -\frac{R}{L} \end{bmatrix} \begin{bmatrix} i_\alpha \\ i_\beta \end{bmatrix} + \begin{bmatrix} \frac{1}{L} & 0 \\ 0 & \frac{1}{L} \end{bmatrix} \left\{ \begin{bmatrix} v_\alpha \\ v_\beta \end{bmatrix} - \begin{bmatrix} v_{s\alpha} \\ v_{s\beta} \end{bmatrix} \right\} \tag{4.1}$$

where v_α, v_β, i_α, i_β are the α- and β- axis inverter's voltages and currents; and $v_{s\alpha}$, $v_{s\beta}$ are the α- and β- axis components of the grid voltage vector.

With the conversion $H(s)$ in (3.4), the discrete-time dynamics of the inverter output current can be given by

$$\begin{bmatrix} i_\alpha(k+1) \\ i_\beta(k+1) \end{bmatrix} = \boldsymbol{A} \begin{bmatrix} i_\alpha(k) \\ i_\beta(k) \end{bmatrix} + \boldsymbol{B} \left\{ \begin{bmatrix} v_\alpha(k) \\ v_\beta(k) \end{bmatrix} - \begin{bmatrix} v_{s\alpha}(k) \\ v_{s\beta}(k) \end{bmatrix} \right\}. \tag{4.2}$$

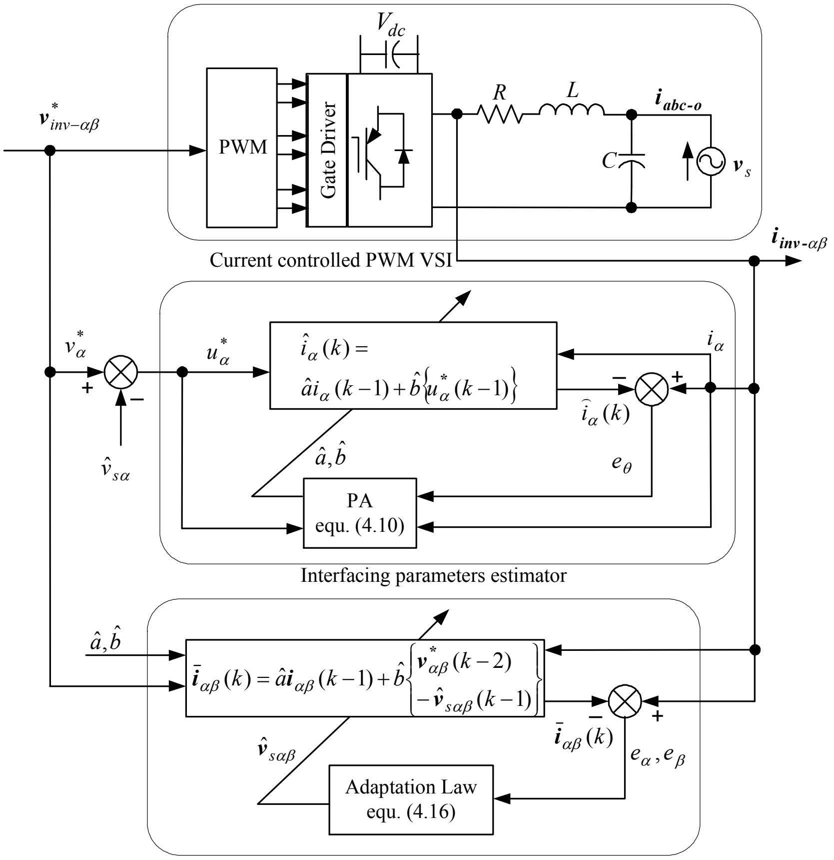

Figure 4.2: Parallel-observers-based monitoring unit.

The matrices of the discrete-time system $\boldsymbol{A}$ and $\boldsymbol{B}$ can be obtained by Taylor's expansion as follows:

$$\boldsymbol{A} = e^{\begin{bmatrix} -R/L & 0 \\ 0 & -R/L \end{bmatrix} T} \simeq \begin{bmatrix} 1 - \frac{TR}{L} & 0 \\ 0 & 1 - \frac{TR}{L} \end{bmatrix} \tag{4.3}$$

$$\boldsymbol{B} = \int_0^T e^{\begin{bmatrix} -R/L & 0 \\ 0 & -R/L \end{bmatrix} \tau} d\tau . \begin{bmatrix} 1/L & 0 \\ 0 & 1/L \end{bmatrix} \simeq \begin{bmatrix} \frac{T}{L} & 0 \\ 0 & \frac{T}{L} \end{bmatrix} . \tag{4.4}$$

A more practical model would consider the calculation delay associated with the digital implementation of the control algorithm. Practically, when a small control period is chosen, inherent and non-negligible delays associated with the implementation of the digital control scheme reduces the stability margins; particularly when high feedback gains are used. Therefore, the discrete-time dynamics in (4.2) is modified as follows:

$$\begin{bmatrix} i_\alpha(k+1) \\ i_\beta(k+1) \end{bmatrix} = \boldsymbol{A} \begin{bmatrix} i_\alpha(k) \\ i_\beta(k) \end{bmatrix} + \boldsymbol{B} \left\{ \begin{bmatrix} v_\alpha(k-1) \\ v_\beta(k-1) \end{bmatrix} - \begin{bmatrix} v_{s\alpha}(k) \\ v_{s\beta}(k) \end{bmatrix} \right\} . \tag{4.5}$$

By time-shifting (4.5) and taking the advantage of the decoupled symmetry of $\boldsymbol{A}$ and $\boldsymbol{B}$ in the stationary reference-frame, (4.5) can be re-written as

$$\begin{bmatrix} i_\alpha(k) \\ i_\beta(k) \end{bmatrix} = a \begin{bmatrix} i_\alpha(k-1) \\ i_\beta(k-1) \end{bmatrix} + b \left\{ \begin{bmatrix} v_\alpha^*(k-2) \\ v_\beta^*(k-2) \end{bmatrix} - \begin{bmatrix} v_{s\alpha}(k-1) \\ v_{s\beta}(k-1) \end{bmatrix} \right\} \tag{4.6}$$

where $a = 1 - \frac{TR}{L}$ and $b = \frac{T}{L}$.

Since the inverter's switching period is much smaller than the power circuit time constant, the actual voltage components can be replaced with the reference ones, denoted by v_α^* and v_β^* in (4.6). As a result, direct measurements, which are affected by the modulation and acquisition noise, are avoided.

In the application of the control system, the actual parameters a and b are assumed to be unknown, and they should be adjusted in real-time by a parameter estimator which can provide estimated values $\hat{a}$ and $\hat{b}$. If the grid voltage is measured, then the dynamics in (4.6) belongs to a linear estimation problem. However, when the grid voltage is unknown, the estimation problem becomes nonlinear and any parameter estimation technique will lead to biased estimates. In this study, the aforementioned problem is addressed by adopting an interfacing parameter estimator combined with a grid-voltage estimator. Both estimators work in parallel to linearize the estimation process, with low computational demand.

Assuming that the disturbance voltage vector $\begin{bmatrix} v_{s\alpha} & v_{s\beta} \end{bmatrix}^T$ is fully compensated by the feed-forward compensation control, the system's model in (4.6) is remarkably simplified and it may be expressed as

$$\begin{bmatrix} i_\alpha(k) \\ i_\beta(k) \end{bmatrix} = a \begin{bmatrix} i_\alpha(k-1) \\ i_\beta(k-1) \end{bmatrix} + b \left\{ \begin{bmatrix} u_\alpha^*(k-1) \\ u_\beta^*(k-1) \end{bmatrix} \right\} \tag{4.7}$$

where $\begin{bmatrix} u_\alpha^*(k-1) \\ u_\beta^*(k-1) \end{bmatrix} = \begin{bmatrix} v_\alpha^*(k-2) \\ v_\beta^*(k-2) \end{bmatrix} - \begin{bmatrix} \hat{v}_{s\alpha}(k-1) \\ \hat{v}_{s\beta}(k-1) \end{bmatrix}$, and superscripts "^" and "*" denote estimated and reference quantities, respectively.

There are only two parameters to be estimated; therefore either the α- or β- current dynamics can be used in the estimation phase. Relying on the simplified model in (4.7) and using the α-axis current dynamics, let the dynamics to be identified in the form:

$$i_\alpha(k) = a i_\alpha(k-1) + b u_\alpha^*(k-1) = \boldsymbol{R}^T(k-1)\Theta(k) \tag{4.8}$$

where $\boldsymbol{R}(k-1) = \begin{bmatrix} R_1(k-1) & R_2(k-1) \end{bmatrix}^T = \begin{bmatrix} i_\alpha(k-1) & u_\alpha^*(k-1) \end{bmatrix}^T$is the input/output measurement vector, and $\Theta(k) = \begin{bmatrix} \theta_1(k) & \theta_2(k) \end{bmatrix}^T = \begin{bmatrix} a(k) & b(k) \end{bmatrix}^T$ is a parameter vector. Based on (4.8), a simple adaptive observer can be constructed as follows:

$$\hat{i}_\alpha(k) = \sum_{i=1}^{2} R_i(k-1)\hat{\theta}_i(k). \tag{4.9}$$

The observer in (4.9) has the natural dynamic characteristics of the current dynamics, such as bounded-input bounded-output stability, provided that the estimated parameters are bounded within certain limits. Therefore, the convergence of the proposed estimator can be achieved with an appropriate parameter vector adaptation using the estimation error.

Using (4.8) and (4.9), the current estimation error $e_\theta \equiv i_\alpha(k) - \hat{i}_\alpha(k)$ will be produced due to any mismatch between the estimated current and the actual one. This error is produced mainly by parameter variation. Accordingly, it can be used to adaptively adjust the parameter vector $\hat{\Theta}(k) = \begin{bmatrix} \hat{\theta}_1(k) & \hat{\theta}_2(k) \end{bmatrix}^T = \begin{bmatrix} \hat{a}(k) & \hat{b}(k) \end{bmatrix}^T$ in a manner that minimizes the error. To achieve this objective, an iterative gradient algorithm based on the PA is used.

The weight vector $\hat{\Theta}(k)$ is recursively updated using the PA as follows:

$$\hat{\Theta}(k+1) = \hat{\Theta}(k) + \frac{r\boldsymbol{R}(k-1)e_\theta(k)}{\varepsilon + \boldsymbol{R}^T(k-1)\boldsymbol{R}(k-1)} \tag{4.10}$$

where r is a reduction factor and ε is a small value to avoid division by zero if $\boldsymbol{R}^T(k-1)\boldsymbol{R}(k-1) = 0$.

In the foregoing analysis, it is assumed that the grid voltage is reliably estimated; hence, unbiased estimation results can be obtained with the parameter estimator. To estimate unknown grid voltage vector, an adaptive observer with the following input/output relation can be constructed as follows:

$$\begin{bmatrix} \bar{i}_\alpha(k) \\ \bar{i}_\beta(k) \end{bmatrix} = a \begin{bmatrix} i_\alpha(k-1) \\ i_\beta(k-1) \end{bmatrix} + b \left\{ \begin{bmatrix} v^*_\alpha(k-2) \\ v^*_\beta(k-2) \end{bmatrix} - \begin{bmatrix} \hat{v}_{s\alpha}(k-1) \\ \hat{v}_{s\beta}(k-1) \end{bmatrix} \right\} \tag{4.11}$$

where $\begin{bmatrix} \bar{i}_\alpha & \bar{i}_\beta \end{bmatrix}^T$is the output of the grid voltage observer, and$\begin{bmatrix} \hat{v}_{s\alpha} & \hat{v}_{s\beta} \end{bmatrix}^T$is the estimated grid voltage vector.

The convergence of the grid-voltage estimator can be achieved with an adaptive adjustment of the estimated grid-voltage $\begin{bmatrix} \hat{v}_{s\alpha} & \hat{v}_{s\beta} \end{bmatrix}^T$ in order to minimize a predefined performance index. To show the adaptation algorithm, the estimation error vector can be defined as

$$\begin{bmatrix} e_\alpha(k) \\ e_\beta(k) \end{bmatrix} \equiv \begin{bmatrix} i_\alpha(k) \\ i_\beta(k) \end{bmatrix} - \begin{bmatrix} \bar{i}_\alpha(k) \\ \bar{i}_\beta(k) \end{bmatrix}. \tag{4.12}$$

Due to the properties of guaranteed convergence, and optimizing the performance, a discrete-type quadratic error function is defined as

$$E(k) = \frac{1}{2}\left(e_\alpha(k)^2 + e_\beta(k)^2\right). \tag{4.13}$$

The disturbance voltage can be adaptively estimated by minimizing the error function $E(k)$ using the steepest descent method. Accordingly, one can evaluate the following

Jacobian:

$$J = \begin{bmatrix} \frac{\partial E}{\partial \hat{v}_{s\alpha}} \\ \frac{\partial E}{\partial \hat{v}_{s\beta}} \end{bmatrix} = \begin{bmatrix} \frac{\partial E}{\partial \bar{i}_{\alpha}} \frac{\partial \bar{i}_{\alpha}}{\partial \hat{v}_{s\alpha}} \\ \frac{\partial E}{\partial \bar{i}_{\beta}} \frac{\partial \bar{i}_{\beta}}{\partial \hat{v}_{s\beta}} \end{bmatrix}. \tag{4.14}$$

The right-hand side term of (4.14) can be evaluated as

$$J = \left\{ \begin{bmatrix} i_{\alpha}(k) \\ i_{\beta}(k) \end{bmatrix} - \begin{bmatrix} \bar{i}_{\alpha}(k) \\ \bar{i}_{\beta}(k) \end{bmatrix} \right\} b \tag{4.15}$$

Therefore, the change in the estimate is given by

$$\begin{aligned} \begin{bmatrix} \hat{v}_{s\alpha}(k+1) \\ \hat{v}_{s\beta}(k+1) \end{bmatrix} &= \begin{bmatrix} \hat{v}_{s\alpha}(k) \\ \hat{v}_{s\beta}(k) \end{bmatrix} + \begin{bmatrix} \Delta\hat{v}_{s\alpha}(k) \\ \Delta\hat{v}_{s\beta}(k) \end{bmatrix} = \begin{bmatrix} \hat{v}_{s\alpha}(k) \\ \hat{v}_{s\beta}(k) \end{bmatrix} - \gamma J \\ &= \begin{bmatrix} \hat{v}_{s\alpha}(k) \\ \hat{v}_{s\beta}(k) \end{bmatrix} - \gamma b \left\{ \begin{bmatrix} i_{\alpha}(k) \\ i_{\beta}(k) \end{bmatrix} - \begin{bmatrix} \bar{i}_{\alpha}(k) \\ \bar{i}_{\beta}(k) \end{bmatrix} \right\} \end{aligned} \tag{4.16}$$

where γ is a positive adaptation gain.

The adaptive learning law in (4.16) provides a simple iterative gradient algorithm designed to minimize (4.13) in real-time. As a result, the estimate can be reliably used for the feed-forward control.

The estimate $\begin{bmatrix} \hat{v}_{s\alpha} & \hat{v}_{s\beta} \end{bmatrix}^T$ is fed-forward to (4.8) resulting in equivalent excitation signal to cancel the voltage disturbance. As a result, the unbiased parameter estimate $\hat{\Theta}$ can be reliably used to tune the grid-voltage estimator in (4.11). Subsequently, the disturbance voltage information can be precisely observed even under parameter variation. Using the preceding recursive process, the voltage disturbance and the interfacing parameters will quickly converge into their real values. The estimated quantities can be reliably used to realize a robust grid-voltage sensorless interfacing scheme [99].

4.2.2 Stability and Convergence Analysis

This section analyzes the stability of the proposed adaptive-observers-based estimation unit and gives a guideline in tuning the unit parameters using a Lyapunov function.

Two Lyapunov function candidates for the error equation (4.12) and the parameter estimator (4.10) are utilized. The total Lyapunov function is selected as

$$\begin{aligned} V_T\left(e_{\alpha}(k), e_{\beta}(k), \tilde{\Theta}(k), k\right) &= V_1\left(e_{\alpha}(k), e_{\beta}(k), k\right) + V_2\left(\tilde{\Theta}(k), k\right) \\ &= \frac{1}{2}\left[e_{\alpha}(k)^2 + e_{\beta}(k)^2\right] + \tilde{\Theta}(k)^T \tilde{\Theta}(k) \end{aligned} \tag{4.17}$$

where $e_{\alpha}(k)$ and $e_{\beta}(k)$ are the estimation errors defined in (4.12); and $\tilde{\Theta}(k)$ is the interfacing parameter estimation error, defined as

$$\tilde{\Theta}(k) \equiv \Theta(k) - \hat{\Theta}(k). \tag{4.18}$$

The Lyapunov's convergence criterion must be satisfied such that

$$V_T(k)\Delta V_T(k) < 0 \tag{4.19}$$

where $\Delta V_T(k) = \Delta V_1(k) + \Delta V_2(k)$ is the change in the total Lyapunov function.

The stability condition in (4.19) is satisfied when $\Delta V_T(k) < 0$ as $V_T(k)$ is defined as an arbitrary positive. Firstly, $\Delta V_1(k)$ is given by

$$\Delta V_1(k) = V_1\left(e_\alpha(k+1), e_\beta(k+1)\right) - V_1\left(e_\alpha(k), e_\beta(k)\right) < 0. \tag{4.20}$$

Since the grid voltage can be assumed to be naturally continuous and its bandwidth is much lower than the observation period, the change in the error $\Delta e_\alpha(k)$ and $\Delta e_\beta(k)$ due to the adaptation process of the grid-voltage estimator can be given by

$$\begin{aligned}\begin{bmatrix}\Delta e_\alpha(k)\\ \Delta e_\beta(k)\end{bmatrix} = \begin{bmatrix} e_\alpha(k+1) - e_\alpha(k)\\ e_\beta(k+1) - e_\beta(k)\end{bmatrix} &= \begin{bmatrix}\frac{\partial e_\alpha(k)}{\partial \hat{v}_{s\alpha}}\Delta \hat{v}_{s\alpha}(k)\\ \frac{\partial e_\alpha(k)}{\partial \hat{v}_{s\beta}}\Delta \hat{v}_{s\beta}(k)\end{bmatrix}\\ &= \gamma\begin{bmatrix}\frac{\partial e_\alpha(k)}{\partial \hat{v}_{s\alpha}}\frac{\partial \bar{i}_\alpha(k)}{\partial \hat{v}_{s\alpha}}e_\alpha(k)\\ \frac{\partial e_\beta(k)}{\partial \hat{v}_{s\beta}}\frac{\partial \bar{i}_\beta(k)}{\partial \hat{v}_{s\beta}}e_\beta(k)\end{bmatrix}.\end{aligned} \tag{4.21}$$

Accordingly, $\Delta V_1(k)$ can be represented as

$$\begin{aligned}\Delta V_1(k) &= e_\alpha(k)\Delta e_\alpha(k) + e_\beta(k)\Delta e_\beta(k) + \frac{1}{2}\left(\Delta e_\alpha(k)^2 + \Delta e_\beta(k)^2\right)\\ &= \gamma\left\{\frac{\partial e_\alpha(k)}{\partial \hat{v}_{s\alpha}}\frac{\partial \bar{i}_\alpha(k)}{\partial \hat{v}_{s\alpha}}e_\alpha(k)^2 + \frac{\partial e_\beta(k)}{\partial \hat{v}_{s\beta}}\frac{\partial \bar{i}_\beta(k)}{\partial \hat{v}_{s\beta}}e_\beta(k)^2\right\}\\ &\quad + \frac{\gamma^2}{2}\left\{\left\|\frac{\partial e_\alpha(k)}{\partial \hat{v}_{s\alpha}}\right\|^2\left\|\frac{\partial \bar{i}_\alpha(k)}{\partial \hat{v}_{s\alpha}}\right\|^2 e_\alpha(k)^2 + \left\|\frac{\partial e_\beta(k)}{\partial \hat{v}_{s\beta}}\right\|^2\left\|\frac{\partial \bar{i}_\beta(k)}{\partial \hat{v}_{s\beta}}\right\|^2 e_\beta(k)^2\right\}\end{aligned} \tag{4.22}$$

where $\|\,.\,\|$ is the Euclidean norm in $\Re^n$.
Since $\frac{\partial \bar{i}_\alpha(k)}{\partial \hat{v}_{s\alpha}} = -\frac{\partial e_\alpha(k)}{\partial \hat{v}_{s\alpha}}$ and $\frac{\partial \bar{i}_\beta(k)}{\partial \hat{v}_{s\beta}} = -\frac{\partial e_\beta(k)}{\partial \hat{v}_{s\beta}}$, then (4.22) can be evaluated as

$$\begin{aligned}\Delta V_1(k) = &-\left\{\gamma\left\|\frac{\partial \bar{i}_\alpha(k)}{\partial \hat{v}_{s\alpha}}\right\|^2 - \frac{\gamma^2}{2}\left\|\frac{\partial \bar{i}_\alpha(k)}{\partial \hat{v}_{s\alpha}}\right\|^4\right\}e_\alpha(k)^2\\ &-\left\{\gamma\left\|\frac{\partial \bar{i}_\beta(k)}{\partial \hat{v}_{s\beta}}\right\|^2 - \frac{\gamma^2}{2}\left\|\frac{\partial \bar{i}_\beta(k)}{\partial \hat{v}_{s\beta}}\right\|^4\right\}e_\beta(k)^2.\end{aligned} \tag{4.23}$$

To satisfy the stability condition in (4.20), the learning rate γ is chosen as

$$0 < \gamma < \frac{2}{\max_k\left[\left\|\frac{\partial \bar{i}_\alpha(k)}{\partial \hat{v}_{s\alpha}}\right\|^2, \left\|\frac{\partial \bar{i}_\beta(k)}{\partial \hat{v}_{s\beta}}\right\|^2\right]}. \tag{4.24}$$

Secondly, the change in the Lyapunov function for the parameter estimator $\Delta V_2(k)$ is given by

$$\Delta V_2(k) = V_2\left(\tilde{\Theta}(k+1)\right) - V_2\left(\tilde{\Theta}(k)\right) < 0. \tag{4.25}$$

By using the parameter estimation error dynamics, $\Delta V_2(k)$ can be evaluated as

$$\begin{aligned}\Delta V_2(k) &= \left\| \tilde{\Theta}(k) - \frac{r\boldsymbol{R}(k-1)\boldsymbol{R}(k-1)\tilde{\Theta}(k)}{\varepsilon + \boldsymbol{R}^T(k-1)\boldsymbol{R}(k-1)} \right\|^2 - \tilde{\Theta}(k)^T\tilde{\Theta}(k) \\ &= \frac{r\left[\tilde{\Theta}(k)^T\boldsymbol{R}(k-1)\right]^2}{\varepsilon + \boldsymbol{R}^T(k-1)\boldsymbol{R}(k-1)}\left[-2 + \frac{r\boldsymbol{R}^T(k-1)\boldsymbol{R}(k-1)}{\varepsilon + \boldsymbol{R}^T(k-1)\boldsymbol{R}(k-1)}\right].\end{aligned} \tag{4.26}$$

If $\varepsilon > 0$ and $0 < r < 2$ are assumed, the bracketed term in (4.26) is negative and consequently the stability condition in (4.25) is satisfied.

Using the abovementioned conditions, it can be shown that $\Delta V_T(k) = \Delta V_1(k) + \Delta V_2(k) < 0$ and it follows that the augmented error is monotonically non-increasing. Therefore, the convergence is guaranteed and the estimates can be reliably used in the control system design.

4.3 Interface Monitoring Unit – Design #2

Due to the nonlinear nature of the estimation problem and the periodic time-varying nature of the grid voltage, a NN-based identification approach has been investigated. The self-learning feature of the NN adaptation algorithm allows a feasible and easy adaptation design at different operating conditions [100]-[103].

Figure 4.3 shows the second design of the proposed interface monitoring unit. The algorithm utilizes an adjustable current dynamics reference model in the stationary-reference frame, which runs in parallel with the actual inverter current dynamics; the later acts as a reference model [104]. The grid voltage estimator utilizes a NN-based adaptation algorithm, which employs a three-layer feed-forward NN working as a real-time optimization agent for the present estimation problem. The estimated grid voltage can be regarded as a quasi-input signal, which can be included in the model excitation voltage; hence, undisturbed model is yielded. Relying on the undisturbed model, a simple parameter estimator is used to estimate unknown interfacing parameters by minimizing the parameter estimation error via an iterative gradient algorithm offered by the PA.

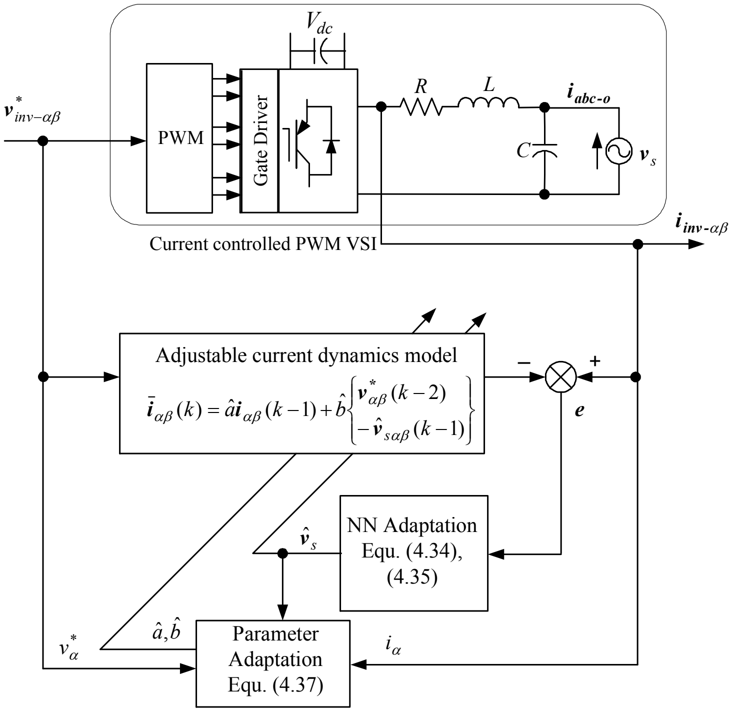

Figure 4.3: NN-based interface monitoring unit.

4.3.1 Estimation Algorithm

To estimate the grid voltage vector, suppose that the interfacing parameters R and L are exactly known. An adjustable model with the following input/output relation can be constructed:

$$\begin{bmatrix} \hat{i}_\alpha(k) \\ \hat{i}_\beta(k) \end{bmatrix} = a \begin{bmatrix} i_\alpha(k-1) \\ i_\beta(k-1) \end{bmatrix} + b \left\{ \begin{bmatrix} v^*_\alpha(k-2) \\ v^*_\beta(k-2) \end{bmatrix} - \begin{bmatrix} \hat{v}_{s\alpha}(k-1) \\ \hat{v}_{s\beta}(k-1) \end{bmatrix} \right\} \tag{4.27}$$

where superscripts "^" and "*" denote estimated and reference quantities, respectively.

The convergence of the adjustable model in (4.27) can be achieved with an appropriate adaptation algorithm using the estimation error:

$$\boldsymbol{e}(k) \equiv \begin{bmatrix} e_\alpha(k) \\ e_\beta(k) \end{bmatrix} = \begin{bmatrix} i_\alpha(k) - \hat{i}_\alpha(k) \\ i_\beta(k) - \hat{i}_\beta(k) \end{bmatrix}. \tag{4.28}$$

A three-layer NN, as shown in Figure 4.4, which comprises an input layer (the i layer), a hidden layer (the j layer), and an output layer (the k layer), is adopted to implement the proposed NN-based adaptation algorithm. The inputs of the NN adaptation algorithm are $e(k)$ and $\Delta e(k)$, whereas the output is the estimated grid voltage vector $\hat{\boldsymbol{v}}_s$. The connective weights of the NN are adjusted online to adjust the model in (4.27), so that

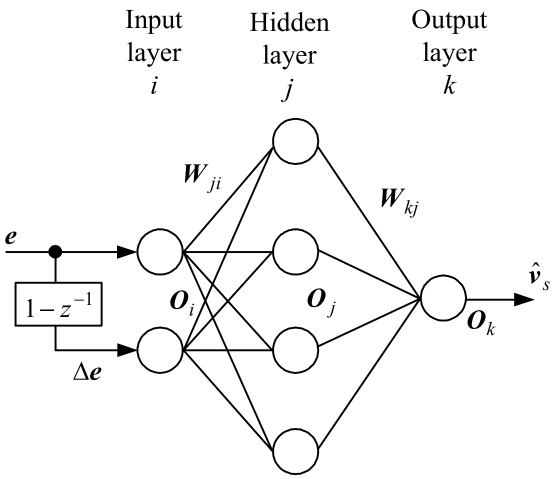

Figure 4.4: NN structure.

the estimation error in (4.28) is minimized. The signal propagation and the fundamental function of each layer are summarized as follows:

Input Layer:

$$\begin{aligned} \boldsymbol{net}_i &= \boldsymbol{x}_i, \\ \boldsymbol{O}_i &= \left[\begin{array}{cc} O_i^\alpha & O_i^\beta \end{array}\right]^T = f_i(\boldsymbol{net}_i), \\ f_i(\varphi) &= \varphi, \\ i &= 1, 2 \end{aligned} \tag{4.29}$$

where $\boldsymbol{x}_1 = \boldsymbol{e}(k)$ and $\boldsymbol{x}_2 = (1 - z^{-1})\boldsymbol{e}(k)$ are the network inputs.

Hidden Layer:

$$\begin{aligned} \boldsymbol{net}_j &= \left[\begin{array}{cc} \sum_i W_{ji}^\alpha O_i^\alpha & \sum_i W_{ji}^\beta O_i^\beta \end{array}\right]^T, \\ \boldsymbol{O}_j &= \left[\begin{array}{cc} O_j^\alpha & O_j^\beta \end{array}\right]^T = f_j(\boldsymbol{net}_j), \\ f_j(\varphi) &= \frac{1}{1 + e^{-\varphi}} \\ j &= 1, ..., 4 \end{aligned} \tag{4.30}$$

where $\boldsymbol{W}_{ji} = \left[\begin{array}{cc} W_{ji}^\alpha & W_{ji}^\beta \end{array}\right]^T$ are the connective weights between the input and the hidden layers, and f_j is the activation function.

Output Layer:

$$\begin{aligned} \boldsymbol{net}_k &= \left[\begin{array}{cc} \sum_j W_{kj}^\alpha O_j^\alpha & \sum_i W_{kj}^\beta O_j^\beta \end{array}\right]^T, \\ \boldsymbol{O}_k &= \left[\begin{array}{cc} O_k^\alpha & O_k^\beta \end{array}\right]^T = f_k(\boldsymbol{net}_k), \\ f_k(\varphi) &= \varphi, \\ k &= 1, 2 \end{aligned} \tag{4.31}$$

where $\boldsymbol{W}_{kj} = \left[\begin{array}{cc} W_{kj}^{\alpha} & W_{kj}^{\beta} \end{array} \right]^T$ are the connective weights between the hidden and the output layers.

In the present online learning algorithm, the weight adaptation rules are synthesized as follows. A discrete-time Lyapunov candidate function is selected as

$$V_3(\boldsymbol{e}(k), k) = \frac{1}{2}\boldsymbol{e}^T(k)\boldsymbol{e}(k). \tag{4.32}$$

The Lyapunov's convergence criterion must be satisfied such that

$$V_3(k)\Delta V_3(k) < 0 \tag{4.33}$$

where $\Delta V_3(k)$ is the change in the Lyapunov function.

The stability condition in (4.33) is satisfied when $\Delta V_3(k) < 0$ as $V_3(k)$ is defined as an arbitrary positive.

For the error dynamics in (4.28) and with the chosen Lyapunov function, the sensitivity of the controlled system is not required in the online learning algorithm. On the other hand, complex identification techniques are needed to identify the Jacobian of the controlled plant in the traditional back-propagation learning algorithm [101]-[102]. The learning algorithm aims at evaluating the derivatives of the Lyapunov energy function with respect to the network parameters, so that $\Delta V_3(k) < 0$ is satisfied. Accordingly, the output layer weights $\boldsymbol{W}_{kj}$ are updated as follows:

$$\Delta \boldsymbol{W}_{kj}(k) = -\eta_{kj}\frac{\partial \dot{V}_3}{\partial \hat{\boldsymbol{v}}_s}\frac{\partial \hat{\boldsymbol{v}}_s}{\partial \boldsymbol{O}_k}\frac{\partial \boldsymbol{O}_k}{\partial \boldsymbol{net}_k}\frac{\partial \boldsymbol{net}_k}{\partial \boldsymbol{W}_{kj}} = -b\eta_{kj}\left[\begin{array}{c} e_{\alpha}(k)O_j^{\alpha} \\ e_{\beta}(k)O_j^{\beta} \end{array} \right] \tag{4.34}$$

where η_{kj} is the learning rate of the connected weight vector $\boldsymbol{W}_{kj}$. Similarly, the hidden layer weights are updated as follows:

$$\begin{aligned} \Delta \boldsymbol{W}_{ji}(k) &= -\eta_{ji}\frac{\partial \dot{V}_3}{\partial \boldsymbol{net}_k}\frac{\partial \boldsymbol{net}_k}{\partial \boldsymbol{O}_j}\frac{\partial \boldsymbol{O}_j}{\partial \boldsymbol{net}_j}\frac{\partial \boldsymbol{net}_j}{\partial \boldsymbol{W}_{ji}} \\ &= -b\eta_{ji}\left[\begin{array}{c} e_{\alpha}(k)W_{kj}^{\alpha}f'\left(\sum_i W_{ji}^{\alpha}O_i^{\alpha}\right)O_i^{\alpha} \\ e_{\beta}(k)W_{kj}^{\beta}f'\left(\sum_i W_{ji}^{\beta}O_i^{\beta}\right)O_i^{\beta} \end{array} \right] \end{aligned} \tag{4.35}$$

where η_{ji} is the learning rate of the connected weight vector $\boldsymbol{W}_{ji}$.

The update rules in (4.34) and (4.35) provide an iterative gradient algorithm designed to minimize the energy function in (4.30). Since the gradient vector is calculated in the direction opposite to the energy flow, the convergence of the NN is feasible.

With the NN grid voltage estimator, the estimated grid voltage can be regarded as a quasi-input signal, which can be used for feed-forward control. Subsequently, the current dynamics model becomes undisturbed. Therefore, the α-axis current dynamics,

$$i_{\alpha}(k) = ai_{\alpha}(k-1) + bu_{\alpha}^*(k-1) = \boldsymbol{R}^T(k-1)\Theta(k) \tag{4.36}$$

where $\boldsymbol{R}(k-1) = \left[\begin{array}{cc} i_\alpha(k-1) & u^*_\alpha(k-1) \end{array}\right]^T$ is the input/output measurement vector, and $\Theta(k) = \left[\begin{array}{cc} a(k) & b(k) \end{array}\right]^T$ is a parameter vector, and they can be used in a recursive estimation process to provide an estimate $\hat{\Theta}(k) = \left[\begin{array}{cc} \hat{a}(k) & \hat{b}(k) \end{array}\right]^T$ of unknown plant parameters. The estimation error $\left\{i_\alpha(k) - \boldsymbol{R}^T(k-1)\hat{\Theta}(k)\right\}$ will be produced mainly by parameter variation. The parameter vector $\hat{\Theta}(k)$ is recursively updated using the PA as follows:

$$\hat{\Theta}(k+1) = \hat{\Theta}(k) + \frac{r\boldsymbol{R}(k-1)\left\{i_\alpha(k) - \boldsymbol{R}^T(k-1)\hat{\Theta}(k)\right\}}{\varepsilon + \boldsymbol{R}^T(k-1)\boldsymbol{R}(k-1)} \tag{4.37}$$

where $r \in [0, 2]$ is a reduction factor, and ε is a small value to avoid division by zero if $\boldsymbol{R}^T(k-1)\boldsymbol{R}(k-1) = 0$.

As stated earlier, the continuous update of the parameter estimate and the grid voltage yields unbiased parameter estimate and accurate grid-voltage information. The estimated quantities can be reliably used to realize an adaptive grid-voltage sensorless interfacing scheme.

4.3.2 Stability and Convergence Analysis

This section analyzes the stability of the proposed NN-based estimation unit and gives a guideline in tuning the unit parameters using a Lyapunov function.

Two Lyapunov function candidates for the error vector $\left[\begin{array}{cc} e_\alpha & e_\beta \end{array}\right]^T$ and the parameter estimator error vector $\tilde{\Theta}(k) \equiv \Theta(k) - \hat{\Theta}(k)$ are utilized. The total Lyapunov function is selected as

$$\begin{aligned} V_T\left(e_\alpha(k), e_\beta(k), \tilde{\Theta}(k), k\right) &= V_1\left(e_\alpha(k), e_\beta(k), k\right) + V_2\left(\tilde{\Theta}(k), k\right) \\ &= \frac{1}{2}\left[e_\alpha(k)^2 + e_\beta(k)^2\right] + \tilde{\Theta}(k)^T\tilde{\Theta}(k). \end{aligned} \tag{4.38}$$

The Lyapunov's convergence criterion must be satisfied such that $V_T(k)\Delta V_T(k) < 0$ where $\Delta V_T(k) = \Delta V_1(k) + \Delta V_2(k)$ is the change in the total Lyapunov function.

Firstly, the change in the Lyapunov function $\Delta V_1(k)$ is given by

$$\Delta V_1(k) = V_1\left(e_\alpha(k+1), e_\beta(k+1)\right) - V_1\left(e_\alpha(k), e_\beta(k)\right) < 0. \tag{4.39}$$

The change in the error $\Delta e_\alpha(k)$ and $\Delta e_\beta(k)$ due to the adaptation of the weight vector $\boldsymbol{W}_{kj}$ can be given by

$$\left[\begin{array}{c} \Delta e_\alpha(k) \\ \Delta e_\beta(k) \end{array}\right] = \left[\begin{array}{c} e_\alpha(k+1) - e_\alpha(k) \\ e_\beta(k+1) - e_\beta(k) \end{array}\right] = \left[\begin{array}{c} \frac{\partial e_\alpha(k)}{\partial W^\alpha_{kj}}\Delta W^\alpha_{kj} \\ \frac{\partial e_\beta(k)}{\partial W^\beta_{kj}}\Delta W^\beta_{kj} \end{array}\right]. \tag{4.40}$$

Since $\left[\begin{array}{cc} \frac{\partial e_\alpha(k)}{\partial W_{kj}^\alpha} & \frac{\partial e_\beta(k)}{\partial W_{kj}^\beta} \end{array}\right]^T = b\eta_{kj}\left[\begin{array}{c} O_j^\alpha \\ O_j^\beta \end{array}\right]$, then the following incremental error dynamics can be obtained:

$$\left[\begin{array}{c} \Delta e_\alpha(k) \\ \Delta e_\beta(k) \end{array}\right] = -b^2\eta_{kj}\left[\begin{array}{c} e_\alpha(k)\left(O_j^\alpha\right)^2 \\ e_\beta(k)\left(O_j^\beta\right)^2 \end{array}\right]. \tag{4.41}$$

By substituting (4.41) in (4.40), $\Delta V_1(k)$ can be represented as

$$\begin{aligned}\Delta V_1(k) &= e_\alpha(k)\Delta e_\alpha(k) + e_\beta(k)\Delta e_\beta(k) + \frac{1}{2}\left(\Delta e_\alpha(k)^2 + \Delta e_\beta(k)^2\right) \\ &= -b^2\eta_{kj}e_\alpha(k)^2\left(O_j^\alpha\right)^2\left(1 - \frac{b^2\eta_{kj}\left(O_j^\alpha\right)^2}{2}\right) - b^2\eta_{kj}e_\beta(k)^2\left(O_j^\beta\right)^2\left(1 - \frac{b^2\eta_{kj}\left(O_j^\beta\right)^2}{2}\right).\end{aligned} \tag{4.42}$$

To satisfy the convergence condition $\Delta V_1(k) < 0$, the learning rate η_{kj} should satisfy

$$0 < \eta_{kj} < \frac{2}{\max_k\left[b^2\left\|O_j^\alpha(k)\right\|^2, b^2\left\|O_j^\beta(k)\right\|^2\right]}. \tag{4.43}$$

Since $0 < O_j^\alpha < 1$, $0 < O_j^\beta < 1$, and j=1,..,R_{kj}, where R_{kj} is the number of weights between the output and hidden layer, then by the definition of he usual Euclidean norm in $\Re^n$, $\left\|O_j^\alpha\right\| \leq \sqrt{R_{kj}}$ and $\left\|O_j^\beta\right\| \leq \sqrt{R_{kj}}$.

The change in the error $\Delta e_\alpha(k)$ and $\Delta e_\beta(k)$ due to the adaptation of the weight vector W_{ji} can be given by

$$\left[\begin{array}{c} \Delta e_\alpha(k) \\ \Delta e_\beta(k) \end{array}\right] = \left[\begin{array}{c} e_\alpha(k+1) - e_\alpha(k) \\ e_\beta(k+1) - e_\beta(k) \end{array}\right] = \left[\begin{array}{c} \frac{\partial e_\alpha(k)}{\partial W_{ji}^\alpha}\Delta W_{ji}^\alpha \\ \frac{\partial e_\beta(k)}{\partial W_{ji}^\beta}\Delta W_{ji}^\beta \end{array}\right]. \tag{4.44}$$

Since $\left[\begin{array}{c} \frac{\partial e_\alpha(k)}{\partial W_{ji}^\alpha} \\ \frac{\partial e_\beta(k)}{\partial W_{ji}^\beta} \end{array}\right] = b\left[\begin{array}{c} W_{kj}^\alpha f'\left(\sum_i W_{ji}^\alpha O_i^\alpha\right)O_i^\alpha \\ W_{kj}^\beta f'\left(\sum_i W_{ji}^\beta O_i^\beta\right)O_i^\beta \end{array}\right]$, the following incremental error dynamics can be obtained

$$\left[\begin{array}{c} \Delta e_\alpha(k) \\ \Delta e_\beta(k) \end{array}\right] = -b^2\eta_{ji}\left[\begin{array}{c} e_\alpha(k)\left(W_{kj}^\alpha\right)^2\left(f'\left(\sum_i W_{ji}^\alpha O_i^\alpha\right)\right)^2\left(O_i^\alpha\right)^2 \\ e_\beta(k)\left(W_{kj}^\beta\right)^2\left(f'\left(\sum_i W_{ji}^\beta O_i^\beta\right)\right)^2\left(O_i^\beta\right)^2 \end{array}\right]. \tag{4.45}$$

By substituting (4.45) in (4.44), $\Delta V_1(k)$ can be represented as

$$\begin{aligned}\Delta V_1(k) &= e_\alpha(k)\Delta e_\alpha(k) + e_\beta(k)\Delta e_\beta(k) + \frac{1}{2}\left(\Delta e_\alpha(k)^2 + \Delta e_\beta(k)^2\right) \\ &= -b^2\eta_{ji}e_\alpha(k)^2\left(M_{ji}^\alpha\right)^2\left(1 - \frac{b^2\eta_{ji}\left(M_{ji}^\alpha\right)^2}{2}\right) - b^2\eta_{ji}e_\beta(k)^2\left(M_{ji}^\beta\right)^2\left(1 - \frac{b^2\eta_{ji}\left(M_{ji}^\beta\right)^2}{2}\right)\end{aligned} \tag{4.46}$$

where $\begin{bmatrix} \left(M_{ji}^{\alpha}\right)^2 \\ \left(M_{ji}^{\beta}\right)^2 \end{bmatrix} = \begin{bmatrix} \left(W_{kj}^{\alpha}\right)^2 \left(f'\left(\sum_i W_{ji}^{\alpha} O_i^{\alpha}\right)\right)^2 \left(O_i^{\alpha}\right)^2 \\ \left(W_{kj}^{\beta}\right)^2 \left(f'\left(\sum_i W_{ji}^{\beta} O_i^{\beta}\right)\right)^2 \left(O_i^{\beta}\right)^2 \end{bmatrix}$.

To satisfy the convergence condition $\Delta V_1(k) < 0$, the learning rate η_{ji} should satisfy

$$0 < \eta_{ji} < \frac{2}{\max_k \left[\left\| M_{ji}^{\alpha}(k) \right\|^2, \left\| M_{ji}^{\beta}(k) \right\|^2 \right]}. \tag{4.47}$$

Provided that $f_j(\varphi) \in [0,1]$ and $f_j'(\varphi) = f_j(\varphi) - (f_j(\varphi))^2$, then $\max\left[f_j'(\varphi)\right] = \frac{1}{4}$. Therefore, $\left\| M_{ji}^{\alpha}(k) \right\|^2 \leq \frac{\left(W_{kj-\max}^{\alpha}\right)^2 \left(O_{i-\max}^{\alpha}\right)^2}{16}$ and $\left\| M_{ji}^{\beta}(k) \right\|^2 \leq \frac{\left(W_{kj-\max}^{\beta}\right)^2 \left(O_{i-\max}^{\beta}\right)^2}{16}$.

Since the weights-update rules are synthesized in the direction opposite to the energy flow, the weights between the hidden and output layers are bounded. Since the parameters of the NN are bounded, the convergence is guaranteed.

Secondly, the change in the Lyapunov function for the parameter estimator satisfies $\Delta V_2(k) = V_2\left(\tilde{\Theta}(k+1)\right) - V_2\left(\tilde{\Theta}(k)\right) < 0$ as shown in (4.26).

Using the abovementioned conditions, it can be shown that $\Delta V_T(k) = \Delta V_1(k) + \Delta V_2(k) < 0$. Therefore, the convergence is guaranteed and the estimates can be reliably used in the control system design.

4.4 Grid-Voltage-Vector Position Estimation

Smooth and accurate information of the position of the grid-voltage vector is necessary to guarantee high power quality injection. In many cases, the grid voltage might be contaminated by harmonics, which may have been produced by the power converter itself or propagated through the system. In addition, the presence of negative sequence component, due to grid voltage unbalance, appears as a second harmonic in the stationary reference frame. Therefore, there is a strong need to provide a smooth estimate of the grid-voltage position even under distorted grid voltage at the PCC.

Toward this, a simple and robust synchronization method is proposed. The method utilizes a new sensorless *dq*-PLL with a resonant filter tuned at the fundamental grid frequency. The utilization of resonant filters in the synchronization problem provides high attenuation for the frequency modes to be eliminated from the controlled tracking error. In addition, the states of a second order resonant filter are in quadrature. This feature enables the utilization of only one filter for both voltage components in the stationary reference-frame, hence, yielding a computationally efficient solution.

The following state-space model represents a second order resonant filter tuned at the fundamental power frequency:

$$\frac{d\boldsymbol{x}_f}{dt} = \boldsymbol{A}_f\boldsymbol{x}_f + \boldsymbol{B}_f u_f \tag{4.48}$$

$$y = \boldsymbol{C}\boldsymbol{x}_f \tag{4.49}$$

with

$$\boldsymbol{x}_f = \begin{bmatrix} x_{f1} \\ x_{f2} \end{bmatrix} \quad \boldsymbol{A}_f = \begin{bmatrix} 0 & \omega_1 \\ -\omega_1 & 0 \end{bmatrix}$$

$$\boldsymbol{B}_f = \begin{bmatrix} K_f \\ 0 \end{bmatrix} \quad \boldsymbol{C} = \begin{bmatrix} 1 & 0 \end{bmatrix}$$

where ω_1 is the fundamental power frequency; x_f is the filtered signal vector; u_f is the input signal; and K_f is the filter gain.

For digital implementations, the discretized model of (4.48) and (4.49) can be obtained as follows:

$$\boldsymbol{x}_f(k+1) = \boldsymbol{A}_{fd}x_f(k) + \boldsymbol{B}_{fd}u_f(k) \tag{4.50}$$

$$y(k) = \boldsymbol{C}\boldsymbol{x}_f(k) \tag{4.51}$$

where

$$\boldsymbol{A}_{fd} \simeq I_{2\times 2} + \boldsymbol{A}_f T = \begin{bmatrix} 1 & \omega_1 T \\ -\omega_1 T & 1 \end{bmatrix} \qquad \boldsymbol{B}_{fd} \simeq \boldsymbol{B}_f T = \begin{bmatrix} K_f T \\ 0 \end{bmatrix}.$$

Figure 4.5 depicts the structure of the proposed grid-voltage sensorless PLL algorithm. The input signal u_f is the estimated α-axis component of the grid voltage vector in the stationary reference frame. The filtered state vector $\boldsymbol{x}_f = \begin{bmatrix} \hat{v}_{s\alpha f} & \hat{v}_{s\alpha f} \end{bmatrix}^T$ is transformed to the synchronous reference frame using the estimated grid angle $\hat{\theta}$. The q-axis grid voltage is used to generate the estimated grid angle using a digital loop filter. A PI digital loop filter can be represented by:

$$G_{LF} = K_P \frac{z\left(z - (1 - T/\tau)\right)}{(z-1)^2} \tag{4.52}$$

where K_P is the proportional gain and τ is loop filter time constant.

Since the resonant filter handles the disturbance rejection function, the loop filter parameters could be chosen to achieve predefined tracking characteristics in the sense of a standard second order system, which represents the small signal dynamics of the PLL. The disturbance rejection performance of the resonant filter depends on the filter gain K_f. Figure 4.6 shows the frequency response of the closed loop dynamics of the resonant filter for different values of the loop gain. It is clear that with lower values of the filter gain, better attenuation is yielded. However, the transient response becomes slower. Therefore, a tradeoff between the transient response and the attenuation performance of the resonant filter should be made when choosing the filter gain.

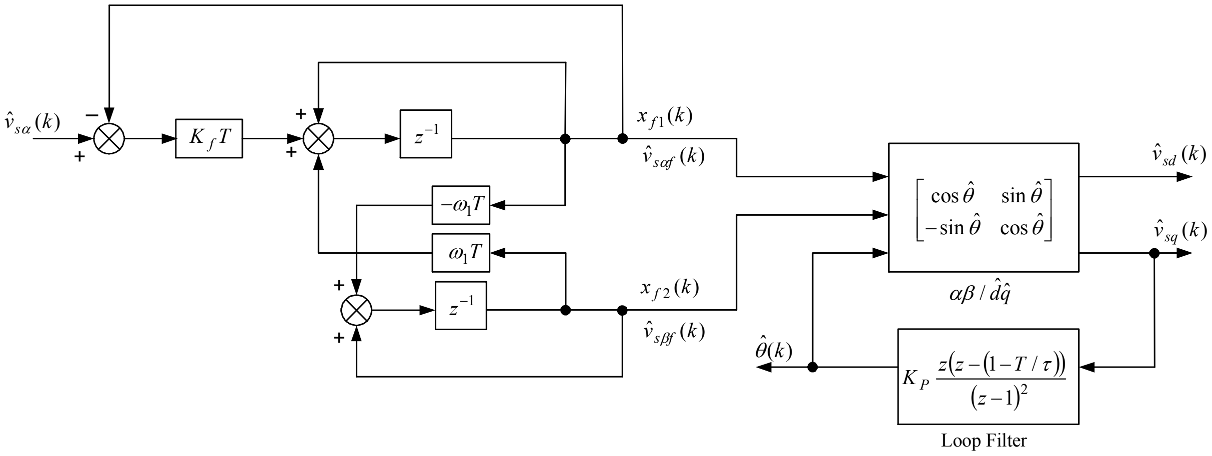

Figure 4.5: Proposed grid-voltage sensorless robust PLL algorithm.

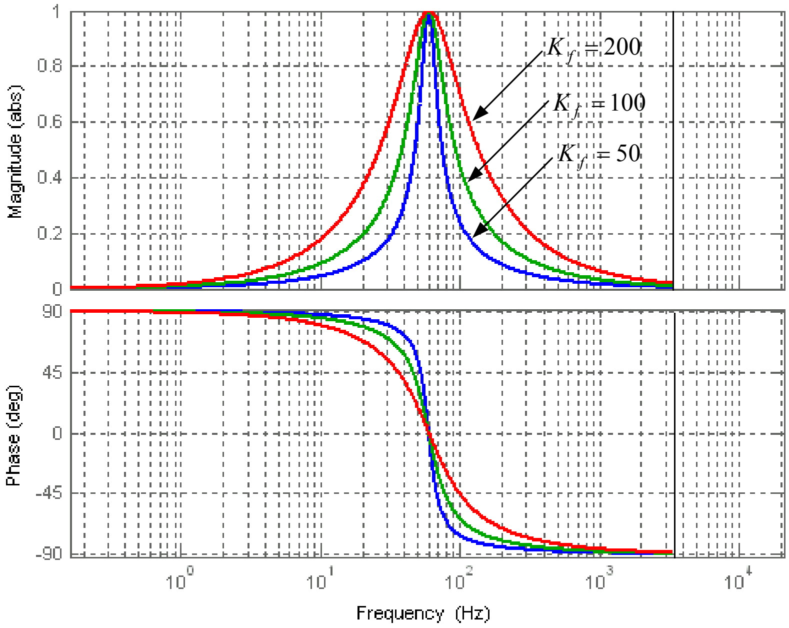

Figure 4.6: Frequency characteristics of the PLL resonant filter.

4.5 Adaptive Self-Tuning Deadbeat Current Control

A newly designed adaptive grid-voltage sensorless deadbeat controller can be extended from the deadbeat current inverter output control algorithm presented in Chapter 3. By examining the outputs of the adaptive estimation unit, it can be noticed that the predictive nature of the proposed grid voltage estimator has the necessary phase advance of the estimated voltage to partially compensate for system delays. Furthermore, the interfacing parameter estimator can provide a reliable unbiased real-time estimate of plant parameters. Therefore, an adaptive deadbeat control performance can be yielded by utilizing the outputs of the identification unit for real-time design of the deadbeat controller.

Following the detailed approach in Section 3.2, the current dynamics can be controlled to yield a deadbeat current control response, in the presence of system delays, with the following control law:

$$v_{inv}^*(k+1) = \frac{1}{b}\left\{i_{inv}^*(k+2) - a^2 i_{inv}(k) - ab\left(v_{inv}(k) - v_s(k)\right)\right\} + v_s(k+1). \tag{4.53}$$

Using the estimated quantities, the control voltage can be calculated as follows:

$$v_{inv}^*(k+1) = \frac{1}{\hat{b}}\left\{i_{inv}^*(k+2) - \hat{a}^2 i_{inv}(k) - \hat{a}\hat{b}\left(v_{inv}(k) - \hat{v}_s(k)\right)\right\} + \hat{v}_s(k+1). \tag{4.54}$$

The resulting deadbeat controller differs from existing methods [58]-[70] in the following ways: 1) robust current control performance can be yielded under the occurrence of large system uncertainties due to the self-tuning feature; 2) high robustness under the challenging condition of grid voltage sensorless operation, as the estimated grid voltage is used to calculate the control voltage; 3) no additional hardware is needed for delay compensation; and 4) inherent self-commissioning/self-tuning features.

4.6 Grid-Voltage Sensorless Power Control

The power control loop can be realized to achieve either instantaneous or average power control performance. Instantaneous power control is more suitable for active filtering and harmonics compensation. On the other hand, the average power is more suited for high power quality injection. The proposed interfacing scheme fits both power control strategies. In particular, the robust deadbeat current control performance enables fast an accurate tracking of highly dynamic reference current trajectories. In this chapter, a grid-voltage sensorless average power control loop is proposed.

To ensure high power quality, the outer power control loop should offer a relatively slowly changing current reference trajectory. Since the required power transient response is much slower than the current dynamics, the reference current can be filtered to ensure high quality inductor current. Based on the time-scale separation between the power and current dynamics, the output power variation depends only on the variation of the grid voltage within the control cycle. Using the active and reactive power references p^* and q^* and grid voltage components v_{sq} and v_{sd}, the reference currents can be simply calculated as follows:

$$\begin{bmatrix} i^*_{invd} \\ i^*_{invq} \end{bmatrix} = \frac{1}{\|\boldsymbol{v}_s\|^2} \begin{bmatrix} v_{sd} & -v_{sq} \\ v_{sq} & v_{sd} \end{bmatrix} \begin{bmatrix} p^* \\ q^* \end{bmatrix}. \tag{4.55}$$

To compensate for the filter-capacitor current component, the inductor current references are calculated by adding a simple feed-forward compensation term as follows:

$$\begin{bmatrix} i^*_{invd} \\ i^*_{invq} \end{bmatrix} = \frac{1}{\|\boldsymbol{v}_s\|^2} \begin{bmatrix} v_{sd} & -v_{sq} \\ v_{sq} & v_{sd} \end{bmatrix} \begin{bmatrix} p^* \\ q^* \end{bmatrix} + \frac{1}{Z_c} \begin{bmatrix} v_{sd} \\ v_{sq} \end{bmatrix} \tag{4.56}$$

where Z_c is the capacitor impedance.

The voltage-sensorless power controller can be realized using the estimated voltage components as

$$\begin{bmatrix} i^*_{invd} \\ i^*_{invq} \end{bmatrix} = \frac{1}{\|\hat{\boldsymbol{v}}_s\|^2} \begin{bmatrix} \hat{v}_{sd} & -\hat{v}_{sq} \\ \hat{v}_{sq} & \hat{v}_{sd} \end{bmatrix} \begin{bmatrix} p^* \\ q^* \end{bmatrix} + \frac{1}{Z_c} \begin{bmatrix} \hat{v}_{sd} \\ \hat{v}_{sq} \end{bmatrix}. \tag{4.57}$$

To provide a sufficient attenuation for the harmonic content in reference current vector, a low pass filter (LPF) is adopted and digitally implemented as follows:

$$\begin{bmatrix} i^*_{df}(k) \\ i^*_{qf}(k) \end{bmatrix} = \frac{2\sigma - T}{2\sigma + T} \begin{bmatrix} i^*_{df}(k-1) \\ i^*_{qf}(k-1) \end{bmatrix} + \frac{T}{2\sigma + T} \begin{bmatrix} i^*_{invd}(k) - i^*_{invd}(k-1) \\ i^*_{invq}(k) - i^*_{invq}(k-1) \end{bmatrix} \tag{4.58}$$

where i^*_{df} and i^*_{qf} are the filtered d- and q- axis reference current components, respectively, and $\frac{1}{\sigma}$ is the filter cut-off frequency. It should be noted that the filter cut-off frequency should be low enough to provide sufficient attenuation of reference-current harmonics caused by voltage harmonics. At the same time, it should be high enough to provide a reasonable dynamic response of the power control loop. Figure 4.7 depicts the structure of the proposed voltage-sensorless power controller.

4.7 Results

To evaluate the performance of the proposed control scheme, a grid connected PWM-VSI-based DG unit incorporated with the proposed control scheme, as reported in Figure

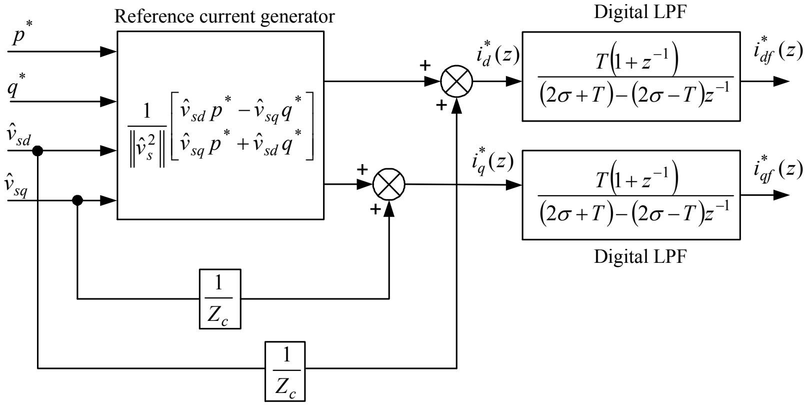

Figure 4.7: Proposed voltage-sensorless average power controller.

4.1, has been used. The system parameters are as follows: supply phase voltage=120 V at 60 Hz, dc-link voltage=500 V, nominal system parameters are: L_o=2.5 mH, R_o=1.0 Ω. The overall system is digitally simulated under Matlab/Simulink environment with real-time code generation support. A converter switching frequency of 6.67 kHz has been selected. As a result, a control sampling time T=150 μs is yielded.

Various comparative tests are conducted to verify the feasibility of the proposed controller under different operating conditions. Some results are reported as follows.

4.7.1 Dynamic Performance of the Proposed Monitoring Unit

To evaluate the performance of the proposed monitoring unit, uncertainties in the interfacing parameters as 60% mismatch in L and 50% mismatch in R are considered. First, the parallel-observers-based monitoring unit is tested. The convergence time of the grid voltage estimator is adjusted by selecting an appropriate adaptation gain γ to achieve adequate convergence properties with enough robustness, and to cope with the bandwidth characteristics of the observed voltage. Same observations hold for the selection of the reduction factor r in the interfacing parameter identifier, which determines the stability and convergence properties of the projection-learning algorithm. The following design parameters are used to yield fast and stable performance of the proposed estimation unit: r=0.65, ε=0.001, initial parameter vector $\hat{\Theta}(0) = [a_o, b_o]^T$= $[0.9418, 0.0582]^T$, γ=450, and K_f=100.

Figure 4.8 depicts the dynamics of the proposed parallel-observers-based monitoring unit. In this scenario, the d-axis current command is set to 20 A at $t \geq 0.0167$ s and the q-axis current command is set to zero. Figure 4.8(a) shows phase-a current response with the proposed control scheme. In spite of the presence of large system uncertainties, the actual current tracks its reference trajectory precisely due to the self-tuning control. Figure 4.8(b) shows the estimated phase-a grid voltage. The estimate converges to its real value within 1.0 ms. Figure 4.8(c) shows the estimated interfacing resistance. The estimate converges in less than 15 iterations (2.2 ms) to 1.51 Ω, which is very close to the expected value 1.5 Ω. Figure 4.8(d) shows the estimated interfacing inductance. The estimate converges in less than 15 iterations (2.2 ms) 4.025 mH, which is very close to the expected value 4 mH.

Second, the NN-based monitoring unit is tested. The following design parameters are used to yield fast and stable performance of the NN-based estimation unit: r=0.65, ε=0.001, initial parameter vector $\hat{\Theta}(0) = [a_o, b_o]^T$= [0.9418, 0.0582]^T, η_{kj}=450, K_f=100, and η_{ji} is dynamically adjusted according to (4.47).

Figure 4.9 depicts the dynamics of the proposed NN-based monitoring unit. In this scenario, the d-axis current command is set to 20 A at $t\geq$ 0.0167 s and the q-axis current command is set to zero. Figure 4.8(a) shows phase-a current response. Figure 4.9(b) shows the estimated phase-a grid voltage. Figure 4.9(c) shows the estimated interfacing resistance. Figure 4.9(d) shows the estimated interfacing inductance. It is clear that more smooth estimates are obtained with the proposed NN-algorithm. However, this comes at the cost of additional computational burden.

Figures 4.8 and 4.9 reveal that both the monitoring units guarantee precise unbiased estimates with fast convergence properties. Therefore, the estimated quantities can be reliably used in different control blocks within the interfacing scheme. Furthermore, the fact that the proposed grid-voltage sensorless algorithm has a natural sensitivity to the system perturbations can be utilized to achieve a low-cost islanding-detection method, which can be classified as a passive method where no external excitation signals are needed.

4.7.2 Dynamic Performance of the Proposed Self-Tuning Current Control

The proposed monitoring unit enables powerful adaptation features that can be utilized to achieve an adaptive self-tuning control structure as shown in (4.54). For the sake of performance comparison, the proposed current controller is compared to the conventional deadbeat current controller [59]. Both controllers are tuned using the nominal plant parameters. The interfacing parameters are set to their nominal values as well. Figure 4.10 shows the steady state performance of the conventional deadbeat current controller implemented in a full digital system with a 150 μs control period. The d-axis current command is set to 20 A, whereas the q-axis current command is set to zero. Since one

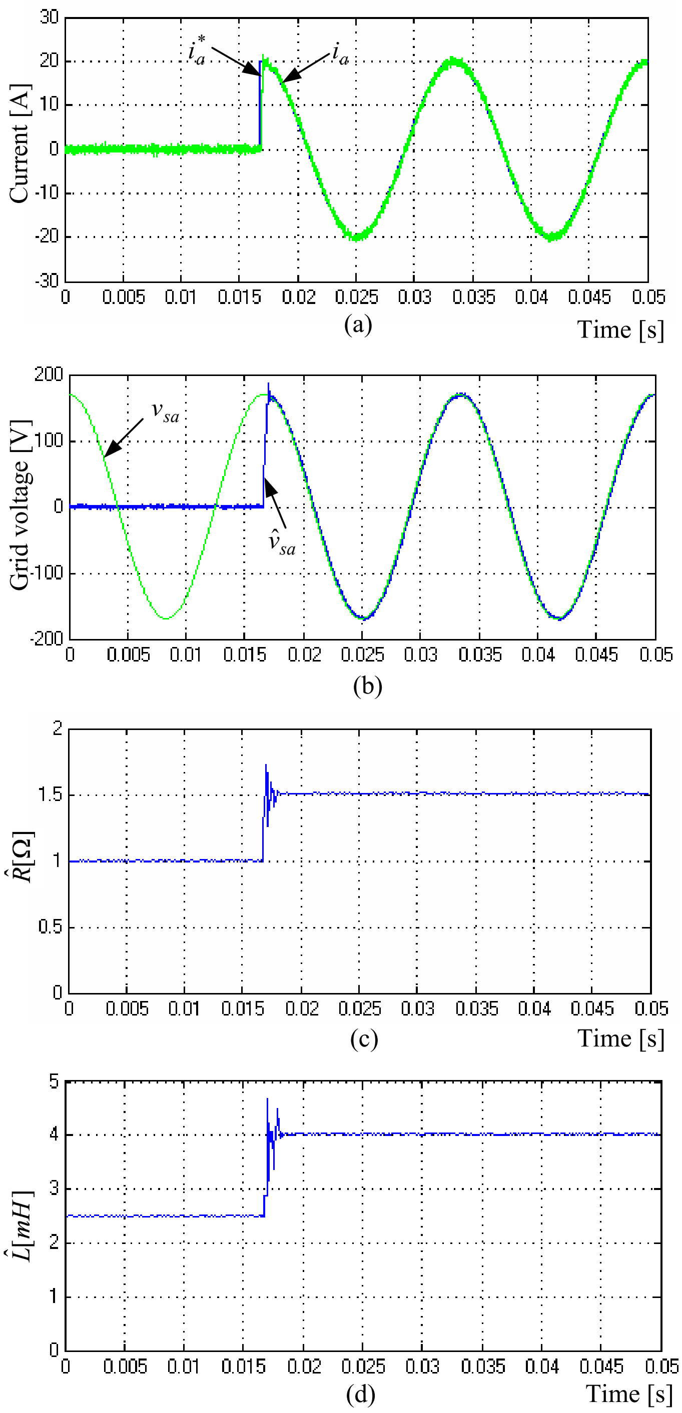

(a)

(b)

(c)

(d)

Figure 4.8: Dynamics of the proposed parallel-observers-based monitoring unit. (a) Phase-a current. (b) Actual and estimated grid voltage. (c), (d) Estimated interfacing resistance and inductance.

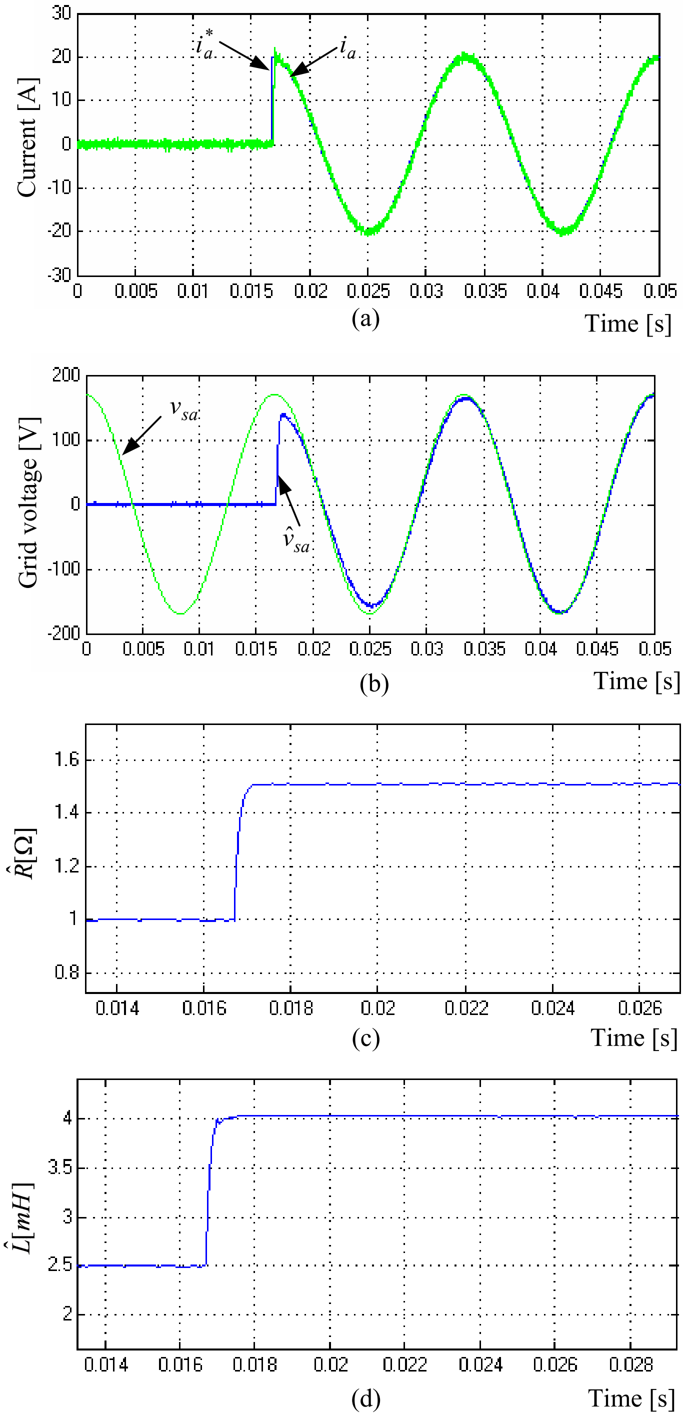

Figure 4.9: Dynamics of the proposed NN-based monitoring unit. (a) Phase-a current. (b) Actual and estimated grid voltage. (c), (d) Estimated interfacing resistance and inductance.

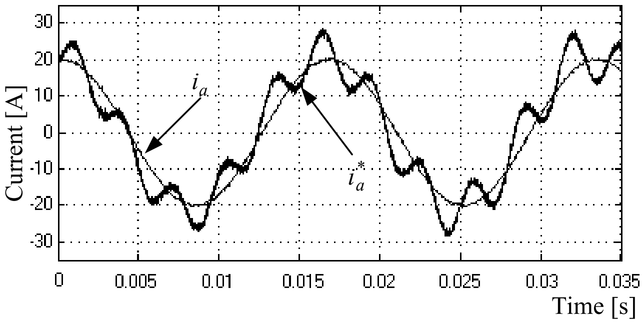

Figure 4.10: Performance of the conventional deadbeat current controller implemented in full digital system.

more period is needed for the control voltage calculation, the conventional deadbeat algorithm leads to sustained oscillations (limit cycles) in the phase-a current response as depicted in Figure 4.10. These oscillations and the poor dynamic response are indeed the result of the instability of the control system. The over-modulation of the PWM limits the magnitude of these oscillations. In a trade-off between the bandwidth requirements and the stability, the conventional deadbeat controller should be designed with a lower equivalent feedback gains; this negates the deadbeat control performance and, therefore, lower control bandwidth is yielded.

Figure 4.11 shows the current response of the proposed deadbeat controller. In Figure 4.11(a), the d-axis current command is changed from 0 to 20 A at t=0.0167 s, i.e., a rising step current command. It can be seen that the actual d-axis current component tracks its reference trajectory precisely with a rise time about 280 μs. In Figure 4.11(b), the q-axis current command is set to zero. The actual q-axis current component is well regulated to the commanded value. The q-axis current slightly deviates from zero in the transient state of the d-axis component and has no steady-state error. The corresponding phase-a current response is depicted in Figure 4.11(c).

The stability and robustness of the inner current control is mainly affected by parameter variation. The sensitivity to parameter variation increases when the grid voltage is estimated. Figure 4.12 depicts the results of sensitivity analysis. Figure 4.12(a) shows the level of uncertainty in L at which instability occurs, in the conventional controller, at different values of L_o with R_o as a parameter. Two cases are considered, first when the grid voltage is measured; second, when the grid voltage is estimated. As the figure reveals, the conventional deadbeat current controller is driven into instability with about 10% mismatch in L when the grid voltage is measured. When the grid voltage is estimated, the conventional deadbeat controller becomes unstable with 5% mismatch in L. Further, if R_o is small, the conventional controller can be driven into instability

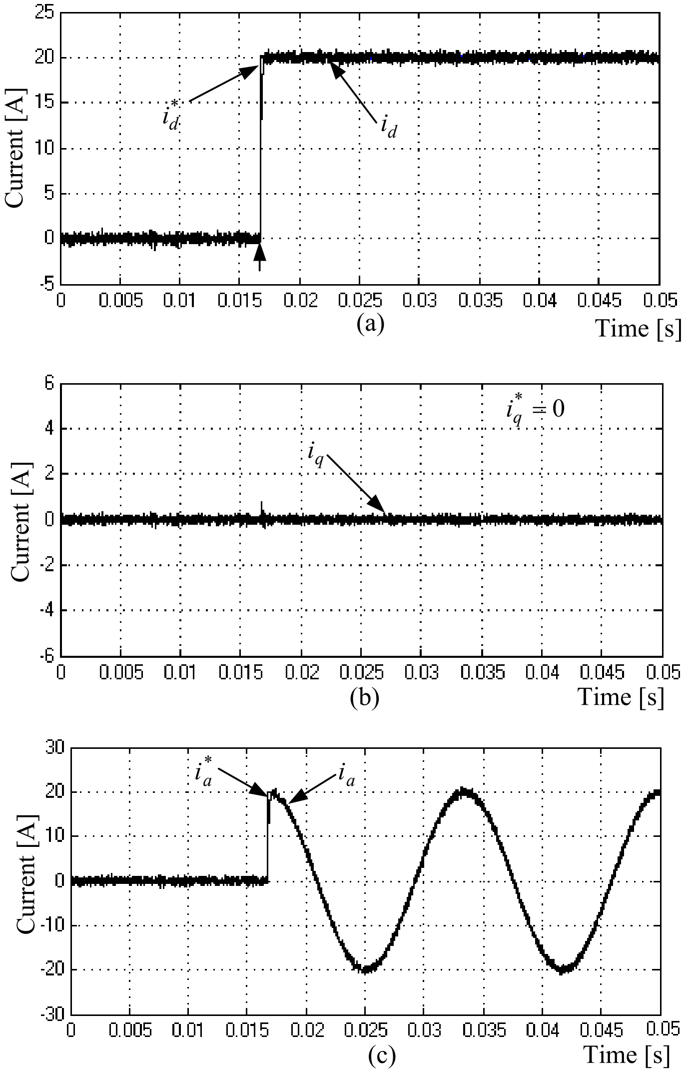

Figure 4.11: Performance of the proposed self-tuning deadbeat current controller implemented in full digital system.

with small levels of uncertainty in L. This observation shows that a practical deadbeat controller should offer enough robustness against the variation in both R and L. The stability margin is greatly reduced when the grid voltage is estimated as depicted in Figure 4.12(a). In the proposed controller, where both parameters R and L are reliably estimated and used for the self-tuning control, which in turns enables the "re-design" of the deadbeat controller in real-time at different parameters, the stability of the deadbeat controller becomes independent of system parameters.

Even with small changes in system parameters, the relative stability of the conventional deadbeat current controller is affected. Figure 4.12 (a), (b) evaluates the relative stability of the conventional and proposed controllers in terms of the peak overshoot in step response as a function of the uncertainty in L and R, respectively. With the conventional controller, small changes in the interfacing parameters lead to considerable drift in poles locations, hence affecting the relative stability of the closed loop system. More degradation in the relative stability is yielded when the grid voltage is estimated. On the other hand, it can be seen that the peak overshoot obtained with the proposed controller is almost zero at different levels of uncertainties.

For further performance comparison, the proposed controller is compared to the robust predictive current controller proposed in [67]. Figure 4.13 shows the time-domain current responses of the conventional deadbeat controller, the robust predictive controller in [67], and the proposed controller, respectively. These results are obtained with 60% mismatch in L and 50% mismatch in R; whereas the d-axis current command is set to 20 A and the q-axis current command is set to zero. Figure 4.13(a) shows that the conventional controller is unstable and generates significant low-order harmonics, leading to a THD of 66.12% up to 8.16 kHz (i.e., up to the 136th harmonic). This result does not meet the IEEE Standard 1547 requirement of THD [45], which is below 5%. It should be noted that the power quality is determined by the voltage quality when the voltage is allowed to be a controlled variable. If the grid voltage is stiff, then the voltage cannot be controlled, and the power quality is solely determined by the current quality. Although the predictive controller in [67] is robust up to 53% mismatch in the interfacing inductance, the stability and robustness are remarkably degraded at higher values of uncertainty, and when the effect of uncertainty in the interfacing resistance is considered as shown in Figure 4.13(b). The instability in the current response combined with the saturation effect of the over-modulation generates more low order harmonics, leading to a THD of 13.37% up to 8.16 kHz. In contrast, the proposed algorithm is still stable and generates the minimal low-order harmonics even with 60% mismatch in L and 50% mismatch in R, as shown in Figure 4.13 (c). In this case, the THD up to 8.16 kHz is 0.95%.

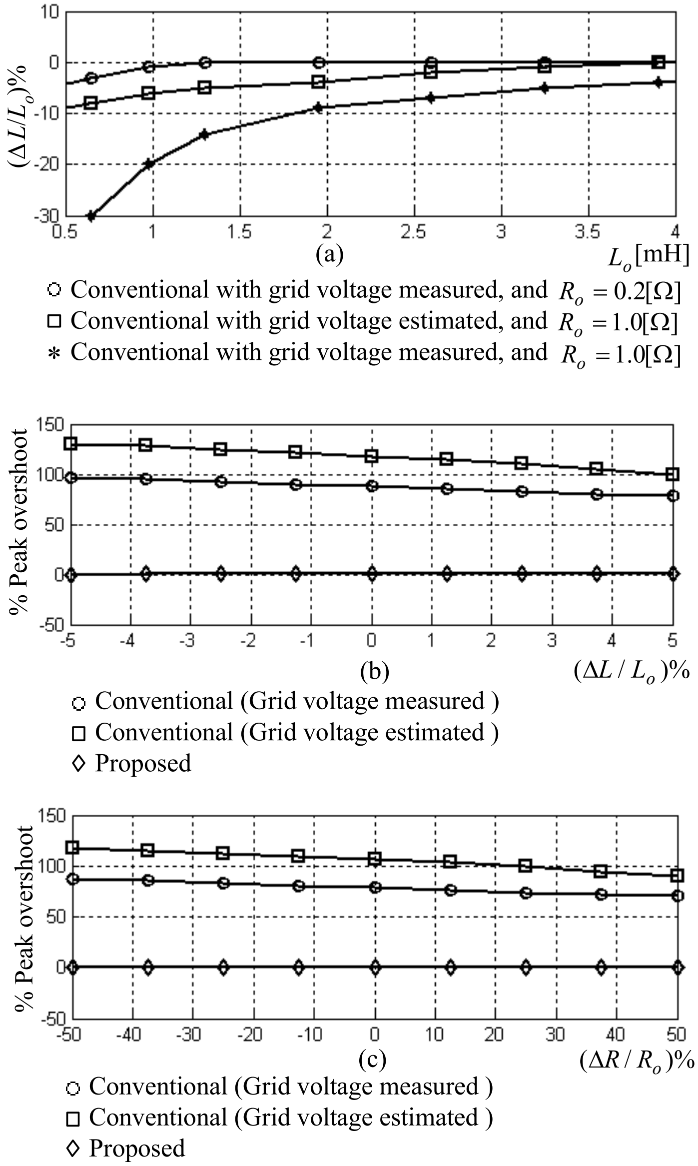

Figure 4.12: Robustness and relative stability of the conventional and proposed current controllers with measured and estimated grid-voltage. (a) The amount of uncertainty in L at which instability occurs in the conventional controller vs. L_o and with R_o as a parameter. (b) The peak overshoot vs. the uncertainty in L for both controllers. (c) The peak overshoot vs. the uncertainty in R for both controllers.

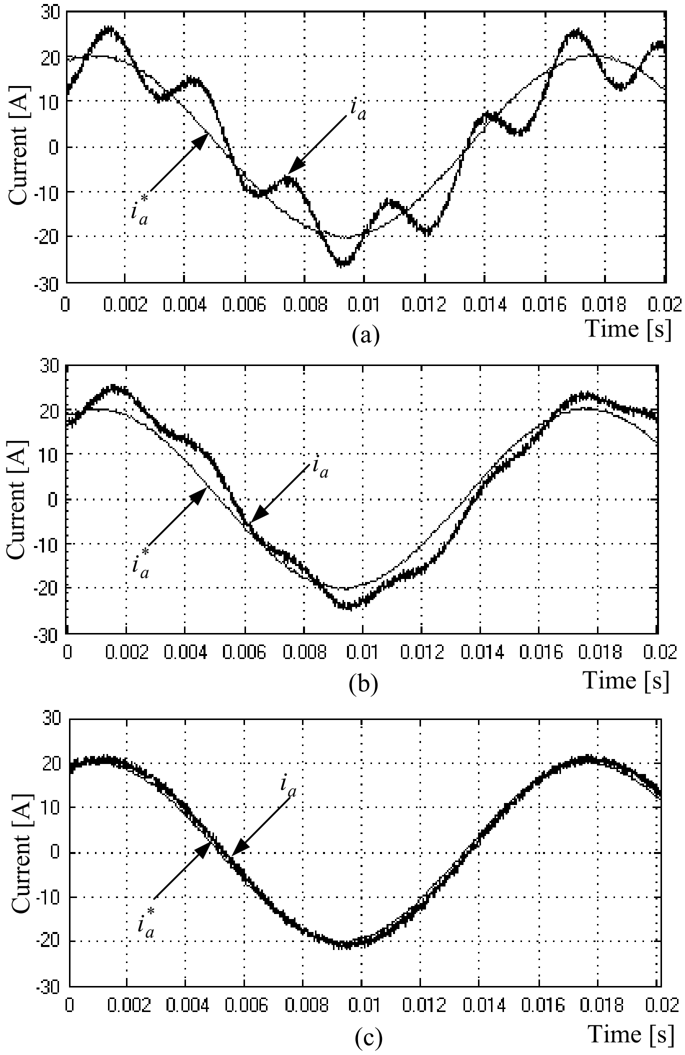

Figure 4.13: Performance of the conventional current controller, the robust current controller [67], and the proposed current controller with 60% uncertainty in L and 50% uncertainty in R. (a) The conventional controller. (b) The robust controller proposed in [67]. (c) The proposed controller.

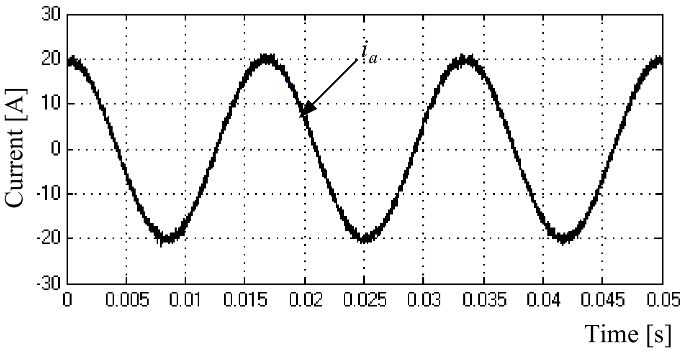

Figure 4.14: Performance of the current controller in [67] with the proposed identification unit, under 60% uncertainty in L and 50% uncertainty in R.

To show the compatibility of the proposed estimation unit with different control techniques, the identification unit has been added to the deadbeat controller in [67]. The controller is tested with 60% mismatch in L and 50% mismatch in R, while the d-axis current command is set to 20 A and the q-axis current command is set to zero. Figure 4.14 depicts the control performance obtained in this case. As expected, the stability of the algorithm in [67] is extended due to self-tuning control.

4.7.3 Overall Performance of the Proposed Grid-Voltage Sensorless Interface

To evaluate the performance of the overall system, a step change in the demanded active power from 0 to 5.2 kW is given at $t \geq 0.0167$ s, whereas the reference reactive power is set to zero to maintain a unity power factor. The grid voltage harmonics are as follows: 3% 5th harmonic, 2% 7th harmonic, and 1% 11th harmonics. Figure 4.15(a) shows the reference and actual active and reactive power components. It can be seen that the active power output of the inverter can be correctly estimated and the actual power follows its reference correctly. Figure 4.15(b) shows the reference d-axis current component and the output three-phase currents. The actual current tracks the reference trajectory precisely with zero steady-state error and zero overshoot. Because the injected power in only active, the output current appears in phase with the estimated fundamental grid voltage as shown in Figure 4.15(c). Figure 4.15(c) shows also the actual phase-a grid voltage and the estimated fundamental component of phase-a voltage. The phase-a current is well synchronized with the fundamental grid voltage. Figure 4.15(d) shows the estimated angular frequency of the supply voltage. The estimate quickly converges to the fundamental angular frequency in the presence of supply distortion. Figure 4.15(e) depicts the estimated grid voltage vector position.

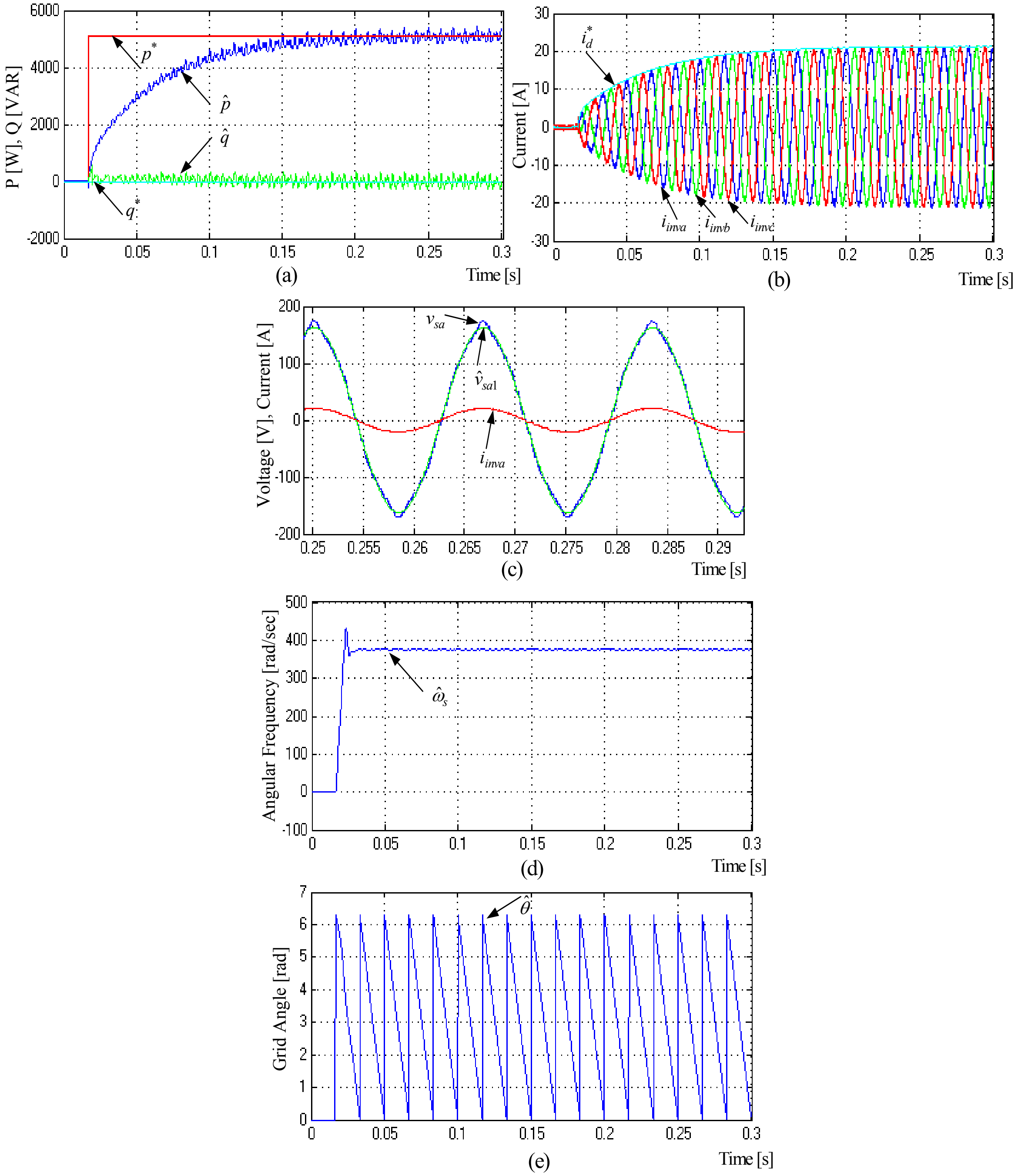

Figure 4.15: Performance of the proposed voltage-sensorless DG interface. (a) Power response. (b) Reference d-axis current and three-phase injected currents. (c) Grid voltage, estimated fundamental grid voltage component, and injected current. (d) Estimated angular frequency of the supply voltage. (e) Estimated grid voltage vector position.

Figure 4.16 shows the start-up performance of the proposed interface. Figure 4.16(a) shows the reference d-axis current component and the output three-phase currents. The actual current tracks the reference trajectory precisely with zero steady-state error and zero overshoot. Figure 4.16(b) depicts the inverter control voltages. The utilization of the estimated grid voltage provides a robust control performance against grid voltage disturbance, even at system starting. Figure 4.16(c) shows the actual grid voltages and the estimated phase-a grid voltage. The estimate quickly converges and closely tracks the actual grid voltage. Figure 4.16(d) shows the estimated fundamental components of the grid voltage. Due to the robust PLL algorithm, the fundamental components can be smoothly detected with fast convergence properties. Figure 4.16(e) shows that the current synchronization with the estimated fundamental grid voltage occurs in less than 10ms. In addition, during the synchronization period, the phase error due the synchronization decreases swiftly; which indicates that controllable power transfer can be made feasible once the DG interface is started.

The reported results indicate that the proposed scheme results in robust grid-voltage sensorless operation and favorable current and power tracking responses even under distorted grid conditions and the occurrence of large uncertainties in system parameters.

4.8 Summary

In this chapter, a novel adaptive discrete-time grid-voltage sensorless interfacing scheme for DG inverters has been introduced. Two designs have been investigated. First, an interface-monitoring unit, based on parallel adaptive observers, has been designed with low computational demand to estimate the grid voltage and the interfacing parameters simultaneously. Second, due to the nonlinear nature of the estimation problem and the periodic time-varying nature of the grid voltage, the second design of the adaptive estimation unit utilizes a NN-based adaptation algorithm, which works as a real-time optimization agent. Both designs have yielded accurate and unbiased estimates. Further, a robust synchronization algorithm, which utilizes the estimated grid voltage to extract the grid voltage vector position has been presented. The estimated grid voltage has been utilized to realize a grid-voltage sensorless average-power control loop, which guarantees high power quality injection. Furthermore, the outputs of the estimation unit have been utilized to realize an adaptive self-tuning deadbeat current controller. Comparative evaluation results have been presented to demonstrate the effectiveness of the proposed control scheme. The proposed identification unit is independent on the type of the current controller; therefore, it can be used to enhance the robustness of existing controllers. In addition, the proposed grid-voltage sensoless interfacing scheme

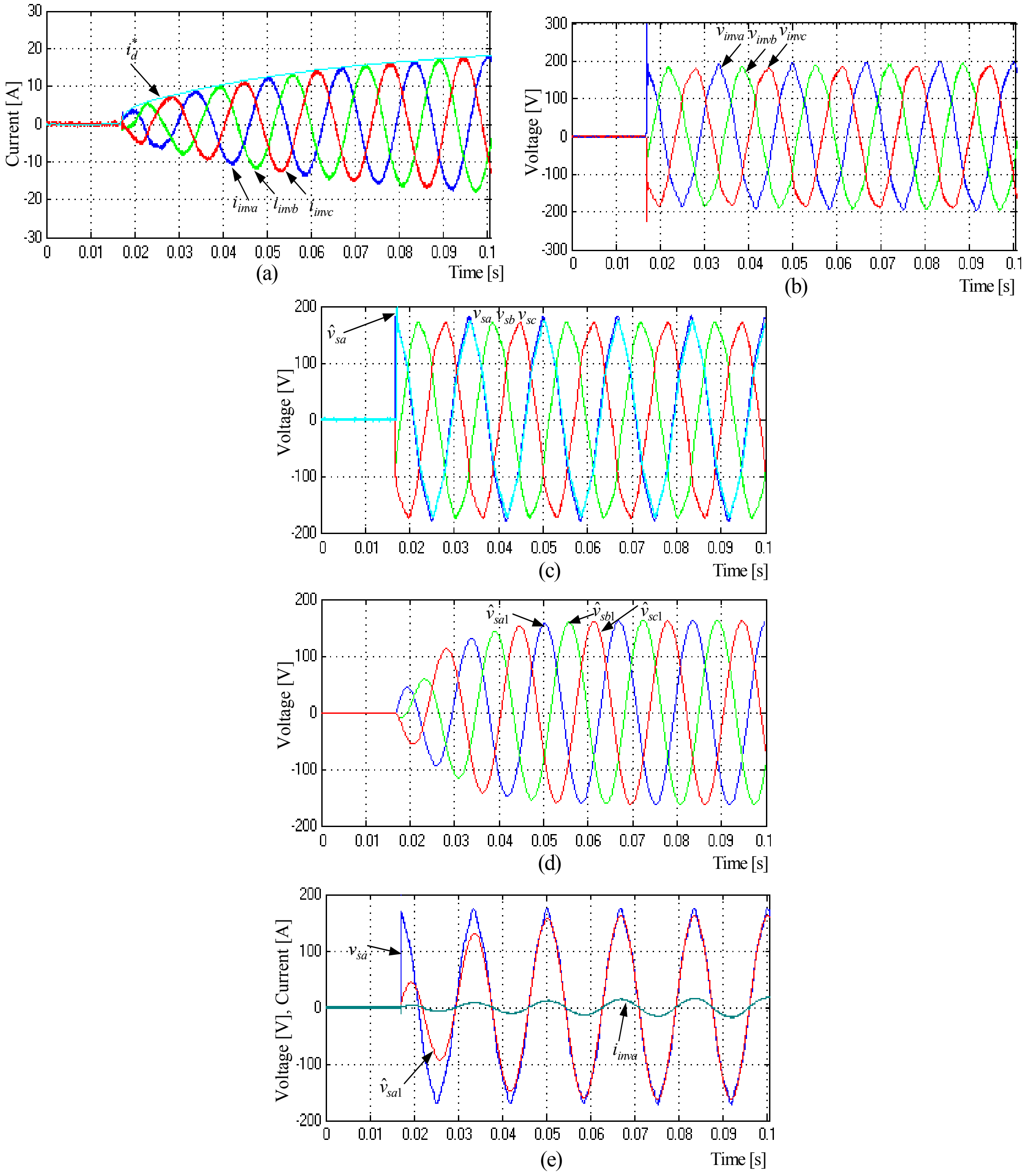

Figure 4.16: Start-up performance of the proposed voltage-sensorless DG interface. (a) Reference d-axis current and three-phase injected currents. (b) Demodulated inverter voltages. (c) Grid voltages and estimated phase-a grid voltage, (d) Estimated fundamental component of grid voltages. (e) Grid voltage, estimated fundamental grid voltage component, and injected current.

is inherently self-commissioning/self-tuning and guarantees optimum performance, without the constraint conditions and detailed prior knowledge of the inverter system and grid parameters.

Chapter 5

Fast Load Voltage Regulation Scheme With High Disturbance Rejection Performance

5.1 Introduction

Fast load voltage regulation is a necessary requirement in a power distribution system; particularly in feeders serving voltage-sensitive loads. Severe and random voltage disturbances might be initiated by time-varying loads, non-dispatchable generation, voltage transients associated with parallel connected loads, and voltage transients caused by capacitor switching. These voltage disturbances are stochastic in nature with durations that vary from a fraction of a cycle to few cycles. As detailed in Section 2.3.2, existing voltage control methods fall short in achieving high disturbance rejection performance against dynamic voltage disturbances.

To ensure perfect regulation of the voltage at the point of common coupling (PCC) and provide means for rejecting voltage disturbances, the voltage control loop should offer a high disturbance rejection performance. This chapter presents a newly designed load voltage control scheme, for the DG interface, based on a hybrid linear with variable-structure control (VSC) voltage controller. The proposed voltage controller can embed a wide band of frequency modes through an equivalent internal model. Subsequently, wide range of voltage perturbations, including capacitor-switching voltage disturbances, can be rejected. To account for unbalanced voltage disturbances, a dual-sequence hybrid linear with VSC voltage controller is developed. Further, an evolutionary search algorithm, based on the particle swarm optimization (PSO) technique, is proposed for optimum tuning of the proposed voltage control scheme under practical system constraints. To provide accurate and robust tracking of the estimated grid voltage and to enhance the

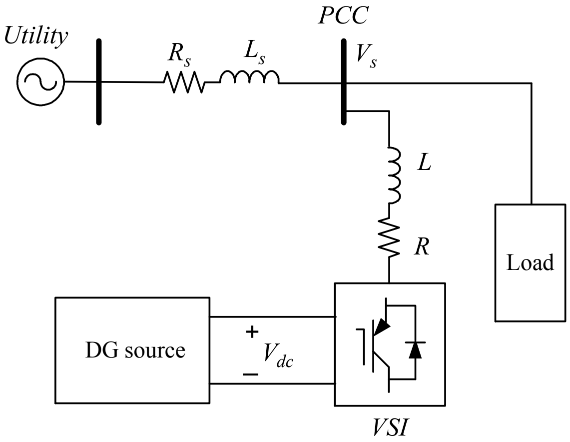

Figure 5.1: Network connection of a VSI with DG.

current control accuracy, the disturbance slowly varying assumption is relaxed in the proposed design. In addition, the tracking and disturbance rejection performances of the current control loop are improved. Theoretical analysis and comparative evaluation tests are presented to demonstrate the effectiveness of the proposed control scheme.

The remainder of this chapter is organized as follows. System configuration and modeling of a voltage-oriented current controlled DG interface are presented in Section 5.2. Section 5.3 presents the proposed voltage control scheme. Results of comparative evaluation tests are presented in Section 5.4. A summary is drawn in Section 5.5.

5.2 System Configuration and Modeling of a Voltage-Oriented Current Controlled DG Interface

Figure 5.1 shows a network connection of a gird-connected VSI used to interface a DG unit; where R and L represent the equivalent resistance and inductance of the ac filter, coupling transformer, and connection cables; R_s and L_s represent the feeder resistance and inductance up to the PCC, respectively; $\boldsymbol{v}_s$ is the supply voltage vector at the PCC; and V_{dc} is the dc-link voltage.

Using the voltage-oriented control, the active and reactive power injection can be controlled via a current-controlled VSI. To impose an arbitrary current in the inductive coupling impedance, a current controller is usually adopted to shape the voltage applied on the inductor so that minimum current error is achieved. An outer power/voltage control loop can be used to generate the reference current vector.

In Park's d-q frame that rotates synchronously with the grid angular speed ω, the current dynamics can be reasonably represented by the following equations:

$$v_q = Ri_q + L\frac{di_q}{dt} + L\omega i_d + v_{sq} \tag{5.1}$$

$$v_d = Ri_d + L\frac{di_d}{dt} - L\omega i_q + v_{sd} \tag{5.2}$$

where v_d, v_q, i_d, i_q are the d- and q- axis inverter's voltages and currents; L is the coupling inductance; R is the coupling resistance; and v_{sd}, v_{sq} are the d- and q- axis components of the supply voltage at the PCC.

The injected active and reactive power components, p and q, can be represented in terms of the d- and q-axis components of the supply voltage at the PCC and the injected currents as follows:

$$p = \frac{3}{2}\left(v_{ds}i_d + v_{qs}i_q\right) \tag{5.3}$$

$$q = \frac{3}{2}\left(v_{qs}i_d - v_{ds}i_q\right). \tag{5.4}$$

In addition, the magnitude of the voltage at the PCC is given by:

$$\|\boldsymbol{v}_s\| = \sqrt{v_{sd}^2 + v_{sq}^2}. \tag{5.5}$$

Considering the physical constraints, the preceding model is subjected to the following limits. The injected current is limited to the maximum continuous current of the inverter or to the maximum available current of the inverter in a limited short-time operation. Also, the load voltage is limited to the maximum available output voltage of the inverter, depending on the dc-link voltage. Since the distribution system is uncertain and dynamic in nature and its parameters vary frequently due to factors such as cable overload, transformer saturation, and temperature effects, the uncertainty in system parameters should be considered in control system design.

By considering the grid-voltage components as a dynamic disturbance, the current dynamics of the voltage-controlled inverter can be represented by the following state space equation:

$$\begin{aligned} \dot{\boldsymbol{x}} &= \boldsymbol{A}_c\boldsymbol{x} + \boldsymbol{B}_c\boldsymbol{u} + \boldsymbol{G}_c\boldsymbol{f} \\ \boldsymbol{y} &= \boldsymbol{C}\boldsymbol{x} \end{aligned} \tag{5.6}$$

with

$$\begin{aligned} \boldsymbol{x} &= \begin{bmatrix} i_q & i_d \end{bmatrix}^T & \boldsymbol{u} &= \begin{bmatrix} v_q - \omega L i_d & v_d + \omega L i_q \end{bmatrix}^T \\ \boldsymbol{f} &= \begin{bmatrix} v_{sq} & v_{sd} \end{bmatrix}^T & \boldsymbol{A}_c &= \begin{bmatrix} -R/L & 0 \\ 0 & -R/L \end{bmatrix} \\ \boldsymbol{B}_c &= \begin{bmatrix} 1/L & 0 \\ 0 & 1/L \end{bmatrix} & \boldsymbol{G}_c &= \begin{bmatrix} -1/L & 0 \\ 0 & -1/L \end{bmatrix} \\ \boldsymbol{C} &= \begin{bmatrix} 1 & 0 \\ 0 & 1 \end{bmatrix} \end{aligned}$$

where $\boldsymbol{A}_c$, $\boldsymbol{B}_c$, $\boldsymbol{G}$ and $\boldsymbol{C}$ are the state-space model matrices of the continuous time system; $\boldsymbol{u}$ is the equivalent control input vector; and $\boldsymbol{f}$ is the grid voltage vector, which might contain other unstructured uncertainties, such as estimation disturbances that are yielded by the slowly varying assumption.

In the case of slow and small voltage perturbation, the nonlinearity of the voltage control problem is limited, and a linear voltage regulator can be synthesized in the sense of the small signal model. However, for fast and large voltage disturbances, the nonlinear nature of the voltage dynamics cannot be neglected, and the voltage controller should be synthesized in the sense of the large signal dynamics of the voltage control loop.

5.3 Voltage Control Scheme

5.3.1 Voltage Control Law

A variable-structure control (VSC) approach is proposed to design the voltage controller. In the case where the perturbations are random and non-periodic, VSC perhaps is the best solutions when high performance is required. Moreover, the VSC is well suited for nonlinear dynamic systems with uncertainties [105]-[106]. In the VSC approach, a discontinuous fast switching control law forces an infinite gain at the equilibrium point. Subsequently, a wide band of frequency modes are supplied through an equivalent internal model. By this technique, wide range of voltage perturbations can be rejected. However, the VSC approach has practical limitations such as chattering and nonlinear sliding motion effects, which arise from the extremely high gain around the equilibrium and the limited switching frequency. Subsequently, not all the frequency modes can be rejected in a practical VSC. In addition, the chattering effect might counteract the power quality requirements imposed on the injected power. Therefore, a hybrid voltage controller combining a linear with VSC element and switching function approximation is proposed for fast voltage regulation performance with a capability of mitigating fast voltage disturbances. The hybrid voltage control law gives more degrees of freedom to achieve adequate control performance with enough robustness against fast voltage disturbances with reduced chattering. Further, the invariance property to system uncertainties in the sliding mode enhances the robustness against the active and reactive power coupling dynamics.

The main objective of the voltage controller is to achieve fast and accurate generation of the reactive current reference. To achieve this objective, a positive sequence linear with variable structure controller is adopted as shown in Figure 5.2. In the VSC strategy, a switching control law is used to drive the plant's state trajectory onto a chosen surface

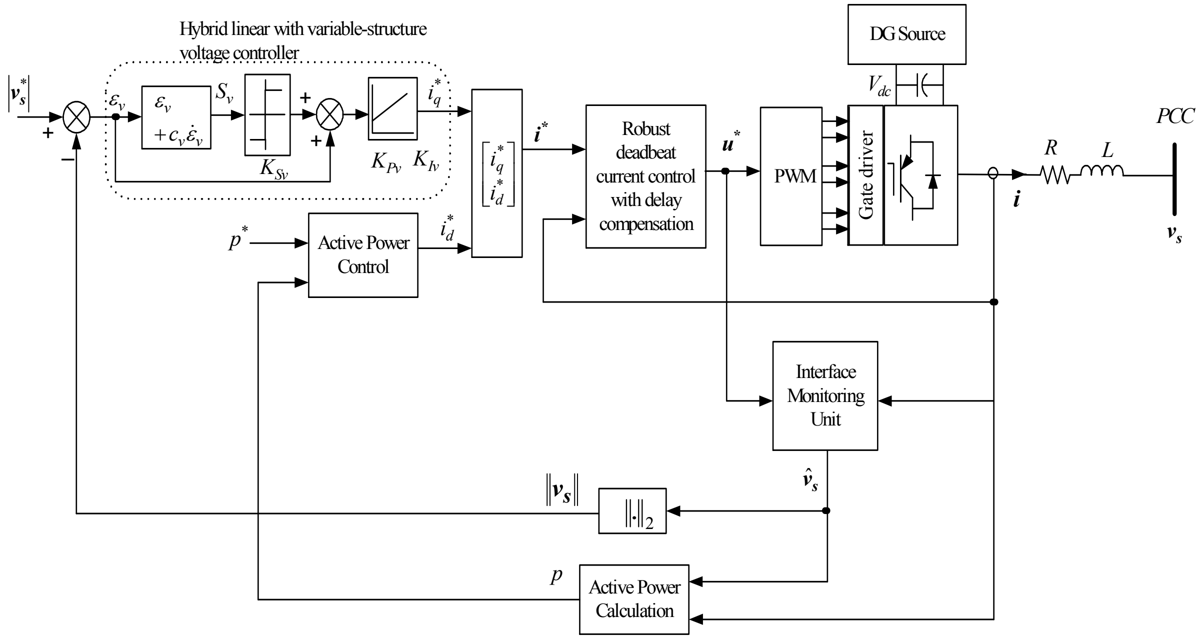

Figure 5.2: Proposed positive-sequence voltage control scheme in the synchronous reference-frame.

in the state space (sliding surface). In the present design problem, the sliding surface is selected to achieve first order dynamics for the sliding-mode operation as follows:

$$S_v = \varepsilon_v + c_v \frac{d\varepsilon_v}{dt} \tag{5.7}$$

where $\varepsilon_v = \|\boldsymbol{v}_s^*\| - \|\boldsymbol{v}_s\|$ is the voltage control error; c_v is the coefficient of the sliding surface; and the symbol "*" denotes the reference value.

In the sliding mode, it is required to restrict the controlled state onto its corresponding sliding surfaces. This is exclusively governed by $S_v = \dot{S}_v = 0$. At this condition, the equivalent dynamics can be described as

$$\varepsilon_v = -c_v \frac{d\varepsilon_v}{dt}. \tag{5.8}$$

The sliding surface coefficient can be chosen to achieve the required dynamic performance on the sliding surface.

In order to reduce the chattering effect and to increase the degrees of freedom in tuning the controller, the following linear with variable structure control input is used:

$$i_q^* = \left(K_{Pv} + \frac{K_{Iv}}{s}\right)(\varepsilon_v + K_{Sv}\mathrm{sgn}(S_v)) \tag{5.9}$$

where s is the Laplace operator; K_{Pv} and K_{Iv} are the gains of the linear proportional plus integral (PI) part of the control law; and K_{Sv} is the switching gain of the VSC. The control law in (5.9) employs a linear PI controller with a variable structure controller in a parallel structure. This configuration has a dual behavior by generating a switching excitation signal, superimposed by a smooth linear control effort and the slow motion integral of the switching signal. It is clear that the VSC behavior can be controlled by K_{Sv}, whereas the linear control behavior is controlled by K_{Pv} and K_{Iv}. The control law gain vector can be defined as

$$K = \left[\begin{array}{ccc} K_{Pv} & K_{Iv} & K_{Sv} \end{array} \right]. \tag{5.10}$$

The control law in (5.9) restricts the system states onto the surface S_v in the sliding mode. Besides, it gives more degrees of freedom to achieve adequate control performance with enough robustness. However, under steady-state conditions, the voltage tracking error will be close to zero. Under this condition, the VSC will be very sensitive to any noise in the system and control chattering will be yielded. However, the chopped control effort at the steady-state condition can be suppressed by approximating the switching function $\operatorname{sgn}(S_v(t))$ by $\frac{S_v(t)}{|S_v(t)|+r}$, where r is given by

$$r = \begin{cases} 0, & |S_v(t)| \geq \delta \\ \lambda, & |S_v(t)| < \delta \end{cases} \tag{5.11}$$

where λ is a large positive value, and δ is a small positive constant. The values of λ and δ can be selected in a trade-off between the robustness and the chattering performance. Further, a post-filter action can be embedded to constrain the chattering performance. Practically, adequate performance can be obtained by using these approximations [107].

Since the PI part independently operates on the variable structure part, the PI element can be tuned for the tracking performance, whereas the VSC element can be tuned for the regulation performance. Generally, the VSC design procedure requires the switching gains to be large enough to achieve wide band disturbance rejection.

The voltage regulation scheme, aforementioned, takes into account only the positive sequence case. However, the uneven distribution of single-phase loads and the diversity in their demands give rise to mild voltage unbalance. In other cases, severe short-tem unbalances can be yielded in the case of system faults. The direct result of these unbalances is additional losses, performance degradation of line-start motors, motor drives and power-electronic converters. Therefore, the voltage regulation scheme should incorporate a negative-sequence regulator. The proposed voltage control scheme can be extended to mitigate load voltage unbalance by adding a negative-sequence regulator. Figure 5.3 depicts the proposed dual-sequence control structure. The actual grid voltage vector is compared to the reference one. The later is composed of the desired grid voltage magnitude and desired power angle. The voltage vector control error is projected

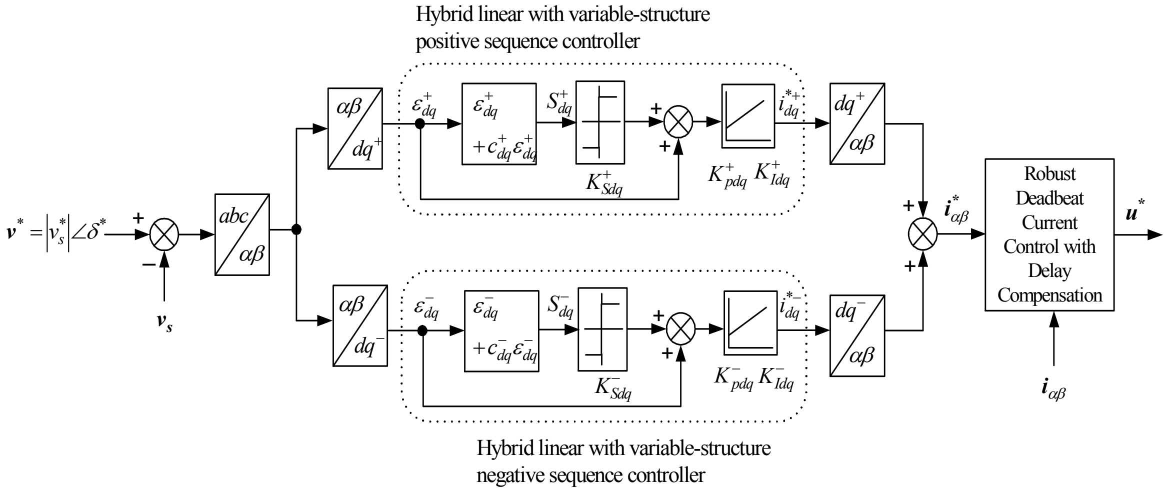

Figure 5.3: Proposed dual-sequence voltage control scheme.

into positive- and negative-sequence synchronous frames using a filtered-forward- and reverse-rotating synchronous frames, denoted by dq^+ and dq^-, respectively. The positive sequence error vector ε_{dq}^+ is processed by a hybrid variable-structure positive-sequence controller to generate the positive-sequence reference current vector i_{dq}^{*+}. Similarly, the hybrid variable-structure negative-sequence controller generates the negative-sequence reference current vector i_{dq}^{*-} using the negative-sequence error vector ε_{dq}^-. A deadbeat current control scheme is utilized to impose the total reference current in the coupling-filter inductive winding.

5.3.2 Voltage Control Tuning

In the case of slow and small voltage perturbation, a linear voltage regulator can be synthesized in the sense of the small signal dynamics, and designed using root locus, Bode/Nyquist plots, and other conventional linear control-design techniques [80]-[81]. However, for fast and large voltage disturbances, which are the main scope of this chapter, the small signal-based tuning approach will not be appropriate. Further, the small signal approach is not appropriate with the proposed VSC voltage controller, which is highly nonlinear. In this chapter, the tuning problem is formulated as a constrained optimization problem and solved via an evolutionary search algorithm based on the PSO technique [108]. Generally, evolutionary algorithms can handle nonlinear and multi-objective optimization problems in a non-gradient-based manner. Further, the PSO technique has better search characteristics as compared to other evolutionary computing algorithms [109]. Besides, it has a very simple structure and it can be implemented with few lines of code. Therefore, a simple and structured tuning methodology can be obtained. The tuning methodology can be extended for optimum tuning of similar controllers.

The objective of the present design problem is to determine the optimum gain vector K_{opt} of the proposed voltage controller. Provided that the switching functions of the VSC law are not differentiable, it is hard to derive a closed form of derivatives for a gradient-based optimization algorithm. Accordingly, a statistical optimization algorithm would be an attractive solution in the present problem [110].

To formulate the problem, a quadratic performance index J is considered as follows:

$$J = \sum_{n=1}^{m} [nT\varepsilon_v(n)]^2 \tag{5.12}$$

where $\varepsilon_v(n)$ is the voltage tracking error at the time n; T is the sampling time; and m is the total number of samples.

In (5.12), the voltage-tracking error $\varepsilon_v(n)$ is weighted by the respective time nT. Therefore, a more representative objective function is yielded. The scaling gain vector is determined so as to satisfy the following objective function:

$$f_J = \min_K \sum_{n=1}^{m} [nT\varepsilon_v(n)]^2 \tag{5.13}$$

where f_J is the objective function.

The present optimization problem is subjected to a physical constraint defined by the following criterion:

$$i_q^*(n) \leq I_{q\max} \tag{5.14}$$

where I_{qmax} is the maximum allowable reactive current component depending on the inverter rating.

The problem can be solved using the PSO technique. Generally, the PSO technique is based on the social behavior that a population of individuals adapts to its environment by returning to promising regions that were previously discovered. This adaptation to the environment is a stochastic process that depends on both the memory of each individual as well as the knowledge gained by the population. The PSO algorithm is superior to other evolutionary computing algorithms regarding the memory, and computational time requirements as it relies on very simple mathematical operations. Unlike other evolutionary computing algorithms, the PSO doesn't rely on the famous Darwinian natural selection "*survival of the fittest*", but mainly depends on "*constructive co-operation*" among individuals (agents). The main idea of the PSO algorithm is to create a population of particles (agents), referred to as "swarm" where each particle represents a potential solution to the objective function under consideration. The particles of the swarm are assumed to travel the problem search space in a discrete rather than continuous time domain. The swarm is randomly initialized within the search space. Each particle (i) in the swarm can memorize its current position that is determined by the evaluated objective function, velocity, and the best position visited during its tour in the problem search space. Personal best position p_{bst} indicates the position that yields the highest fitness value for that particle. To simulate the effect of "*constructive co-operation*" among particles, the best position visited by all the particles is memorized. The global best position is nothing but the best position among all personal best positions. The global best position is denoted by g_{bst}.

The numerical implementation repeatedly updates the position of each particle over a time period to simulate the adaptation of the swarm to the environment. The position of each particle is updated using the current position, a velocity vector, and a time increment.

The new position of each particle at iteration n+1 is calculated with a unity time-step as follows:

$$x^i_{n+1} = x^i_n + v^i_{n+1} \tag{5.15}$$

where x^i_{n+1} is the position of particle i at iteration n+1, and v^i_{n+1} is the corresponding velocity vector.

At each time step, the velocity of each particle is modified using its current velocity and its distance from the personal and global best positions as follows:

$$v^i_{n+1} = wv^i_n + c_1r_1(p_{bst} - x^i_n) + c_2r_2(g_{bst} - x^i_n) \tag{5.16}$$

where w is the inertia weight; r_1 and r_2 are random numbers between 0 and 1; p_{bst} is the best position found by particle i so far; g_{bst} is the best position in the swarm at iteration n; c_1 and c_2 are the "trust" parameters.

Equation (5.16) simulates the movement of the particle toward a new position. The first term in (5.16) represents the particle's memory of its current velocity (change in position) in the different dimensions of the search space. The second term is associated with "*cognition*" since it only takes into account the particle's own experience, while the third one represents the "*social interaction*" between the particles. The trust parameters indicate how much confidence the particle has in itself (c_1) and how much confidence it has in the swarm (c_2).

In the subject constrained problem, violated agents are corrected by means of a two-level correction routine: 1) correction based on the random behavior of the velocity update gains r_1 and r_2, 2) if the first-level correction fails, the second level correction will take place by setting the agent position back to the personal pest position.

The following self-explanatory pseudo code shows the computational flow of the proposed PSO-based tuning algorithm.

```
BEGIN

  1. Initialize the swarm positions and velocities as follows:
                    $x_{io} = x_{min} + \texttt{rand(0,1)}(x_{max} - x_{min})$
                    $v_{io} = x_{min} + \texttt{rand(0,1)}(x_{max} - x_{min})$
     where $x_{min}$ and $x_{max}$ are the vectors of the lower and upper
     limits of the controller gain vector respectively, and rand(0,1) is a
     random number between 0 and 1.

  2. Carry out time-domain simulation using the maximum expected
     voltage disturbance.  A capacitor-switching voltage disturbance
     is a good candidate.

  3. Objective function and fitness evaluation using (5.12)

  4. if fitness(x)>fitness($p_{bst}$) then; $p_{bst}$=x; endif

  5. if fitness(x)>fitness($g_{bst}$) then; $g_{bst}$=x; endif

  6. Velocity update using (5.16)

  7. Position update using (5.15)

  8. Check for violated design gains using the violation criterion in (5.14)

     if 'constraint is violated' then

              if violation flag=1 then
                   $v^i_{n+1} = wv^i_n + c_1r_1(p_{bst} - x^i_n) + c_2r_2(g_{bst} - x^i_n)$
              elseif violation flag=1 then
                             $x^i_{n+1} = p_{bst}$
              endif

      endif

  9.  Check for convergence

      if 'convergence is met' then  output 'Kopt'
      else goto step 2
      endif

END
```

5.3.3 Relaxing the Slowly Varying Assumption in Grid-Voltage Estimation and Current Control

For fast and dynamic voltage disturbances, the disturbance slowly varying assumption might not be fulfilled. Further, under dynamic and fast voltage disturbances, significant degradation in the tracking and disturbance rejection performances of the current controller will be yielded [111]-[112].

The concept of "active damping" or "active resistance" is introduced in [111]-[112] to increase the damping of disturbances and variations in the counter voltage. However, this method provides a negligible attenuation for high-frequency disturbances. The internal model control has been considered for current control in [113], where a static internal model is added to enhance the robustness and decoupling characteristics in the current control loop. However, a static internal model cannot provide the necessary attenuation to the high-frequency disturbances caused by fast grid/load disturbances. The lack of robustness against fast disturbances characterizes the robust current controller reported in literature [59]-[72]. To ensure perfect tracking of the output current in the presence of uncertainties and provide means for attenuating low- and high- frequency system disturbances, the frequency modes of the disturbances to be eliminated should be included in the stable closed loop system [83]. To achieve this objective and to provide a high bandwidth estimate of the grid voltage, an adaptation law is derived, in the sense of Lyapunov functions, using the nominal current dynamics. To cope with the high bandwidth property of the voltage disturbances, the disturbance slowly varying assumption is relaxed in the proposed controller. The relaxation is achieved by adopting a curbing sliding-mode-based feedback gain within the internal model observation system.

To estimate the voltage dynamics, an adaptive natural observer with the following input/output relation can be constructed:

$$\dot{\hat{\boldsymbol{x}}} = \boldsymbol{A}_c\hat{\boldsymbol{x}} + \boldsymbol{B}_c\boldsymbol{u} + \boldsymbol{G}_c\hat{\boldsymbol{f}} \tag{5.17}$$

where the subscript "$\hat{}$" denotes estimated values.

Under the same input voltage and disturbance, the estimated state vector approaches the actual state vector. Therefore, convergence of the proposed observer can be achieved with an appropriate disturbance voltage adaptation using the estimation error $\boldsymbol{e} = [\begin{array}{cc} e_{iq} & e_{id} \end{array}]^T \equiv \boldsymbol{x} - \hat{\boldsymbol{x}}$.

Using (5.6) and (5.17), the following error dynamics can be obtained:

$$\dot{\boldsymbol{e}} = \boldsymbol{A}_c\boldsymbol{e} + \boldsymbol{G}_c\tilde{\boldsymbol{f}} \tag{5.18}$$

where $\tilde{\boldsymbol{f}} = \boldsymbol{f} - \hat{\boldsymbol{f}}$ is the voltage estimation error vector. For typical system parameters, the matrix $\boldsymbol{A}_c$ is Hurwitz. Further, the damping rate of $\boldsymbol{A}_c$ can be easily controlled by adding a feedback gain matrix for the estimation error.

To stabilize (5.18), define a Lyapunov function candidate as follows:

$$V_T\left(\boldsymbol{e}(t), \tilde{\boldsymbol{f}}(t), t\right) = \frac{1}{2}\boldsymbol{e}^T(t)\boldsymbol{e}(t) + \frac{1}{2\gamma}\tilde{\boldsymbol{f}}^T(t)\tilde{\boldsymbol{f}}(t) \tag{5.19}$$

where γ is a positive adaptation gain.

Using (5.18), and assuming that the error dynamics and the observed quantities are naturally continuous, the time derivative of the Lyapunov function in (5.19) can be obtained as

$$\dot{V}_T(t) = \boldsymbol{e}^T\boldsymbol{A}_c\boldsymbol{e} + \boldsymbol{e}^T\boldsymbol{G}_c\tilde{\boldsymbol{f}} + \frac{1}{\gamma}\tilde{\boldsymbol{f}}^T(t)\dot{\tilde{\boldsymbol{f}}}(t). \tag{5.20}$$

If the uncertainty function $\boldsymbol{f}$ is assumed to be naturally continuous and its bandwidth is much lower than the observation period, then the uncertainty adaptation rule can be derived from (5.20) to satisfy the stability condition $\dot{V}_T(t) \leq 0$ as

$$\dot{\hat{\boldsymbol{f}}} = \gamma\boldsymbol{G}_c\boldsymbol{e}. \tag{5.21}$$

The adaptive estimation law in (5.21) provides a simple iterative gradient algorithm designed to stabilize (5.18). However, the disturbance slowly varying assumption could not be fulfilled for highly dynamic disturbances, which might exist in practical operating conditions. To relax this assumption, the observation system design is modified.

The time derivative of the Lyapunov function in (5.19) can be written as

$$\begin{aligned}\dot{V}_T(t) &= \boldsymbol{e}^T\left(\boldsymbol{A}_c\boldsymbol{e} + \boldsymbol{G}_c\tilde{\boldsymbol{f}}\right) + \frac{1}{\gamma}\tilde{\boldsymbol{f}}^T(t)\left(\dot{\boldsymbol{f}}(t) - \dot{\hat{\boldsymbol{f}}}(t)\right)\\ &= \boldsymbol{e}^T\left(\boldsymbol{A}_c\boldsymbol{e} + \boldsymbol{G}_c\tilde{\boldsymbol{f}}\right) - \frac{1}{\gamma}\tilde{\boldsymbol{f}}^T(t)\dot{\hat{\boldsymbol{f}}}(t) + \mu_q(t) + \mu_d(t)\end{aligned} \tag{5.22}$$

where $\mu_q(t) = \frac{1}{\gamma}\tilde{f}_q(t)\dot{f}_q(t)$ and $\mu_d(t) = \frac{1}{\gamma}\tilde{f}_d(t)\dot{f}_d(t)$ represent, respectively, the *d*- and *q*-uncertainty components due to the slowly varying assumption. In practical converter applications, μ_q and μ_d can be assumed bounded. With the adaptation law in (5.21), the stability of (5.22) can be guaranteed if a positive observation gain, which is larger than the absolute bound of $\mu_q(t) + \mu_d(t)$, is added to the observation system such that $\dot{V}_T(t) \leq 0$. To derive the observation gain vector, (5.22) can be re-written as:

$$\dot{V}_T(t) = \boldsymbol{e}^T\left(\boldsymbol{A}_c\boldsymbol{e} + \boldsymbol{G}_c\tilde{\boldsymbol{f}} + \boldsymbol{\rho}\right) - \frac{1}{\gamma}\tilde{\boldsymbol{f}}^T(t)\dot{\hat{\boldsymbol{f}}}(t) \tag{5.23}$$

where $\boldsymbol{\rho} = \begin{bmatrix} \rho_q & \rho_d \end{bmatrix}^T$ represents the *d*- and *q*-uncertainty components, which are caused by the slowly varying assumption; and they are mapped to the current dynamics such that $\mu_q(t) = (e_{iq} + r)\rho_q$ and $\mu_d(t) = (e_{id} + r)\rho_d$, where r is a small positive constant. To stabilize (5.23), a curbing sliding-mode-based feedback gain vector is added to the internal model observation system.

The new observation system is constructed as follows:

$$\dot{\hat{\boldsymbol{x}}} = \boldsymbol{A}_c\hat{\boldsymbol{x}} + \boldsymbol{B}_c\boldsymbol{u} + \boldsymbol{G}_c\hat{\boldsymbol{f}} + \boldsymbol{K}_{sm} \tag{5.24}$$

$$\dot{\hat{\boldsymbol{f}}} = \gamma\boldsymbol{G}_c\boldsymbol{e} \tag{5.25}$$

where $\boldsymbol{K}_{sm} = \begin{bmatrix} K_{siq}\mathrm{sgn}(e_{iq}) & K_{sid}\mathrm{sgn}(e_{id}) \end{bmatrix}^T$ is the sliding gain vector; sgn(.) is the signum function; and $\begin{bmatrix} K_{siq} & K_{sid} \end{bmatrix}^T > |\boldsymbol{\rho}|$.

Define a Lyapunov function candidate as follows:

$$V_T\left(\boldsymbol{e}(t), \tilde{\boldsymbol{f}}(t), t\right) = \frac{1}{2}\boldsymbol{e}^T(t)\boldsymbol{e}(t) + \frac{1}{2\gamma}\tilde{\boldsymbol{f}}^T(t)\tilde{\boldsymbol{f}}(t). \tag{5.26}$$

Using (5.24), the time derivative of the Lyapunov function in (5.26) can be obtained as

$$\dot{V}_T(t) = \boldsymbol{e}^T\left(\boldsymbol{A}_c\boldsymbol{e} + \boldsymbol{G}_c\tilde{\boldsymbol{f}} + \boldsymbol{\rho} - \boldsymbol{K}_{sm}\right) - \frac{1}{\gamma}\tilde{\boldsymbol{f}}^T(t)\dot{\hat{\boldsymbol{f}}}(t). \tag{5.27}$$

Substituting (5.25) in (5.27), then

$$\begin{aligned} \dot{V}_T(t) &= \boldsymbol{e}^T\boldsymbol{A}_c\boldsymbol{e} + \boldsymbol{e}^T\boldsymbol{\rho} - \boldsymbol{e}^T\boldsymbol{K}_{sm} \\ &= \boldsymbol{e}^T\boldsymbol{A}_c\boldsymbol{e} + \boldsymbol{e}^T\boldsymbol{\rho} - \left|\boldsymbol{e}^T\right|\begin{bmatrix} K_{siq} & K_{sid} \end{bmatrix}^T \\ &\leq \boldsymbol{e}^T\boldsymbol{A}_c\boldsymbol{e} + \left|\boldsymbol{e}^T\right||\boldsymbol{\rho}| - \left|\boldsymbol{e}^T\right|\begin{bmatrix} K_{siq} & K_{sid} \end{bmatrix}^T \\ &= \boldsymbol{e}^T\boldsymbol{A}_c\boldsymbol{e} + \left|\boldsymbol{e}^T\right|(|\boldsymbol{\rho}| - \begin{bmatrix} K_{siq} & K_{sid} \end{bmatrix}^T). \end{aligned} \tag{5.28}$$

If the design parameters are chosen as $\begin{bmatrix} K_{siq} & K_{sid} \end{bmatrix}^T > |\boldsymbol{\rho}|$, then

$$\dot{V}_T(t) \leq 0. \tag{5.29}$$

This result implies that $\boldsymbol{e}(t) \rightarrow \boldsymbol{0}$ and $\tilde{\boldsymbol{f}}(t) \rightarrow \boldsymbol{0}$ as $t \rightarrow \infty$. Subsequently, the stability of the proposed observation system is guaranteed. As a result, the estimate can be reliably used to embed an internal model for the uncertainty function within the current feedback structure, resulting in equivalent control to cancel the voltage disturbances with relaxed uncertainty slowly-varying assumption [114].

5.4 Results

To evaluate the performance of the proposed control scheme, a three-phase grid connected PWM-VSI DG interface incorporated with the proposed control scheme has been

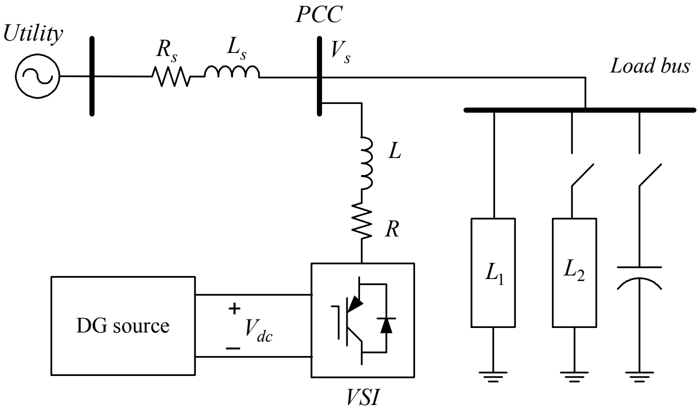

Figure 5.4: Test system.

connected to a test network, as shown in Figure 5.4. The system parameters are given in Appendix A. The overall system is digitally simulated under Matlab/Simulink environment with real-time code generation support. A converter switching frequency of 6.67 kHz has been selected. As a result, a control sampling time T=150 μs is yielded.

For the variable structure voltage controller, the coefficient of the sliding surface is chosen as c_v= 0.0015. As a result, the time constant of S_v dynamics is set to 1.5 ms. The control parameters are obtained through the PSO study to achieve appropriate control performance with careful consideration of the control effort saturation and practical operating conditions as described earlier. The trust parameters are set as c_1=1.7 and c_2 = 2. Since c_2 is higher than c_1, more trust in the swarm is assumed. Figure 5.5 shows the convergence characteristics of the PSO tuning algorithm with constant and dynamic values of the inertia weight w. The minimum normalized value of the objective function is 0.015; it is obtained with dynamic inertia weight. The minimum and maximum inertia weights are 0.35 and 0.95; respectively. The weight update rule is based on the coefficient of variation of the objective function values for a 15% subset of best particles. The control law parameters are set as K_{Pv}=0.2, K_{Iv}=380, and K_{Sv}=140.

To verify the feasibility of the proposed controller, different operating conditions have been considered. For the purpose of performance comparison, some selected results are presented as follows.

To evaluate the performance of the proposed interface to compensate for the PCC voltage fluctuation under the condition of a sudden load change, the switched load (L2) is turned on at t=0.045 s. The reference voltage at the PCC is set to 1.0 p.u. Figure 5.6 shows the voltage profile without regulation, where Figure 5.6(a) shows the line-voltage waveform and Figure 5.6(b) shows the magnitude of the line voltage at the PCC. Figure 5.6 shows that the instantaneous voltage dip is about 0.5 p.u and the steady-state voltage

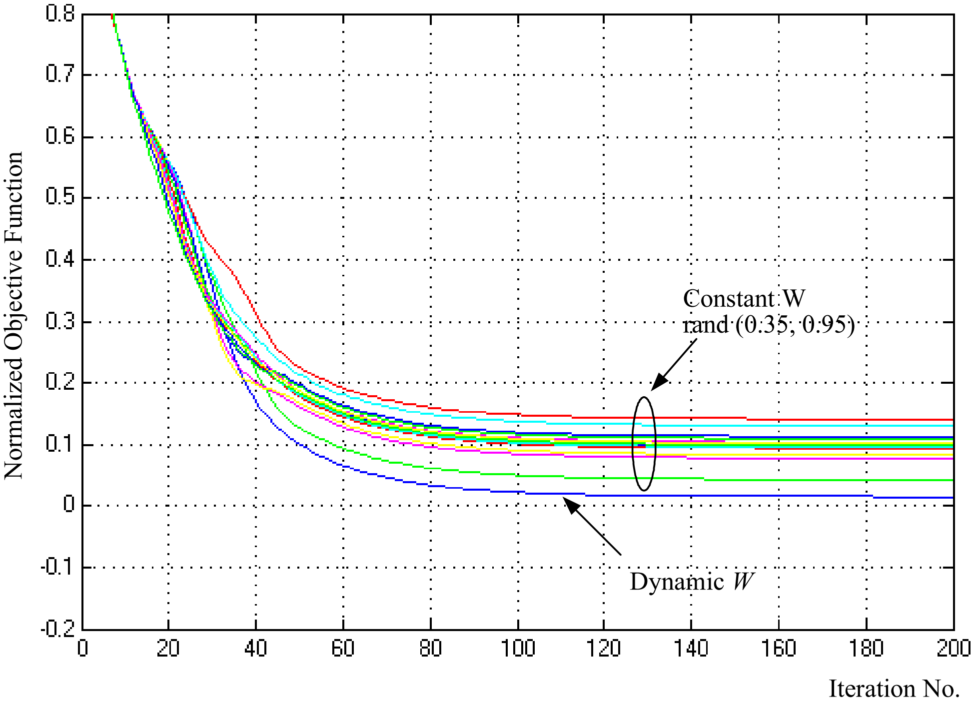

Figure 5.5: The convergence characteristics of the PSO algorithm.

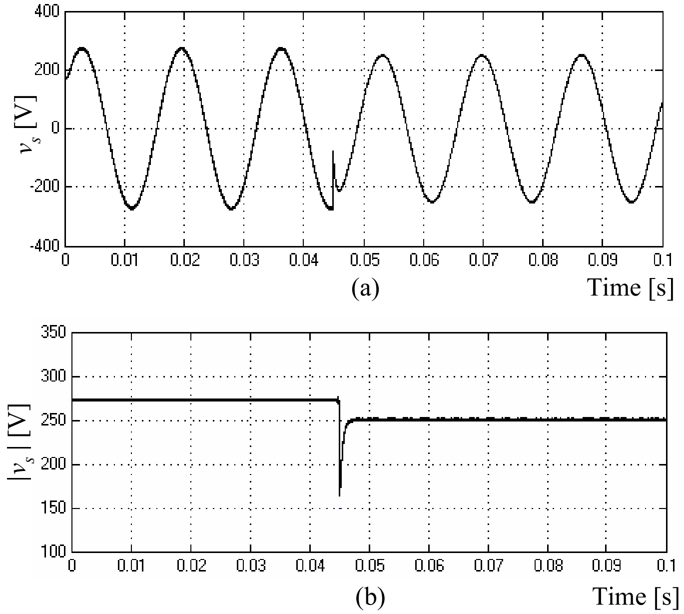

Figure 5.6: Voltage drop due to sudden loading of load L2. (a) Voltage waveform. (b) Voltage magnitude at the PCC.

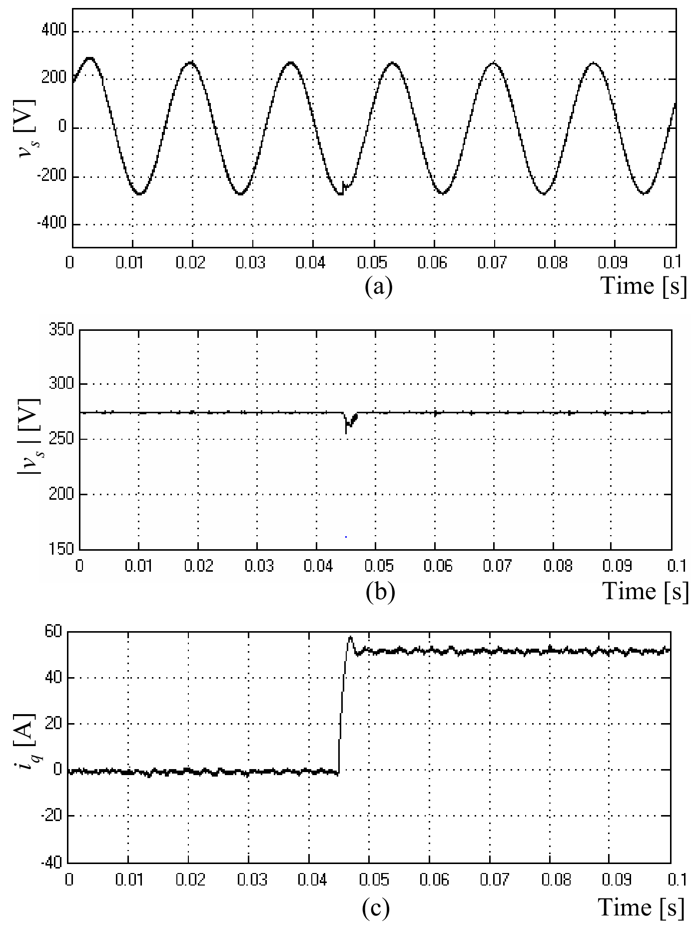

Figure 5.7: Voltage regulation performance with the proposed controller at sudden loading of load L2. (a) Voltage waveform. (b) Voltage magnitude at the PCC. (c) Reactive current injected.

drop is about 0.15 p.u. Figure 5.7 shows the control performance when the proposed voltage regulation scheme is enabled. Figure 5.7(a),(b) shows that the instantaneous voltage dip is less than 0.09 p.u with a recovery time of about 3 ms. Figure 5.7(c) shows the corresponding q-axis current injected to the grid. The reactive current component is quickly generated to regulate the bus voltage and reject the voltage disturbance.

Capacitor switching generates highly dynamic voltage disturbances, which directly impact the voltage quality. Figure 5.8(a),(b) shows the voltage waveform when the capacitor is switched on at t=0.045 s and without voltage regulation. Severe degradation in the voltage quality is yielded by the switching transient. Figure 5.9 shows the control performance when the proposed voltage regulation scheme is enabled. Figure 5.9(a), (b) shows that the quality of the voltage waveform is remarkably improved, where most of the transient waveform has been mitigated by the voltage controller. Figure 5.9(c)

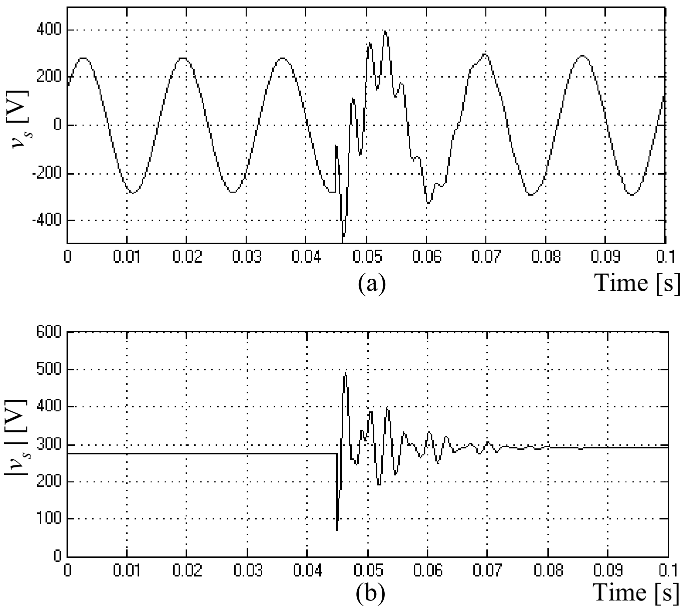

Figure 5.8: Voltage transients due to capacitor switching. (a) voltage waveform. (b) voltage magnitude at the PCC.

shows the corresponding q-axis current injected to the grid. The reactive current component is quickly generated to regulate the bus voltage and reject the voltage disturbance. The wide-band disturbance rejection feature of the variable structure voltage controller enables effective mitigation of fast and dynamic voltage disturbances, such as the capacitor-switching transients. Figure 5.9(d) shows the estimated grid voltage components. It is clear that the proposed voltage estimator can track the actual grid-voltage disturbance. Therefore, the effect of these disturbances on the current control loop can be mitigated.

For further performance comparison, the proposed voltage control scheme is compared to the conventional PI voltage regulator, i.e. without the VSC element. Figure 5.10 shows the control performance of the PI voltage controller. Figure 5.10(a) depicts the magnitude of the line voltage at the PCC when the switched load (L2) is turned on at t=0.045 s. The instantaneous voltage dip is about 0.4 p.u. and the recovery time is about 30 ms. Figure 5.10(b) depicts the magnitude of the line voltage at the PCC when the capacitor is switched on at t=0.045 s. Remarkable degradation in the voltage quality is yielded by the switching transient. As Figure 5.10(b) reveals, the voltage recovery time approaches 35 ms. PI regulators with their pole at zero-frequency cannot achieve fast voltage regulation, and certainly cannot mitigate fast voltage disturbances. On the contrary, the hybrid VSC control offers a high disturbance rejection performance, as indicated in Figures 5.7 and 5.9.

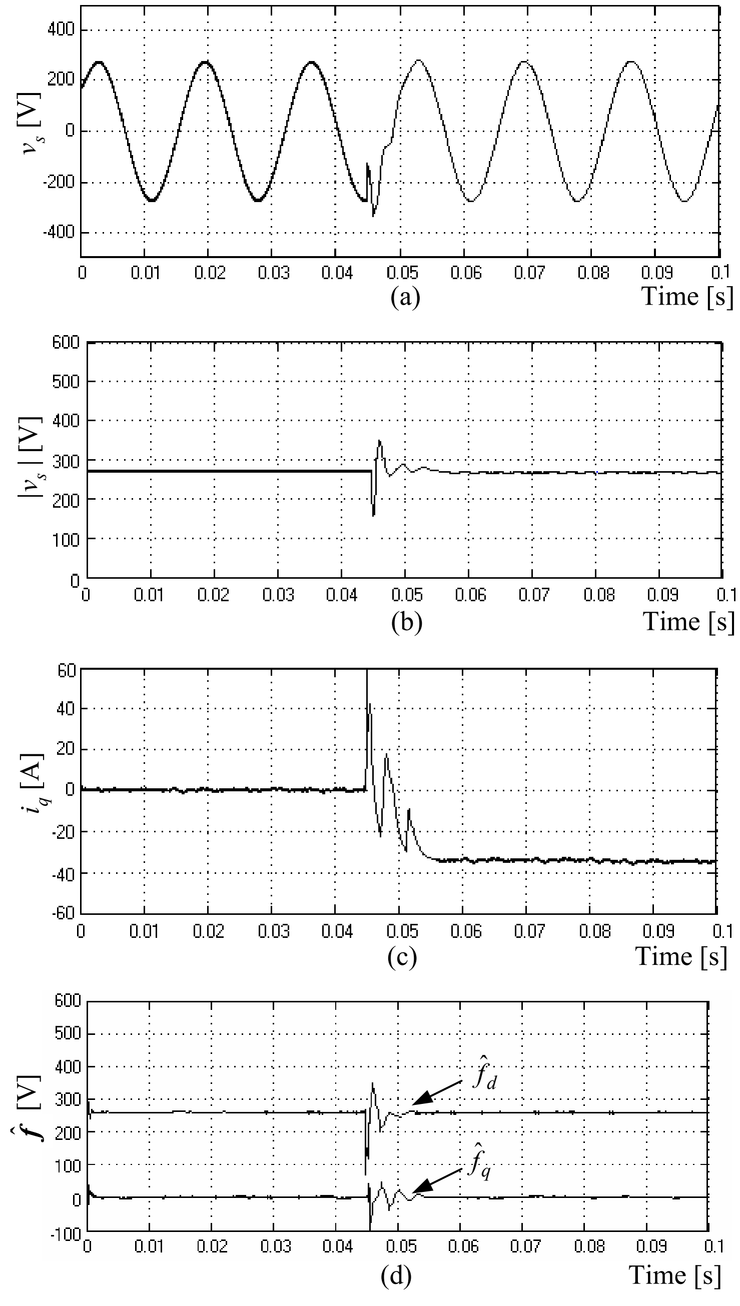

Figure 5.9: Disturbance rejection performance with the proposed controller against voltage transients initiated by capacitor switching. (a) Voltage waveform. (b) Voltage magnitude at the PCC. (c) Reactive current injected. (d) Estimated uncertainty function.

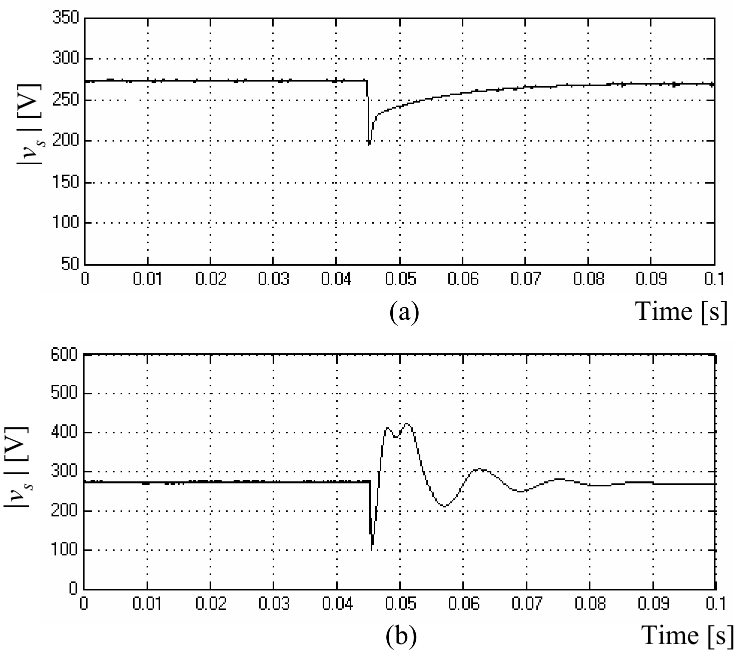

Figure 5.10: Disturbance rejection performance with the conventional PI voltage controller. (a) Voltage magnitude at the PCC at sudden loading of load L2. (b) Voltage magnitude at the PCC at capacitor switching.

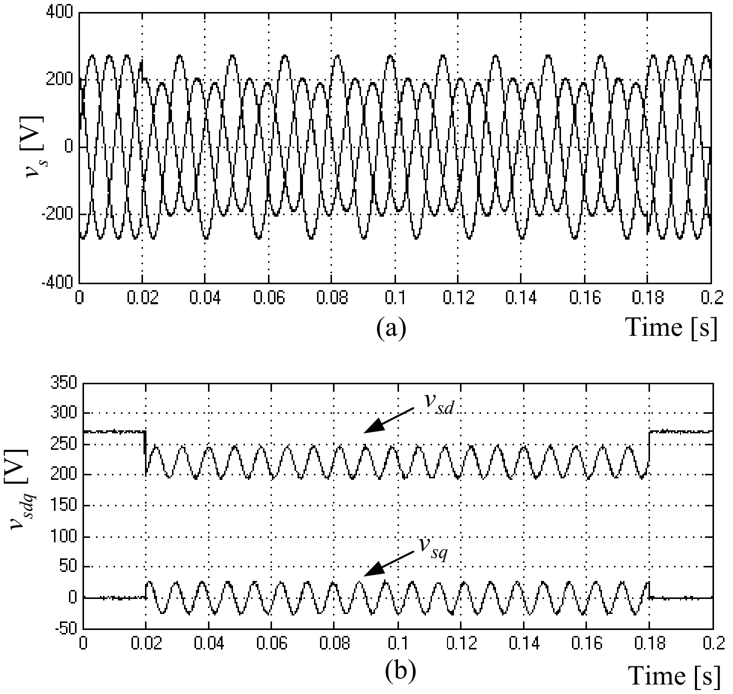

Figure 5.11: Grid voltage at the PCC during unbalanced voltage disturbance. (a) Voltage waveforms. (b) Grid voltage dq components.

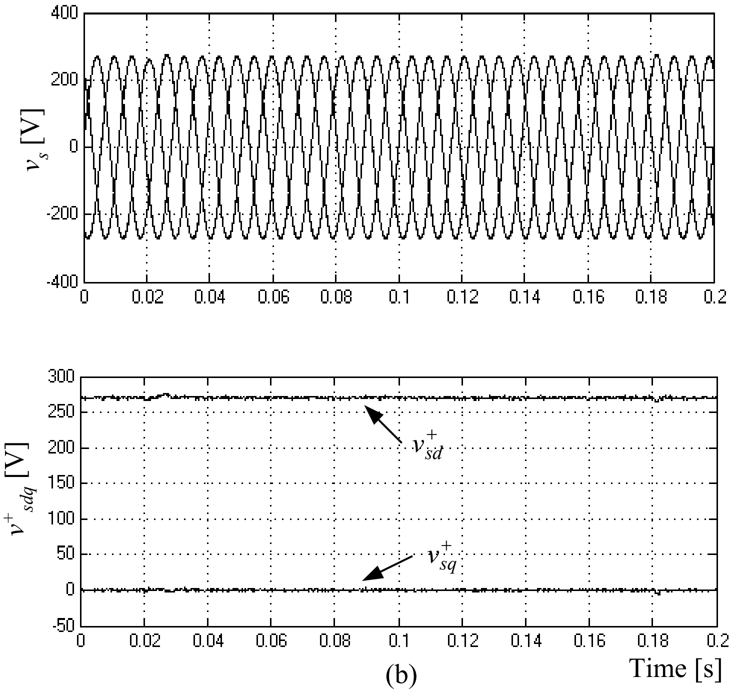

Figure 5.12: Control performance of the proposed scheme during unbalanced voltage disturbance. (a) Voltage waveforms. (b) Grid voltage dq components.

To evaluate the voltage regulation performance under unbalanced grid voltage conditions, the proposed dual-sequence voltage controller, which is depicted in Figure 5.3, has been tested.

Figure 5.11 shows the grid voltage at the PCC during unbalanced voltage disturbance initiated by heavily unbalanced loading to emulate unsymmetrical fault conditions. A relatively large unbalanced voltage dip with 8.7% voltage unbalance factor takes place for 9.6 cycles, by means of unbalanced loading, as shown in Figure 5.11(a). The presence of the negative-sequence component leads to double power-frequency oscillations in the dq components of the grid voltage as shown in Figure 5.11(b).

Figures 5.12 and 5.13 depict the control performance of the proposed scheme under the unbalanced grid voltage illustrated in Figure 5.11. Figure 5.12(a) shows the 3-phase voltages; which are well regulated under the unbalanced disturbance. Figure 5.12(b) shows the positive-sequence dq components of the grid voltage, whereas Figure 5.13(a) shows the corresponding negative sequence components. Since the inverter interface is supporting the grid reactively in a fast manner, only the d-component of the positive sequence grid voltage appears, whereas other sequence components vanish swiftly. Figure 5.13(b), (c) shows the sequence components of the injected current. The fast action of the proposed controller in regulating the line voltage is obvious. Provided that

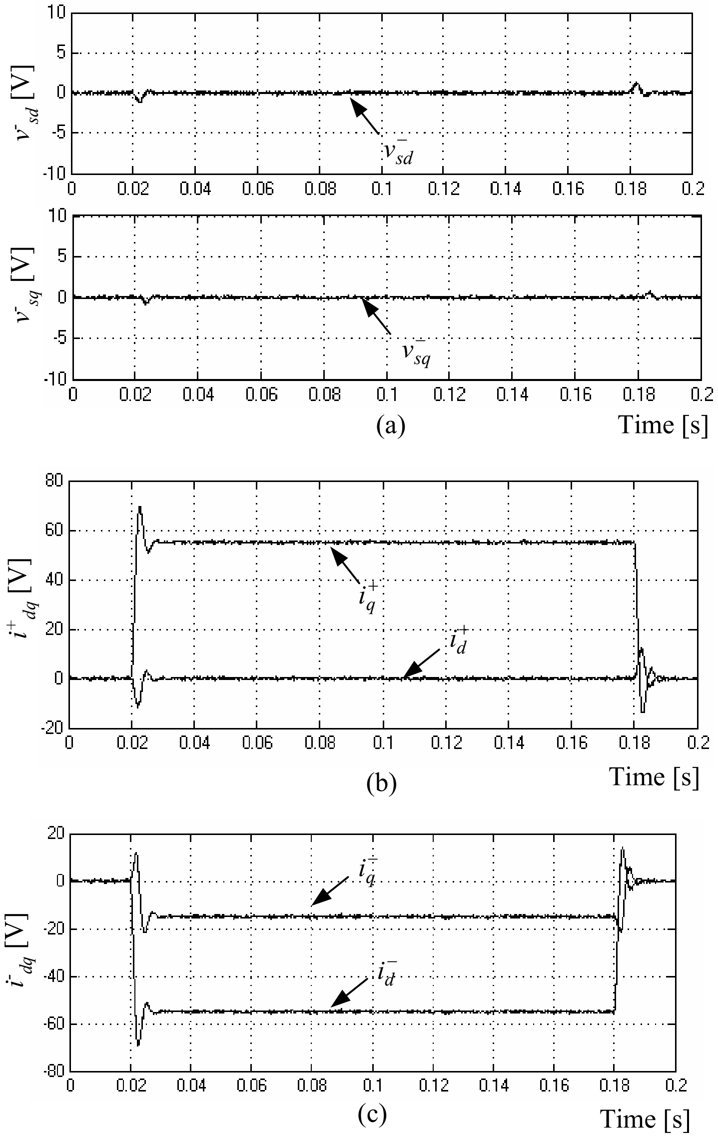

Figure 5.13: Control performance of the proposed scheme during unbalanced voltage disturbance. (a) Negative *dq* sequence components of the grid voltage. (b) Positive *dq* sequence components of injected currents. (c) Negative *dq* sequence components of injected currents.

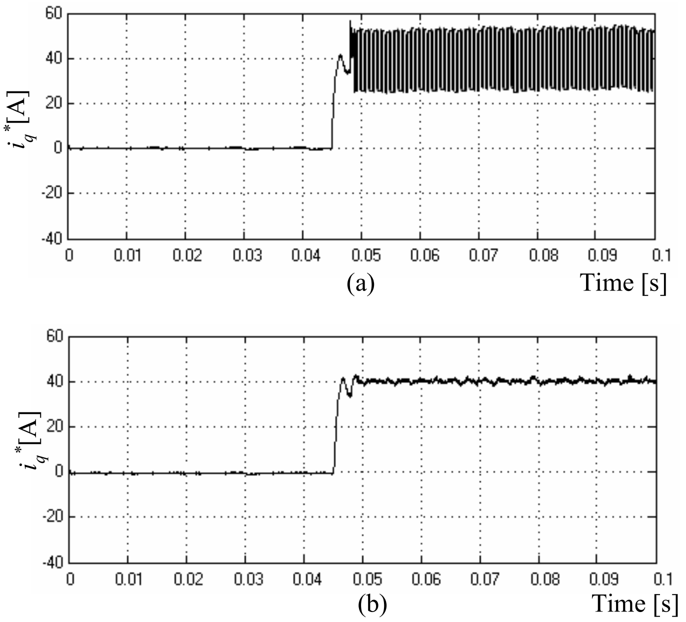

Figure 5.14: Control effort of the proposed voltage controller. (a) With a hard switching function. (b) With switching-function approximation.

there is enough reactive power rating, the proposed interface can over-ride larger voltage disturbances initiated by up-stream grid faults.

The control chattering phenomenon associated with the VSC might counteract the stability and power quality requirements of the converter system. However, the switching function approximation approach can relax this problem. Figure 5.14(a) shows the q-axis reference current command in the proposed controller with a hard switching function. The converter is commanded to start at t=0.045 s under 15% reduction in the grid voltage magnitude. It is clear that the VSC voltage controller provides a good transient response to regulate the PCC voltage; however, the control chattering at the steady-state is obvious. Figure 5.14(b) shows the q-axis reference current command with switching-function approximation. The transient response is almost preserved, whereas the steady-state performance is remarkably improved. A smooth reactive current reference with negligible ripples is obtained.

5.5 Summary

In this chapter, a new control scheme for the DG interface featuring fast load voltage regulation and effective mitigation of fast voltage disturbances has been presented. A hybrid voltage controller combining a linear with VSC element has been proposed and applied to an inverter-based DG interface to regulate the voltage at the PCC. The controller successfully embeds a wide band of frequency modes through an equivalent internal model. Subsequently, wide range of voltage perturbations, including capacitor-switching disturbances, has been effectively mitigated. To provide effective mitigation of unbalanced voltage disturbances, a dual-sequence voltage controller has been developed. Provided that there is enough reactive power rating, the proposed interface can override unbalanced voltage disturbances initiated by up-stream grid faults. To optimally tune the proposed nonlinear voltage controller, the tuning problem has been formulated as a constrained optimization problem and solved via an evolutionary search algorithm based on the PSO technique. Therefore, a simple and structured tuning methodology has been obtained. To ensure accurate and robust tracking of the estimated grid voltage and the generated current trajectory, the disturbance slowly varying assumption has been relaxed in the proposed design. Theoretical analysis and comparative evaluation results have revealed the effectiveness of the proposed control scheme.

Chapter 6

Adaptive Decentralized Control to Preserve Power-Sharing Stability of Paralleled-Inverters in DG Micro-Grids

6.1 Introduction

There are several operating regimes possible for DG. Among them is the micro-grid, in which a cluster of DG units serviced by a distribution system is formed to maintain the reliability of critical loads, mainly when the utility supply is not available. However, a reliable and robust operation of a micro-grid centers on an efficient control scheme of micro-grid generators.

The basic control objective in a micro-grid is to achieve accurate power sharing while maintaining close regulation of the micro-grid voltage magnitude and frequency. As detailed in Section 2.3.3; the development of an autonomous power sharing strategy for micro-grid inverters with effective damping of low frequency modes demands special attention.

This chapter addresses the low-frequency relative stability problem in paralleled inverter-based DG units in micro-grids. In the sense of the small-signal dynamics of a micro-grid, it can be shown that as the demanded power of each inverter changes, the low-frequency modes of the power sharing dynamics drift to new locations and the relative stability is remarkably affected and eventually, instability can be yielded. To preserve the power-sharing stability, an adaptive decentralized droop-controller of paralleled inverter-based DG units is proposed in this chapter. The proposed power sharing strategy is based on the static droop characteristics combined with an adaptive transient droop function. Unlike conventional droop controllers, which yield one-degree of-freedom

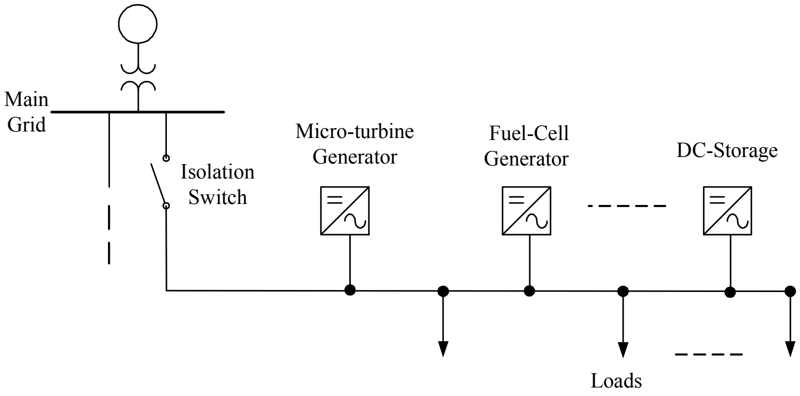

Figure 6.1: A micro-grid system.

tunable controller, the proposed droop controller yields two-degree-of-freedom tunable controller. Subsequently, the dynamic performance of the power sharing mechanism can be adjusted, without affecting the static droop gain, to damp the oscillatory modes of the power-sharing controller. To account for the power modes immigration at different loading conditions, the transient droop gains are adaptively scheduled via small signal analysis of the power-sharing mechanism along the loading trajectory of each DG unit to yield the desired transient and steady-state response. The gain adaptation scheme utilizes the filtered active and reactive powers as indices; therefore, a stable and smooth power injection performance can be obtained at different loading conditions. It can be shown that the adaptive nature of the proposed controller ensures active damping of power oscillations at different operating conditions, and yields a stable and robust performance of the paralleled inverter system.

The residual part of this chapter is organized as follows. In Section 6.2, modeling of a micro-grid-connected inverter-based DG unit is presented. In Section 6.3, the power-sharing dynamic performance in a micro-grid with conventional droop controller is analyzed. In Section 6.4, the proposed power-sharing controller is presented. Simulation results are provided to demonstrate the effectiveness of the proposed control scheme in Section 6.5. A summary is drawn in Section 6.6.

6.2 Modeling of a Micro-grid-Connected Voltage Source Inverter (VSI)

Figure 6.1 shows a micro-grid system made of a cluster of inverter-based DG units empowered by micro-sources, such as fuel cells, micro-turbines, dc storage…etc. A dc/ac VSI is commonly used as an interfacing module.

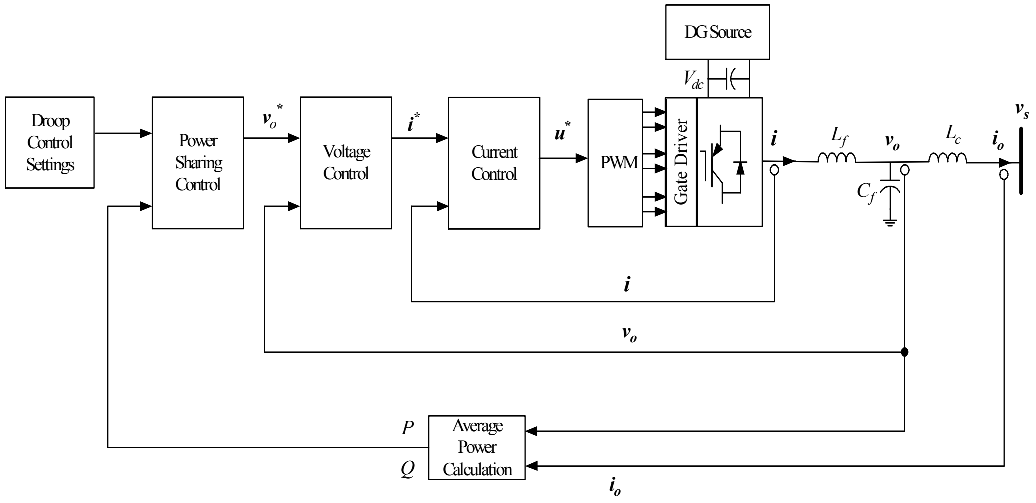

Figure 6.2: Per-phase power circuit and simplified control structure of a micro-grid-connected VSI.

Figure 6.2 shows a simplified block diagram of a micro-grid-connected VSI. A three-leg VSI with an LC filter and a coupling inductor form the power circuit, whereas three control loops form the control structure. Specifically, a power-sharing controller is used to generate the magnitude and the frequency of the fundamental output voltage of the inverter according to the droop characteristics, by emulating the operation of a conventional synchronous generator; a voltage controller is used to synthesize the reference filter-inductor current vector; and a current controller is adopted to generate the command voltage vector to be synthesized by a PWM module. Both the voltage and current control loops should provide enough damping for the output T-filter that is composed of the LC filter and the coupling inductor. The coupling inductor shapes the output impedance of the inverter so that the active-reactive power coupling is minimized.

In Park's d-q frame that rotates synchronously with the inverter output voltage angular speed ω_o, the current and voltage dynamics can be reasonably represented by the following equations:

$$\frac{di_d}{dt} = \frac{-R_f}{L_f} i_d + \omega_o i_q + \frac{1}{L_f}\left(v_d - v_{od}\right) \tag{6.1}$$

$$\frac{di_q}{dt} = \frac{-R_f}{L_f} i_q - \omega_o i_d + \frac{1}{L_f}\left(v_q - v_{oq}\right) \tag{6.2}$$

$$\frac{dv_{od}}{dt} = \omega_o v_{oq} + \frac{1}{C_f}\left(i_d - i_{od}\right) \tag{6.3}$$

$$\frac{dv_{oq}}{dt} = -\omega_o v_{od} + \frac{1}{C_f}\left(i_q - i_{oq}\right) \tag{6.4}$$

$$\frac{di_{od}}{dt} = \frac{-R_c}{L_c} i_{od} + \omega_o i_{oq} + \frac{1}{L_c}\left(v_{od} - v_{sd}\right) \tag{6.5}$$

$$\frac{di_{oq}}{dt} = \frac{-R_c}{L_c} i_{oq} - \omega_o i_{od} + \frac{1}{L_c}\left(v_{oq} - v_{sq}\right) \tag{6.6}$$

where v_d, v_q, i_d, and i_q are the d- and q-axis inverter's voltages and currents; v_{od}, v_{oq}, i_{od}, and i_{oq} are the d- and q-axis output voltages and currents; v_{sd} and v_{sq} are the d- and q- axis bus voltages; R_f, L_f, and C_f are the per-phase resistance, inductance, and capacitance of the LC filter, respectively; and R_c and L_c are the per-phase resistance and inductance of the coupling inductor, respectively.

Using the two-axis theory, the injected instantaneous active and reactive power components, p and q, are given by

$$p = \frac{3}{2}\left(v_{od} i_{od} + v_{oq} i_{oq}\right) \tag{6.7}$$

$$q = \frac{3}{2}\left(v_{od} i_{oq} - v_{oq} i_{od}\right). \tag{6.8}$$

To allow sufficient time-scale separation between the power and current control loops and to achieve high power quality injection [99], the average active and reactive powers corresponding to the fundamental components are subjected to the control action, and they are obtained by means of a low-pass filter as

$$P = \frac{\omega_c}{s + \omega_c} p \tag{6.9}$$

$$Q = \frac{\omega_c}{s + \omega_c} q \tag{6.10}$$

where ω_c is the filter cut-off frequency.

To realize a power-sharing function, the conventional droop characteristics are usually used in paralleled inverter systems to introduce the following droops in the fundamental voltage frequency and magnitude of the output voltage:

$$\omega_o = \omega^* - mP \tag{6.11}$$

$$v_{od}^* = V^* - nQ \tag{6.12}$$

where ω^* and V^* are the nominal frequency and voltage set-points, respectively, and m and n are the static droop gains, and they can be calculated for a given range of frequency and voltage magnitude as follows:

$$m = \frac{\omega_{\max} - \omega_{\min}}{P_{\max}} \tag{6.13}$$

$$n = \frac{V_{od\max} - V_{od\min}}{Q_{\max}}. \tag{6.14}$$

The set points in (6.13) and (6.14) act as a virtual communication agent for different inverters for autonomous operation. The d-component of the output voltage is used in (6.14); as per the voltage-oriented control, the reference of the output voltage magnitude is aligned with the d-axis of the inverter reference frame.

To provide close voltage regulation, inverter output voltage control is adopted. To examine the micro-grid performance with standard controls, the voltage controller employs PI regulators with decoupling and feed-forward control loops to generate the reference current vector. The dynamics of the voltage controller can be given by

$$i_d^* = K_{pv}(v_{od}^* - v_{od}) + K_{iv}\int(v_{od}^* - v_{od})dt - \omega^* C_f v_{oq} + H i_{od} \tag{6.15}$$

$$i_q^* = K_{pv}(v_{oq}^* - v_{oq}) + K_{iv}\int(v_{oq}^* - v_{oq})dt + \omega^* C_f v_{od} + H i_{oq} \tag{6.16}$$

where K_{pv} and K_{iv} are the proportional and integral gains, respectively; C_f is the filter capacitance; and H is the feed-forward gain.

A current controller is needed to shape the voltage across the filter inductor, so that minimum current error is yielded. A standard PI current regulator with decoupling and feed-forward control loops is adopted for current regulation in order to examine the micro-grid performance with conventional controls. The dynamics of the current controller can be given by

$$v_d^* = K_{pi}(i_d^* - i_d) + K_{ii}\int(i_d^* - i_d)dt - \omega^* L_f i_q + v_{od} \tag{6.17}$$

$$v_q^* = K_{pi}(i_q^* - i_q) + K_{ii}\int(i_q^* - i_q)dt + \omega^* L_f i_d + v_{oq} \tag{6.18}$$

where K_{pi}, $K_{ii}$are the proportional and integral gains, respectively.

Equations (6.1)-(6.18) describe the dynamic behavior of a single inverter unit with the conventional current, voltage, and droop-based power controllers. Small signal analysis can provide a useful tool to analyze the dynamic performance and to design the control system [115], [18]. The above equations can be linearized, and the following state-space model of a single inverter unit can be obtained:

$$\Delta\dot{\boldsymbol{x}}_{DG} = \boldsymbol{A}_{DG}\Delta\boldsymbol{x}_{DG} + \boldsymbol{B}_{DG}\Delta\boldsymbol{v}_s \tag{6.19}$$

where

$$\Delta\boldsymbol{x}_{DG} = \begin{bmatrix} \Delta\delta & \Delta P & \Delta Q & \Delta C_V & \Delta C_C & \Delta i_{dq} & \Delta v_{odq} & \Delta i_{odq} \end{bmatrix}^T$$

in which, δ represents the angle between the inverter reference frame and a common reference frame; C_V and C_C are the states of the voltage and current controllers (the integrator states), respectively; $\boldsymbol{v}_s$ is the supply voltage at the point of common coupling (PCC) transferred to a common reference frame; and $\boldsymbol{A}_{DG}$ and $\boldsymbol{B}_{DG}$ are the state and input matrices, and they are given by

$$\boldsymbol{A}_{DG} = \left[\begin{array}{ccccccc}
0 & -m & 0 & 0 & 0 & 0 & 0 \\
0 & -\omega_c & 0 & 0 & 0 & 0 & 0 \\
0 & 0 & -\omega_c & 0 & 0 & 0 & 0 \\
0 & 0 & -n & 0 & 0 & 0 & 0 \\
0 & 0 & 0 & 0 & 0 & 0 & 0 \\
0 & 0 & -nK_{pv} & K_{pi} & 0 & 0 & 0 \\
0 & 0 & 0 & 0 & K_{pi} & 0 & 0 \\
0 & -mI_q & \frac{-nK_{pi}K_{pv}}{L_f} & \frac{K_{pi}}{L_f} & 0 & \frac{K_{ii}}{L_f} & 0 \\
0 & mI_d & 0 & 0 & \frac{K_{pi}}{L_f} & 0 & \frac{K_{ii}}{L_f} \\
0 & -mV_{oq} & 0 & 0 & 0 & 0 & 0 \\
0 & mV_{od} & 0 & 0 & 0 & 0 & 0 \\
\frac{1}{L_c}\begin{pmatrix} V_{sd}\sin\delta_o \\ -V_{sq}\cos\delta_o \end{pmatrix} & -mI_{oq} & 0 & 0 & 0 & 0 & 0 \\
\frac{1}{L_c}\begin{pmatrix} V_{sd}\cos\delta_o \\ +V_{sq}\sin\delta_o \end{pmatrix} & mI_{od} & 0 & 0 & 0 & 0 & 0
\end{array} \right.$$

$$\left. \begin{array}{cccccc}
0 & 0 & 0 & 0 & 0 & 0 \\
0 & 0 & \omega_c I_{od} & \omega_c I_{od} & \omega_c V_{od} & \omega_c V_{oq} \\
0 & 0 & \omega_c I_{oq} & -\omega_c I_{od} & -\omega_c V_{oq} & \omega_c V_{od} \\
0 & 0 & -1 & 0 & 0 & 0 \\
0 & 0 & 0 & -1 & 0 & 0 \\
-1 & 0 & -K_{pv} & -\omega^* C_f & H & 0 \\
0 & -1 & \omega^* C_f & -K_{pv} & 0 & H \\
\frac{-K_{pi}-R_f}{L_f} & \omega_o - \omega^* & \frac{-1-K_{pi}K_{pv}}{L_f} & \frac{-\omega^* C_f K_{pi}}{L_f} & \frac{K_{pi}H}{L_f} & 0 \\
\omega_o - \omega^* & \frac{-K_{pi}-R_f}{L_f} & \frac{\omega^* C_f K_{pi}}{L_f} & \frac{-1-K_{pi}K_{pv}}{L_f} & 0 & \frac{K_{pi}H}{L_f} \\
\frac{1}{C_f} & 0 & 0 & \omega_o & \frac{-1}{C_f} & 0 \\
0 & \frac{1}{C_f} & -\omega_o & 0 & 0 & \frac{-1}{C_f} \\
0 & 0 & \frac{1}{L_c} & 0 & \frac{-R_c}{L_c} & \omega_o \\
0 & 0 & 0 & \frac{1}{L_c} & -\omega_o & \frac{-R_c}{L_c}
\end{array} \right]$$

$$\boldsymbol{B}_{DG} = \begin{bmatrix}
0 & 0 & 0 & 0 & 0 & 0 & 0 & 0 & 0 & 0 & 0 & \frac{-1}{L_c}\cos\delta_o & \frac{-1}{L_c}\sin\delta_o \\
0 & 0 & 0 & 0 & 0 & 0 & 0 & 0 & 0 & 0 & 0 & \frac{-1}{L_c}\sin\delta_o & \frac{-1}{L_c}\cos\delta_o
\end{bmatrix}^T .$$

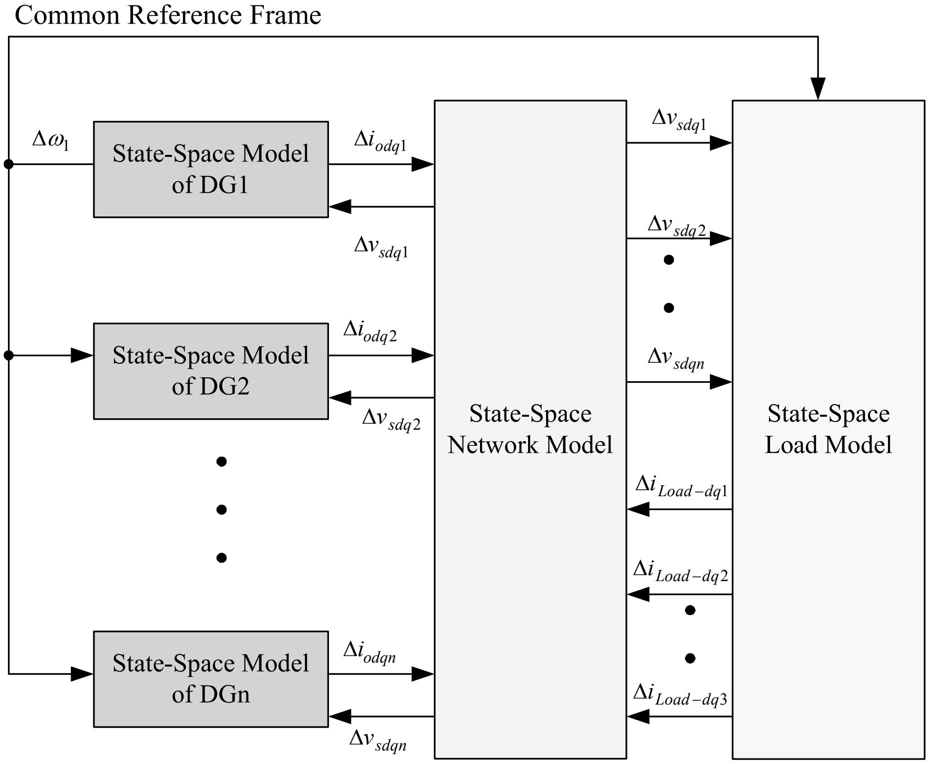

Figure 6.3: Construction and signal flow in a small signal model of a micro-grid system.

6.3 Power-Sharing Dynamic Performance in a Micro-grid With Conventional Droop Controller

To study the dynamic behavior of the power-sharing mechanism in a micro-grid, the small signal dynamic model of the micro-grid is constructed. The overall model embeds individual small signal models of different inverters combined with the small signal models of the network impedances including the load dynamics. It is more accurate to represent the dynamic models of the network and loads by their equivalent differential equations. The conventional approach in power system stability analysis is to represent these subsystems by a static relation based on the circuit phasor equations [115]. However, in a micro-grid system, where the grid size is limited, there is a room to embed these dynamics to evaluate all possible dynamic modes. Figure 6.3 shows a generalized construction and signal flow diagram for different sub-systems in a micro-grid small-signal state-space model.

A test micro-gird system is depicted in Figure 6.4. The test system parameters are given in Appendix B.

The overall linearized model of a micro-grid system can be given in the standard

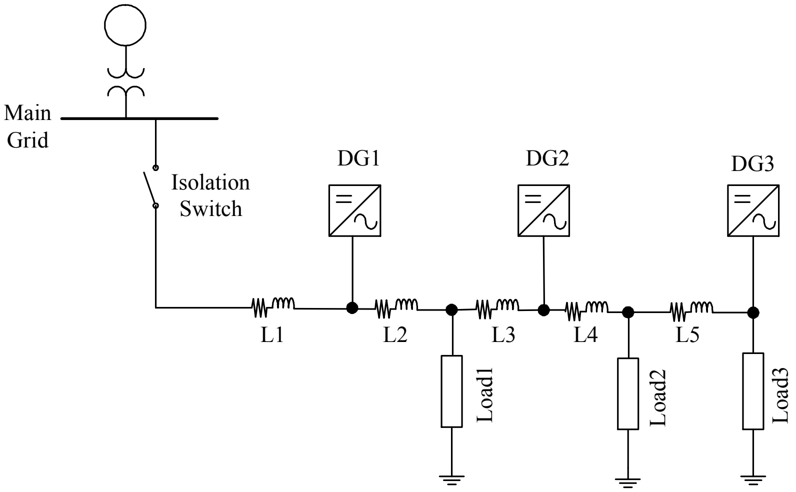

Figure 6.4: Micro-grid study system.

from of

$$\Delta\dot{\boldsymbol{x}} = \boldsymbol{A}\Delta\boldsymbol{x} + \boldsymbol{B}\Delta\boldsymbol{u}. \tag{6.20}$$

For the system under study, the state vector of the micro-grid in (6.20) includes the states of the three inverters and the line and load states (determined by the number of energy storage elements in the network).

Figure 6.5 shows the complete modes of the micro-gird study system, obtained at the steady-state initial operating conditions (0.7 p.u. loading of the micro-grid), which are evaluated by means of load flow analysis. Figure 6.5 indicates that wide band of dynamic modes can be observed in the micro-grid system. The frequency-scale separation between different modes is expected due to the time-scale separation between different control loops. The low-frequency modes are mainly dictated by the power-sharing controllers and the power filters, which are designed with low bandwidth (about 2-10 Hz). The medium-frequency modes are mainly dictated by the voltage control loops, which are designed with medium bandwidth (400-600 Hz). The high-frequency modes are dictated by the T-filters and the current control loops, which should be designed with high resonance frequencies (1-3 kHz).

It should be noted that the aforementioned frequency/time separation is necessary and intentionally designed in a typical inverter system. For a given switching frequency, which is mainly dictated by the inverter's rating to constraint the switching losses, the maximum bandwidth of the inner current control loop is determined accordingly. On the other hand, the resonance frequency of the ac filter should be designed with enough margins from the first switching frequency to avoid any harmonic resonance at the

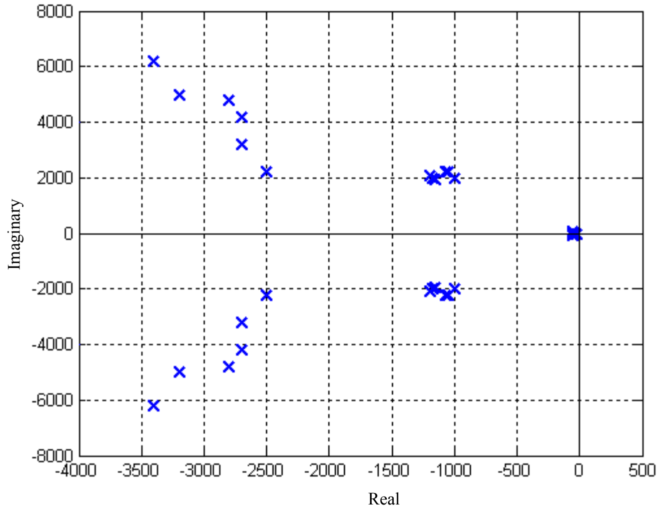

Figure 6.5: Complete eigenvalues of micro-grid study system (0.7 p.u. loading).

switching frequency. At the same time, the resonance frequency should not be very low to avoid any low-order harmonic resonance due to grid-voltage harmonics. In case of high power inverters, the resonance frequency of the T-filter should be lower to provide better filtering properties. Under these practical design and cost constraints, a typical current-controlled DG inverter can be designed with a current control loop bandwidth of about 1.0-1.5 kHz for high and medium power inverters. Since micro-grid inverters should generate a regulated power, a voltage control loop is usually adopted to generate the reference current vector for the inner current loop. As a cascaded control system, the voltage control loop should be designed with a bandwidth that is at least 4-5 times slower than that of the inner current loop to preserve the stability and tracking resolution of the reference current command. The outermost control loop, which is the power control loop, should be designed with much lower bandwidth for two reasons. First, in case of grid- or micro-grid-connected inverters, the average power control is adopted to ensure high power quality injection[1]. In this case, the outer power control loop should offer a relatively slowly changing reference voltage vector. Second, to extract the average power components from the measured dq instantaneous power components, low pass filters with low cut-off frequencies should be designed. As a result, the outer average power control loop will roughly designed with a bandwidth in the range of 2-10 Hz. The frequency separation is a salient feature that inherently exists in a well-designed inverter system. Even with different inverters, the frequency separation between different dy-

---

[1] On the contrary, instantaneous and direct power control techniques offer a relatively high bandwidth, and they are more suitable for active power conditioners and active rectifiers.

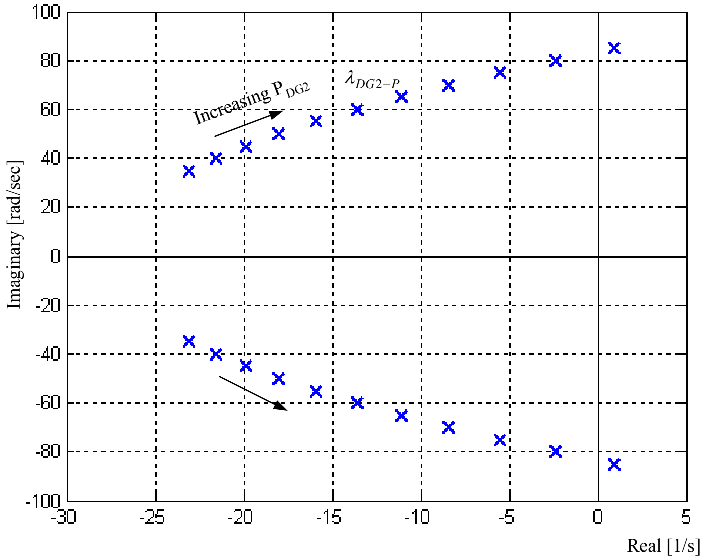

Figure 6.6: Dominant low-frequency modes of DG2 with increasing output active power.

namic modes will inherently exist. It should be noted that the power response time with the conventional droop controller might not be the same for different inverters within the micro-grid. This is due to the setting of the droop gains according to the regulation requirements and the inverter ratings. In other words, the power ramping time of different inverter-based generators will not be the same. From the micro-grid operation perspective, more robust control performance can be achieved when different units operate with close power response times that can be also controlled without affecting the regulation performance. This is one of the main objectives of the proposed micro-grid control scheme.

Figure 6.5 reveals that the power sharing states dictate the dominant dynamics of the micro-grid system.

Figure 6.6 shows a trace of the dominant low-frequency mode of DG2, which can be evaluated using eigen-sensitivity analysis, as the active output power of DG2 increases from 0.5 kW to 20 kW. It is clear in Figure 6.6 that the damping of the dominant low-frequency mode is highly dependent on the operating condition. Figure 6.6 indicates that the mode can be unstable by increasing the output power of the DG unit. Even with small changes around the operating point, the relative stability is remarkably affected; hence power oscillations and transient circulating currents are yielded.

The aforementioned sensitivity analysis confirms that the low-frequency modes are mainly dictated by the droop controller. Therefore, small signal analysis of the power-sharing droop controller can be a simplified tool to study the dominant dynamics of a micro-grid system.

The conventional droop control law given in (6.11) controls the angular frequency of the inverter as a function of the real power output, under the conventional decoupling principle. The phase angle between the inverter reference frame and the voltage vector at the PCC (the power angle) is controlled accordingly to specify the amount of power transfer. The power transfer equation that relates the average active output power to the power angle of the inverter can be given as follows:

$$P = \frac{V_o V_s \sin(\delta_o - \delta_s)}{X_c} \tag{6.21}$$

$$(\delta_o - \delta_s) = \int (\omega_o - \omega_s) dt \tag{6.22}$$

where V_o and V_s are the magnitudes of the inverter output voltage and the PCC voltage, respectively; δ_o and δ_s are the phase angle of the inverter output voltage and the PCC voltage vectors, respectively; and X_c is the reactance of the coupling inductor.

The small signal model of (6.11), (6.21), and (6.22) can be constructed around an operating point (δ_o^o, δ_s^o, V_o^o, V_s^o) as follows:

$$\Delta P(s) = \frac{H_P}{s + mH_p} \Delta\omega^* - \frac{H_P}{s + mH_p} \Delta\omega_s \tag{6.23}$$

$$H_P = \frac{V_o^o V_s^o \cos(\delta_o^o - \delta_s^0)}{X_c}. \tag{6.24}$$

From (6.11) and (6.23) it can be concluded that the droop gain m influences both the regulation and dynamic performance of the linearized active power transfer mechanism. The eigenvalue of (6.23) is given by

$$\lambda_{Po} = -mH_P. \tag{6.25}$$

If the droop gain is selected according to the regulation requirements, the eigenvalue in (6.25) will be directly determined by the operating condition. Accordingly, the damping of the dominant modes will be dependant on the output power, and the eigenvalue immigration will be significant as shown in Figure 6.6. It can be seen that the conventional droop controller lacks the ability of controlling the damping of the low-frequency power modes at different operating conditions without affecting the frequency regulation, which is a stiff requirement at steady-state operation.

The output voltage magnitude of the inverter is drooped as a function of the injected reactive power as shown in (6.12). The relation between the voltage magnitude V_o and the corresponding output reactive power Q can be given by:

$$Q = \frac{V_o^2 - V_o V_s \cos(\delta_o - \delta_s)}{X_c}. \tag{6.26}$$

The small signal model of (6.12) and (6.26) can be constructed around an operating point (δ_o^o, δ_s^o, V_o^o, V_s^o) as follows:

$$\Delta Q(s) = \frac{H_Q}{1+nH_Q}\Delta V^*(s) + \frac{H_{Q2}}{1+nH_Q}\Delta V_s(s) \tag{6.27}$$

$$H_Q = \frac{2V_o^o - V_s^o\cos(\delta_o^o - \delta_s^0)}{X_c} \tag{6.28}$$

$$H_{Q2} = \frac{-V_o^o\cos(\delta_o^o - \delta_s^0)}{X_c}. \tag{6.29}$$

From (6.12) and (6.27) it can be concluded that the regulation performance is controllable by the droop gain n, whereas the dynamic performance of the linearized reactive power transfer mechanism is not controllable.

It should be noted that (6.25) shows that the eigenvalues of the active power-sharing dynamics are real. However, due to the presence of the power filters (with a fixed pole in the s-domain as given in (6.9) and (6.10)), and the weak effect of coupling among power components, a third order small-signal dynamics will characterize the power angle response. However, the damping is dominantly governed by (6.25) due to the dominant low damping nature of the sinusoidal P-δ dynamics, particularly at large power angle swings. To confirm this fact, let us consider the effects of the power filters and the P-Q coupling on the power angle dynamics. The coupled small-signal power transfer dynamics, around an operating point (δ_o^o, δ_s^o, V_o^o, V_s^o), can be constructed as follows:

$$\begin{bmatrix} \Delta P(s) \\ \Delta Q(s) \end{bmatrix} = \begin{bmatrix} \left(\frac{\partial P}{\partial(\delta_o-\delta_s)}\right)_o & \left(\frac{\partial P}{\partial V_o}\right)_o \\ \left(\frac{\partial Q}{\partial(\delta_o-\delta_s)}\right)_o & \left(\frac{\partial Q}{\partial V_o}\right)_o \end{bmatrix} \begin{bmatrix} \Delta\left(\delta_o - \delta_s\right)(s) \\ \Delta V_o(s) \end{bmatrix}. \tag{6.30}$$

Since the calculated power components are low-pass-filtered to extract the average power components, then the filter effect can be incorporated in (6.30) as follows:

$$\begin{bmatrix} \Delta P_{av}(s) \\ \Delta Q_{av}(s) \end{bmatrix} = \begin{bmatrix} \frac{\omega_c}{s+\omega_c} & 0 \\ 0 & \frac{\omega_c}{s+\omega_c} \end{bmatrix} \begin{bmatrix} \left(\frac{\partial P}{\partial(\delta_o-\delta_s)}\right)_o & \left(\frac{\partial P}{\partial V_o}\right)_o \\ \left(\frac{\partial Q}{\partial(\delta_o-\delta_s)}\right)_o & \left(\frac{\partial Q}{\partial V_o}\right)_o \end{bmatrix} \begin{bmatrix} \Delta\left(\delta_o - \delta_s\right)(s) \\ \Delta V_o(s) \end{bmatrix}. \tag{6.31}$$

By adding the droop functions to (6.31), the following dynamics can be obtained:

$$\begin{aligned} \begin{bmatrix} \Delta\omega_o(s) \\ \Delta V_o(s) \end{bmatrix} = \begin{bmatrix} \Delta\omega^*(s) \\ \Delta V^*(s) \end{bmatrix} &+ \begin{bmatrix} \frac{-m\omega_c}{s+\omega_c} & 0 \\ 0 & \frac{-n\omega_c}{s+\omega_c} \end{bmatrix} \\ &\times \begin{bmatrix} \left(\frac{\partial P}{\partial(\delta_o-\delta_s)}\right)_o & \left(\frac{\partial P}{\partial V_o}\right)_o \\ \left(\frac{\partial Q}{\partial(\delta_o-\delta_s)}\right)_o & \left(\frac{\partial Q}{\partial V_o}\right)_o \end{bmatrix} \begin{bmatrix} \frac{\Delta\omega_o(s)-\Delta\omega_s(s)}{s} \\ \Delta V_o(s) \end{bmatrix}. \end{aligned} \tag{6.32}$$

Then the dynamics of (6.32) is governed by the following characteristic equation:

$$s^3\Delta\omega_o(s) + \alpha s^2\Delta\omega_o(s) + \beta s\Delta\omega_o(s) + \gamma\Delta\omega_o(s) = 0 \tag{6.33}$$

where

$$
\begin{aligned}
\alpha &= \omega_c \left(n \left(\frac{\partial Q}{\partial V_o} \right)_o + 2 \right) \\
\beta &= \omega_c \left(n \omega_c \left(\frac{\partial Q}{\partial V_o} \right)_o + m \left(\frac{\partial P}{\partial \left(\delta_o - \delta_s \right)} \right)_o + \omega_c \right) \\
\gamma &= m \omega_c^2 \left(n \left(\frac{\partial P}{\partial \left(\delta_o - \delta_s \right)} \right)_o \left(\frac{\partial Q}{\partial V_o} \right)_o + \left(\frac{\partial P}{\partial \left(\delta_o - \delta_s \right)} \right)_o - n \left(\frac{\partial P}{\partial V_o} \right)_o \left(\frac{\partial Q}{\partial \left(\delta_o - \delta_s \right)} \right)_o \right).
\end{aligned}
$$

Further, the sensitivity functions can be obtained as follows:

$$\left(\frac{\partial P}{\partial \left(\delta_o - \delta_s \right)} \right)_o = \frac{V_o^o V_s^o X_c \cos\left(\delta_o^o - \delta_s^o \right) + V_o^o V_s^o R_c \sin\left(\delta_o^o - \delta_s^o \right)}{R_c^2 + X_c^2} \tag{6.34}$$

$$\left(\frac{\partial P}{\partial V_o} \right)_o = \frac{V_s^o X_c \sin\left(\delta_o^o - \delta_s^o \right) - V_s^o R_c \cos\left(\delta_o^o - \delta_s^o \right) + 2 V_o^o R_c}{R_c^2 + X_c^2} \tag{6.35}$$

$$\left(\frac{\partial Q}{\partial V_o} \right)_o = \frac{2 V_o^o X_c - V_s^o X_c \cos\left(\delta_o^o - \delta_s^o \right) - V_s^o R_c \sin\left(\delta_o^o - \delta_s^o \right)}{R_c^2 + X_c^2} \tag{6.36}$$

$$\left(\frac{\partial Q}{\partial \left(\delta_o - \delta_s \right)} \right)_o = \frac{V_o^o V_s^o X_c \sin\left(\delta_o^o - \delta_s^o \right) - V_o^o V_s^o R_c \cos\left(\delta_o^o - \delta_s^o \right)}{R_c^2 + X_c^2}. \tag{6.37}$$

Using (6.33), the damping of the dominant eigenvalues can be traced along the whole loading trajectory. The obtained damping characteristics can be compared to these obtained by using (6.25). Note that the eigenvalue in (6.25) exactly describes the small signal dynamics of $\Delta\omega_o(s)$ when it is derived from (6.23).

Figure 6.7 depicts the damping of the dominant low-frequency mode as the active output power of DG2 increases from 0.5 kW to 20 kW by using (6.33) and (6.25). The close matching between both results confirms that a micro-grid system can be stabilized by means of an active damping feature in the power sharing-controller of each DG unit.

6.4 Proposed Power-Sharing Scheme

To overcome the aforementioned difficulties, a newly designed power-sharing scheme is proposed. The power-sharing controller adopts a modified droop function with controllable gain transient droop characteristics. This configuration leads to a two-degree-of-freedom tunable controller, where the droop gain is selected to determine the frequency/voltage regulation performance and the transient gains can be adaptively tuned to damp the oscillatory modes at different operating conditions.

To provide means of adaptive active damping of the low-frequency power-sharing modes, and to increase the controllability of the reactive power sharing-controller, the

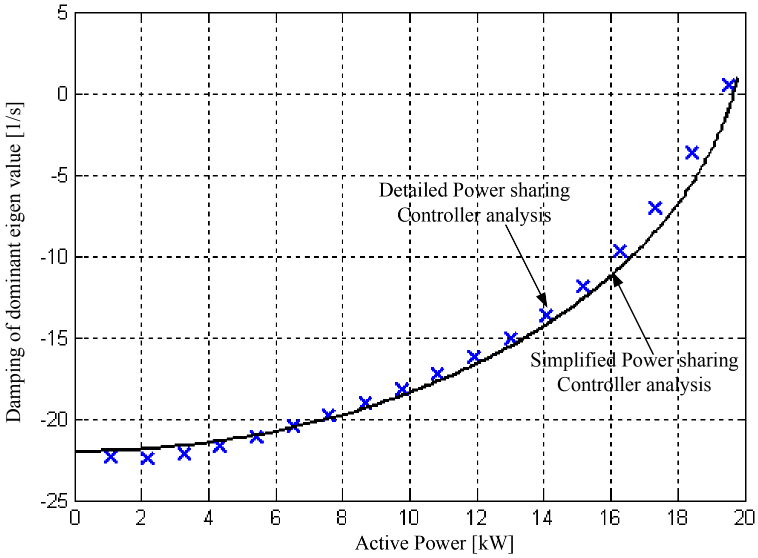

Figure 6.7: Damping of the dominant low-frequency mode of DG2 with increasing the output active power: detailed power-sharing controller and simplified power sharing controller small signal analysis.

following droop functions are proposed:

$$\omega_o = \omega^* - mP - \hat{m}_d \frac{dP}{dt} \tag{6.38}$$

$$v_{od}^* = V^* - nQ - \hat{n}_d \frac{dQ}{dt} \tag{6.39}$$

where $\hat{m}_d$ and $\hat{n}_d$ are adaptive transient droop gains.

The proposed droop functions employ additional derivative terms with adaptive gains. With this configuration, the power angle dynamics will be controlled in (6.38) with an equivalent PI control dynamics. Furthermore, the adaptation of the transient droop gain shapes the dynamic performance of the equivalent control dynamics in a manner that preserves the power sharing stability. The simplicity of the PI structure enables a simple first order equivalent dynamics, where the adaptation mechanism can be derived as a pole placement problem. Similar observations can be extended to the proposed voltage droop function reported in (6.39). Accordingly, the above droop functions have been specifically selected [116]. In what follows, a small-signal analysis will be presented to prove the salient features of the proposed controller in achieving robust power-sharing performance with a simple structure and easily-derived adaptation gains.

The small signal model of (6.38), (6.21) and (6.22) can be constructed around an operating point (δ_o^o, δ_s^o, V_o^o, V_s^o) as follows:

$$\Delta P(s) = \frac{H_P}{\left(1 + \hat{m}_d H_P\right) s + m H_P} \Delta\omega^* - \frac{H_P}{\left(1 + \hat{m}_d H_P\right) s + m H_P} \Delta\omega_s. \tag{6.40}$$

From (6.38) and (6.40) it can be seen that the regulation performance is decoupled from the dynamic performance of the linearized active power transfer mechanism. The eigenvalue of (6.40) is

$$\lambda_P = \frac{-mH_P}{1+\hat{m}_d H_P}. \tag{6.41}$$

Therefore, the desired dynamic performance can be achieved by varying $\hat{m}_d$ without affecting the steady-state regulation performance.

Similarly, the small signal model of (6.39) and (6.26) can be constructed around an operating point (δ_o^o, δ_s^o, V_o^o, V_s^o) as follows:

$$\Delta Q(s) = \frac{H_Q}{\hat{n}_d H_Q s + (1+nH_Q)} \Delta V^*(s) + \frac{H_{Q2}}{\hat{n}_d H_Q s + (1+nH_Q)} \Delta V_s(s). \tag{6.42}$$

The eigenvalue of (6.42) is

$$\lambda_Q = \frac{-(1+nH_Q)}{\hat{n}_d H_Q}. \tag{6.43}$$

which implies that the dynamic performance of the reactive power-sharing controller can be adjusted by $\hat{n}_d$ without compromising the voltage regulation performance dictated by n.

Using (6.41) and (6.43), the adaptive gains $\hat{m}_d$ and $\hat{n}_d$ can be simply scheduled by means of pole placement technique, mainly to adjust the damping of the active and reactive power-sharing controllers along the loading trajectory.

Figure 6.8(a) shows a trace of $\hat{m}_d$ as a function of the output active power of DG2 to fix the damping of the active power-sharing dynamics at -50 s^{-1}. It can be shown that the gain increases at high power levels to impose the additional damping required to constraint the dynamic performance of the active power-sharing controller. Similarly, the adaptive gain $\hat{n}_d$ can be scheduled along the reactive power-loading trajectory. Figure 6.8(b) shows the gain schedule of $\hat{n}_d$ for DG2. The gain schedules of $\hat{m}_d$ and $\hat{n}_d$ utilize the static droop gains, which are fixed for each inverter unit, the preset eigenvalues, which are design parameters, and the value of the coupling reactance X_c. The robustness against the uncertainty in X_c (90% X_{co} to 110% X_{co}, where the subscript "o" denotes the nominal value) is investigated as shown in Figure 6.8. It can be noticed that both the gain schedules show small sensitivity to the uncertainty in X_c. Accordingly, even with considerable variations in X_c, the damping of the power-sharing modes will drift slightly from the preset values that are used to generate the gain schedules.

6.5 Results

To evaluate the performance of the proposed control scheme, the micro-grid study system - depicted in Figure 6.3 - has been used. The system parameters are given in Appendix

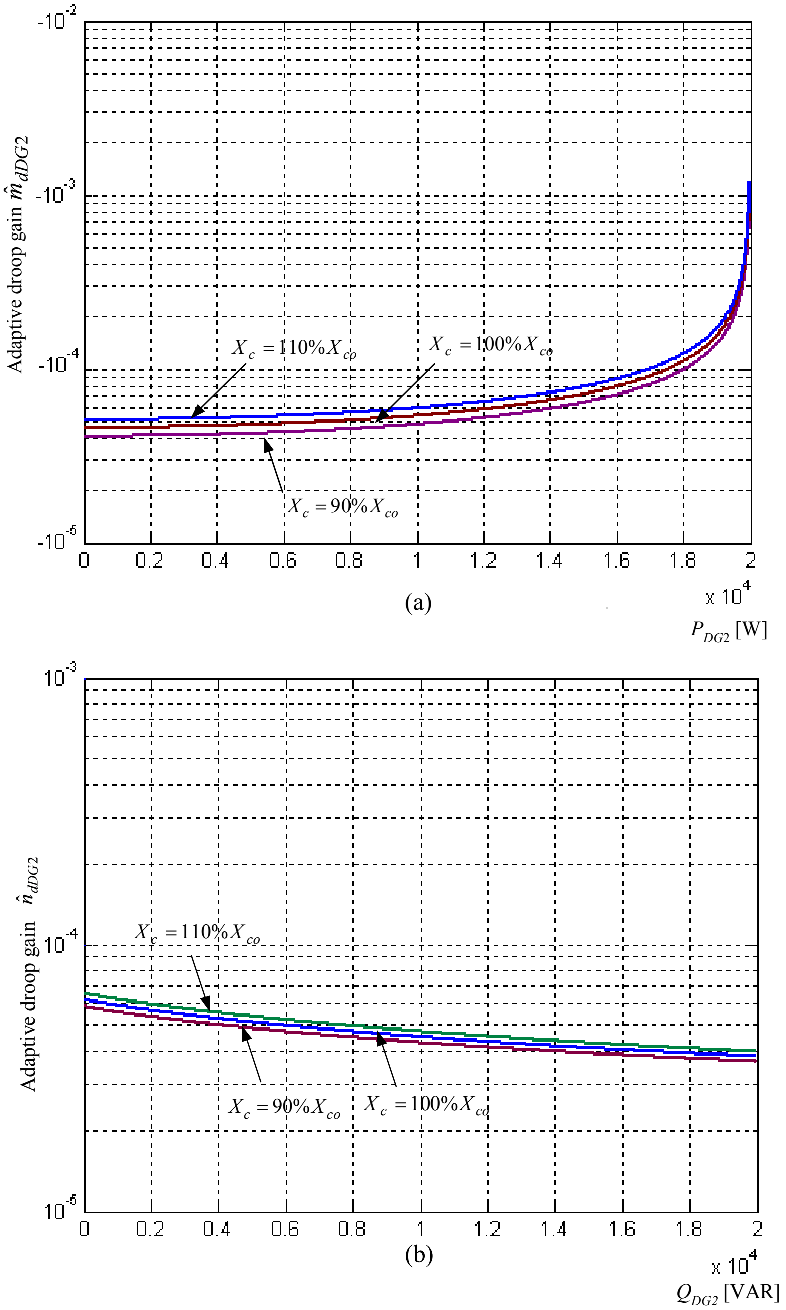

Figure 6.8: Gain schedules of DG2. (a) $\hat{m}_d$. (b) $\hat{n}_d$.

B. Each inverter unit employs the power circuit and control structure as depicted in Figure 6.2. The system is simulated under Matlab/Simulink environment. A control period T=150 μs is selected. With this setting, a switching frequency 6.7 kHz has been obtained. The current and voltage control loops are designed to yield bandwidth characteristics of 1.5 kHz and 0.5 kHz, respectively.

To verify the feasibility of the proposed controller, different operating conditions have been considered. For the purpose of performance comparison, the proposed control scheme is compared to the conventional droop controller. Some selected results are presented as follows.

A step change of 8 kW /3 kVAR increase in load2 is considered. Figure 6.9 shows the active power sharing performance of different DG units. The low damping of the dominant power-sharing modes leads to a large transient response and oscillatory performance in the injected powers. For example, the power oscillations occur around 8 Hz with a damping around 7 s^{-1} for DG2; these results closely match the small-signal analysis results reported in Figures 6.6 and 6.7. Since DG2 is the closest to the load, the power performance of DG2 exhibits the largest transient response and it supplies most of the transient power due to the proximity to the load. For large power transients, the unit protection might be activated and the micro-grid might not be able to maintain the load; hence the overall system stability can be violated. Figure 6.10 shows the reactive power sharing performance of different DG units. The total reactive power generation exceeds the load demand by 0.65 kVAR due to the reactive power requirement of the network lines and coupling filters of different DG units. The low-frequency modes can be traced in the injected reactive powers. However, they are less severe than those observed in the active power injections. This is due to the absence of the eigenvalue immigration problem in the conventional droop controller as shown in (6.27).

Figure 6.11 shows the start-up phase-a current of DG2 with the conventional droop-controller with 85% loading factor of DG2. It is obvious that the poorly damped power response leads to large transient currents that might overload the unit and activate the unit protection.

Under the same load disturbance, 8 kW/3 kVAR increase in load2, the proposed power-sharing controller is tested. Figure 6.12(a),(c),(e) shows the active power sharing performance of different DG units. It can be observed that the transient response is well damped and smooth power injection is yielded. Further, the load power is accurately shared according to the ratings of different generators. Figure 6.12(b),(d),(f) shows the corresponding adaptive active droop gains of different DG units. Depending on the injected average active power, the $\hat{m}_d$ gain is adjusted to preserve a well damped dynamic performance for each DG unit. Since the average power is used as an index

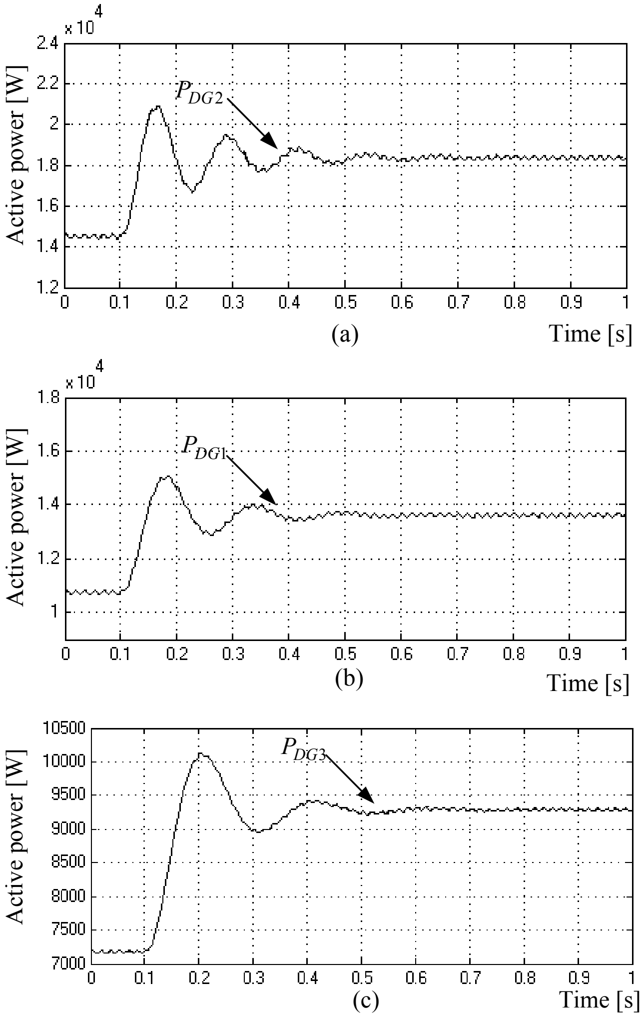

Figure 6.9: Active power response of different DG units due to step change in load2 with the conventional droop controller.

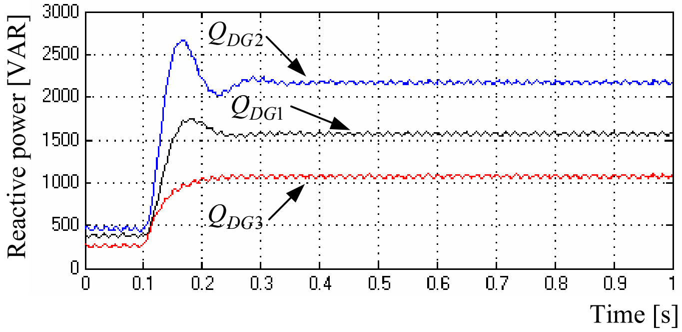

Figure 6.10: Reactive power response of different DG units due to step change in load2 with the conventional droop controller.

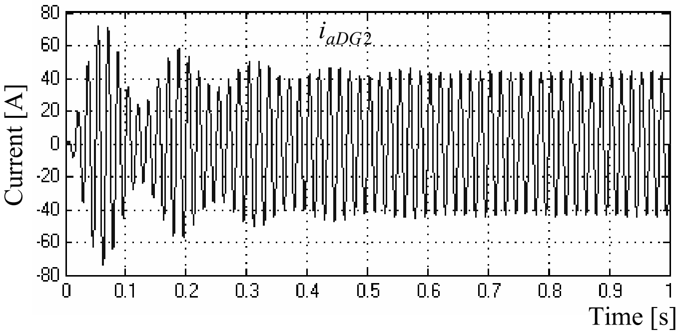

Figure 6.11: Start-up current of DG2 with the conventional droop controller.

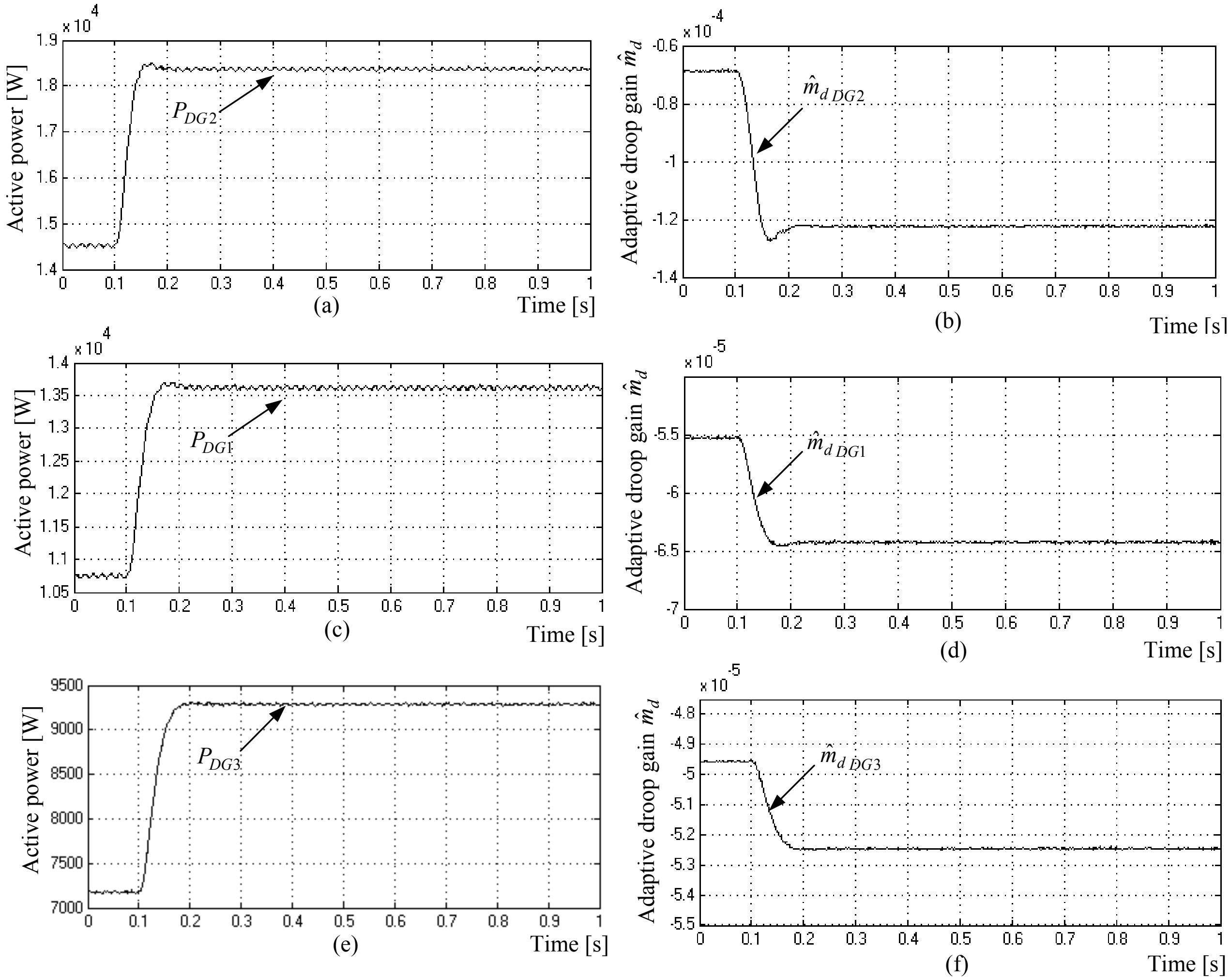

Figure 6.12: Active power-sharing performance with the proposed controller due to step change in load2. (a), (c), (e) Active power responses of different DG units, (b), (d), (f) Corresponding adaptive active droop gains of different DG units.

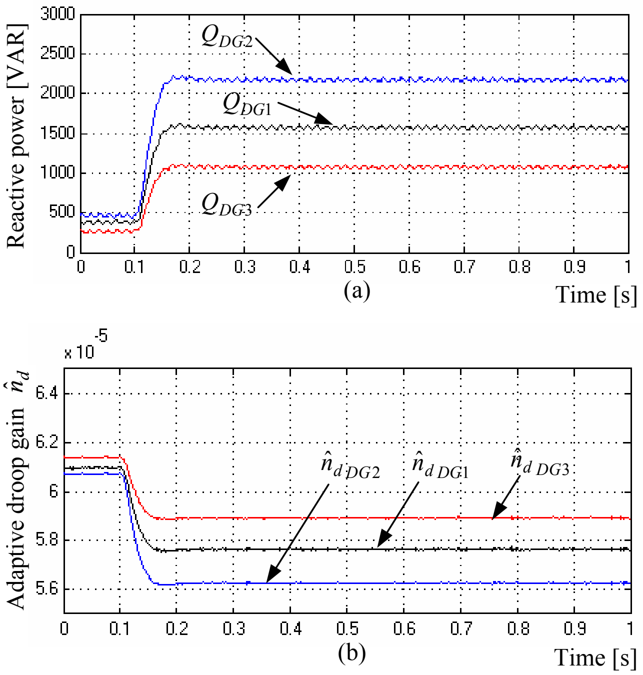

Figure 6.13: Reactive power-sharing performance with the proposed controller due to step change in load2. (a) Reactive power responses of different DG units. (b) Corresponding adaptive reactive droop gains of different DG units.

for adaptation, smooth gain adaptation with high noise immunity is yielded for different DG units as depicted in Figure 6.12(b), (d), (f).

Figure 6.13 shows the reactive power sharing performance with the proposed controller. Figure 6.13(a) shows the reactive power responses of different DG units. Damped reactive power sharing performance is yielded. Further, it can be noticed that the dynamic performance, in terms of the rise time, has been unified for different DG units. Figure 6.13(b) shows the corresponding adaptive reactive droop gains of different DG units. Depending on the injected average active power, the $\hat{n}_d$ gain is adjusted to preserve a well damped dynamic performance for each DG unit.

Due to the damped transient response of the proposed controller, the transient start-up currents can be significantly suppressed. This is obvious in Figure 6.14, which depicts the start-up phase-a current of DG2 using the proposed power-sharing controller.

6.6 Summary

An adaptive decentralized droop-based power-sharing control scheme for paralleled inverters in DG micro-grids has been presented in this chapter. The proposed control

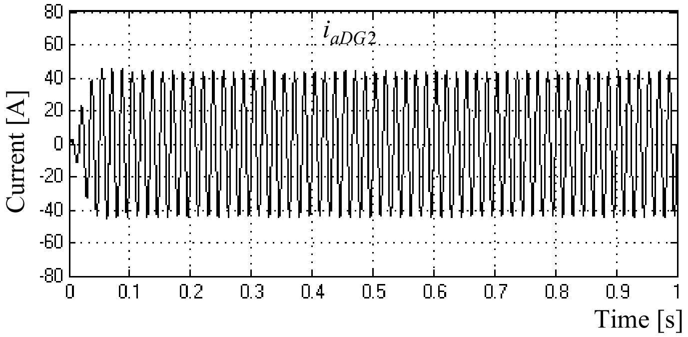

Figure 6.14: Start-up current of DG2 with the proposed power-sharing controller.

structure preserves the dynamics and stability of each inverter unit at different loading conditions. The proposed power-sharing strategy is based on the static droop characteristics combined with an adaptive transient droop function. Unlike conventional droop controllers, which yield one-degree-of-freedom tunable controller, the proposed droop controller yields two-degree-of-freedom tunable controller. Subsequently, the dynamic performance of the power-sharing mechanism can be adjusted, without affecting the static droop gain, to damp the oscillatory modes of the power-sharing controller. To account for the power modes immigration at different loading conditions, the transient droop gains have been adaptively tuned via small signal analysis of the power-sharing mechanism along the operation trajectory of each DG unit to yield the desired transient and steady-state responses. Theoretical analysis and simulation results reveal that the adaptive nature of the proposed controller ensures active damping of power oscillations at different operating conditions; subsequently, stable and robust power-sharing performance has been obtained in the paralleled inverter system. As a result, the proposed scheme significantly contributes to preserving micro-grid stability and reliability.

Chapter 7

A Robust Bidirectional DG Interface for Grid-Connected and Micro-Grid Systems

7.1 Introduction

With higher penetration of clean and renewable energy sources, stricter demands for grid-connection and islanded operation are needed. In particular, there is a strong need to develop a robust DG interface that guarantees stable and high power quality injection under the grid-connected and micro-grid modes. Since DG units are usually installed in weak grids, the DG interface should offer high robustness against grid disturbances. These disturbances include harmonic distortion, unbalance, fast and slow voltage disturbances, parameter variation, and uncertain dynamic interactions between the DG interface and the grid. On the other hand, the small size of a micro-grid system and the high penetration of inverter-based DG units (fuel cells, micro-turbines, photovoltaic arrays, and full-scale converter-based wind turbines) make a micro-grid system potentially susceptible to oscillation resulting from system disturbances. Severe and random disturbances might be initiated in a micro-grid system, due to load changes, the power sharing mechanism of micro-grid generators, and interactions between the DG interface and the network.

Through the previous chapters, it can be noticed that a “divide and conquer” approach has been utilized to design new control algorithms for the DG interface to mitigate wide range of critical DG integration problems. In this chapter, the developed control algorithms are integrated to realize a novel and robust DG interface that broadly addresses the aforementioned integration issues in gird-connected and micro-grid systems.

The residual part of this chapter is organized as follows. In Section 7.2, the conceptual design and overall structure of the proposed robust DG interface is presented. In Section 7.3, case studies with evaluation results are presented to demonstrate the effectiveness of the proposed interface. A summary is drawn in Section 7.4.

7.2 Conceptual Design and Overall Structure of the Proposed Robust DG Interface

Figure 7.1 depicts the control structure of the proposed DG interface for grid-connected and micro-grid DG systems. As presented in Chapter 3, the newly designed deadbeat current control algorithms can handle both the current tracking and grid distortion suppression tasks. In addition, instabilities due to mismatches in the interfacing parameters are handled by the current control scheme. As the core algorithm in the DG interface, the developed current controls offer a powerful control infrastructure for the outer loops. For example, the high bandwidth feature allows fast and accurate current tracking and current profiling without increasing the inverter switching frequency. This feature facilitates the design of a fast load-voltage control scheme. On the other hand, accurate and fast current control minimizes the coupling among current, voltage, and power control loops; this is an important feature in micro-grid stability. Further, the proposed current control scheme is characterized by a fixed switching frequency. This is a key factor in determining the power-quality-based penetration limit of DG.

To realize the favorable feature of grid-voltage sensorless control, the grid-interface monitoring unit, presented in Chapter 4, facilitates accurate and fast estimation of the interfacing impedance parameters and the grid voltage vector (magnitude and position) at the point of common coupling. The estimated grid voltage can be utilized to realize a grid-voltage sensorless interfacing scheme, whereas the interfacing parameters can be utilized for the self-tuning control to realize an adaptive DG interface. Further, the developed generalized integrator-based fundamental gird-voltage and frequency estimation method yields accurate information of the fundamental grid-voltage vector in a simple way. The robustly estimated voltage and frequency can be reliably used in islanding detection. The response time of the fundamental positive-sequence grid voltage component is determined by the resonant filter gain. This time separation yields an insensitive interface system to random and very-short grid disturbances; and hence, overcomes inopportune islanding events. This is a crucial feature that must exist in a robust DG interface featuring a fault-ride-through capability. On the other hand, the control structure is fast enough to allow islanding detection and protection tripping, if required.

The reference current vector is generated according to the operation mode. In grid-connected mode, the generation control block generates the active and reactive reference current trajectories. The generation control and the voltage control can be augmented in grid voltage control mode. The new dual-sequence hybrid linear with variable-structure voltage control scheme, which is detailed in Chapter 5, enables close voltage regulation characteristics. The variable-structure controller can reject a wide band of frequency modes through an equivalent internal model with minimized chattering. When combined with the proposed high bandwidth current controller, fast voltage regulation with effective mitigation of fast voltage disturbance becomes feasible. Furthermore, the presence of the negative sequence controller allows fast mitigation of unbalanced voltage disturbances. Provided that there is enough reactive power rating, the proposed interface can over-ride large unbalanced voltage disturbances initiated by up-stream grid faults. Inherently, small and mild voltage unbalances, which are caused by the uneven distribution of single-phase loads and the diversity in their demands, can be mitigated. Since the proposed voltage control scheme enables effective mitigation of fast voltage disturbances, it can be considered as a universal solution to voltage quality problems, where voltage sag, swell and flicker can be inherently mitigated.

In the micro-grid mode, the autonomous power sharing controller and the load voltage controller generate the reference current vector. With the proposed current and voltage control schemes, robust current and voltage control performance can be yielded in a micro-gird system. However, to constrain the drift of the low frequency modes caused by the power-sharing controller, a new transient-based droop controller with adaptive gain is proposed. As presented in Chapter 6, the dynamic performance of the proposed decentralized power sharing mechanism can be adjusted, without affecting the static droop gain, to damp the oscillatory modes of the power-sharing controller. To account for the power modes immigration at different loading conditions, the transient droop gains have been adaptively tuned via small signal analysis of the power-sharing mechanism along the operation trajectory of each DG unit to yield the desired transient and steady state response. The adaptive nature of the proposed controller ensures active damping of power oscillations at different operating conditions; subsequently, stable and robust power-sharing performance is obtained in the paralleled inverter system. The direct result is reserving the micro-grid stability and reliability.

The proposed control scheme, reported in Figure 7.1, is applied to a dispatchable DG source. It can be extended to non-dispatchable inverter-based sources by replacing the active power controller by a dc-link-voltage controller. Figure 7.2 shows the proposed DG interface for a non-dispacthable inverter-based DG unit. Since the reliability of non-dispatchable generation is limited, a micro-grid-based islanded operation of these resources is not desirable.

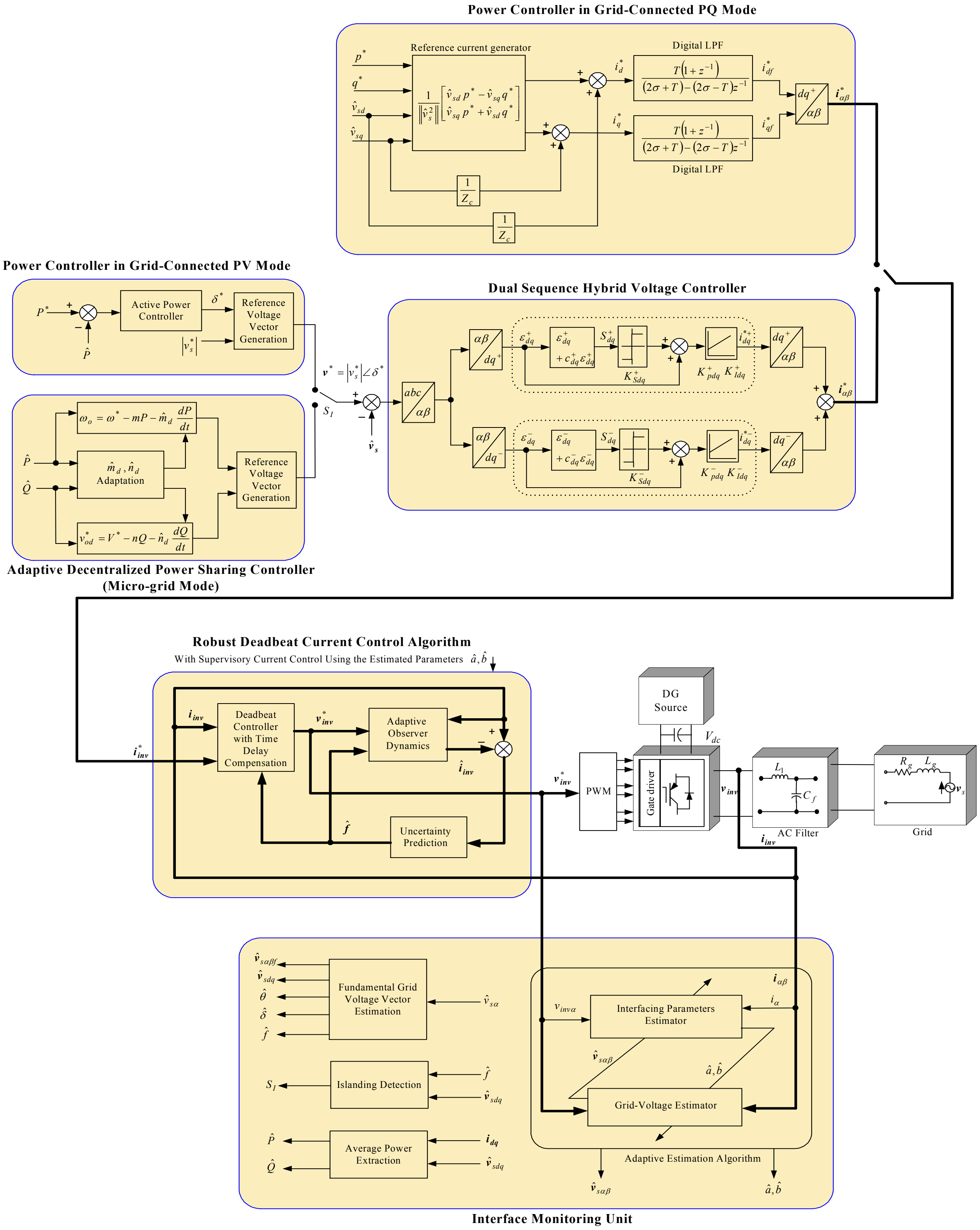

Figure 7.1: Proposed control structure for the DG interface.

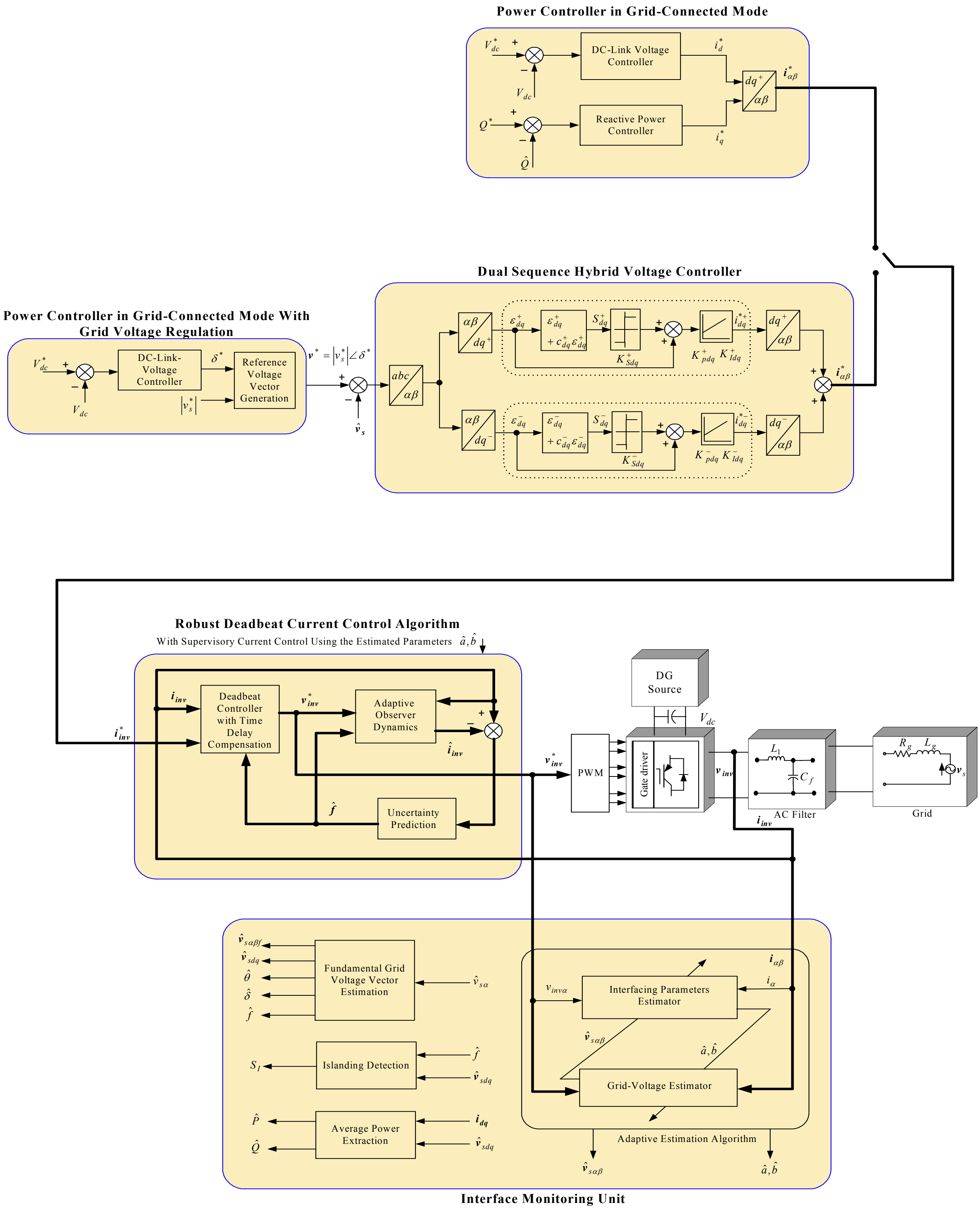

Figure 7.2: Proposed control structure for non-dispatchable sources.

7.3 Case Studies and Results

To evaluate the performance of the proposed DG interface in grid-connected and micro-grid systems, a study system that is adapted from the benchmark system of the IEEE Standard 399-1997 [117] is used. Figure 7.3 shows a single-line diagram of the study system. The system consists of a radial distribution system that is connected to the sub-transmission network via a 69 kV line. The sub-transmission system is represented by a 1000 MVA short-circuit capacity bus with the X/R ratio of 22. The 69 kV/13.8 kV (Δ-Y) distribution substation transformer is rated at 15 MVA; which is the rated feeder capacity. The substation has a 0.5 MVAR shunt capacitor for reactive power compensation. To account for nonlinear loads and grid-voltage unbalance, grid-voltage harmonics and voltage unbalance are considered at the bus under study when needed. The grid voltage harmonics considered as: 3% 5^{th} harmonic, 2% 7^{th} harmonic, and 1% 11^{th} harmonics, whereas the grid voltage unbalance factor is 4%. The network parameters, including the ratings and impedances of system components, are given in Figure 7.3.

In the grid-connected mode, a DG penetration limit of 22.6% is considered in the system under study. The system includes 4 inverter-based DG units. DG1 (0.7 MVA) operates as a PV generator, whereas DG2 (1.2 MVA) and DG3 (1.0 MVA) operate as PQ generators at unity power factor. DG4 (0.5 MVA) is a photovoltaic-based DG unit, which is connected via a current-controlled interface at a unity power factor. Loads $L1$ to $L5$ are considered as sensitive loads that should be serviced when the main grid is disconnected. It should be noted that synchronous-generator-based DG units can be utilized within a micro-grid system. However, it is shown in [18] that due to the time-scale separation between the inverter dynamics and the power-angle dynamics of a synchronous generator, inverter-based DG units have the main role in stabilizing a micro-grid system. Accordingly, an inverter-based micro-grid system is considered in the present case study.

Two main scenarios are considered:

1. Micro-grid formation is not allowed. In this scenario, DG units are allowed to operate under the grid-connected mode only. According to the IEEE Standard 1547 [45], an anti-islanding feature should be embedded in each DG unit. In this mode, the frequency is dictated by the main grid, to which DG units are synchronized. Further, the grid is considered as slack bus that meets the total demand of the feeder without DG installed. Similarly, the reactive power demand is supplied by the main grid and other utility-based reactive power source.

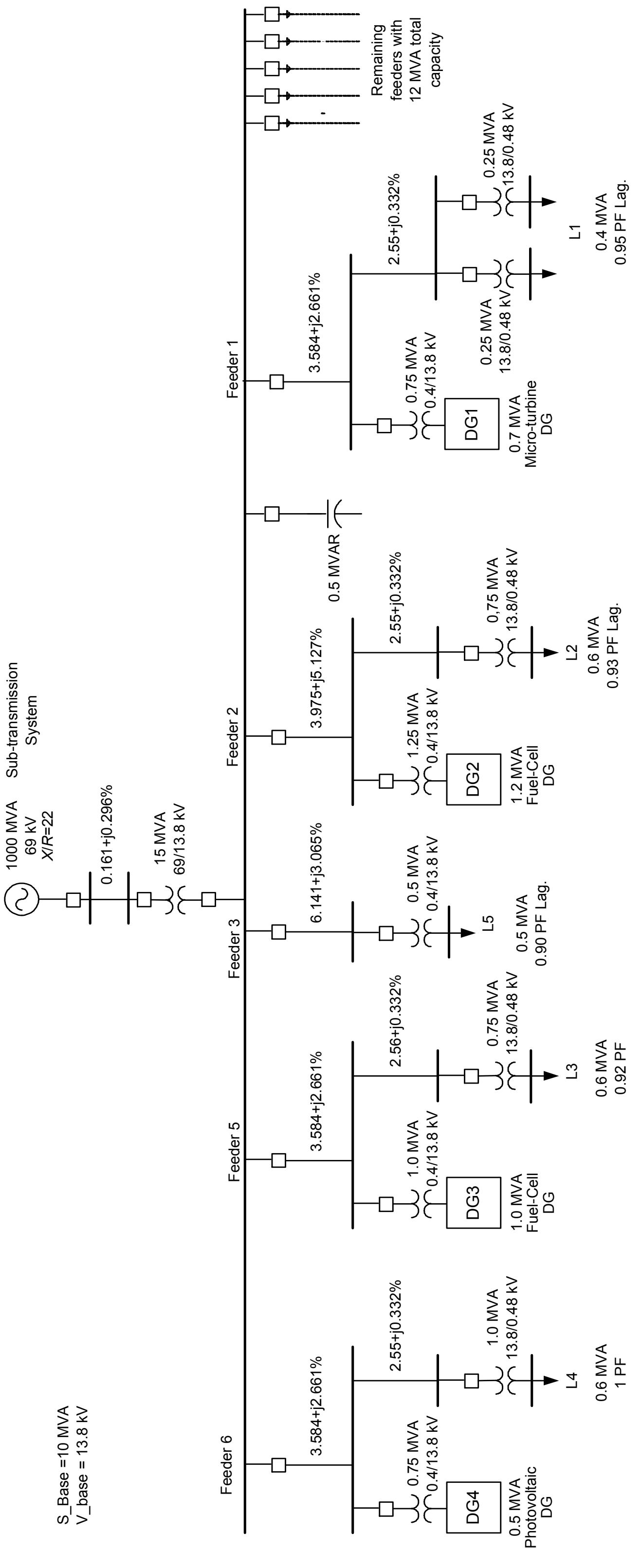

Figure 7.3: Single-line diagram of the study system.

2. Micro-grid formation is allowed. In this scenario, DG units are allowed to form a micro-grid when the main grid is disconnected. This scenario is based on a reliability enhancement objective for sensitive loads. To enhance the reliability of sensitive loads, existing DG units can be utilized as backup sources that can be operated within a micro-grid; basically when the main grid is not available. Agreements between the utility, DG owners, and sensitive-load-customers, can be conducted to allow micro-grid operation with a capacity that meets the sensitive loads. Other non-sensitive loads are assumed to be automatically disconnected by the under-voltage and under-frequency protection. Due to the reliability and power management issues of non-dispatchable sources (these sources are controlled based on an optimal power generation scheme to deliver the maximum available power, normally to a large system), only dispatchable DG units will be utilized in micro-grid operation. Accordingly, the total micro-grid capacity is 2.9 MVA and it is supplied by three DG units; namely DG1, DG2, and DG3.

The performance of the proposed control algorithms under the above scenarios is investigated. Some selected results, that complement the performance evaluation results presented in the previous chapters, are reported as follows.

7.3.1 Grid-Connected Mode

In this mode, the system frequency is dictated by the grid. The tracking and regulation performances of each DG unit are examined in the grid-connected mode.

Figure 7.4(a) shows the grid voltage at bus 1 with DG1 disabled. Grid voltage distortion and unbalance are obvious. In Figure 7.4(b), DG1 is switched on at t=0.0167 s (1 cycle) to regulate voltage at the PCC and to inject 450 kW to the grid. The fast regulation action of the proposed voltage control scheme along with it is ability to reject dynamic voltage disturbances yields close voltage regulation characteristics as shown in Figure 7.4(b). Figure 7.4(c) shows the corresponding current injected by DG2 (the magnitude is normalized to the rms value).

Figure 7.5(a) shows the voltage magnitude at bus 1 with zero grid distortion/unbalance and DG1 disabled, and with the substation capacitor switched on at t=0.045 s. The switching transient remarkably affects the voltage quality, where the maximum instantaneous voltage reaches 1.4 p.u. for about 4 ms, and the steady-state voltage rise is about 0.08 p.u. Figure 7.5(b) depicts the voltage magnitude at bus 1 when DG1 is enabled at t=0. Robust voltage control performance has been obtained, where the maximum instantaneous voltage does not exceed 1.1 p.u. with a zero steady-state voltage regulation.

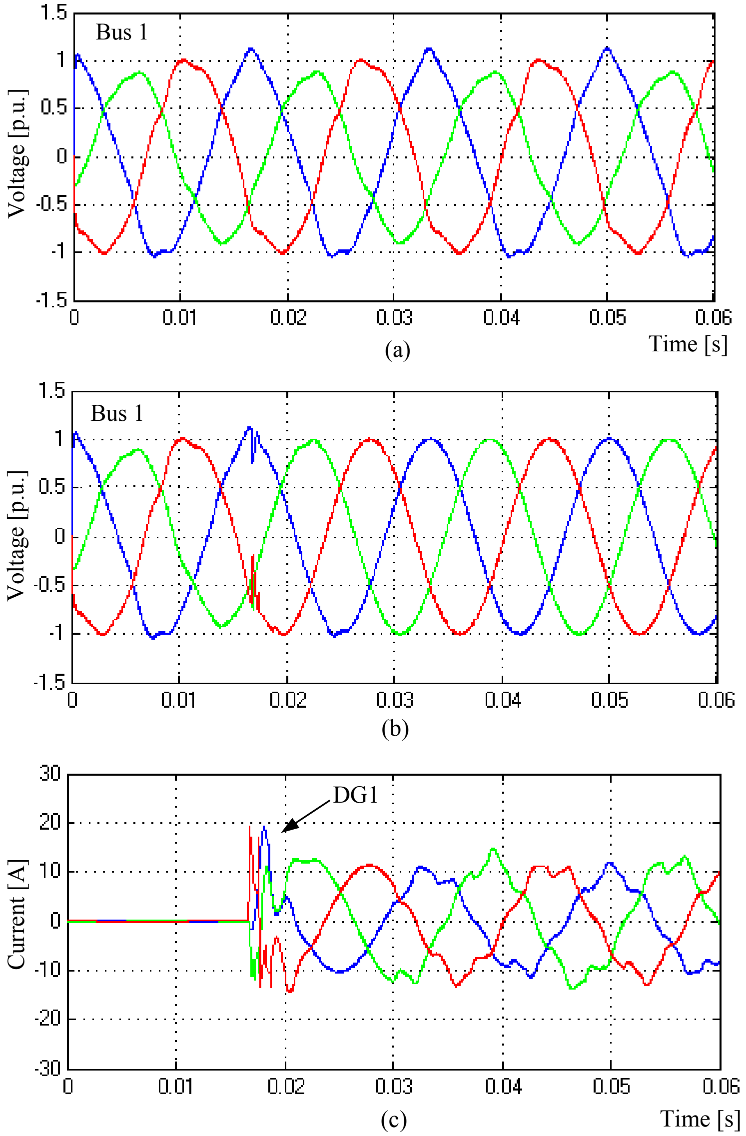

Figure 7.4: Control performance of DG1. (a) Grid voltage with DG1 disabled. (b) DG2 enabled. (c) DG1 injected current.

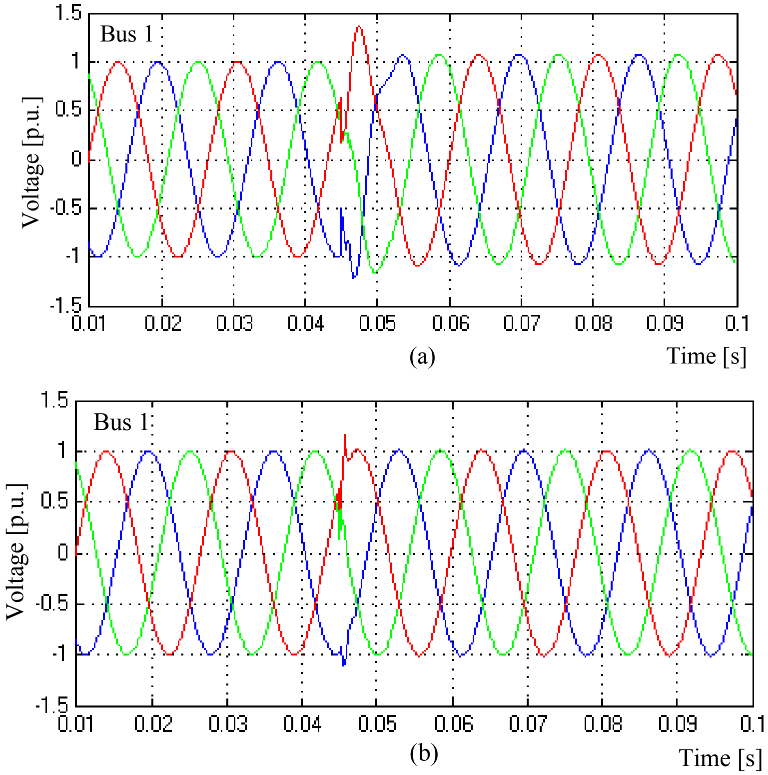

Figure 7.5: Capacitor switching at bus 1. (a) With DG1 disabled. (b) With DG1 enabled.

Figure 7.6(a) shows the grid voltage at bus 2 with DG2 installed and with the grid distortion/unbalance considered. Since DG2 behaves as a PQ-generator, there is no contribution to the voltage quality as expected. However, the grid-side injected current is of high quality as depicted in Figure 7.6(b). This is due to the robust design of the proposed current controller under practical system constraints. Figure 7.6(c) shows the dynamic performance of the injected current of DG2 when the command active power is changed from 0.72 MW to 1.1 MW at t=0.167 s. As the figure reveals, smooth power increase, with a controlled ramp-rate, can be achieved with the proposed interface. Figure 7.6(d) shows the estimated grid frequency using a conventional dq-phase-locked loop synchronization method, whereas Figure 7.6(e) shows the fundamental grid-frequency obtained by the proposed interface monitoring unit. The robust estimation performance allows accurate synchronization with the fundamental grid frequency, and hence high power quality injection, even under the presence of grid distortion and unbalance. On the other hand, the robustly estimated grid voltage vector enables accurate islanding detection.

Figure 7.7(a) shows the grid-side injected current by DG3. Similar to DG2, DG3 behaves as a PQ generator and injects high power quality current waveforms even under

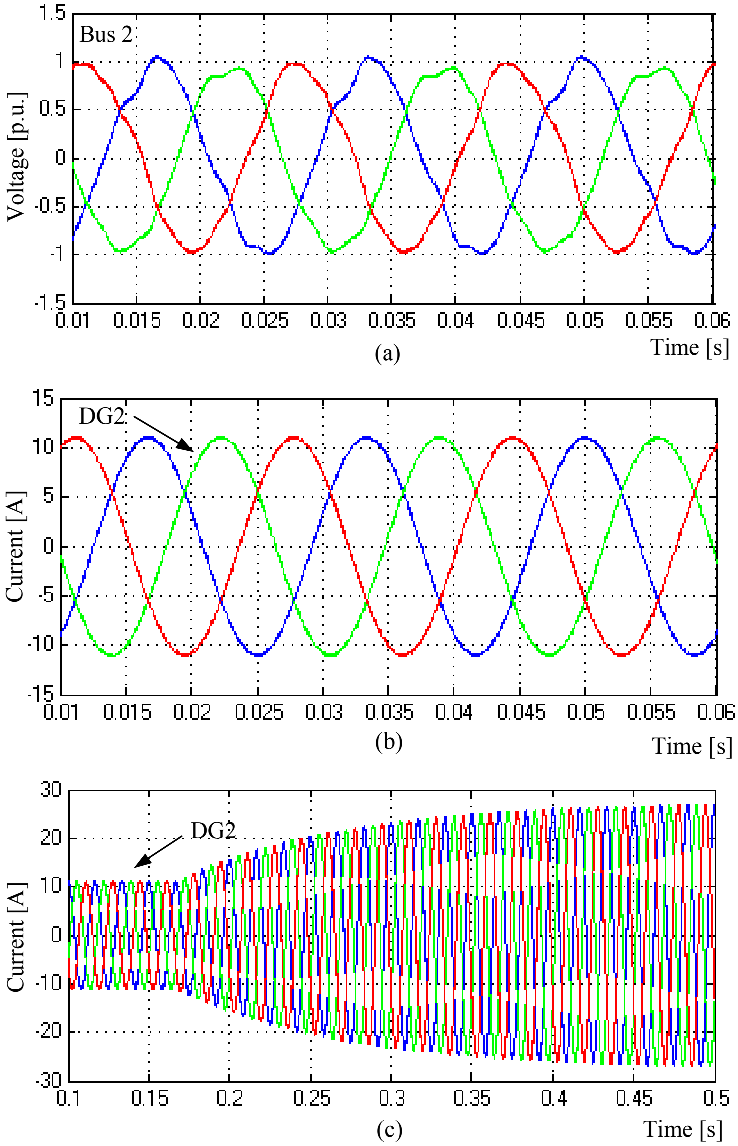

Figure 7.6: Continued,

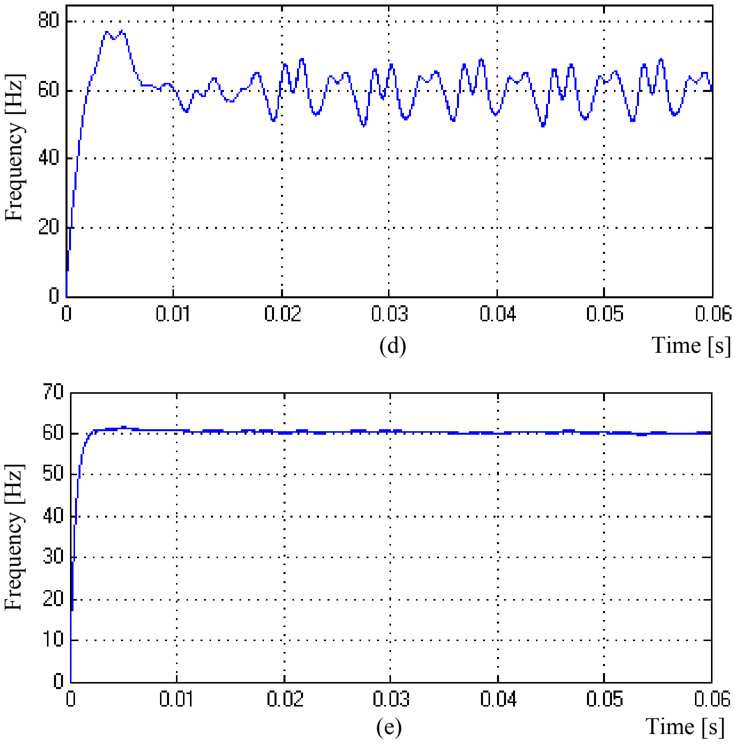

Figure 7.6: Control performance of DG2. (a) Grid voltage. (b) DG2 injected current. (c) DG2 injected current during power increase. (d) Estimated grid frequency using a conventional dq-PLL. (e) Estimated grid frequency using the proposed interface.

the conditions of grid distortion and unbalance. Figure 7.7(b) shows the dynamic performance the injected current of DG3 when the command active power is changed from 0.375 MW to 0.91 MW. Again, smooth power increase, with a controlled ramp-rate, can be achieved with the proposed interface.

Figure 7.8(a) shows the grid voltage at bus 4 with DG4 installed. Since DG4 operates as a current source generator, then no contribution to the voltage quality is expected. Figure 7.8(b) shows the grid-side injected current, which has a THD of about 1.1%. Figure 7.8(c) shows the dynamic performance of the injected current of DG4 when the input power changes from 250 kW to 350 kW. Figure 7.8(d) shows the corresponding dc-link voltage of DG4. The dc-link voltage is quickly regulated by increasing the active power current command of the grid-side converter.

To investigate the performance of the proposed interface under the conditions of supply loss and restoration, the main supply is lost at t=0.1 s and it is restored back again at t=0.35 s. In this scenario, micro-grid formation is not allowed; therefore all DG units should be disconnected within 2 s upon the detection of the islanding event to cope with the IEEE Standard 1547. All DG units utilize a standard frequency-based islanding

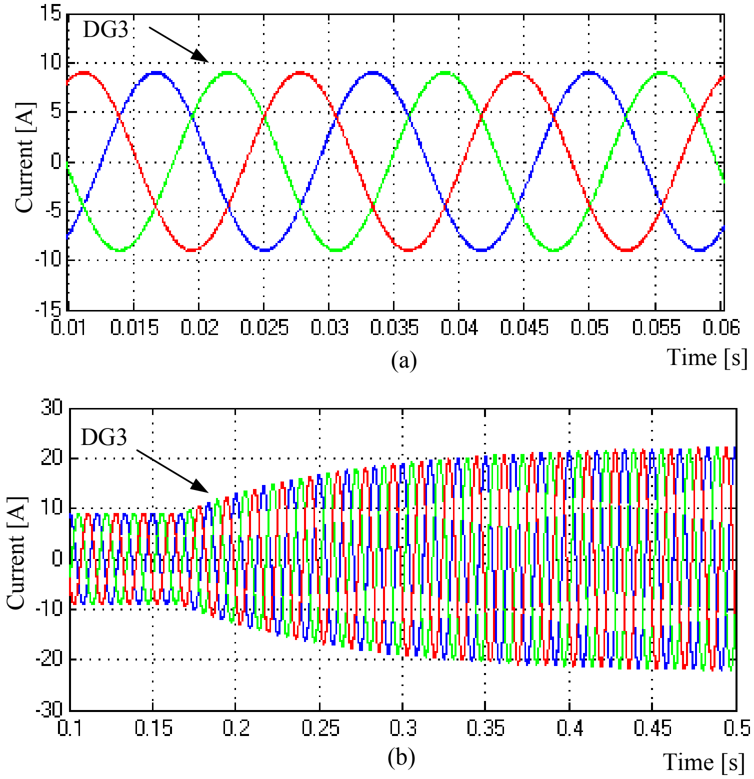

Figure 7.7: Control performance of DG3. (a) DG3 injected current. (b) DG2 injected current during power increase.

detection method with an admissible frequency band of 59.3 Hz to 60.5 Hz. Figure 7.9(a) shows the estimated frequency of DG2. The estimated fundamental frequency has a fast drift after the supply loss, and it becomes unstable. Upon exceeding the lower limit of the admissible frequency band, the pulse-command to the interface is disabled to block the interface from the network.

The time delay between the islanding event and islanding detection is mainly related to the response time of the resonant filter associated with the interface monitoring unit. With this design, the interface will be robust against random and very-short grid disturbances; hence, it can overcome inopportune islanding events. At the same time, the response of the proposed interface is still fast enough to allow fast islanding detection. At t=0.35 s, the main supply is restored. The estimated frequency tracks the grid frequency accurately as shown in Figure 7.9(a). Figure 7.9(b) shows the islanding detection switching logic. Once the frequency is maintained within the admissible band, the interface can be synchronized to the grid voltage again. Figure 7.9(c) shows the corresponding injected currents during the supply loss and synchronization scenarios. Upon islanding, the internal synchronization frequency is missing. With the proposed deadbeat current

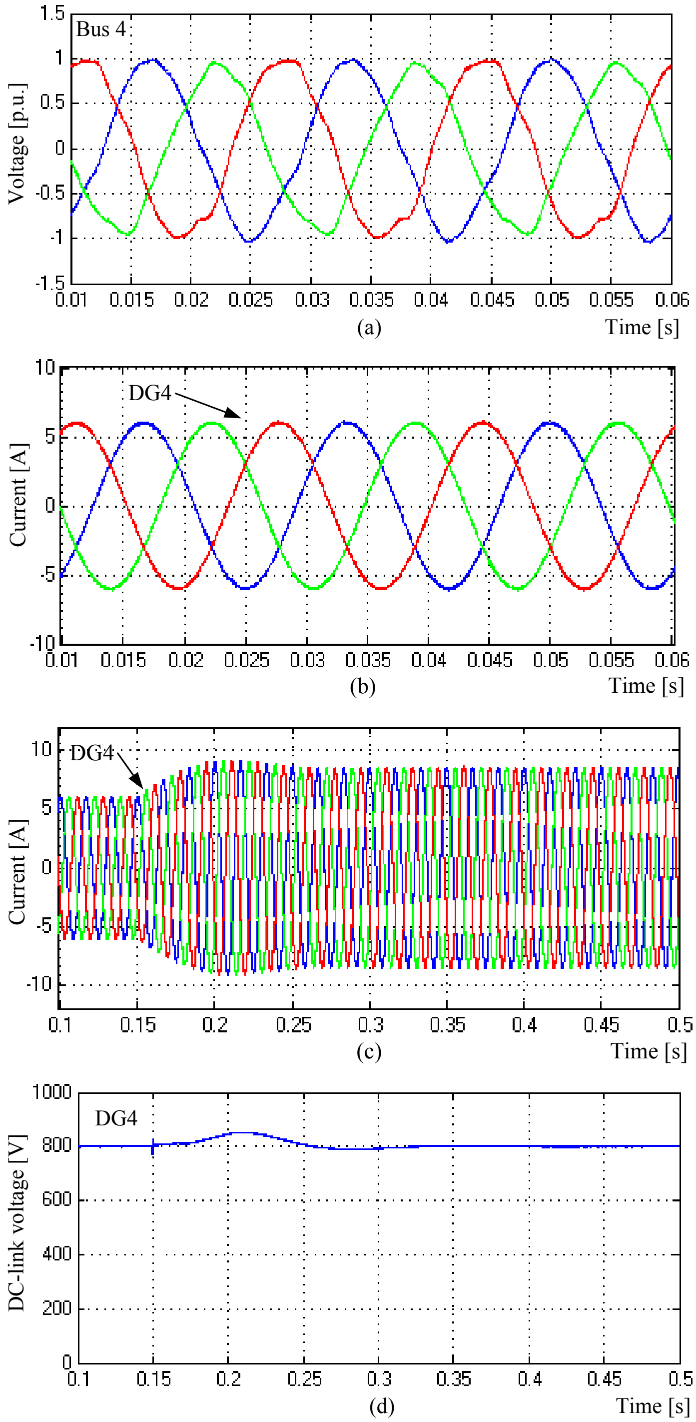

Figure 7.8: Control performance of DG4. (a) Grid voltage. (b) DG2 injected current. (c) DG2 injected current during power increase. (d) DC-link voltage.

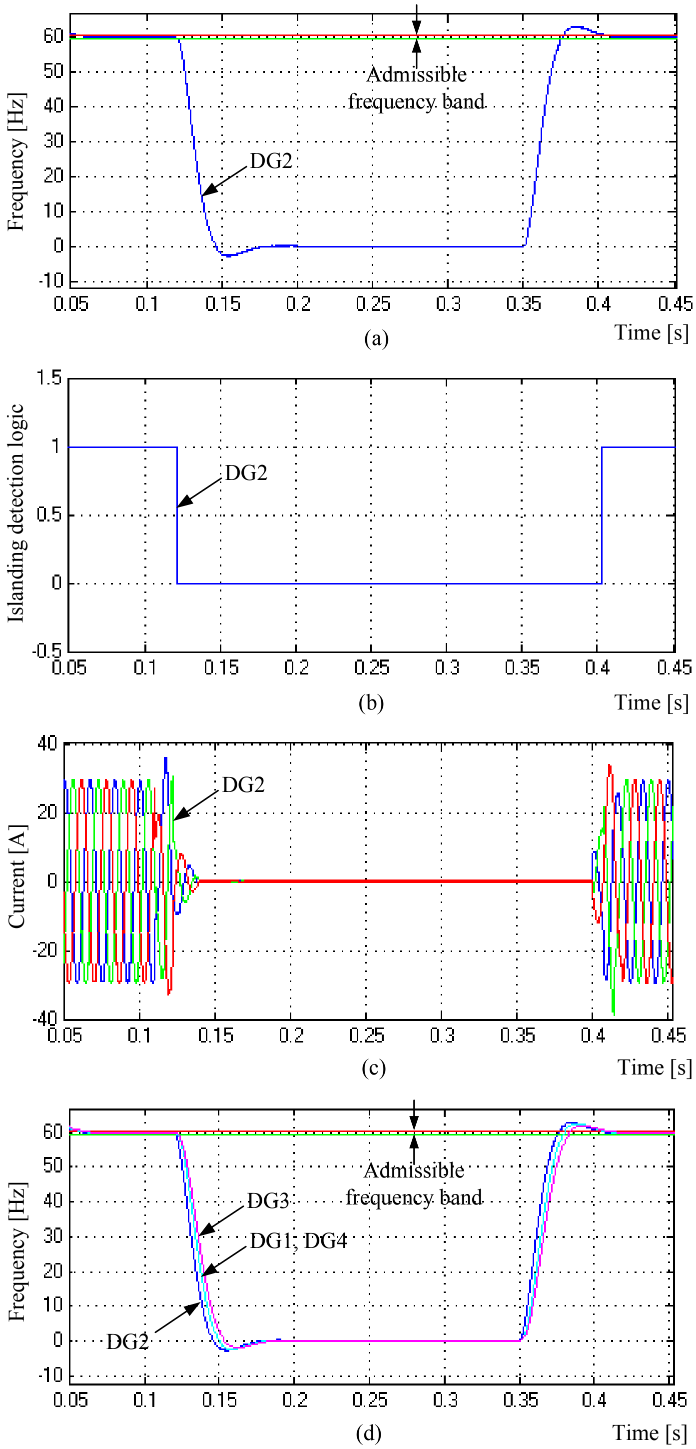

Figure 7.9: Performance of the proposed interface under the conditions of supply loss and restoration.

control algorithm, the sensitivity to frequency variation is swiftly mapped to the current response, reflecting instabilities associated with islanding. This allows a timely islanding detection process by relaxing the coupling between the current dynamics and the islanding detection method. Figure 7.9(d) shows the estimated frequencies of DG1, DG2, DG3, and DG4 under the same supply loss and synchronization scenarios. Accurate frequency estimates are obtained in different cases. The reported results in Figure 7.9 show that the output of the interface monitoring unit can be reliably used in detecting the grid status. It should be noted that with the large body of existing islanding detection techniques [118], various islanding detection algorithms can be implemented to enhance the islanding performance. The proposed voltage-sensorless interface has inherent sensitivity to reflect system perturbations on the estimated quantities.

The aforementioned results indicate the robustness of the proposed DG interface in the grid connected mode.

7.3.2 Micro-Grid Mode

In the micro-grid mode of operation, each DG unit generates a regulated power and contributes to the overall system stability through a power-sharing function. In this scenario, micro-grid formation is allowed and load shedding takes place so that the total connected load is less or equal to the micro-grid capacity.

Figure 7.10 shows the performance of the three DG units during the mode transition at t=0.12 s. Load shedding of insensitive loads takes place to adjust the total micro-grid connected load at 2.3 MVA. Figure 7.10(a) shows the active power response of the three DG units. The power sharing function adjusts the injected power of each DG unit to achieve close power sharing of the total micro-grid connected load. Figure 7.10(b) shows the corresponding reactive power response of different DG units. Figure 7.10(c) shows the p.u. magnitude of the output voltage of different DG units during the mode transition. The proposed interface offers seamless transfer between the grid-connected and micro-grid modes provided that the power continuity constraint is fulfilled, i.e. the total micro-grid connected load meets the micro-grid capacity.

Figure 7.11 shows the performance of the micro-grid system at an increase of the total micro-grid connected from 2.1 MW, 0.65 MVAR to 2.6 MW, 1.5 MVAR. Figure 7.11(a) shows the active power response, whereas Figure 7.11(b) shows the reactive power response. Due to the damped power-sharing control performance, smooth power-sharing performance can be obtained with the proposed DG interface even when the micro-grid loading approaches the micro-grid rated power (approximately 0.95 p.u.).

Figure 7.12 shows the voltage regulation performance with a step 0.75 MW in the

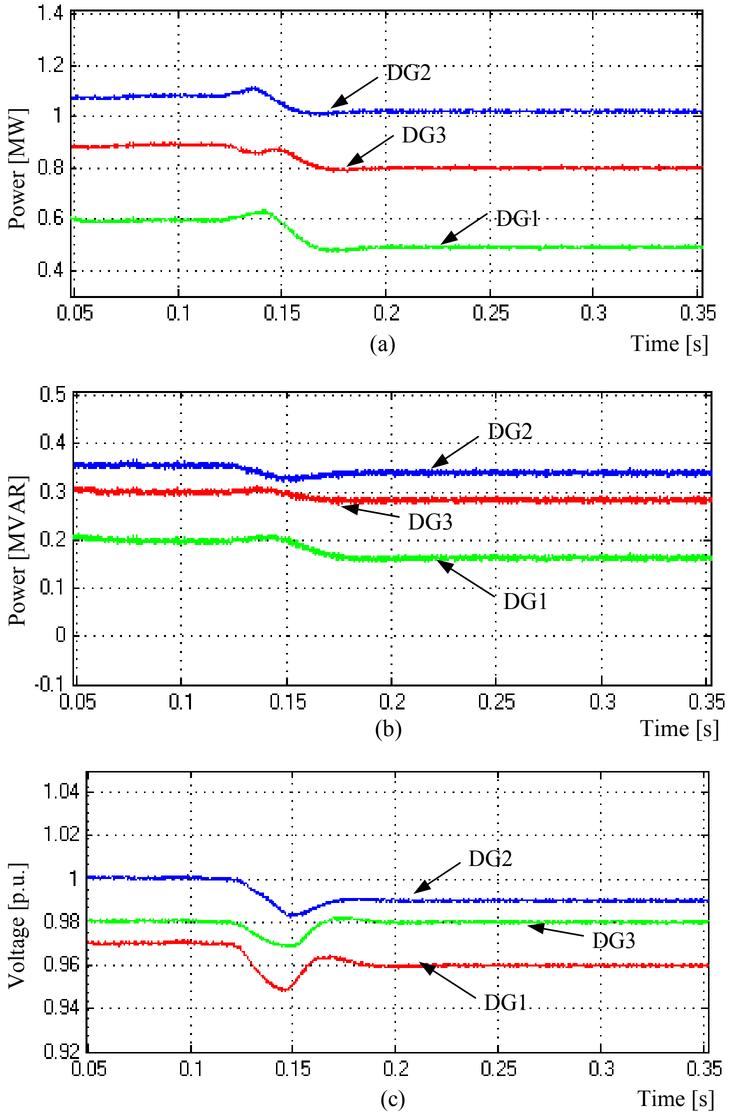

Figure 7.10: Control performance of the proposed interface during micro-grid formation. (a) Active power responses. (b) Reactive power responses. (c) Voltage responses.

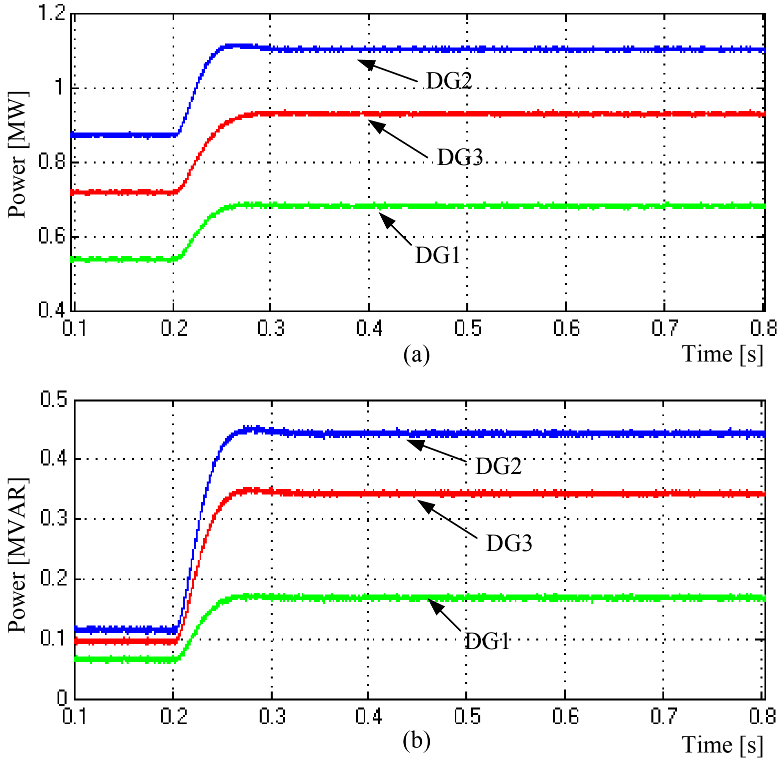

Figure 7.11: Power-sharing performance in micro-grid operation. (a) Active power responses. (b) Reactive power responses.

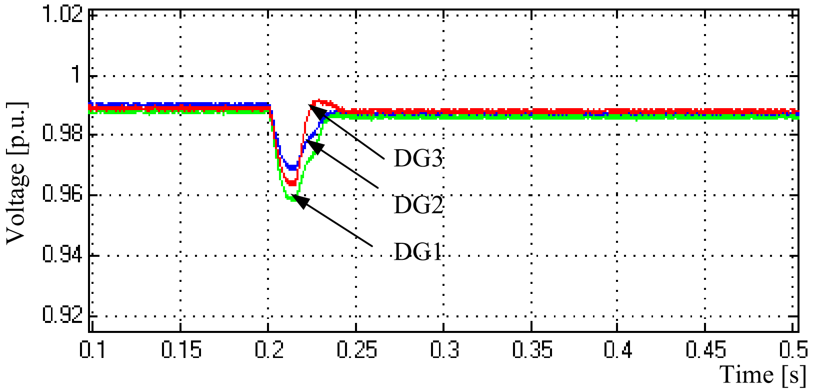

Figure 7.12: Voltage control performance in micro-grid operation with 0.75 MW step load.

total micro-grid connected load. Robust voltage regulation performance is yielded. Since the load disturbance is purely active, the voltages of the three DG units converge to very close values. Slight differences in the voltage magnitude are due the reactive power demand of the line reactances and ac-side filters.

The aforementioned results show that the proposed DG interface can be reliably used in micro-grid operation. In particular, preserving the power-sharing stability and voltage control performance remarkably contributes to the micro-grid stability and reliability.

It is worth to mention that with the expected large penetration of DG, there is a strong need to develop scalable and reliable energy management algorithms to achieve optimum system operation in the grid-connected and micro-grid modes of operations. The proposed DG interface provides a powerful infrastructure for such a supervisory control layer.

7.4 Summary

A robust DG interface that broadly addresses a number of key integration issues has been proposed in this chapter. The proposed interface offers stable and high power quality injection in both the grid-connected and micro-grid modes. In addition, the proposed control scheme allows seamless transfer between grid-connected and micro-grid modes. The proposed interface provides a powerful infrastructure for DG units to meet the stricter demands for grid-connection and islanded operation that will be present in future power girds.

Chapter 8

Conclusions

8.1 Summary and Conclusions

New control algorithms for the inverter-based DG interface, in both the grid-connected and micro-grid modes of operation, have been proposed and presented in this thesis. The proposed control algorithms are designed to realize a robust DG interface that guarantees stable and high power quality injection under the challenging uncertain nature of distribution systems and future micro-grid systems.

In Chapter 3, a newly designed deadbeat current regulation scheme has been introduced. The proposed design guarantees high power quality current injection under the presence of different disturbing parameters, such as grid voltage distortion, interfacing parameters variation, and inverter system delays. The proposed current control algorithm has been applied to the case of inverter output current control. Further, it has been extended, through a modified power circuit model and a new intermediate voltage control approach, to the case of grid current control in a DG interface with a T-type filter.

In Chapter 4, a novel adaptive discrete-time grid-voltage sensorless interfacing scheme for DG inverters has been introduced. Two designs for a new interface monitoring unit have been investigated. Firstly, an interface-monitoring unit, based on parallel adaptive observers, has been designed with low computational demand to estimate the grid voltage and the interfacing parameters simultaneously. Secondly, to cope with the nonlinear nature of the estimation problem and the periodic time-varying nature of the grid voltage, the second design utilizes a neural-network based adaptation algorithm, which works as a real-time optimization agent in the grid-voltage estimator. Both designs have yielded accurate and unbiased estimates. Further, a simple and robust synchronization algorithm and a voltage-sensorless average power control loop have been proposed to realize an adaptive voltage-sensorless DG interface.

A new voltage control scheme for the DG interface featuring fast load voltage regulation and effective mitigation of fast voltage disturbances has been introduced in Chapter 5. The proposed voltage control scheme targets the problem of fast and large-signal-based voltage disturbances, which is common in typical distribution feeders. A hybrid voltage controller combining a linear with a variable-structure control element has been proposed for the DG interface. Positive and dual-sequence versions of the proposed voltage controller have been developed. The proposed voltage controller successfully embeds a wide band of frequency modes through an equivalent internal model. Subsequently, wide range of balanced and unbalanced voltage perturbations, including capacitor-switching disturbances, has been effectively mitigated.

In Chapter 6, an adaptive decentralized droop-based power-sharing control scheme for paralleled inverters in DG micro-grids has been introduced. First, theoretical analysis of micro-grid dynamics with the conventional droop-based power-sharing mechanism has been presented. Second, a new adaptive power-sharing controller with active damping feature has been designed to preserve the dynamic performance and stability of each inverter unit at different loading conditions. Unlike conventional droop controllers, the proposed droop controller yields two-degree-of-freedom tunable controller. Subsequently, the dynamic performance of the power-sharing mechanism can be adjusted, without affecting the static droop gain, to damp the oscillatory modes of the power-sharing controller.

In Chapter 7, the proposed control algorithms have been integrated to realize a robust DG interface for both the gird-connected and micro-grid systems. Additional evaluation results have been presented to demonstrate the effectiveness of the proposed DG interface.

8.2 Contributions

The main contributions of this thesis can be highlighted as follows:

1. The development of new deadbeat current control algorithms for the inverter-based DG interface. The new current control algorithms yield a stable and high-power quality current control performance under the challenging uncertain nature of distribution systems and practical system constraints. Both cases of the inverter-output current control and grid-side current control are considered. Hence, a wide applicability scope is yielded. The salient features of the proposed current controllers are: 1) high power quality current injection even under distorted grid conditions; 2) high bandwidth characteristics without increasing the switching frequency

and with considerably low computational demand; 3) high robustness against uncertainties in the interfacing parameters; 4) no additional hardware is needed for delay compensation; 5) the high bandwidth feature allows current profiling control; a key feature to facilitate the design of a fast load-voltage control scheme; 6) the deadbeat response helps in minimizing the coupling among current, voltage, and power control loops; this is an important feature in micro-grid stability; and 7) fixed switching frequency, which is a key factor in determining the power-quality-based penetration limit of DG.

2. The development of a novel grid-voltage sensorless DG interface with an adaptive estimation unit that performs multiple tasks, such as interface-parameter monitoring, synchronization, and self-commissioning/self-tuning control, within the DG interface. The proposed grid-voltage sensorless interfacing scheme is inherently self-commissioning/self-tuning and guarantees optimum performance, without the constraint conditions and detailed prior knowledge of the inverter system and grid parameters. Sensorless control schemes enhance the system reliability and decrease the cost. Along with the reliability and cost enhancements, significant performance enhancements can be obtained by eliminating the grid voltage sensors in the proposed inverter-based DG interface. Among these are: 1) the elimination of the residual negative sequence and voltage feed-forward compensation errors (the injected currents are so sensitive to minute variations in the reference voltage vector, which highly depends on the feed-forward compensation control), and 2) the positive contribution to the robustness of the power sharing mechanism in paralleled inverter systems, where the power-sharing mechanism is generally based on open-loop controllers.

3. The development of a novel hybrid-type voltage control scheme for the DG interface featuring fast voltage regulation and effective mitigation of dynamic voltage disturbances. The proposed voltage control scheme provides means for mitigating fast and dynamic voltage disturbances, such as capacitor switching transients. Further, with the proposed controller, the DG interface can over-ride unbalanced voltage disturbances initiated by up-stream grid faults provided that there is enough reactive power rating. The fast voltage regulation performance along with the ability of rejecting dynamic voltage disturbances give the proposed voltage controller the ability to act as a universal solution for the voltage quality problems, where voltage sag, swell, and flicker can be inherently mitigated. As a result, the proposed voltage control scheme remarkably contributes to boosting the voltage reliability in micro-grids and distribution systems; particularly in week grids and/or in systems

feeding sensitive loads.

4. Addressing the problem of fast and dynamic voltage disturbances motivated the research on relaxing the slowly varying assumption in the grid voltage estimator. A contribution to relax this assumption has been made through the development of a novel curbing sliding-mode-based observation system. The observation system can be generalized to the case of estimating fast and dynamic uncertainties; a typical challenge in grid-connected converters and machine-drives.

5. The development of a structured and simple tuning method for the proposed voltage control scheme. The tuning problem is formulated as a constrained optimization problem and solved via a particle-swarm-optimization routine.

6. The development of a novel adaptive decentralized droop-based power-sharing control scheme for paralleled inverters in DG micro-grids, which form a key player in future electricity systems. The adaptive nature of the proposed controller ensures active damping of power oscillations at different operating conditions; subsequently, stable and robust power-sharing performance is obtained in the paralleled inverter system. A key contribution in the proposed scheme is the absence of any communication infrastructure. As a result, the proposed scheme can be considered as a low cost solution that significantly contributes to preserving micro-grid stability and reliability.

7. The development of a robust DG interface that utilizes the developed control algorithms in a way to preserve the generation stability and power quality under the challenging uncertain and dynamic nature of typical distribution systems and micro-grids. The overall DG interface facilitates a stable and reliable micro-grid operation along with a safe plug-and-play integration of DG units in existing distribution systems; hence increasing the system penetration of DG. The direct result of this development is huge financial saving for utilities by capturing the salient features of deploying DG into existing utility networks. Further, these developments are significant to the industry as they provide the blue print for reliable control algorithms in future DG units, which are expected to operate under challenging system conditions.

8.3 Directions for Future Work

In continuation of this work, the following subjects are suggested for future studies:

1. The adaptation and application of the proposed current, voltage, and estimation algorithms to different custom power devices, such as active filters, distribution static synchronous compensators, and unified power conditioners.
2. The extension of the proposed active damping control in micro-grids to increase the damping of the medium-frequency modes, which can be excited by micro-grid harmonics.
3. The utilization of the proposed DG interface within an operational planning and energy management algorithms for a distribution system with embedded generation, and/or micro-grids, in the presence of a low-bandwidth supervisory communication system.
4. The optimization of the power sharing control settings for minimum operation cost of a micro-grid system.
5. The development of reliable micro-grid dispatch tools that can be integrated within the energy management algorithms in micro-grids.

Appendix A

Parameters of the Studied System Shown in Figure 5.4

The parameters of the studied system shown in Figure 5.4 are given as follows:

- Nominal grid phase-voltage at the PCC =110 V at 60 Hz;
- R_s=0.08 Ω;
- L_s=1 mH;
- DC-link voltage=600 V;
- Load L1: 20 kW at 0.9 lagging power factor;
- Load L2: 30 kW at 0.85 lagging power factor;
- Switching capacitor: 20 kVAR;
- Nominal equivalent interfacing inductance L_o=2.5 mH;
- Nominal equivalent interfacing resistance R_o=1.0 Ω.

Appendix B

Parameters of the Studied System Shown in Figure 6.4

The parameters of the studied system shown in Figure 6.4 are given as follows:

- **DG1**: 15 kVA, 208 V (L-L), 60 Hz, L_f=1.5 mH, R_f=0.15 Ω, C_f=45 μF, L_c=0.53 mH, R_c=0.05 Ω, m=1.33×10^{-4} rad/s/W, n=1.33×10^{-3} V/VAR, ω_c=30 rad/sec, K_{pi}=10, K_{ii}=15300, K_{pv}=0.045, K_{iv}=400, H=0.68;

- **DG2**: 20 kVA, 208 V (L-L), 60 Hz, L_f=1.5 mH, R_f=0.15 Ω, C_f=45 μF, L_c=0.53 mH, R_c=0.05 Ω, m=1.0×10^{-4} rad/s/W, n=1.0×10^{-3} V/VAR, ω_c=30 rad/sec, K_{pi}=10, K_{ii}=15300, K_{pv}=0.045, K_{iv}=400, H=0.7;

- **DG3**: 10 kVA, 208 V (L-L), 60 Hz, L_f=1.5 mH, R_f=0.15 Ω, C_f=45 μF, L_c=0.53 mH, R_c=0.05 Ω, m=2.0×10^{-4} rad/s/W, n=2.0×10^{-3} V/VAR, ω_c=30 rad/sec, K_{pi}=10, K_{ii}=15300, K_{pv}=0.045, K_{iv}=400, H=0.75;

- **L1**: 0.1+0.35j Ω, **L2**: 0.05+0.1j Ω, **L3**: 0.03+0.13j, **L4**: 0.01+0.02j Ω, **L5**: 0.02+0.1j Ω.

Bibliography

[1] "Special issue on distributed power generation," *IEEE Transactions on Power Electronics*, vol. 19, no. 5, p. 1157, Sep. 2004.

[2] F. Blaabjerg, Z. Chen, and S. B. Kjaer, "Power electronics as efficient interface in dispersed power generation systems," *IEEE Transaction on Power Electronics*, vol. 19, no. 5, pp. 1184–1194, Sep. 2004.

[3] B. Maurhoff and G. Wood, "Dispersed generation to reduce power costs and improve service reliability," In Proc. *Rural Electric Power Conference*, pp. C5/1-C5/7, 2000.

[4] J. Gutierrez-Vera, "Use of renewable sources of energy in Mexico," *IEEE Transactions on Energy Conversion*, vol. 9, pp. 442 –450, Sept. 1994.

[5] J. L. Del Monaco, "The role of distributed generation in the critical electric power infrastructure," In Proc. *IEEE-Power Engineering Society Winter Meeting*, vol. 1, pp. 144 – 145, 2001.

[6] L. Philipson, "Distributed and dispersed generation: addressing the spectrum of consumer needs," In Proc. *IEEE-Power Engineering Society Summer Meeting*, vol. 3, pp. 1663 –1665, 2000.

[7] D. Casadei, G. Grandi, R. K. Jardan, and F. Profumo, "Control strategy of a power line conditioner for cogeneration plants," In Proc. *IEEE-Power Electronics Specialists Conference, PESC'99*, vol. 2, pp. 607-612, 1999.

[8] R. K. Jardan, O. Dranga, and D. Bereknyei, "Standby power supply using alternative energy through cogeneration technologies," In Proc. *3rd International Conference TELESCON Telecommunications Energy Special,* pp. 215-219, 2000.

[9] F. Blaabjerg, R. Teodorescu, M. Liserre, and A.V. Timbus, "Overview of control and grid synchronization for distributed power generation systems," *IEEE Transaction on Industrial Electronics,* vol 53, pp. 1398-1409, Oct. 2006.

[10] B. Lasseter, "Microgrids," In Proc. *IEEE-Power Engineering Society Winter Meeting*, vol. 1, pp. 146-149, 2001.

[11] L. J. J. Offringa and J. L. Duarte, "A 1600 kW IGBT converter with interphase transformer for high speed gas turbine power plants," In Proc. *IEEE-IAS Conf. Record*, vol. 4, pp. 2243 –2248, 2000.

[12] H. Akagi, "Large static converters for industry and utility applications," *Proceedings of the IEEE*, vol. 89, pp. 1384-1392, July 2004.

[13] H. Bindner and P. Lundsager, "Integration of wind power in the power system," in *Proc. IEEE Industrial Electronics Society Conference IECON '02*, vol. 4, Nov. 2002, pp. 3309–3316.

[14] M. Liserre, R. Teodorescu, and F. Blaabjerg, "Stability of photovoltaic and wind turbine grid-connected inverters for a large set of grid impedance values," *IEEE Transactions on Power Electronics*, vol. 21, no. 1, pp. 263-272, Jan. 2006.

[15] M. Calais, J. Myrzik, T. Spooner, and V. G. Agelidis, "Inverters for single-phase grid connected photovoltaic systems—an overview," in *Proc. IEEE Power Electronics Specialists Conference (PESC'02)*, 2002, pp. 1995–2000.

[16] E. Twinning, "Modeling grid-connected voltage source inverter operation," in *Proc. AUPEC'01*, 2001, pp. 501–506.

[17] E. Twinning and D. G. Holmes, "Grid current regulation of a three-phase voltage source inverter with an LCL input filter," *IEEE Transactions on Power Electronics*, vol. 18, no. 3, pp. 888–895, May 2003.

[18] F. Katiraei and M. R. Iravani, "Power management strategies for a microgird with multiple distributed generation units," *IEEE Transactions on Power Systems*, vol. 21, pp. 1821-1831, Nov. 2006.

[19] M. Suter, "Active filter for a microturbine," in Proc. *The Twenty-Third International Telecommunications Energy Conference, INTELEC 2001*, 2001, pp. 162–165.

[20] M. Etezadi-Amoli and K. Choma, "Electrical performance characteristics of a new microturbine generator," in Proc. *IEEE-Power Engineering Society Winter Meeting*, vol. 2, pp. 736-740, 2001.

[21] M. W. Davis, A. H. Giffors, and T. J. Krupa, "Micoturbines- an economic and reliability evaluation for commercial, residential, and remote load applications," *IEEE Transactions on Power Systems*, vol. 14, pp. 1556-1562, Nov. 1999.

[22] M. Pipattanasomporn, M. Willingham, and S. Rahman, "Implications of on-site distributed generation for commercial/industrial facilities," *IEEE Transactions on Power Systems*, vol. 20, pp. 206-212, Feb. 2005.

[23] M.W. Ellis, M.R. Von Spakovsky, and D.J. Nelson, "Fuel cell systems: efficient, flexible energy conversion for the 21st century," *Proceedings of the IEEE*, vol. 89, issue 12, December 2001, pp. 1808–1818.

[24] M. Farooque and H.C. Maru, "Fuel cells—the clean and efficient power generators," *Proceedings of the IEEE*, vol. 89, issue 12, 2001, pp. 1819–1829.

[25] Yoon-Ho Kim and Sang-Sun Kim, "An electrical modeling and fuzzy logic control of a fuel cell generation system," *IEEE Transactions on Energy Conversion*, vol. 14, no. 2, p. 239-244, June 1999.

[26] T. Petru and T. Thiringer, "Modeling of wind turbines for power system studies," *IEEE Transactions on Power Systems*, vol. 17, pp. 1132-1139, Nov. 2002.

[27] B. C. Ummels, M. Gibescu, E. Pelgrum, W. L. Kling, and A. J. Brand, "Impacts of wind power on thermal generation unit commitment and dispatch," *IEEE Transactions on Energy Conversion*, vol. 22, pp. 44-51, March 2007.

[28] E. Muljadi, C. P. Butterfield, B. Parsons, and A. Ellis, "Effect of variable speed wind turbine generator on stability of a weak grid," *IEEE Transactions on Energy Conversion*, vol. 22, pp. 29-36, March 2007.

[29] D. Andersson, A. Petersson, E. Agneholm, and D. Karlsson, "Kriegers Flak 640 MW off-shore wind power connection – a real project case study," *IEEE Transactions on Energy Conversion*, vol. 22, pp. 79-85, March 2007.

[30] R. Billinton and W. Wangdee, "Reliability-based transmission reinforcement planning associated with large-scale wind farms," *IEEE Transactions on Power Systems*, vol. 22, pp. 34-41, Feb. 2007.

[31] T. Thiringer, "Power quality measurements performed on a low-voltage grid equipped with two wind turbines," *IEEE Transactions on Energy Conversion*, vol. 11, pp. 601-606, Sept. 1996.

[32] J. Matevosyan and L. Soder, "Minimization of imbalance cost trading on the short-term power market," *IEEE Transactions on Power Systems*, vol. 21, pp. 1396-1404, Aug. 2006.

[33] *Wind Power in Power Systems*, Edited by Thomas Ackermann, J. Willy Press, 2003.

[34] R. Kyoungsoo and S. Rahman, "Two-loop controller for maximizing performance of a grid-connected photovoltaic-fuel cell hybrid power plant," *IEEE Transactions on Energy Conversion*, vol. 13, pp. 276-281, 1998.

[25] H. Weiss and Jian Xiao, "Fuzzy system control for combined wind and solar power distributed generation unit," In Proc. *IEEE International Conference on Industrial Technology*, vol. 2, pp. 1160-1165, 10-12 Dec. 2003.

[26] Y. T. Tan and S. D. Kirschen, "Impact on the power system of a large penetration of photovoltaic generation," In Proc. *IEEE-Power Engineering Society General Meeting 2007*, (PEGSM 07), pp. 24-28, June 2007.

[37] E. C. Kern, E. M. Gulachenski, and G. A. Kern, "Cloud effects of distributed photovoltaic generation: slow transients at the Gardner, Massachusetts photovoltaic experiment," *IEEE Transactions on Energy Conversion*, vol. 4, pp. 184-190, June 1989.

[28] W. Xiao, W. G. Dunford, P. R. Palmer, and A. Capel, "Regulation of photovoltaic voltage," *IEEE Transactions on Industrial Electronics*, vol. 54, pp. 1365-1374, June 2007.

[39] M. A. Green, "Recent developments and future prospects for third generation and other advanced cells," in Proc. *IEEE 4th World Conference on Photovoltaic Energy Conversion*, pp. 15-19, May 2006.

[40] P. F. Ribeiro, B. K. Johnson, M. L. Crow, A. Asroy, and Y. Lie, "Energy storage systems for advanced power applications," *Proceedings of the IEEE*, vol. 89, pp. 1744-1765, Dec. 2001.

[41] J. A. McDowall, "Opportunities for electricity storage in distributed generation and renewables," in Proc. *IEEE/PES Transmission and Distribution Conference and Exposition*, 2001, pp. 1165-1168.

[42] K. Rajashekara, "Hybrid fuel-cell strategies for clean power generation," *IEEE Transactions on Industry Applications*, vol. 41, pp. 682-689, May-June 2005.

[43] S. A. Daniel and N. A. Gounden, "A novel hybrid isolated generating system based on PW fed inverter-assisted wind-driven induction generator," *IEEE Transactions on Energy Conversion*, vol. 19, pp. 416-422, June 2004.

[44] www.eia.doe.gov

[45] IEEE Standard for interconnecting distributed resources with electric power systems, IEEE Standard 1547-2003, Jul. 2003.

[46] IEEE Recommended practice for utility interface of photovoltaic (PV) systems, IEEE Standard 929-2000, April 2000.

[47] M. Liserre, R. Teodorescu, and F. Blaabjerg, "Multiple harmonics control for three-phase grid converter systems with the use of PI-RES current controller in a rotating frame," *IEEE Transactions on Power Electronics*, vol. 21, pp. 836-841, May 2006.

[48] M. P. Kazmierkowski and L. Malesani, "Current control techniques for three-phase voltage-source PWM converters: a survey," *IEEE Transactions on Industrial Electronics*, vol. 45, pp. 691-703, Oct. 1998.

[49] J. Holtz, "Pulsewidth modulation for electronic power conversion," *Proceedings of the IEEE,* vol. 82, pp. 1194-1214, Aug. 1994.

[50] B. K. Bose, "An adaptive hysteresis-band current control technique of a voltage-fed PWM Inverter for Machine Drive System," *IEEE Transactions on Industrial Electronics*, vol. 37, pp. 402-408, Oct. 1990.

[51] B. –H. Kwon, T. –W. Kim, and J. –H. Youn, "A novel SVM-based hysteresis current controller," *IEEE Transactions on Power Electronics,* vol. 13., pp. 297-307, Mar. 1998.

[52] C. T. Pan and T. Y. Chang, "An improved hysteresis current controller for reducing switching frequency," *IEEE Transactions on Power Electronics*, vol. 9, pp. 97-104, Jan. 1994.

[53] R. D. Lorenz and D. B. Lawson, "Performance of feed forward current regulator for field oriented induction machine controllers," *IEEE Transactions on Industrial Applications*, pp. 597-602, Jul./Aug. 1987.

[54] D. N. Zmood, D. G. Holmes, and G. H. Bode, "Frequency-domain analysis of three-phase linear current regulators," *IEEE Transactions on Industrial Applications*, vol. 37, pp. 601-610, Mar./Apr. 2001.

[55] D. N. Zmood and D. G. Holmes, "Stationary frame current regulation of PWM inverters with zero steady-state error," *IEEE Transactions on Power Electronics*, vol. 18, pp. 814-822, May 2003.

[56] S. Fukuda and R. Imamura, "Application of a sinusoidal internal model to current control of three-phase utility-interface converters," *IEEE Transactions on Industrial Electronics*, vol. 52, pp. 420-426, Apr. 2005.

[57] T. M. Rowan and R. J Kerkman, "A new synchronous current regulator and analysis of current regulated PWM inverters," *IEEE Transactions on Industrial Applications*, vol. IA-22, pp. 678-690, 1986.

[58] C. T. Rim, N. S. Choi, G. C. Cho, and G. H. Cho, "A complete DC and AC analysis of three-phase controlled-current PWM rectifier using circuit D-Q transformation," *IEEE Transactions on Power Electronics,* vol. 9, pp. 390-396, July 1994.

[59] T.G. Habetler, "A space vector-based rectifier regulator for AC/DC/AC converters," *IEEE Transactions on Power Electronics*, vol. 8, pp. 30-36, Jan. 1993.

[60] H. L.- Huy, K. Slimani, and P. Viarouge, "Analysis and implementation of a real-time predictive current controller for permanent-magnet synchronous servo drives," *IEEE Transactions on Industrial Electronics*, vol. 41, pp. 110-117, Feb. 1994.

[61] J. Mossoba and P. Lehn, "A controller architecture for high bandwidth active power filters," *IEEE Transactions on Power Electronics*, vol. 18, pp. 317-325, Jan. 2003.

[62] H. Abu-Rub, J. Guzinski, Z. Krzeminski, and H. A. Toliyat, "Predictive current control of voltage-source inverters," *IEEE Transactions on Industrial Electronics,* vol. 51, pp. 585-593, June 2004.

[63] O. Kukrer, "Discrete-time current control of voltage-fed three-phase PWM inverters," *IEEE Transactions on Power Electronics*, vol. 11, pp. 260-269, March 1996.

[64] D. G. Holmes and D. A. Martin, "Implementation of a direct digital predictive current controller for single and three phase voltage source inverters," *in Proc. Annu. Meeting IEEE Industrial. Applications* 1996, pp. 906-913.

[65] H. –T. Moon, H. –S. Kim, and M. –J. Youn, "A discrete-time predictive current control for PMSM," *IEEE Transactions on Power Electronics*, vol. 18, pp. 464-472, Jan. 2003.

[66] Y. –Y. Tzou and S. –Y. Lin, "Fuzzy-Tuning Current-Vector Control of a Three-Phase PWM Inverter for High-Performance AC Drives," *IEEE Transactions on Industrial Electronics*, vol. 45, pp. 782-791, Oct. 1998.

[67] G. H. Bode, P. C. Loh, M. J. Newman, and D. G. Holmes, "An improved robust predictive current regulation algorithm," *IEEE Transactions on Industrial Applications*, vol. 41, pp. 1720-1733, Nov./Dec. 2005.

[68] L. Springob and J. Holtz, "High-bandwidth current control for torque-ripple compensation in PM synchronous machines," *IEEE Transactions on Industrial Electronics*, vol. 45, pp. 713-721, Oct. 1998.

[69] L. Malesani, P. Mattavelli, and S. Buso, "Robust dead-beat current control for PWM rectifiers and active filters," *IEEE Transactions on Industrial Applications*, vol. 35, pp. 613-620, May/June. 1999.

[70] K. H. Kim, I. C. Baik, G.-W. Moon, and M.-J. Youn, "A current control for a permanent magnet synchronous motor with a simple disturbance estimation scheme," *IEEE Transactions on Control Systems Technology,* vol. 7, pp. 630-633, Sept. 1999.

[71] K. H. Kim and M. J. Yoon, "A simple and robust digital current control technique of a PM synchronous motor using time delay control approach," *IEEE Transactions on Power Electronics,* vol. 16, pp. 72-82, Jan. 2001.

[72] D. -C. Lee, S. -K. Sul, and M. -H. Park, "High performance current regulator for a field-oriented controlled induction motor drive," *IEEE Transactions on Industrial Applications.*, vol. 30, pp. 1247-1257, Sept./Oct. 1994.

[73] U. Borup, F. Blaabjerg, and P. Enjeti, "Sharing of nonlinear load in parallel-connected three-phase converters," *IEEE Transactions on Industrial Applications*, vol. 37, no. 6, pp. 1817–1823, Nov./Dec. 2001.

[74] A. Wolf and M. Thamodharan, "Reactive power reduction in three-phase electric arc furnace," *IEEE Transactions on Industrial Electronics,* vol. 47, pp. 729-733, Aug. 2000.

[75] C. Moreno, H. Duarte, and J. Garcia, "Propagation of flicker in electric power networks due to wind energy conversions systems," *IEEE Transactions on Energy Conversion*, vol. 17, pp. 267-272, June 2002.

[76] A. Woyte, V. Thong, R. Belmans, and J. Nijs, "Voltage fluctuations on distribution level introduced by photovoltaic systems," *IEEE Transactions on Energy Conversion,* vol. 21, pp. 202-209, March 2006.

[77] J. Gomez and M. Morcos, "Voltage sag effects on sensitive equipment due to starting cycles of induction motor," *IEEE Power Engineering Review,* vol. 22, pp. 51-52, Aug. 2002.

[78] N. Kolcio, J. Halladay, G. Allen, and E. Fromholtz, "Transient overvoltages and overcurrents on 12.47 kV distribution lines: field test results," *IEEE Transactions on Power Delivery,* vol. 7, pp. 1359-1370, July 1992.

[79] A. Jain, K. Joshi, A. Behal, and N. Mohan, "Voltage regulation with STATCOMs: modeling, control and results," *IEEE Transactions on Power Delivery,* vol. 21, pp. 726-735, April 2006.

[80] P. W. Lehn and M. R. Iravani, "Experimental evaluation of STATCOM closed loop dynamics," *IEEE Transactions on Power Delivery*, vol. 13, no. 4, pp. 1378–84, Oct. 1998.

[81] H. Fujita and K. Akagi, "Voltage-regulation performance of a shunt active filter intended for installation on a power distribution system," *IEEE Transactions on Power Electron*, vol. 22, pp. 1046-1053, May 2007.

[82] M. Marei, E. El-Saadany, and M. Salama, "A novel control algorithm for the DG interface to mitigate power quality problems," *IEEE Transactions on Power Delivery,* vol. 19, pp. 1384-1392, July 2004.

[83] M. Morari and E. Zafiriou, *Robust Process Control.* Englewood Cliffs, NJ: Prentice-Hall, 1989.

[84] G. Weiss, Q. Zhong, T. Green, and J. Liang, “H_∞ repetitive control of DC-AC converters in microgrids,” *IEEE Transactions on Power Electronics*, vol. 19, pp. 219-230, Jan. 2004.

[85] R. H. Lasseter and P. Paigi, “Microgrid: a conceptual solution,” In Proc. *IEEE Power Electronics Specialists Conference (PESC’04)*, June 2004, pp. 4285-4290.

[86] J. A. P. Lopes, C. L. Moreira, and A. G. Madureira, “Defining control strategies for microgrids islanded operation,” *IEEE Transactions on Power Systems*, vol. 21, pp. 916, 924, May 2006.

[87] P. Piagi, and R. H. Lasseter, “Autonomous control of microgrids,” In Proc. *IEEE Power Engineering Society General Meeting*, June 2006.

[88] M.C. Chandorkar, D.M. Divan, and R. Adapa, “Control of Parallel Connected inverters in standalone ac supply systems,” *IEEE Transactions on Industry Applications*, vol. 29, no. 1, January/February 1993, pp. 136-143.

[89] J. Guerrero, L. de Vicuna, J. Matas, M. Castilla, and J. Miret, “A wireless controller to enhance dynamic performance of parallel inverters in distributed generation system,” *IEEE Transactions on Power Electronics*, vol. 19, no. 5, pp. 1205-1213, Sept. 2004.

[90] S. J. Chiang, C. Y. Yen, and K. T. Chang, “A multimodule parallelable series-connected PWM voltage regulator,” *IEEE Transactions on Industrial Electronics*, vol. 48, pp. 506–516, June 2001.

[91] T. Lin and P. Cheng, “Design of a new cooperative harmonic filtering strategy for distributed generation interface converters in an islanding network,” *IEEE Transactions on Power Electronics*, vol. 22, no. 5, pp. 1919-1927, Sept. 2007.

[92] R C. Dugan, T. S. Key, and G. J. Ball, “Distributed resources standards,” *IEEE Industry Applications Magazine*, vol. 12, Feb. 2006, pp. 27-34.

[93] M. Malinowksi, M. P. Kazmierkowski, S. Hansen, F. Blaabjerg, and G. Marques, “Virtual flux based direct power control of three-phase PWM rectifiers,” *IEEE Transaction on Industrial Applications*, vol. 37, no. 4, pp. 1019–1027, Jul./Aug. 2001.

[94] T. Noguchi, H. Tomiki, S. Kondo, and I. Takahashi, “Direct power control of PWM converter without power-source voltage sensors,” *IEEE Transactions on Ind. Applications*, vol. 34, no. 3, pp. 473–479, May–Jun. 1998.

[95] K. J. Astrom and B. Wittenmark, *Adaptive Control.* New York: Addison-Wesley, 1995.

[96] Y. A.-R. I. Mohamed and E. F. El-Saadany, “An improved deadbeat current controller with a novel adaptive self-tuning load model for a three-phase PWM voltage source inverter,” *IEEE Transactions on Industrial Electronics*, vol. 54, no. 4, pp. 747-759, Aug. 2007.

[97] Matlab 6.5, User’s Guide, The MathWorks Inc., 2003.

[98] G. C. Goodwin and K. S. Sin, *Adaptive Filtering, Prediction, and Control.* Englewood Cliffs, NJ: Prentice-Hall, 1994.

[99] Y. A.-R. I. Mohamed and E. F. El-Saadany, "Adaptive discrete-time grid-voltage sensorless interfacing scheme for grid-connected DG-inverters based on neural-network identification and deadbeat current regulation," *IEEE Transactions on Power Electronics*, vol. 23, no. 1, pp. 308-321, Jan. 2008.

[100] B. K. Bose, "Neural network applications in power electronics and motor drives—An introduction and perspective," *IEEE Transactions on Industrial Electronics*, vol. 54, no. 1, pp. 14–33, Feb. 2007.

[101] K. S. Narenda and K. Parthasarathy, "Identification and control of dynamical systems using neural networks," *IEEE Transactions on Neural Networks*, vol. 1, no. 1, pp. 4–27, Jan. 1990.

[102] J. R. Noriega and H. Wang, "A direct adaptive neural-network control for unknown nonlinear systems and its application," *IEEE Transactions on Neural Networks*, vol. 9, no. 1, pp. 27–34, Jan. 1998.

[103] P. Vas, *Artificial-intelligence-Based Electrical Machines and Drives: Application of Fuzzy, Neural, Fuzzy-Neural and Genetic-Algorithm-Based Techniques*, Monographs in Electrical and Electronic Engineering. Oxford, U.K.: Oxford Univ. Press, 1999.

[104] Y. A.-R. I. Mohamed, E. F. El-Saadany, and M. M. A. Salama, "An adaptive grid-voltage sensorless interfacing scheme for inverter-based distributed generation units," *IEEE Transactions on Energy Conversion*, to appear.

[105] V. I. Utkin, "Sliding mode control design principles and applications to electric drives," *IEEE Transactions on Industrial Electronics,* vol. 40, pp. 23-36, Feb. 1993.

[106] Y. A.-R. I. Mohamed, "A novel hybrid-type variable-structure instantaneous torque controller with a robust adaptive torque observer for a high performance direct-drive PMSM," *IEEE Transactions on Industrial Electronics*, (*Special Issue on Variable Speed Drives and Electric Machines*), vol. 54, no. 5, pp. 2491-2499, Oct. 2007.

[107] Y. A.-R. I. Mohamed and E. F. El-Saadany, "A control scheme of grid-connected PWM voltage-source inverters for fast load voltage regulation and effective mitigation of unbalanced voltage disturbances," *IEEE Transactions on Industrial Electronics*, vol. 55, no. 5, pp. 2072-2084, May 2008.

[108] J. Kennedy and R. Eberhart, "A new optimization using Particle Swarm Theory," in *Proc. of the Sixth Int. Symposium of Micro Machine and Human Science*, Nagoya, Japan, 1995, pp. 39-43.

[109] F. Van den Bergh, "An analysis of Particle Swarm Optimizer", PhD dissertation, University of Pretoria, Pretoria, South Africa, 2001.

[110] Y. A.-R. I. Mohamed and E. F. El-Saadany, "Hybrid variable-structure control with evolutionary optimum-tuning for fast grid-voltage regulation using inverter-based distributed generation," *IEEE Transactions on Power Electronics*, vol. 23, no. 3, pp. 1334-1341, May 2008.

[111] F. B. del Blanco, M. W. Degner, and R. D. Lorenz, "Dynamic analysis of current regulators for ac motors using complex vectors," *IEEE Transactions Industrial Applications*, vol. 35, no. 6, pp. 1424-1432, Nov./Dec. 1999.

[112] L. Harnefors, K. Pietiläinen, and L. Gertmar, “Torque-maximizing field weakening control: Design, analysis, and parameter selection,” *IEEE Transactions Industrial Electronics*, vol. 48, no. 1, pp. 161-168, Feb. 2001.

[113] L. Harnefors and H.-P. Nee, “Model-based current control of AC machines using the internal model control method,” *IEEE Transactions Industrial Applications*, vol. 34, no. 1, pp. 133-141, Jan./Feb. 1998.

[114] Y. A.-R. I. Mohamed and E. F. El-Saadany, “Robust high-bandwidth discrete-time predictive current control with predictive internal model – a unified approach for voltage-source PWM converters,” *IEEE Transaction on Power Electronics*, vol. 23, no. 1, pp. 126-136, Jan. 2008.

[115] P. Kundur, *Power System Stability and Control.* New York: McGraw-Hill, 1994.

[116] Y. A.-R. I. Mohamed and E. F. El-Saadany, “Adaptive decentralized droop controller to preserve power-sharing stability of paralleled-inverters in distributed generation micro-grids,” *IEEE Transaction on Power Electronics*, to appear.

[117] IEEE Recommended Practice for Industrial Commercial Power System Analysis, IEEE Standard 399-1997, 1997.

[118] P. Mahat, Chen Zhe, and B. Bak-Jensen, ”Review of islanding detection methods for distributed generation,” *In Proc. Third International Conference on Electric Utility Deregulation and Restructuring and Power Technologies*, 2008, pp. 2743 - 2748.